6-27-2022

Provenance, Composition and Transport Processes of Pleistocene-Recent Turbidite Sediments of the SE Nazca Plate, ODP Site 1232

Kimberly D. Beck
Florida International University, kbeck001@fiu.edu

FLORIDA INTERNATIONAL UNIVERSITY

Miami, Florida

PROVENANCE, COMPOSITION AND TRANSPORT PROCESSES OF PLEISTOCENE-RECENT TURBIDITE SEDIMENTS OF THE SE NAZCA PLATE, ODP SITE 1232

A dissertation submitted in partial fulfillment of

the requirements for the degree of

DOCTOR OF PHILOSOPHY

in

EARTH SYSTEMS SCIENCE

by

Kimberly Beck

2022

To: Dean Michael R, Heithaus
College of Arts, Sciences and Education

This dissertation, written by Kimberly Beck, and entitled Provenance, Composition and Transport Processes of Pleistocene-Recent Turbidite Sediments of the SE Nazca Plate, ODP Site 1232, having been approved in respect to style and intellectual content, is referred to you for judgment.

We have read this dissertation and recommend that it be approved.

_____
Laurel Collins

_____
Andrew Macfarlane

_____
Joseph Lichter

_____
Rosemary Hickey-Vargas, Major Professor

Date of Defense: June 27, 2022

The dissertation of Kimberly Beck is approved.

_____
Dean Michael R, Heithaus
College of Arts, Sciences and Education

_____
Andrés G. Gil
Vice President for Research and Economic Development
and Dean of the University Graduate School

Florida International University, 2022

DEDICATION

I dedicate my dissertation thesis to my amazingly smart and talented daughter, Skylar James. Never change the amazing person that you are and do not ever feel like you need to let the world dictate the person that you become. All of my love forever and always.

ACKNOWLEDGMENTS

First, I would like to thank my major Advisor, Dr. Rosemary Hickey-Vargas, for guiding and mentoring me as a doctoral student. Her guidance throughout these years has allowed me to become a better researcher. She has always been supportive throughout this journey and helped me with all academic matters. I am grateful to have her as my mentor and major professor.

I would also like to thank my committee members Dr. Laurel Collins, Dr. Andrew Macfarlane, and Dr. Joseph Lichter for accepting their role and for their guidance throughout the dissertation process. They have always helped me in answering my questions, giving invaluable suggestions and ideas, and supporting me on this journey.

I gratefully acknowledge Dr. Kathleen Marsaglia for contributing the original samples from Site 1232, Thomas Beasley of the Florida Center for Analytical Electron Microscopy (FCAEM) at FIU for assisting with SEM analyses, Sarah Jantzi and Ping Jiang of the Trace Evidence Analysis Facility (TEAF) at FIU for assisting with LA-ICP-MS analyses. A special thanks to Dr. Eshita Samajpati for assisting with LA-ICP-MS data collection. I would like to thank Geological Society of America and Society for Sedimentary Geology for the funding provided through the 2019 GSA Graduate Student Research Grant, and 2019 SEPM Student Research Grant. I would like to thank the department of Earth and Environment and the people, especially Gail Excell, Caridad Machado and Diane Pirie for all of their help throughout the years.

Finally, I would like to thank my wonderful friend Vanessa Londono for keeping me sane all of these years, listening to my problems and pushing me to keep moving even when it felt impossible. Thank you for ALL of the things.

ABSTRACT OF THE DISSERTATION

PROVENANCE, COMPOSITION AND TRANSPORT PROCESSES OF PLEISTOCENE-RECENT TURBIDITE SEDIMENTS OF THE SE NAZCA PLATE, ODP SITE 1232

by

Kimberly Beck

Florida International University, 2022

Miami, Florida

Professor Rosemary Hickey-Vargas, Major Professor

A 300 meter sequence of Pleistocene turbidite deposits was recovered on the Nazca Plate at the subducting edge of the Peru-Chile Trench at ODP Site 1232. Analysis of the coarsest particles in the turbidite sequences implies sediment was supplied in some proportion by terrestrial erosion and originated in the coastal, central, and Andean volcanic/magmatic belt which parallels the Southern Chilean coast, and the predominant material type is volcanic. Petrographic and geochemical analyses show that samples from 3 - 140 mbsf contain >43% fresh, angular glass. New calcareous nannofossil biostratigraphy brackets the sediment ages of the upper 288 m of cored section to between 12.47 kyr and 275 kyr. Glass compositional analyses and comparisons with geochemical data from surrounding volcanic sources in southern Chile indicate the volcanic glasses within Site 1232 turbidites originate from a single source. Elemental analyses of individual glass shards show a geochemical signature consistent with origination within the adjacent Andean Southern Volcanic Zone. Similarities in the

incompatible element averages and a strong correlation of trace element ratios coincide with published data from the Central Southern Volcanic Zone (CSVZ), more specifically the Puyehue-Cordon Caulle volcanic complex (PCCVC). Investigation into potential transport processes in Coastal Chile from the CSVZ to Site 1232 reveal that with the distance traveled (>250 km), the Site 1232 turbidites are likely to have experienced multiple transport methods. With the lack of turbidite deposition in the Holocene, despite the consistency of sediment delivered to the continental shelf by adjacent rivers, it is unlikely that the Site 1232 sediments were deposited onto the continental shelf solely by fluvial transport. Glacial shifts in wind patterns and ice distribution likely played a strong role in the dispersal and deposition of the glass shards. Understanding the origin and of the Site 1232 glass shards and how they were emplaced will help to illuminate potential volcanic hazards in South Central Chile. To improve our knowledge and develop correct hazard assessments, high-quality volcanic records are required.

TABLE OF CONTENTS

CHAPTER PAGE

LIST OF TABLES

TABLE PAGE

LIST OF FIGURES

FIGURE PAGE

ABBREVIATIONS AND ACRONYMS

%	Percent
°	Degrees
µ	Microns
°C	Degrees Celsius
Al	Aluminum
Al_2O_3	Aluminium Oxide
APC	Advanced piston corer
Ar	Argon
Ba	Barium
BHVO	Basalt, Hawaiian Volcanic Observatory
BP	Before present
BSE	Backscatter electron
cm	Centimeter
cm/yr	Centimeters per year
Ca	Calcium
CaO	Calcium Oxide
Ce	Cerium
CSVZ	Central Southern Volcanic Zone
Cr	Chromium
CR	Chile Ridge
Cs	Cesium
DI	Deionized water

Dy	Dysprosium
EDS	Energy dispersive spectroscopy
EPMA	Electron probe micro-analyzer
Er	Erbium
Eu	Europium
f_{O2}	Oxygen fugacity
FCAEM	Florida Center for Analytical Electron Microscopy
Fe	Iron
Fe^{2+}	Ferrous iron
Fe^{3+}	Ferric iron
FeO	Iron (II) oxide
Fig	Figure
FIU	Florida International University
g/cc	Grams per cubic centimeter
Gd	Gadolinium
GSA	Geological Society of America
GUC	Gunther Undercurrent
HCl	Hydrochloric acid
Hf	Hafnium
HFSE	High field strength element
Ho	Holmium
HREE	Heavy rare earth elements
Hz	Hertz

JFR	Juan Fernandez Ridge
K	Potassium
K_2O	Potassium oxide
km	Kilometers
kyr	Thousands of years
La	Lanthanum
LA-ICP-MS	Laser ablation inductively coupled plasma mass spectrometry
LGM	Last Glacial Maximum
LILE	Large ion lithophile element
LREE	Light rare earth elements
Lu	Lutetium
m	Meter
Ma	Millions of years before present
mbrf	Meters below rig floor
mbsf	Meters below sea floor
Mg	Magnesium
Mg#	Magnesium number
MgO	Magnesium oxide
MnO	Manganese oxide
MORB	Mid oceanic ridge basalt
MREE	Middle rare earth elements
my	Millions of years before present
Na	Sodium

NaO	Sodium oxide
Nb	Niobium
Nd	Neodymium
Ni	Nickel
NIST	National Institute of Standards and Technology
ODP	Ocean Drilling Program
Pb	Lead
PCCVC	Puyehue-Cordon Caulle volcanic complex
PCC	Peru-Chile Current
PCCC	Peru-Chile Countercurrent
PCCcoast	Peru-Chile Current coastal branch
PCCocean	Peru-Chile Current ocean branch
Pr	Praseodymium
Pm	Promethium
PM	Primitive mantle
ppm	Parts per million
Rb	Rubidium
REE	Rare earth elements
SE	Secondary electron
SEM-EDS	Scanning electron microscope with energy dispersive system
SEPM	Society for Sedimentary Geology
Si	Silicon
SiO_2	Silicon dioxide

SVZ	Southern Volcanic Zone
SSVZ	Southern Southern Volcanic Zone
Sm	Samarium
Sr	Strontium
T	Temperature
Ta	Tantalum
TEAF	Trace Evidence Analysis Facility
Tb	Terbium
Th	Thorium
Ti	Titanium
TiO_2	Titanium dioxide
TSVZ	Transitional Southern Volcanic Zone
U	Uranium
USGS	United States Geological Survey
UV	Ultraviolet
V	Vanadium
wt%	Weight percent
XCB	Extended core barrel
Y	Yttrium
Yb	Ytterbium
Zr	Zircon

1. Introduction

Ocean Drilling Project (ODP), Leg 202, Site 1232 located off the coast of Central Chile provides a unique opportunity to study turbidites on the seaward side of a trench. It is uncommon for turbidites to traverse a trench and therefore, infrequently documented (Lyle et al., 1997, Fouquet et al., 1998, Blumberg et.al, 2007, Völker et.al, 2008 and Bernhardt et al., 2015). The Chilean margin is an active convergent plate margin with the oceanic Nazca Plate subducting under the continental South American Plate. The Chilean Margin and Trench have been the focus of multiple studies but an in-depth investigation into the source and transport of these turbidites has yet to be seen.

Previous studies close in proximity to Site 1232 have investigated relationships between climate and sedimentation, taking into consideration the effect of glaciation and ice-sheet erosion as well as shifts in climate patterns. Galli-Oliver (1969), Lamy et al., (1998), Blumberg et al., (2008) and Völker et al., (2008) agree that climate has a strong influence on the sedimentation and turbidite distribution in this area and a large increase in sediment supply and turbidite deposition during the last glacial maximum (Hebbeln et al., 2007, Völker et al., 2008). Many have also shown a relation to the sudden change in sedimentary input and turbidite deposition corresponding with global warming and sea level rise that took place at the end of the last glaciation (Muralti et al., 2010, Völker et al., 2013, Bernhardt et al., 2017). To date, using turbidites to study the effect of erosional patterns of the Patagonian ice sheet in relation to the continent and the shelf on a single particle scale yet to be explored.

Compositionally, Site 1232 sediments have mainly been explored through bulk sediment analysis. Contamination of chemical analyses of bulk detritus is a possible

drawback of the bulk method, however, analysis of individual grains of glass and minerals could refine the data ensuring grains are not mixed. Mineralogy of the detrital sediments in and around Site 1232 is thought to be primarily controlled by composition and weathering potential of source rock, distribution of magmatism, climate and weathering in the area, and the structure of the continental margin, shelf and trench (Thornberg and Kulm 1987, Lamy et al., 1998). Typically, the trench is considered a barrier to seaward terrestrial sediment deposition, and few studies have found sediments such as turbidites, beyond the outer confines of the trench (Lyle et al., 1997, Fouquet et al., 1998, Blumberg et.al, 2007, Völker et.al, 2008 and Bernhardt et al., 2015). Terrestrial weathering of material can produce an excess of sediment to build up on the continental shelf, where it continues to build until failure leads to a mass wasting event. Weathering mechanisms such as gravity, wind, water, mud flow and ice can cause fragments of organic or inorganic particles to move and redeposit. One or more of these modes of sediment transport may have affected the depositional environment of Site 1232. Knowing the source material of these turbidites can provide unique insight into the mode of travel, time of transport and mechanism of deposition. The present study explores mineralogical and sedimentological properties of marine turbidite sediments of the Nazca Plate to decipher detailed mineralogical and geochemical composition of sediments, spatial variation, provenance, and transport pathways of terrigenous detrital sediment from South American sources.

ODP expedition Leg 202 collected samples from 11 sites based on varying sedimentation rate. At Site 1232, 416.8m of Pleistocene sediment was recovered from the Nazca Plate within the Chile Basin (Fig. 1.1). Recent examination of a set of these

samples provided by Dr. Kathleen Marsaglia (California State University, Northridge) shows shards of remarkably fresh, angular volcanic glass, in addition to mineral fragments and microfossils. The discovery of volcanic glass-bearing turbidites on the Nazca Plate is perplexing. Turbidites are commonly found on the landward side of a trench, or within the trench itself, but less commonly so on the seaward side of the trench. A limited number of studies have shown the occurrence of turbidites seaward of the trench, but little is known of the mechanisms that enabled them to travel such distance and traverse the trench. The remarkable amount of pristine volcanic glass recovered from the turbidites is intriguing, differing from any known turbidite descriptions (Cochran et al., 1989, Moore et al., 2001, Tamura et al., 2013 and Li et al., 2015). The abundant glass at Site 1232 has not been described in surrounding sites, or other known deposits.

The Leg 202 expedition intended to examine the relationships between global climate and the biological cycle on a vast scale (Mix et al., 2003). The purpose of this dissertation is to better understand the processes of erosional patterns, sediment transport and the implications for sediment deposition pathways. ***Specific objectives are to: 1) determine the materials present within the samples and the proportions of each material 2) determine the likely area of origin of the glass, minerals and microfossils given the regional geology; 3) determine how sediment sources varied over time, compared with the present; 4) use that information to infer possible pathways of sediment transport to the Nazca Plate Site; and 5) collect and use new age information to correlate with age data from previous methods and to investigate the potential relationship of Site 1232 turbidites to climatic events.***

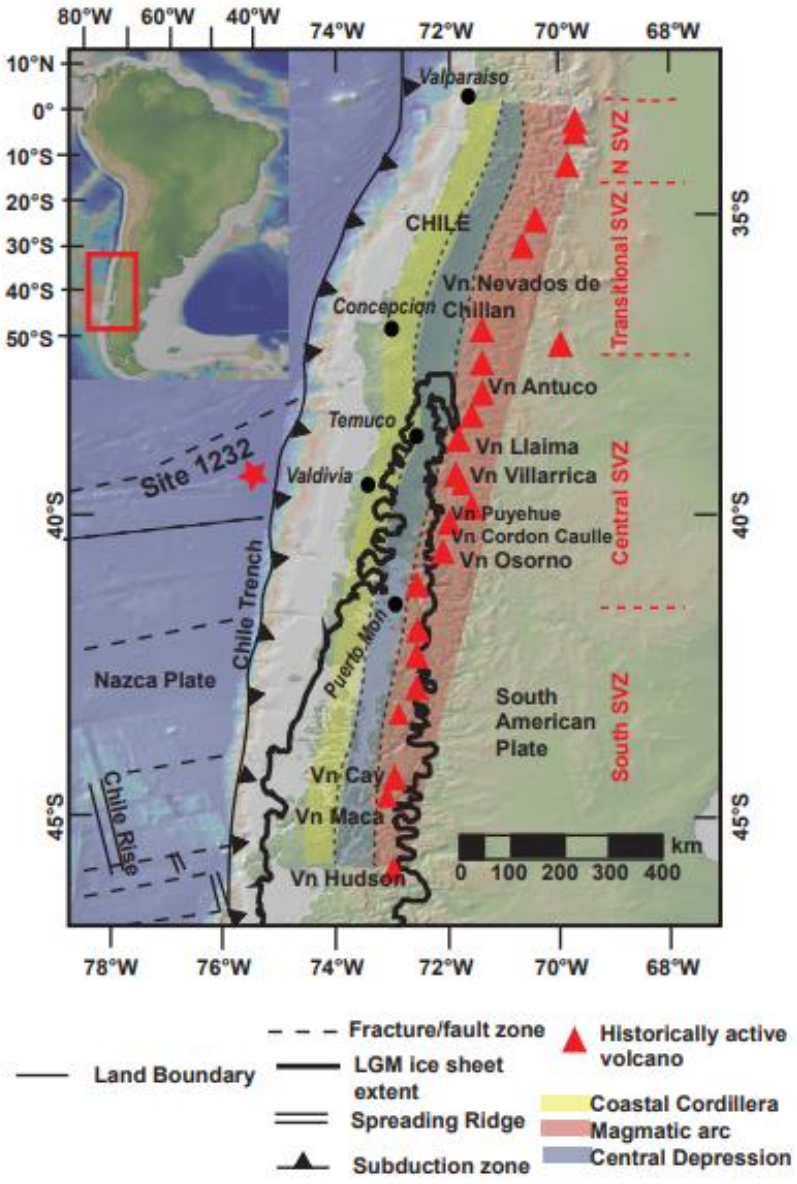

Figure 1.1: Global multi-resolution topography (GMRT) map of southwest South America (South-central Chile) and adjacent Nazca plate ocean floor showing the location of ODP Site 1232. Figure made with GeoMapApp (www.geomapapp.org). Geographic location of the 3 compositional belts of interest for sediment genesis are highlighted in yellow, blue and red. Extent of the Patagonian Ice Sheet during the Pleistocene Glacial Maximum is represented by a thick solid line, after (Porter, 1981; McCulloch et al., 2000; Hulton et al., 2002b). Triangles represent volcanoes active during the Pleistocene in the southern volcanic zone (Stern et al., 2007; Venzke, 2021)

1.1 Background Geologic history of the area

The active continental margin of Chile is produced as the oceanic Nazca Plate subducts beneath the continental South American Plate. The oceanic Nazca Plate is

beneath the South Pacific Ocean, surrounded by the Pacific, South American, Antarctic, Cocos and Caribbean plates. The Nazca Plate is moving in a slightly northeastward direction in relation to the Pacific Plate, driven by the East Pacific Rise (EPR), and with a convergence rate of ~8 cm/yr between 10°S and 40°S since 26 Ma at the convergent boundary with the South American Plate in the Peru-Chile Trench (Angermann et al., 1999). The Peru-Chile Trench spans 5,900 km along the South American coastline and ranges in depth (~5.5-8km), angle of subduction (~10°-35°) and amount of sedimentary fill (Scholl et.al., 1968, Völker et al., 2008 and 2013, and Blumberg et al., 2008). The portion of the trench from 39°S to 40°S, the focus of this study, has ~2.5 km of sedimentary trench fill and abundant deposits of turbidites (Scholl et al, 1968 and 1970, Schweller et al, Völker et al., 2008 and 2013, and Blumberg et al., 2008). Sediments have hydrothermal, biogenic, and detrital, and terrigenous sources (Dymond, 1981, Angermann et al., 1999, Völker et al., 2008 and 2013, and Blumberg et al., 2008). Differences in sediment types are attributed to current flow, proximity to the mid-ocean ridge and hydrothermal sources, differences in biogenic productivity and availability of terrigenous sediment. Increasingly rapid sediment accumulation occurs southward along the trench (Bernhardt et al., 2015 and 2016). The sedimentation rate in and around Site 1232 is high, ranging from 1,500 - 2,000 m/my (Blumberg et al., 2008, Bernhardt et al., 2015 and 2016). Earthquakes are produced as a product of subduction and can range in scale, frequency, and magnitude (Blumberg et.al, 2008). Subduction earthquakes occur when the subducting and overriding plates rub against one another in the subduction process. The crust sticks in some places, storing up energy which released in the form of earthquakes. Subduction zones are the only sources of earthquakes greater than

magnitude 8.5. The Nazca Plate subduction zone has produced a magnitude 9.5 earthquake in the past and has the potential to do so again (Blumberg et.al, 2007).

Potential sources of ocean transported sediment

Three geologic belts or zones (Fig. 1.1) that are potential sources of the turbidic sediments at Site 1232 run parallel to the coastline: the coastal metamorphic zone, the central depression and the Andean volcanic arc (lying farthest inland). The Paleozoic metamorphic basement is exposed from 32°S to 42°S along the coastal cordillera of Chile. The metamorphic complexes consist primarily of phyllite, metamorphic basement originated from both continental and oceanic sources (Jenks, 1956). The central depression between the Andean arc and the coastal metamorphic belt contains Mesozoic to Quaternary continental and marine sediments that have been heavily reworked. The central depression also houses remnants of glacial sediments and large lakes (Jenks, 1956).

South America's Southern Volcanic Zone (SVZ) of central and southern Chile runs from latitudes 33°S-46°S. The SVZ is divided into four geochemically distinct zones (Fig. 1.2): The Northern Southern Volcanic Zone (NSVZ), Transitional Southern Volcanic Zone (TSVZ), Central Southern Volcanic Zone (CSVZ), and Southern Southern Volcanic Zone (SSVZ) (Hickey et al., 2002). The NSVZ at the northernmost point of the SVZ between 33°S and 34.5°S is ~320km from the Peru-Chile Trench and is characterized by primarily andesitic volcanoes (Hickey-Vargas et al., 2016). The TSVZ spans 34.5°S to 37°S, ~320km from the Peru-Chile Trench, and is represented by largely andesitic, dacitic and rhyolitic volcanoes (Hickey-Vargas et al., 2016). The CSVZ extends from 37°S to 41.5°S, ~280km from the trench, and is composed of

predominantly basalt to basaltic andesite (Hickey-Vargas et al., 2016). The SSVZ, 41.5° to 46°, is located ~250km from the Peru-Chile Trench and is represented by volcanoes ranging in composition from rhyolite to basalt and dacite (Hickey et al., 1986).

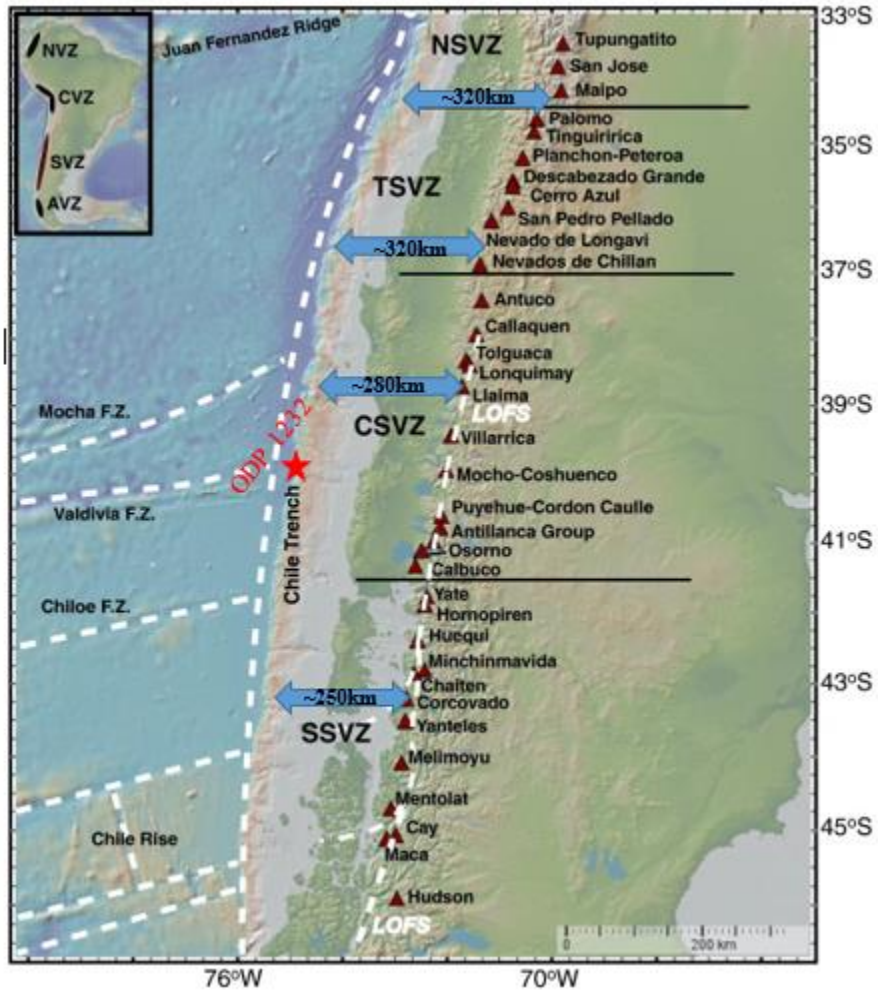

Figure 1.2: Map of Southern Volcanic zone, adapted from Hickey-Vargas et al., 2016, showing SVZ sections, Major Volcanoes and ODP Site 1232 (red star) and distance to Trench (blue arrow). NSVZ – Northern Southern Volcanic Zone, TSVZ – Transitional Southern Volcanic Zone, CSVZ – Central Southern Volcanic Zone, SSVZ – Southern Southern Volcanic Zone, F.Z. – Fracture Zone.

Rivers and submarine canyons

ODP Site 1232 lies between the openings of the Bueno and Calle Calle submarine canyons which are the product of erosion by outflow from the rivers of the same names. Through submarine canyons fluvial sediments can be transported great distances. The

rivers cut across central/southern Chile, originating at lakes and cutting through Paleozoic metamorphic basement, Carboniferous to Permian marine sediments, Jurassic intrusives, Jurassic-Upper Tertiary intrusives, Eocene-Miocene continental sediments, Miocene-Pliocene marine sediments, Pliocene-Pleistocene volcanics and Quaternary continental and marine sediments. Both the Calle Calle and Bueno rivers travel through ultramafic bodies, volcanic calderas, dacite-rhyolite volcanics, basalt-andesite volcanics, andesitic volcanics and areas of active volcanism.

Change in ice coverage and shoreline through the Pleistocene

Glaciers are responsible for extensive weathering of the continental terrane producing large quantities of mixed sedimentary detritus. Widespread glaciation in the central and southern portions of Chile in the Quaternary was responsible for several geographic features (Jenks, 1956). It has been suggested that during the Pleistocene there were at least 10 separate glaciations that affected the Patagonian ice sheet of South America (Glasser and Jansson, 2008). During the Last Glacial Maximum in the Pleistocene, the Patagonian ice sheet almost entirely covered central and southern Chile (seen in Fig. 1.1 in dashed line) (Glasser and Jansson, 2008). Beginning at ~39°S, the ice sheet extended into the coastal cordillera, and below ~41°S the ice sheet extended past the Chilean coastline, up to ~40km in some areas (Melnick and Echtler, 2006, and Glasser and Jansson, 2008). As temperatures began to warm in the late Pleistocene, the Patagonian ice sheet began to melt and recede.

1.2 Core Collection at Site 1232

ODP expedition Leg 202 collected cores used in this study. Leg 202 investigated the relationships between global climate and the biological cycle on a vast scale (Mix et

al., 2003). The researchers chose Site 1232, the focus of this study, because it was calculated to display a high rate of sedimentation on average, around 1,500-2,000 m/my (Woollard et al. 1981). Site 1232 is at 39°53.45', 75°54.08'W on the Nazca Plate, off the coast of Chile. The expedition retrieved three cores from Site 1232: 1232A, 1232B and 1232C. Hole A, the deepest recovery for the three at this Site, was drilled on the seafloor with a starting depth of 4089 mbrf (meters below rig floor). First deployed was a piston corer which drilled to a maximum depth of 112.5 mbsf (meters below seafloor) before drilling became too difficult, resulting in replacement by an extended core barrel and the hole continued from 112.5-371.3 mbsf. For Hole B, drilling began on the seafloor at a depth of 4075 mbrf; a piston corer was used to a depth of 90.1 mbsf where the hole was terminated. Similarly, Hole C originated at a seafloor depth of 4079.8 mbrf and a piston core drilled to a depth of 33.2 mbsf where the hole terminated.

1.3 Previous work on shelf and trench sediments near Site 1232

Chemical and mineralogical composition of sediments on the shelf and within the Peru-Chile Trench is determined by: topography of the continental margin and trench, mineralogical composition and erodibility of the source material, climate patterns, and the distribution and composition of regional volcanism (Thornberg and Kulm, 1987, Lamy et al., 1987, Völker et al., 2008). Thornberg and Kulm (1987) used gross variations in bulk composition, heavy mineral separation and ideal end-member petrofacies to characterize diversity and petrologic composition of the sands within the Peru-Chile Trench. They determined that contemporary volcanism has the potential to inundate and dominate the mineral assemblage and dilute contributions from other sources creating low diversity in some areas (Thornberg and Kulm, 1987). Conversely, where glaciation

was extensive, a variety of source-rocks were actively weathered, creating high diversity petrofacies that were deposited into the adjacent trench (Thornberg and Kulm, 1987). The Peru-Chile Trench, between the Juan Fernandez Ridge (JFR) and the Chile Rise (CR), has an increased volume of sedimentary infill (Figure 1.3) of up to 2.5m thickness in some areas. The large increase in sediment deposition between the JFR and CR caused a change in the convergent margin from erosional to accretionary (Melnik and Echtler, 2006). A massive accumulation of turbidite deposits is located within the trench between the JFR and CR (Thornberg and Kulm, 1987, Völker et al., 2008, Blumberg 2008). Transport of sediment encompasses a wide range of possibilities including river flow through submarine canyons, mass wasting, latitudinal movement within the trench, and transport within underwater currents. Völker et al., (2006) and Raitzch et al., (2007) agree that the principal mode of transport is large mass wasting events, leading to slumping and debris flow as seen in the Reloca Slide (Völker et al., 2009). The materials are then transported within submarine canyons, axial channels or by coast-parallel bottom currents (Völker et al., 2006, Raitzch et al., 2007, Bernhardt et al., 2016).

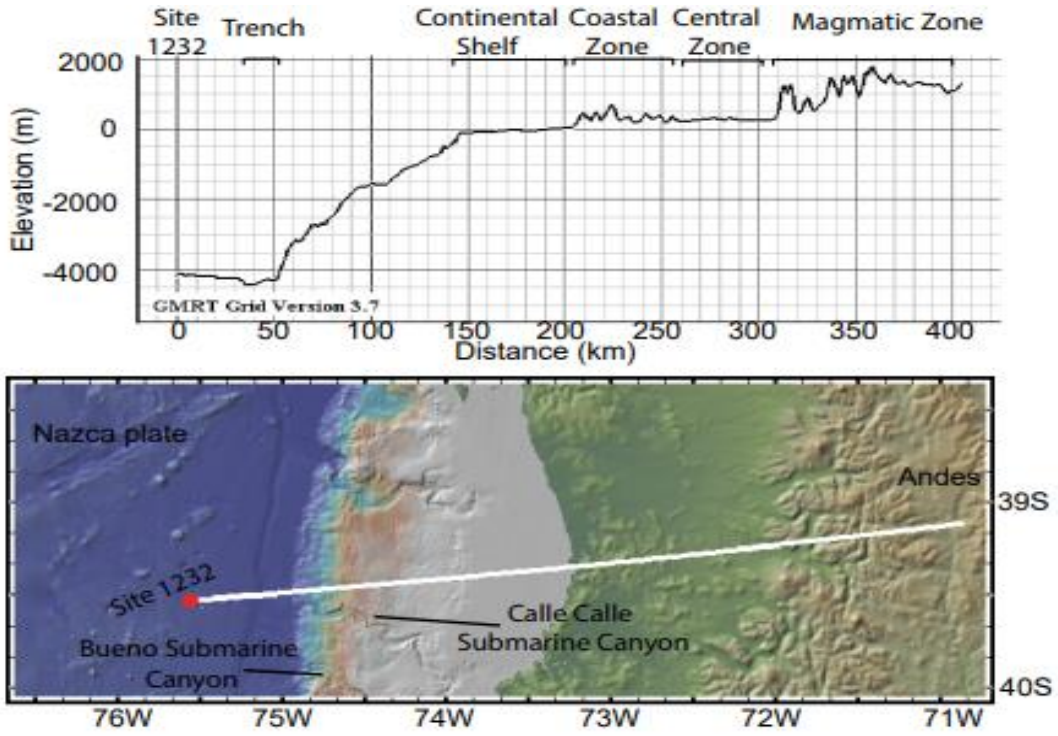

Figure 1.3: a. Topographic/bathymetric cross section from Nazca plate Site 1232 across the Peru-Chile Trench, continental slope and shelf to the Andean Southern Volcanic Zone. b. The line of the section. Figure made with GeoMapApp (www.geomapapp.org). The different geologic belts indicated by brackets at the top.

Investigation of regional distribution patterns and grain size in relation to weathering, sediment input and source rocks indicates that variation was primarily controlled by source material and secondarily controlled by climate (Lamy et al., 1998). Bulk sediment analysis using x-ray powder diffraction (XRD) completed on sediments along the Chilean coast showed clear latitudinal variations in the presence of clay minerals (Lamy et al., 1998). These variations are interpreted to represent variations in weather and relate to different climate zones present in Chile (Lamy et al., 1998). The onset of glacial erosion of sediments by the Patagonian ice sheet caused a marked increase of sediment supply to the shelf and trench (Melnik and Echtler, 2006, Hebbeln et al., 2007 and Muralti et al., 2010). Bulk sediment chemistry completed on marine, and

less effectively river, samples showed a higher concentration of Andean-type material being weathered during times of glacial advance and lower concentrations during glacial retreat (Muralti et al., 2010). This effectively shows that the ice sheet erosion produces a large amount of terrigenous sediment deposited into marine environments, and furthermore plays an active role in the type of material being weathered (Muralti et al., 2010).

Blumberg et al. (2008) completed $\delta^{18}O$ analysis on *G. bulloides* from a subset of samples from Site 1232, they were able to correlate the ages of six turbidite layers with the well-dated oxygen isotope record of core MD-97-2120 from the southwestern Pacific. An age of 12.4 kyr was recorded for 0.6 mcd and an age of 138 kyr for 96.8 mcd (Blumberg et al., 2008). However, Blumberg was unable to date some of the turbidite layers using $\delta^{18}O$ due to a lack of abundance of *G. bulloides,* making it difficult to correlate with oxygen isotope stages and show relation of the turbidites recurrence rate with known seismic events.

1.4 Hypotheses

Hypotheses that will be addressed with the single particle approach are as follows. 1.) Glasses found in turbidites at ODP Site 1232 originated from the Andean magmatic arc. If they came from the arc, the trace element signatures will match those signatures expected from arc settings. 2.) Studies have shown that the major and trace element composition of volcanic glasses can be used in comparison with published data for known volcanic centers to establish their provenance. If the Site 1232 glasses originate from the Andean magmatic arc, then the major and trace elements of the Site 1232 shards can be compared to known data for the SVZ arc regions and a source region or regions

can be established. 3.) Glacial processes contributed to the transport of sediments from the magmatic arc to the continental shelf and then were subsequently carried by turbidity flow. If sediments were glacially transported, sediments would have originated in an area that was affected by glacial processes. The physical appearance of grains would be small, sharp and angular, and show textures commonly seen in glacially transported sediment.

1.5 Overview of Methodology

Sample collection, preparation

Twenty-nine total samples from expedition 202 Site 1232 were utilized in this study. The coarseness of the sediments is sandy silt-sized particles or coarser, and the thickness of the coarse layer is at least 10 cm. Visual inspection of the core photos should show a structure that is representative of turbidites, with characteristic fining upward and a sharp basal contact between turbidite layers and fine pelagic sediments. Sediment samples were dry-sieved to the sediment grain size fraction >63 microns and sent to Dr. Rosemary Hickey-Vargas for exploration and analysis. The coarsest particles (149-210 microns) in the turbidite sequences were utilized. Analysis of the coarsest sandy silt or coarser samples allowed for analysis on an individual particle scale. The following procedure was used throughout the study to prepare the samples for microscopic examination and chemical analysis.

a) Samples were wet sieved to clean and separate grains. An ultrasonicator was used to clean and loosen any silt. Once cleaned, the samples were dried in an oven.

b) Samples viewed under a binocular microscope to identify glassy grains and minerals. Grains with appearance of glass were observed under a petrographic microscope to look for isotropic properties. Isotropic grains mounted on carbon tape.

c) Individual glass and mineral grains were analyzed for major elements using SEM with energy dispersive spectrometer (EDS).

d) Select glass grains were analyzed for trace elements using the LA-ICP-MS.

e) Smear slides were made to aid in the identification of minerals and determine the presence microfossils within the samples, and help to determine the relative abundances of minerals, glass and microfossils. Point counts of glass, clear minerals, mafic minerals, polymineralic grains and felsic polymineralic grains were done using gridded smear slides to allow for determination of proportions of sediment constituents present in the samples.

f) Benthic and planktonic foraminifera are often good indicators of oceanic water depth. Some species are indicative of a habitat and can show changes in depth and environment within an individual sample and throughout the core. Both the planktonic and benthic foraminifera were picked from each sample in this study to determine if there a combination of both shallow-water and deep-water species.

g) Fine-grained samples of corresponding intervals were sent to BugWare of Tampa to study calcareous nannofossils for calcareous nannofossil biostratigraphy.

1.6 Analytical techniques

Scanning electron microscope (SEM)

Volcanic glass shards of both the >149 micron size fraction and the 210 micron size fraction were analyzed for major elements using SEM energy dispersive spectroscopy (EDS). Although SEM-EDS analysis is semi-quantitative, this approach was selected rather than more precise electron probe microanalysis (EPMA) because it was more likely that trace element patterns rather than major element criteria would be

distinctive for identifying a specific volcanic source. Therefore, every effort was made to preserve the small and highly vesicular samples for later LA-ICPMS trace element analysis. Preparing glasses for EPMA requires mounting in epoxy and surface polish which would have resulted in significant loss of material.

Secondary electron (SE) imaging was used to obtain high resolution images of glass shards and grains for examination of texture and backscatter electron imaging (BSE) was used to look for microcrystals and to assess homogeneity. Once identified, homogenous areas of glass were analyzed with the EDS. Grains were analyzed using a 39 micron spot size under high vacuum with a 15kv accelerating voltage; an average of two to three spots were analyzed on each grain depending on grain size. Glass analyses were performed with reference materials Rhyolite (Smithsonian standard NMNH 72854, VG 568), and Hawaiian basaltic glass (BHVO-2) which were run at the beginning, middle and end of each analytical session. The average of three readings was taken for each reference material.

Laser ablation inductively coupled plasma mass spectrometry (LA-ICP-MS)

After SEM with EDS analysis, 119 grains from the 210 micron size fraction were analyzed for trace elements using the LA-ICP-MS (ELAN DRC ICP/MS and New Wave UP 213 nm laser ablation system) at the Trace Evidence Analysis Facility (TEAF), FIU. An additional 95 grains from the > 210 micron fraction from both 1232A and 1232B were analyzed for trace elements using the Aligent Technologies 7700 Series LA-ICP-MS at TEAF, FIU. This size fraction was chosen in order to allow for the maximum surface for repeat analyses. Glasses were analyzed for the trace elements Rb, Sr, Y, Zr, Nb, Ba, La, Ce, Nd, Sm, Eu, Gd, Dy, Er, Yb, Hf, Pb, Th, and U, as well as for the major

element Ti, for comparison with SEM data.

Instrumentation parameters used during LA-ICP-MS glass analysis for both the ELAN and the Aligent laser ablation systems are as follows: a 55 micron laser spot size with a repetition rate of 5hz and dwell time of 60 seconds. Ca was used as the internal standard, NIST (National Institute of Standards and Technology), SRM612 glass was used for calibration, and both NIST SRM 612 and BHVO-2 glass were used to monitor drift during analysis. At least two 55-micron spots were ablated on each grain whenever possible and the data for the two points averaged. In some cases grains were too small or not ideal to make a second ablation and a few grains had breakage during ablation resulting in poor signal collection; in those instances, only one ablation was used. Data reduction was performed using 'Glitter' software (Griffin et al., 2008) with the NIST SRM612 as a standard with the Ca data obtained from the individual glass grains by SEM entered manually.

1.7 Dissertation Structure

The dissertation has three chapters following the Introduction and then the general Conclusions. Each chapter is written in a manuscript style, which includes the objective, methods and results to answer questions about the ODP Site 1232 turbidite sediments.

1) Introduction

2) Chapter 2 - Composition, Age and Origin of Pleistocene Turbidite Deposits at ODP Site 1232, Nazca Plate: implications for Volcanism and Climate Change in Central South Chile

3) Chapter 3- Origin of volcanic glass in turbidite sediments from ODP Site 1232, Nazca Plate: Insights into Pleistocene volcanism in southern South America

4) Chapter 4- Dispersal Patterns and Sediment Transport Processes of Volcanic Glasses of ODP Site 1232: A Source to Sink Comparative Study

5) Chapter 5- General conclusions

1.8 References

Adams, J., 1990, Paleoseismicity of the Cascadia Subduction Zone: Evidence from turbidites off the Oregon-Washington Margin: Tectonics, v. 9, p. 569–583, doi: 10.1029/tc009i004p00569.

Angermann, D., J. Klotz, and C. Reigber, Space-geodetic estimation of the Nazca-South America angular velocity, Earth Planet. Sci. Lett., 171, 329– 334, 1999.

Bernhardt, A., Melnick, D., Hebbeln, D., Lückge, A., and Strecker, M.R., 2015, Turbidite paleoseismology along the active continental margin of Chile – Feasible or not? Quaternary Science Reviews, v. 120, p. 71–92, doi: 10.1016/j.quascirev.2015.04.001.

Bernhardt, A., Hebbeln, D., Regenberg, M., Lückge, A., and Strecker, M.R., 2016, Shelfal sediment transport by an undercurrent forces turbidity-current activity during high sea level along the Chile continental margin: Geology, v. 44, p. 295–298, doi: 10.1130/g37594.1.

Bernhardt, A., Schwanghart, W., Hebbeln, D., Stuut, J.-B.W., and Strecker, M.R., 2017, Immediate propagation of deglacial environmental change to deep-marine turbidite systems along the Chile convergent margin: Earth and Planetary Science Letters, v. 473, p. 190–204, doi: 10.1016/j.epsl.2017.05.017.

Blumberg, S., Lamy, F., Arz, H., Echtler, H., Wiedicke, M., Haug, G., and Oncken, O., 2008, Turbiditic Trench deposits at the South-Chilean active margin: A Pleistocene–Holocene record of climate and tectonics: Earth and Planetary Science Letters, v. 268, p. 526–539, doi: 10.1016/j.epsl.2008.02.007.

Cochran, J.R., Stow, D.A.V., et al., 1989. Proc. ODP, Init. Repts., 116: College Station, TX (Ocean Drilling Program). doi:10.2973/odp.proc.ir.116.1989

Dymond, J., 1981, Geochemistry of Nazca Plate surface sediments: An evaluation of hydrothermal, biogenic, detrital, and hydrogenous sources: Geological Society of America Memoirs Nazca Plate: Crustal Formation and Andean Convergence, p. 133–174, doi: 10.1130/mem154-p133.

Fouquet, Y., Zierenberg, R.A., Miller, D.J., et al., 1998. Proc. ODP, Init. Repts., 169: College Station, TX (Ocean Drilling Program). doi:10.2973/odp.proc.ir.169.1998

Glasser, N., and Jansson, K., 2008, The Glacial Map of southern South America: Journal of Maps, v. 4, p. 175–196, doi: 10.4113/jom.2008.1020. Selected General References on South American Geology, 1956, Geological Society of America Memoirs Handbook of South American Geology: An Explanation of the Geologic Map of South America, p. xi-xii, doi: 10.1130/mem65-pxi.

Galli-Olivier, C., 1969, Climate: A Primary Control of Sedimentation in the Peru-Chile Trench: Geological Society of America Bulletin, v. 80, p. 1849, doi: 10.1130/0016-7606(1969)80[1849:capcos]2.0.co;2.

Hebbeln, D., Lamy, F., Mohtadi, M., and Echtler, H., 2007, Tracing the impact of glacial-interglacial climate variability on erosion of the southern Andes: Geology, v. 35, p. 131, doi: 10.1130/g23243a.1.

Hickey, R.L., Frey, F.A., Gerlach, D.C., and Lopez-Escobar, L., 1986, Multiple sources for basaltic arc rocks from the southern volcanic zone of the Andes (34°–41°S): Trace element and isotopic evidence for contributions from subducted oceanic crust, mantle, and continental crust: Journal of Geophysical Research, v. 91, p. 5963, doi: 10.1029/jb091ib06p05963.

Hickey-Vargas, R., Holbik, S., Tormey, D., Frey, F.A., and Roa, H.M., 2016, Basaltic rocks from the Andean Southern Volcanic Zone: Insights from the comparison of along-strike and small-scale geochemical variations and their sources: Lithos, v. 258-259, p. 115–132, doi: 10.1016/j.lithos.2016.04.014.

Hulton, N.R.J., Purves, R.S., McCulloch, R.D., Sugden, D.E., and Bentley, M.J., 2002b, The Last Glacial Maximum and deglaciation in southern South America: Quaternary Science Reviews, v. 21, doi:10.1016/S0277-3791(01)00103-2.

Jenks, W.F., Selected General References on South American Geology, 1956, Geological Society of America Memoirs Handbook of South American Geology: An Explanation of the Geologic Map of South America, p. xi-xii, doi: 10.1130/mem65-pxi.

Karlin, R.E., and Abella, S.E.B., 1992, Paleoearthquakes in the Puget Sound Region Recorded in Sediments from Lake Washington, U.S.A: Science, v. 258, p. 1617–1620, doi: 10.1126/science.258.5088.1617.

Lamy, F., Hebbeln, D., and Wefer, G., 1998, Terrigenous sediment supply along the Chilean continental margin: modern regional patterns of texture and composition: Geologische Rundschau, v. 87, p. 477–494, doi: 10.1007/s005310050223.

Li, C., Arndt, N.T., Tang, Q., and Ripley, E.M., 2015, Trace element indiscrimination diagrams: Lithos, v. 232, p. 76–83, doi: 10.1016/j.lithos.2015.06.022.

Lyle, M., Koizumi, I., Richter, C., et al., 1997. Proc. ODP, Init. Repts., 167: College Station, TX (Ocean Drilling Program). doi:10.2973/odp.proc.ir.167.1997

McCulloch, R.D., Bentley, M.J., Purves, R.S., Hulton, N.R.J., Sugden, D.E., and Clapperton, C.M., 2000, Climatic inferences from glacial and palaeoecological evidence at the last glacial termination, southern South America: Journal of Quaternary Science, v. 15, doi:10.1002/1099-1417(200005)15:4<409::aid-jqs539>3.0.co;2-%23.

Melnick, D., and Echtler, H.P., 2006, Inversion of forearc basins in south-central Chile caused by rapid glacial age Trench fill: Geology, v. 34, p. 709, doi: 10.1130/g22440.1.
Mix, A.C., Tiedemann, R., Blum, P., Lund, S.P., Stoner, J.S., Proceedings of the Ocean Drilling Program, 202 Initial Reports, 2003, Proceedings of the Ocean Drilling Program, doi: 10.2973/odp.proc.ir.202.2003.

Moernaut, J., Daele, M.V., Heirman, K., Fontijn, K., Strasser, M., Pino, M., Urrutia, R., and Batist, M.D., 2014, Lacustrine turbidites as a tool for quantitative earthquake reconstruction: New evidence for a variable rupture mode in south central Chile: Journal of Geophysical Research: Solid Earth, v. 119, p. 1607–1633, doi: 10.1002/2013jb010738.

Muratli, J.M., Chase, Z., Mcmanus, J., and Mix, A., 2010, Ice-sheet control of continental erosion in central and southern Chile (36°–41°S) over the last 30,000 years: Quaternary Science Reviews, v. 29, p. 3230–3239, doi: 10.1016/j.quascirev.2010.06.037.

Porter, S.C., 1981, Pleistocene glaciation in the southern Lake District of Chile: Quaternary Research, v. 16, doi:10.1016/0033-5894(81)90013-2.

Scholl, D.W., Christensen, M.N., Huene, R.V., and Marlow, M.S., 1970, Peru-Chile Trench Sediments and Sea-Floor Spreading: Geological Society of America Bulletin, v. 81, p. 1339, doi: 10.1130/0016-7606(1970)81[1339:ptsass]2.0.co;2.

Schweller, W.J., Kulm, L.D., and Prince, R.A., 1981, Tectonics, structure, and sedimentary framework of the Peru-Chile Trench: Geological Society of America Memoirs Nazca Plate: Crustal Formation and Andean Convergence, p. 323–350, doi: 10.1130/mem154-p323.

Stern, C.R., Moreno, H., López-Escobar, L., Clavero, J.E., Lara, L.E., Naranjo, J.A., Parada, M.A., and Skewes, M.A., 2007, Chilean volcanoes: Geological Society Special Publication, doi:10.1144/goch.5.

St-Onge, G., Mulder, T., Piper, D.J., Hillaire-Marcel, C., and Stoner, J.S., 2004, Earthquake and flood-induced turbidites in the Saguenay Fjord (Québec): a Holocene paleoseismicity record: Quaternary Science Reviews, v. 23, p. 283–294, doi: 10.1016/j.quascirev.2003.03.001.

Tamura, Y., Busby, C., and Blum, P., 2013. Izu-Bonin-Mariana Rear Arc: the missing half of the subduction factory. International Ocean Discovery Program Scientific Prospectus, 350. http://dx.doi.org/10.2204/iodp.sp.350.2013

Thornburg, T.M., Kulm, L.D., and Hussong, D.M., 1990, Submarine-fan development in the southern Chile Trench: A dynamic interplay of tectonics and sedimentation: Geological Society of America Bulletin, v. 102, p. 1658–1680, doi: 10.1130/0016-7606(1990)102<1658:sfdits>2.3.co;2.

Todd M. Thornburg, Laverne D. Kulm, 1987, Sedimentation in the Chile Trench: Petrofacies and Provenance: SEPM Journal of Sedimentary Research, v. Vol. 57, doi: 10.1306/212f8aa3-2b24-11d7-8648000102c1865d.

Venzke, E. (ed.), 2021, Global Volcanism Program, 2013: Volcanoes of the World v. 4.9.4,.

Völker, D., Reichel, T., Wiedicke, M., and Heubeck, C., 2008, Turbidites depoSited on Southern Central Chilean seamounts: Evidence for energetic turbidity currents: Marine Geology, v. 251, p. 15–31, doi: 10.1016/j.margeo.2008.01.008.

Völker, D., Weinrebe, W., Behrmann, J. H., Bialas, J., and Klaeschen, D.: Mass wasting at the base of the south central Chilean continental margin: the Reloca Slide, Adv. Geosci., 22, 155–167, https://doi.org/10.5194/adgeo-22-155-2009, 2009.

Völker, D., Geersen, J., Contreras-Reyes, E., and Reichert, C., 2013, Sedimentary fill of the Chile Trench (32–46°S): volumetric distribution and causal factors: Journal of the Geological Society, v. 170, p. 723–736, doi: 10.1144/jgs2012-119.

Woollard, G.P., and Kulm, L.D., 1981, History of the Nazca Plate Project: Geological Society of America Memoirs Nazca Plate: Crustal Formation and Andean Convergence, p. 3–24, doi: 10.1130/mem154-p3.

2. COMPOSITION, AGE AND ORIGIN OF PLEISTOCENE TURBIDITE DEPOSITS AT ODP SITE 1232, NAZCA PLATE: IMPLICATIONS FOR VOLCANISM AND CLIMATE CHANGE IN CENTRAL SOUTH CHILE

Abstract

Along the South American coast of Chile, Pleistocene to Recent marine sediments reflect complex sources associated with transport by riverine input, coastal runoff, glacial meltwater, and turbidite plumes. Pleistocene age turbidites were recovered at ODP (Ocean Drilling Program) Site 1232 on the Nazca Plate across the Peru-Chile Trench. Coarsest sediments within the turbidites (<300μ) contain anomalously large amounts of fresh, angular volcanic glass. This study investigated the variation in proportions of glass, minerals, and microfossils downcore with the goal of discerning temporal changes and their underlying causes. Petrographic and geochemical analyses show that samples from 3 to 140 mbsf contain >43% fresh angular glass and that in samples at >140 mbsf, glass decreases significantly and magnetite-bearing clay-rich granules are the dominant coarse particle type. Other phases are devitrified glass, lithic fragments, quartz, feldspar, pyroxene, chlorite, and biotite mica. Based on optical and X-ray imaging, glass grains are fresh and undevitrified. Elemental analyses of individual glass grains show a geochemical signature consistent with origination within the adjacent Andean Southern Volcanic Zone. New calcareous nannofossil biostratigraphy brackets the sediment ages of the upper 288 m of cored section to between 12.47 kyr and 275 kyr.

Analysis of the coarsest particles in the turbidite sequences implies sediment was supplied by erosion and originated in the coastal, central, and Andean volcanic/magmatic belt which parallel the Southern Chilean coast, with the largest proportion of material

being volcanic in origin. A previously undescribed compositional change in the section is a gradual increase in the abundance of fresh, angular glass shards, beginning at 160 mbsf (20% glass in the >149μ fraction) to >43% glass above 140 mbsf, whereas samples below 214 mbsf are made up entirely of altered pumice particles. This change corresponds roughly with a shift from interglacial to glacial conditions in the interval from 214 to 140 mbsf, based on the new ages. One scenario for the shift in sedimentary composition is a change in volcanic activity or the composition of erupted volcanic material directly resulted in differences in volcanic ejecta deposited in turbidite samples at Site 1232. An alternative scenario is that a change in sediment transport pathway or supply associated with the glacial cycles caused a change in the volcanic material reaching the continental shelf. I propose that a combination of processes is likely responsible for compositional changes in the Site 1232 turbidites.

Keywords:
Chile, turbidites, volcanic glass, Nazca Plate, Site 1232, Pleistocene

2.1 Introduction

Pleistocene-Recent sediments drilled offshore of Chile on Ocean Drilling Program (ODP) Leg 202 reflect origination from complex sources and are associated with transport by riverine input, coastal runoff, glacial meltwater, glacial deposition, and turbidite plumes (Galli-Oliver, 1969; Lamy et al., 1998; Völker et al., 2006, 2008; Blumberg et al., 2008). At ODP Site 1232, seaward of the Peru-Chile Trench on the Nazca Plate (Fig. 2.1), a 300-meter sequence of Pleistocene age turbidites was recovered (Mix et al., 2003). The coarsest sediments from turbidite intervals (sandy silt, 30-300 microns) contain large amounts of fresh, angular, volcanic glass, together with

mineral fragments and microfossils. The mineralogy of Nazca Plate (seafloor) glacial turbidite sediments are a useful tool in understanding subglacial and glacial marine processes occurring in continental, subduction, and oceanic environments (Völker et al., 2013; Bernhardt et al., 2016, 2017). The composition of the source region is reflected in the accumulation of characteristic detrital minerals; therefore, diversity in sediment type and abundance deposited in this complex area can provide a detailed record of the evolution of the landscape and allow for the reconstruction of dynamic sediment transport mechanisms (Giorgetti et al., 2009). With the purpose of understanding variations in sediment sources, transport, and depositional processes over the period of time encompassed by the core, the coarsest intervals of turbidite sequences downcore at Site 1232 were examined to define their distribution and textural properties, characterize the mineralogy, and the geochemistry of major elements and trace elements in glasses.

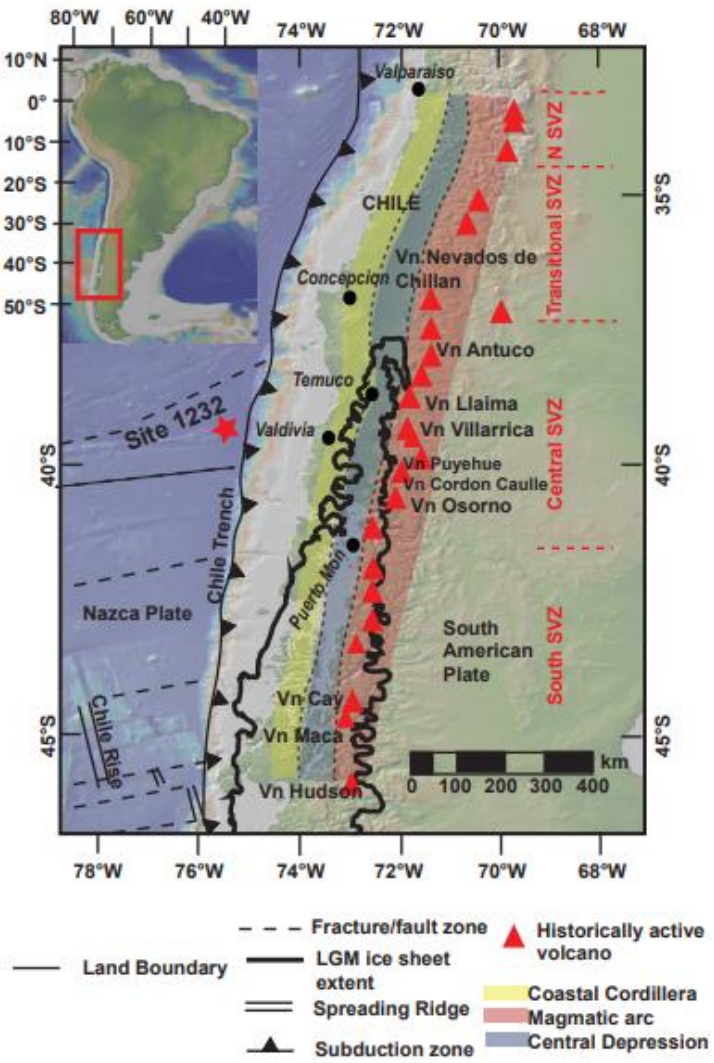

Figure 2.1: Global multi-resolution topography (GMRT) map of southwest South America (South-central Chile) and adjacent Nazca plate ocean floor showing the location of ODP Site 1232. Figure made with GeoMapApp (www.geomapapp.org). Geographic location of the 3 compositional belts of interest for sediment genesis are highlighted in yellow, blue and red. Extent of the Patagonian Ice Sheet during the Pleistocene Glacial Maximum is represented by a thick solid and dashed line, after (Porter, 1981; McCulloch et al., 2000; Hulton et al., 2002b). Triangles represent volcanoes active during the Pleistocene in the southern volcanic zone (Stern et al., 2007; Venzke, 2021)

2.2 Geologic Background

2.2.1 Geologic history of the area

The active continental margin of Chile is produced as the oceanic Nazca Plate subducts beneath the continental South American Plate. The oceanic Nazca Plate is

located in the South Pacific Ocean, surrounded by the Pacific, South American, Antarctic, Cocos, and Caribbean plates. The Nazca Plate is moving in a slightly northeastward direction in relation to the Pacific Plate, driven by the East Pacific Rise (EPR), and with a convergence rate of ~8 cm/yr between 10°S and 40°S since 26 Ma at the convergent boundary with the South American Plate in the Peru-Chile Trench (Angermann et al., 1999). The Peru-Chile Trench spans 5,900 km along the South American coastline and ranges between (~5.5-8km) in depth, (~10°-35°) angle of subduction, and amount of sedimentary fill (Scholl et al, 1968 and 1970, Schweller et al, Völker et al., 2008 and 2013, and Blumberg et al., 2008).

2.2.2 Overview of Site 1232

ODP Site 1232 is located on the Nazca Plate at 39°53.45', 75°54.08'W, and 230km off the coast of Chile, near the Bueno and Calle Calle submarine canyons. The portion of the trench from 39°S to 40°S, adjacent to Site 1232, has ~2.5 km of sedimentary trench fill (Fig. 2.2) and abundant deposits of turbidites (Scholl et al., 1970; Schweller et al., 1981; Thornburg and Kulm, 1987). Increasingly rapid sediment accumulation occurs southward along the trench (Schweller et al., 1981). The sedimentation rate in and around Site 1232 is high, ranging from 1,500 - 2,000 m/my (Schweller et al., 1981). Nazca plate sediments have hydrothermal, biogenic, detrital, and terrigenous sources (Dymond, 1981; Todd M. Thornburg, L. D. Kulm, 1983). Differences in sediment types are attributed to transport through the cold-water Humboldt current, proximity to the mid-ocean ridge and hydrothermal sources, differences in biogenic productivity, and availability of terrigenous sediment.

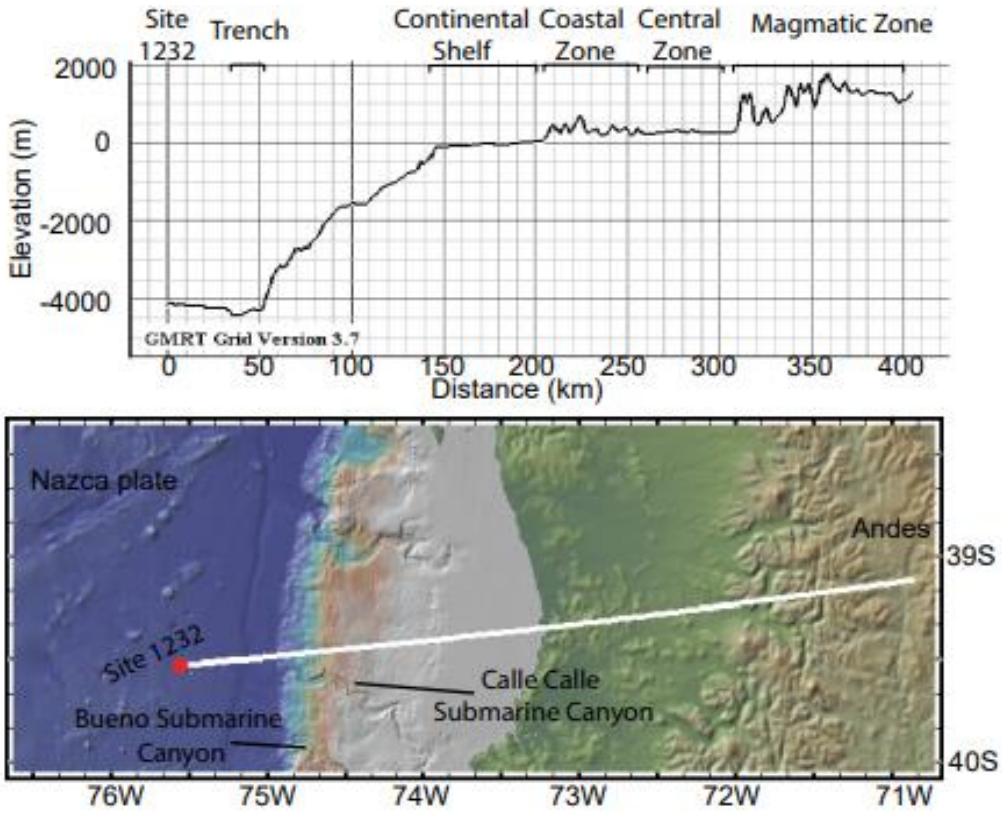

Figure 2.2: a. Topographic/bathymetric cross section from Nazca plate Site 1232 across the Peru-Chile trench, continental slope and shelf to the Andean Southern Volcanic Zone. The line of the section is shown in b. Figure made with GeoMapApp (www.geomapapp.org). The different geologic belts indicated by brackets at the top.

The cores recovered during ODP expedition Leg 202 were used in this study. The purpose of Leg 202 was to investigate the relationships between climate and oceanographic changes and biogeochemical cycles in the southeast Pacific (Mix et al., 2003). Site 1232, on the Nazca plate, was chosen to examine the long-term Neogene response to significant climate and tectonic events (Mix et al., 2003). Hemipelagic sediments were expected; instead, a >300m sequence of Pleistocene turbidites was recovered (Mix et al., 2003). Site 1232 was determined to be of Pleistocene age, < 0.78 Ma using paleomagnetic polarity measurements and 0.46-1.69 Ma using biostratigraphic analysis (Mix et al., 2003). Sediment recovered was predominantly gray to green silty

clay interbedded with black to gray normally graded sandy-silt to silty-sand layers (Mix et al., 2003). The expedition retrieved three cores from Site 1232: 1232A, 1232B, and 1232C. The deepest recovery for the three at this Site, Hole A, was drilled on the seafloor with a starting depth of 4089 mbrf (meters below rig floor) (Fig. 2.3).

First deployed was a piston corer (APC) which drilled to a maximum depth of 112.5 mbsf (meters below seafloor) before drilling became too difficult, resulting in replacement by an extended core barrel (XCB), and the hole continued from 112.5-371.3 mbsf (Mix et al., 2003). For Hole B, drilling began on the seafloor at a depth of 4075 mbsf; a piston corer was used to a depth of 90.1 mbsf where the hole was terminated (Mix et al., 2003). Hole C was a shallow recovery hole drilled at a depth of 4079.8 mbrf using a piston corer to a depth of 33.2 mbsf (Mix et al., 2003). The shipboard was able to correlate the upper 42.58 m of the 1232A and 1232B cores in a composite section using stratigraphic correlation and magnetic susceptibility (Mix et al., 2003).

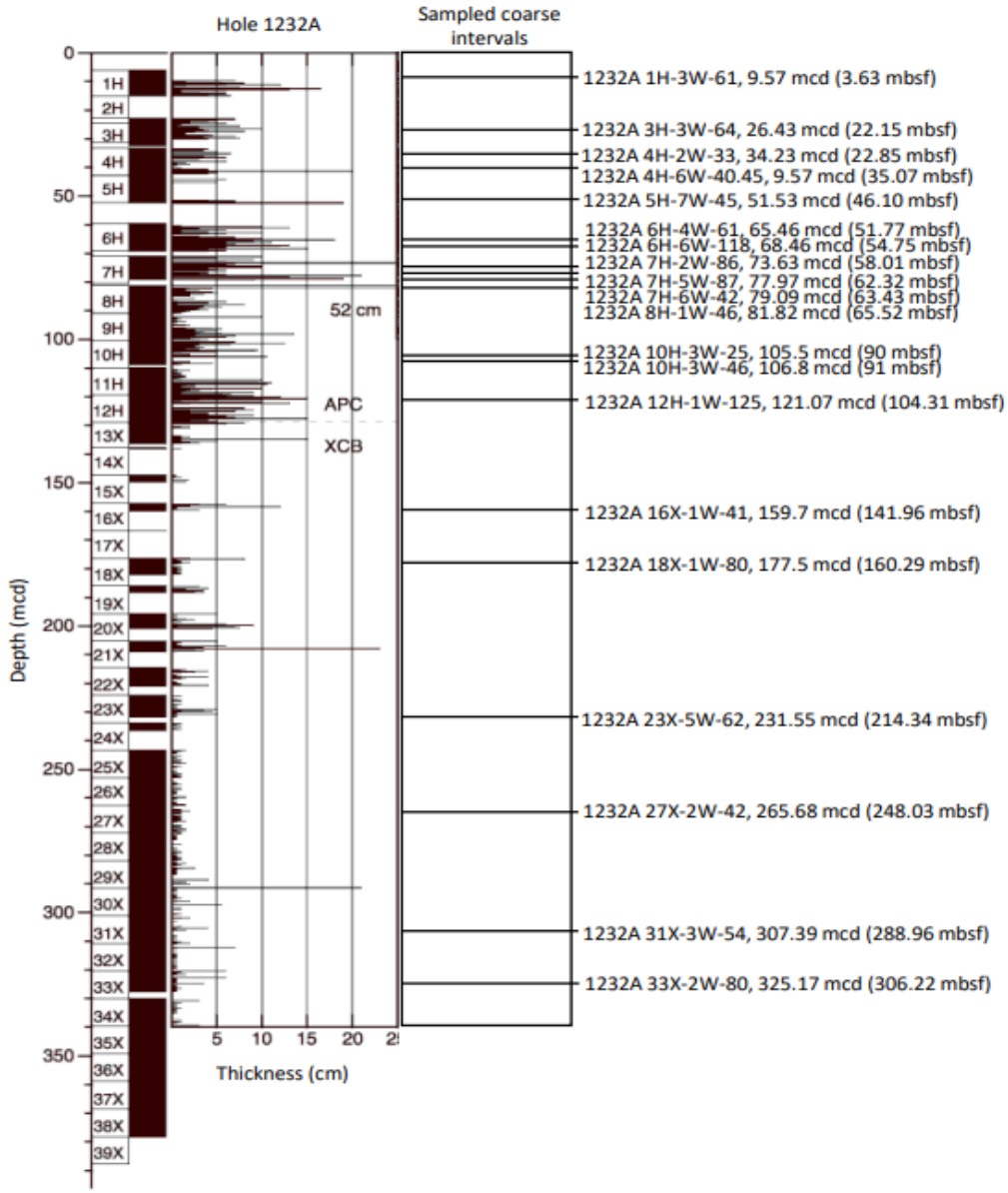

Figure 2.3: Simplified stratigraphic column for ODP Site 1232 showing basal depth and thickness of coarse-grained layers (left) and sampling intervals located within the coarsest sediments of turbidite layers (right). The missing interval between 1232A 5H-6H interval was filled by correlation with Hole 1232B. Figure modified from Mix et al., 2003.

2.2.3 Controls on sedimentation/ potential sediment sources

The three geologic belts

Physical weathering and erosion on land produce mineral associations which are indicative of the composition of their source rocks. Three geologically distinct belts or

zones, seen in Figure 1, are potential sources of the turbiditic sediments at Site 1232. These belts run parallel to the Chilean coastline: the coastal metamorphic zone, the central depression, and the Andean volcanic arc (lying farthest inland). The Paleozoic to Mesozoic (~330-113 Ma) metamorphic basement is exposed from 32°S to 42°S within the coastal cordillera of Chile. The metamorphic complexes consist primarily of phyllite, metagreywacke, metabasite, metaexhalite, serpentine, and some massive sulphides originating from both continental and oceanic sources (Jenks, 1956; Hervé et al., 2007). The Eastern Series of this belt is composed primarily of metagreywackes of turbiditic origin, and Western Series is composed primarily of high pressure, low temperature detrital, and marine metamorphic products (Hervé et al., 2007). Jurassic-Upper Tertiary plutons can be found intruded sporadically through the metamorphic complex (Hervé et al., 2007).

The Andean cordillera, including the Pleistocene - active Southern Volcanic Zone (SVZ), runs from latitudes 33°S-46°S. The SVZ is divided into geochemically distinct zones: The Northern Southern Volcanic Zone (NSVZ), Transitional Southern Volcanic Zone (TSVZ), Central Southern Volcanic Zone (CSVZ), and Southern Southern Volcanic Zone (SSVZ) (Lopez-Escobar et al., 1993; Hickey-Vargas et al., 2002). Volcanic products erupted from centers within the SVZ range in composition from basalt to dacite and rhyolite, with specific geochemical features which may be used to distinguish volcanic rocks from each segment and individual centers from one another (Hickey et al., 1986; Tormey et al., 1991; Stern et al., 2007; Hickey-Vargas et al., 2016).

The central depression is a low-lying region located between the Andean cordillera and the coastal metamorphic belt that formed through successive events of

tectonic compression and extension. The Central Depression is underlain by a basement of Paleozoic metamorphic rocks and Paleozoic to Mesozoic plutonic rocks (Servicio Nacional de Geología y Minería. Mapa geológico de Chile, 1982; Latorre et al., 2007; Encinas et al., 2021). Oligocene-Lower Miocene volcanic rocks are exposed at the surface throughout some parts of the Central Depression and there is a prevalence of large glacially derived lakes (Servicio Nacional de Geología y Minería. Mapa geológico de Chile, 1982; Latorre et al., 2007; Encinas et al., 2021). The exposed surface of the central depression is composed primarily of unconsolidated glacially derived sediments deposited during the LGM. (Jenks, 1956; Hervé et al., 2007; Encinas et al., 2012).

Large interglacial terrace deposits are present from 38°S - 40°S in Valdivia, Chile (Latorre et al., 2007). The deposits are comprised of two main sediment types, the first described as autochthonous metamorphic material interbedded with fine alluvial gravels, and the second an allochthonous medium to fine-grained volcanic sand (Latorre et al., 2007). The volcanic sand is composed of volcanic sediments, ash, pumice, and kaolinite (Latorre et al., 2007). The deposit is interpreted to be Late Pleistocene in age and have originated from a pre- Llanquihue (MIS 2) caldera of Villarrica and have been deposited as a deltaic deposit (Latorre et al., 2007).

Change in ice coverage and shoreline through the Pleistocene

There was widespread glaciation in the central and southern portions of Chile in the Quaternary (Jenks, 1956; Hulton et al., 2002a; Muratli et al., 2010). Glaciers are responsible for extensive weathering of continental terrane producing large quantities of mixed sedimentary detritus. Widespread glaciation in the central and southern portions of Chile in the Quaternary was responsible for several geographic features such as glacial

lakes, ice scoured bedrock, fluvial deposits, glacial lineations, and terminal moraines. (Jenks, 1956; Glasser and Jansson, 2008; Muratli et al., 2010). It has been suggested that there were at least 10 separate glaciations during the Pleistocene that affected the Patagonian ice sheet of South America (Glasser and Jansson, 2008). During the Last Glacial Maximum (LGM) in the Pleistocene, as seen in Figure 1, the Patagonian ice sheet almost entirely covered central and southern Chile (Glasser and Jansson, 2008). Beginning at ~39°S, the ice sheet extended into the coastal cordillera, and further south than ~41°S the ice sheet extended past the modern Chilean coastline, up to ~40 km in some areas (Melnick and Echtler, 2006; Glasser and Jansson, 2008). Temperatures began to warm in a tiered or stepped pattern in the late Pleistocene, with 3 warming events taking place between 14,600-10,000yr BP (Glasser and Jansson, 2008). During these stages of warming, the Patagonian ice sheet began to melt and recede.

Rivers and submarine canyons

ODP Site 1232 lies between the openings of the Bueno and Calle Calle submarine canyons (Figs. 2.2a and 2.2b) which are the product of erosion by outflow from the rivers of the same names. These rivers cut across the three geologic belts of central/southern Chile, with Rio Bueno originating at Lago Ranco and Lago Puyehue and Rio Calle Calle originating at Lago Rinihue. These lakes formed during glacial retreat and are located at the edge of the Andean cordillera, where alpine glaciers, probably filling former river valleys, extended into the central depression (Latorre et al., 2007; Muratli et al., 2010; Encinas et al., 2021). Starting from their sources, both rivers cut through Pliocene to Pleistocene volcanics in the Andean magmatic belt and scattered outcrops of Jurassic-Upper Tertiary intrusives (Servicio Nacional de Geología y Minería. Mapa geológico de

Chile, 1982). Moving then through glacially deposited sediments within the central depression and finally, they travel through Paleozoic to Triassic metamorphic rocks and sporadic surficial outcrops of Jurassic-Upper Tertiary intrusives within the coastal metamorphic belt (Servicio Nacional de Geología y Minería. Mapa geológico de Chile, 1982; Latorre et al., 2007; Encinas et al., 2021). Although there are surface outcrops of Jurassic-Upper Tertiary volcanic rocks within both the magmatic belt and the coastal metamorphic belt, age determination can distinguish between the Andean Pliocene to Pleistocene volcanics from the older plutonic intrusions.

The SVZ is in an area currently dominated by prevailing westerlies. However, studies have reported that during the Pleistocene in the Last Glacial Maximum, there was a northward shifting of both climatic zones and oceanic currents (Hulton et al., 2002b; Marchant et al., 2007). This shift moved the climatic zones up to 10° in a northward direction, potentially bringing polar easterlies into the southern reaches of the SSVZ (Hulton et al., 2002b; Marchant et al., 2007).

Sediment transport by glacier, wind transport, fluvial transport through submarine canyon, lateral movement within the trench, riverine transport, or a combination of the processes mentioned above (e.g., wind transport and deposition to ice sheet followed by glacial transport to deposition site), are all possible drivers of sedimentation in this diverse landscape (Galli-Oliver, 1969; Lamy et al., 1998; Völker et al., 2006, 2008; Blumberg et al., 2008). One or more of these modes of sediment transport may have affected the sediments arriving at Site 1232 and its local depositional environment.

2.3 Methods

2.3.1 Sample description and selection

Twenty-nine total samples from ODP expedition 202 Site 1232 were utilized in this study, all obtained from the Gulf Coast Repository, either through the curator or in-person sampling (Fig. 2.3). Site 1232 cores consist of two main sedimentary facies (Mix et al., 2003). The dominant facies are described as primarily massive clay and silty clay with few sedimentary structures. The color ranges from light greenish gray to light gray to medium gray with light mottling present and infrequent brown nodules (Mix et al., 2003). Thin silt layers are present intermittently; however, sand content is insignificant (Mix et al., 2003). Turbidite layers are found interbedded with the dominant clay. They are comprised of coarser sediment, typically ranging from silty sand to sandy silt. Typically, the coarser sands overlie a sharp basal contact and grade upward to silty clay. There are 1328 coarse layers observed throughout the site, with 772 layers present in the 289 m of core recovered in 1232A (Mix et al., 2003). The thickness of the coarsest sediment layers ranges from 0.5 cm to 52 cm, with an average of 3.2 cm.

The 29 samples were chosen based on two main criteria: 1) maximum coarseness of grain size and 2) maximum thickness of coarse layers. The maximum coarseness of the sediments in the sample is silty-sand-sized particles (4-250 microns), and the thickness of all the coarse layers sampled is at least 4 cm. Visual inspection of the core photos shows a fining upward structure with a sharp basal contact representing turbidites. Coarseness was an important factor for sampling because an analytical strategy (see below) requires at least 150-micron diameter grains. Thick layers of coarse sediment were preferred to thinner ones as they were most likely to represent significant events. Turbidite sediments

were chosen throughout the depth of the Site 1232 cores to evaluate any sedimentological changes with time.

2.3.2 Analytical methods

Samples of sandy silt-sized turbidite material were sieved using deionized water through 75 mesh and 100 mesh resulting in 2 size fractions, >210 microns and > 149 microns, respectively. These size fractions were chosen to obtain geochemical data of individual grains with multiple repetitions. Samples were agitated in an ultrasonicator to clean and loosen any silt, then washed through each mesh sieve one final time. Once cleaned, the samples were placed to dry in an oven at 100°C oven overnight. Samples were picked entirely for benthic and planktonic foraminifera using a binocular microscope, and specimens were mounted onto a foraminiferal slide for sorting and taxonomic identification.

A UV smear slide was made of each fraction by collecting sediments onto the tip of a single-use plastic spatula. Sediment was applied to a cleaned 12x12 grid slide in a drop of deionized water and dried on a hotplate. One to three drops of Norland ultraviolet cured optical adhesive #61 was applied to a coverslip and placed on top of the sample. Slides were dried for five minutes in a UV lightbox. UV smear slides were utilized to complete point counts for most core samples. Point counts were classified into one of five categories as follows: C - clear minerals, G – glass, P – polymineralic grains, Fp – felsic polymineralic, and M – mafic minerals. For the count using the 12x12 gridded slide, 12-24 boxes were chosen at random due to the small sample sizes, and the entirety of the box was counted to reach the desired number of 300-400 points. Boxes were chosen at random to avoid bias, and only grains within the boundaries of the box were counted.

Remaining sediment from each sample was viewed under a binocular microscope to identify glassy grains and minerals. Grains with the appearance of glass were picked and observed under a petrographic microscope to check for optical isotropy. Clean, isotropic grains were picked and mounted on carbon tape disks for analysis. Characteristics of chosen glass shards, including size, color, vesicularity, angularity, and freshness, were documented. Samples were then examined with the Scanning Electron Microscope (SEM) at the Florida Center for Analytical Microscopy (F.C.A.E.M) at Florida International University. Images of glass grains were collected using secondary electron and backscatter electron modes to determine homogeneity. Homogenous glasses were analyzed with the Energy Dispersive System (EDS) to obtain major element data.

Grains were analyzed using a 39 µm spot size under high vacuum with a 15kv accelerated voltage; two to three spots were analyzed on each grain and averaged. EDS analysis provides high-quality semi-quantitative data. Data for glasses were then normalized to analyses of reference materials Rhyolite (Smithsonian standard NMNH 72854, VG 568) and Hawaiian basaltic glass (BHVO-2) collected at the beginning, middle and end of each sample run. Three readings were taken on each standard and averaged. Precision assessed during each analytical run using the EDS on the BHVO-2 and Rhyolite reference glasses show; BHVO-2- SiO_2 = 0.47%, MgO = 2.40% and Na_2O = 4.91%, Rhyolite- SiO_2 = 0.37%, Na_2O = 2.72% and K_2O =1.72%. Values of analytical precision are given for each element in Table 4. Fossils and additional grains with glassy appearance were also analyzed to aid with identification. Mineral grains were identified in a polarized light microscope using optical properties and using SEM-EDS major element analyses.

After SEM with EDS analysis, select grains were analyzed for trace elements using the LA-ICP-MS (ELAN DRC ICP/MS and New Wave UP 213 nm laser ablation system) at the Trace Evidence Analysis Facility (T.E.A.F) at Florida International University. Glasses were analyzed for the trace elements Rb, Sr, Y, Zr, Nb, Ba, La, Ce, Nd, Sm, Eu, Gd, Dy, Er, Yb, Hf, Pb, Th, and U. LA-ICP-MS glass analysis used a 55µm laser spot size with a repetition rate of 5hz and dwell time of 60 seconds. Calibration was performed using NIST (National Institute of Standards and Technology) SRM612 glass and Si and Ca as internal standards. Data were compared with reference materials BHVO-2g and Smithsonian Rhyolite. At least two 55-micron spots were ablated on each grain and averaged. Data reduction was performed with the 'Glitter' software (Griffin et al., 2008). Data for precision and accuracy assessed for each element run with the LA-ICP-MS on the USGS BHVO-2 reference glass are given in Table 4.

Samples evenly dispersed throughout the 1232A and 1232B cores were chosen for analysis of calcareous nannofossil biostratigraphy. Twenty fractions were taken from the unprocessed coarse-grained sediment samples, and another sixteen fractions were taken from the corresponding unprocessed fine-grained sediments (upper parts of the same turbidite). A minimum of 1cc of sediment was collected using a 1ml scoop, placed into a glass vial, and sealed with parafilm. The vials were labeled and mailed, with a corresponding datasheet, to BugWare Inc. Tampa, Florida, where they were analyzed for calcareous nannofossil biostratigraphy.

2.4 Results

2.4.1 Sediment characteristics

2.4.1.1 Description and identification of particles

Smear slide analyses of the turbidite fractions of Site 1232 reveal that the sedimentology of particles are relatively consistent between the 1232A and 1232B Sites, which agrees with the shipboard party's correlation of the upper 42.58 m of the 1232A and 1232B cores. Sedimentology remains relatively consistent throughout the entire length of the 1232B core and the upper two-thirds of the 1232A core. Dominant particle size ranges from clayey silt to silty clay, with the coarsest turbidite intervals being sandy silt to silty sand-sized particles (4-250 microns). Particles consist primarily of clear minerals, polymineralic grains, mafic monomineralic grains and glass. Proportions of these constituents are shown in Figures 2.4a and 2.4b.

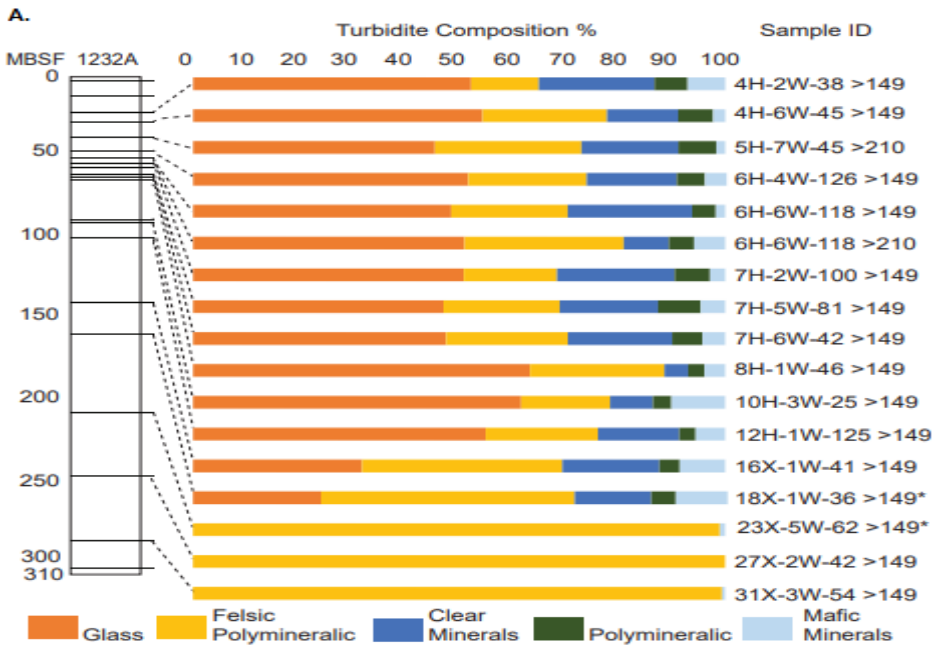

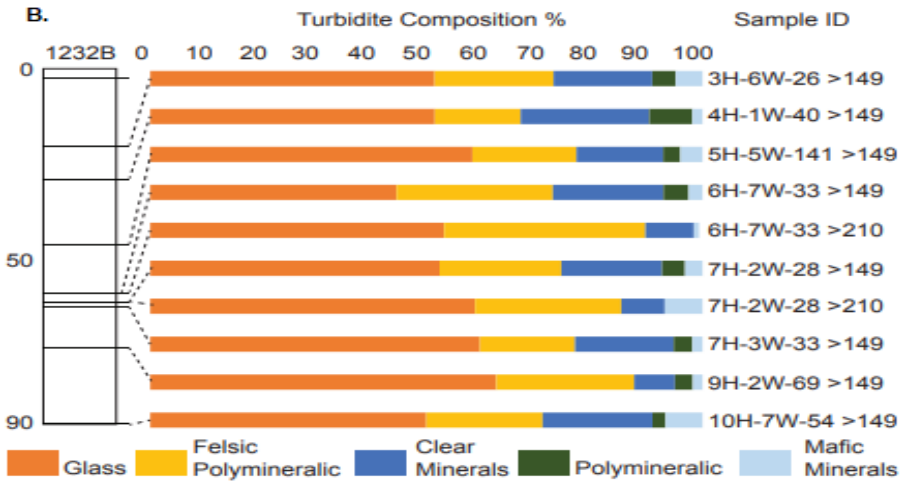

Figure 2.4: Percent abundance of grain types in coarse sediments with depth at Site 1232; glass, clear minerals, felsic and mafic polymineralic grains, and mafic minerals, based on point counts (Table 1). (a) Hole 1232A and (b) Hole 1232B. Point counts show compositions of 45% - 63% glass in turbidites above 100 mbsf.

The predominant particle type in each turbidite layer examined was volcanic glass. At a core depth of around 214 mbsf in the 1232A core, glass and monomineralic grains are absent. The predominant particles are pale, rounded clay-rich felsic polymineralic grains with some reddish-orange staining from oxidized magnetite and other iron constituents.

2.4.1.1 A Glass

Based on optical and SEM imaging, glass grains are relatively unaltered (isotropic) and angular. Edges of glass fragments are irregular and sharp, with little to no evidence of rounding. Colors range from black/dark brown to light tan/clear. Four distinct textural varieties of glasses are identified (Fig. 2.5): 1) dark brown non-vesicular blocky shards; 2) poorly vesicular shards; 3) highly vesicular shards with spherical vesicles; 4) shards with long, pipe vesicles (Scasso and Carey, 2005). Glass shards make up between 45-63 percent of the turbidite samples in the upper 140 mbsf of the 1232A core and the full 90mbsf of the 1232B core. In the 1232A core, below 140 mbsf, the glass

shards reduce in frequency until disappearing altogether at 200 mbsf. The four color/textural glass varieties remain consistently present throughout the first 160 mbsf of the 1232A core and the 90 mbsf of the 1232B core. Some glass grains contain rare mineral inclusions.

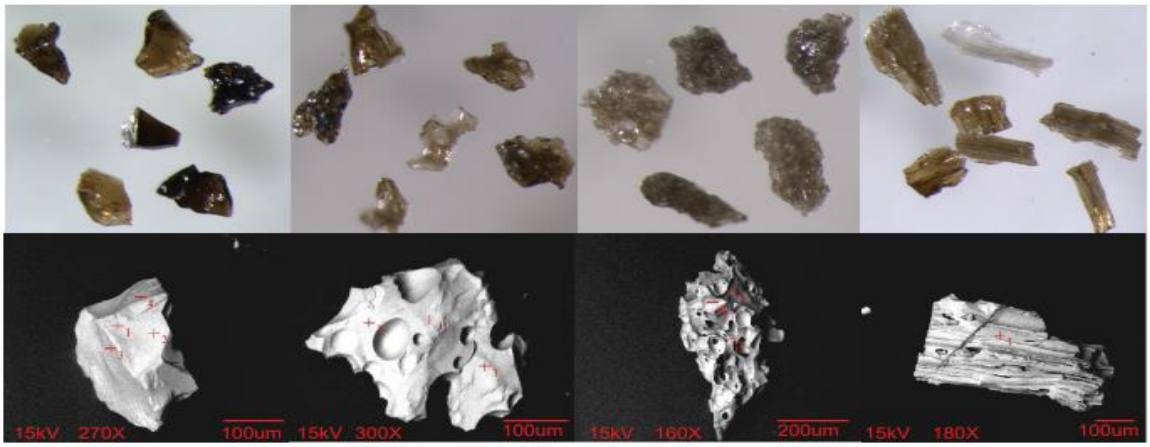

Figure 2.5: Optical microscope (80x magnification) and high-resolution scanning electron microscope images (magnification and scale bar on image) of Site 1232 volcanic glasses. Four distinct varieties of glasses are present: Dark brown non-vesicular blocky shards, poorly vesicular shared, highly vesicular shards with spherical vesicles, and shards with pipe vesicles.

2.4.1.1 B Minerals

Numerous monomineralic grains are found within the turbidite layers of Site 1232 (Fig. 2.6). Common mineral phases include quartz, feldspar (clear minerals), pyroxene, magnetite, muscovite, chlorite, and biotite. Less common mineral phases include hornblende, augite, pyrite, and garnet. Mineral grains vary in physical appearance, and most exhibit edges ranging from angular to subangular, with a small fraction having subrounded edges for 160 mbsf of the 1232A core and the entirety of the 1232B core. At depths in the 1232A core greater than 160 mbsf, grains shift to a more subangular to rounded appearance. At 160 mbsf, the >210μ sample is composed entirely of large crystals of anhydrite encased in the white felsic polymineralic material introduced in 2.4.1.1 and described in greater depth in 2.4.1.1C. Samples below 214 mbsf are

composed entirely of white to reddish-orange felsic polymineralic particles that are subrounded to rounded in appearance.

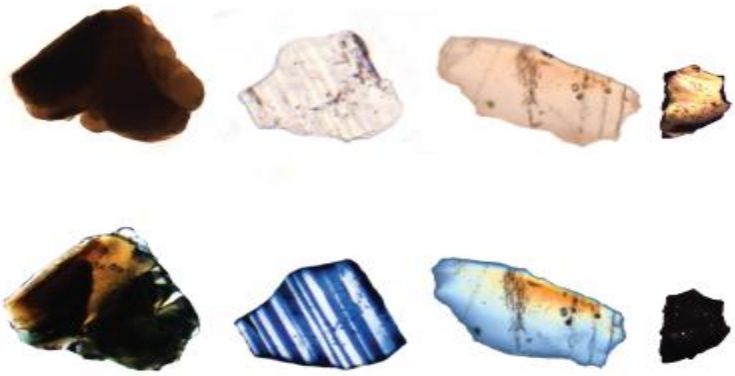

Figure 2.6: Petrographic images taken at 100x magnification showing biotite, feldspar, quartz and garnet in plane light above and crossed polarized light below, found at Site 1232.

2.4.1.1 C Poly-mineralic particles

The poly-mineralic particles (Figs. 2.4a and 2.4b) are comprised primarily of felsic polymineralic particles and sedimentary lithic fragments. Felsic polymineralic particles are white to reddish-orange in appearance with distinct feldspar laths, quartz grains, and magnetite grains embedded, some containing anhydrite grains, in a fine-grained clay matrix. The reddish-orange color in some grains represents oxidation of iron-bearing minerals, suggesting that they have been exposed at or near surface for some time. Grains have the overall appearance and composition of altered pumice (Fig. 2.7). Sedimentary lithic fragments contain silt size particles of quartz, feldspar, magnetite, and mica in a finer-grained clay matrix; particles are similar in comparison to sedimentary lithics reported in (Ramirez and Milliken, 2016). Sedimentary lithic particles have the rounded appearance of allogenic sediments formed in a sedimentary environment and transported as lithified grains, thus not formed in situ.

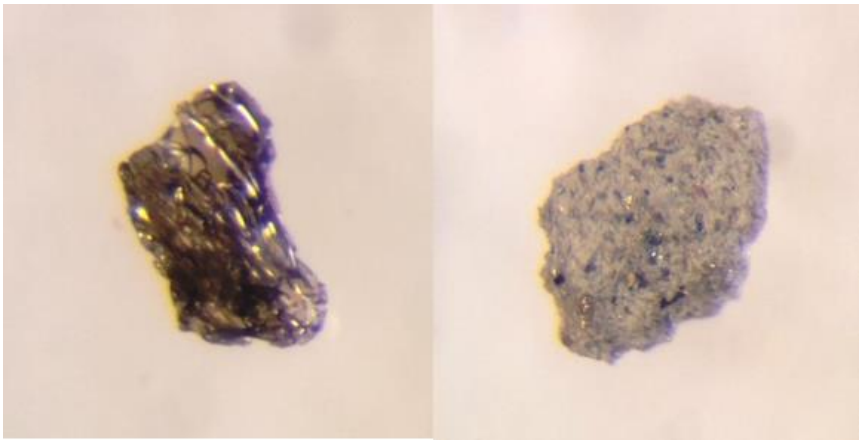

Figure 2.7: Optical microscope (120x magnification) images taken in incident light showing a comparison of volcanic glass (left, from core 1232A-27X-2W-42 >149µ) and altered pumice (right, 1232A-27X-2W-42 >149µ).

2.4.1.1 D Microfossils

The foraminiferal investigation of the 1232A and 1232B cores shows poor abundance of both benthic and planktonic foraminifera throughout the site. Benthic foraminifera recovered from the samples include the species: *Globocassidulina subglobosa, Buliminella elegantissima, Pyrgo murrhine, Cibicidoides mundulus, Hoeglundina elegans, Uvigerina hispida, Uvigerina peregrina, Nonionella atlantica, Oridorsalis umbonatus* and *Cicicidoides sp.* Planktonic foraminifera recovered include the species: *Globirotalia inflata, Globigerina bulloides, Globigerina falconensis and Orbulina universa.* Most foraminifera recovered are in good condition and well preserved with only minimal pitting, signs of abrasion or infilling. Some broken tests are present; however, samples were wet-sieved and ultrasonicated to process for analysis which may have potentially led to some degree of mechanical breakage. Examined samples in the 1232A core are barren in the upper 20 m and from 141 mbsf to 306 mbsf. The 1232B core is barren in the top 2 m in the examined samples, with most examined samples through the remaining 90 m containing moderate to few foraminifera. The relative

abundance of both benthic and planktonic foraminifera varies greatly throughout the entirety of both the 1232A and 1232B cores.

The corresponding coarse and fine-grained sediment samples analyzed for calcareous nannofossil biostratigraphy were consistent with an origin in turbidites and showed the presence of both coccolithophore nannofossils and diatoms (Figs. 2.8a and 2.8b). Site 1232A showed the presence of *Emiliania huxleyi, Coccolithus pelagicus Group, Reticulofenestra minuta Group, Calcidiscus leptoporus, Gephyrocapsa aperta, Gephyrocapsa carribeanica, Gephyrocapsa oceanica, Pseudoemiliania ovata* and *Pseudoemiliania lacunosa*. Site 1232B showed the presence of *Emiliania huxleyi, Coccolithus pelagicus Group, Reticulofenestra minuta Group, Calcidiscus leptoporus, Gephyrocapsa aperta, Gephyrocapsa carribeanica* and *Gephyrocapsa oceanica*.

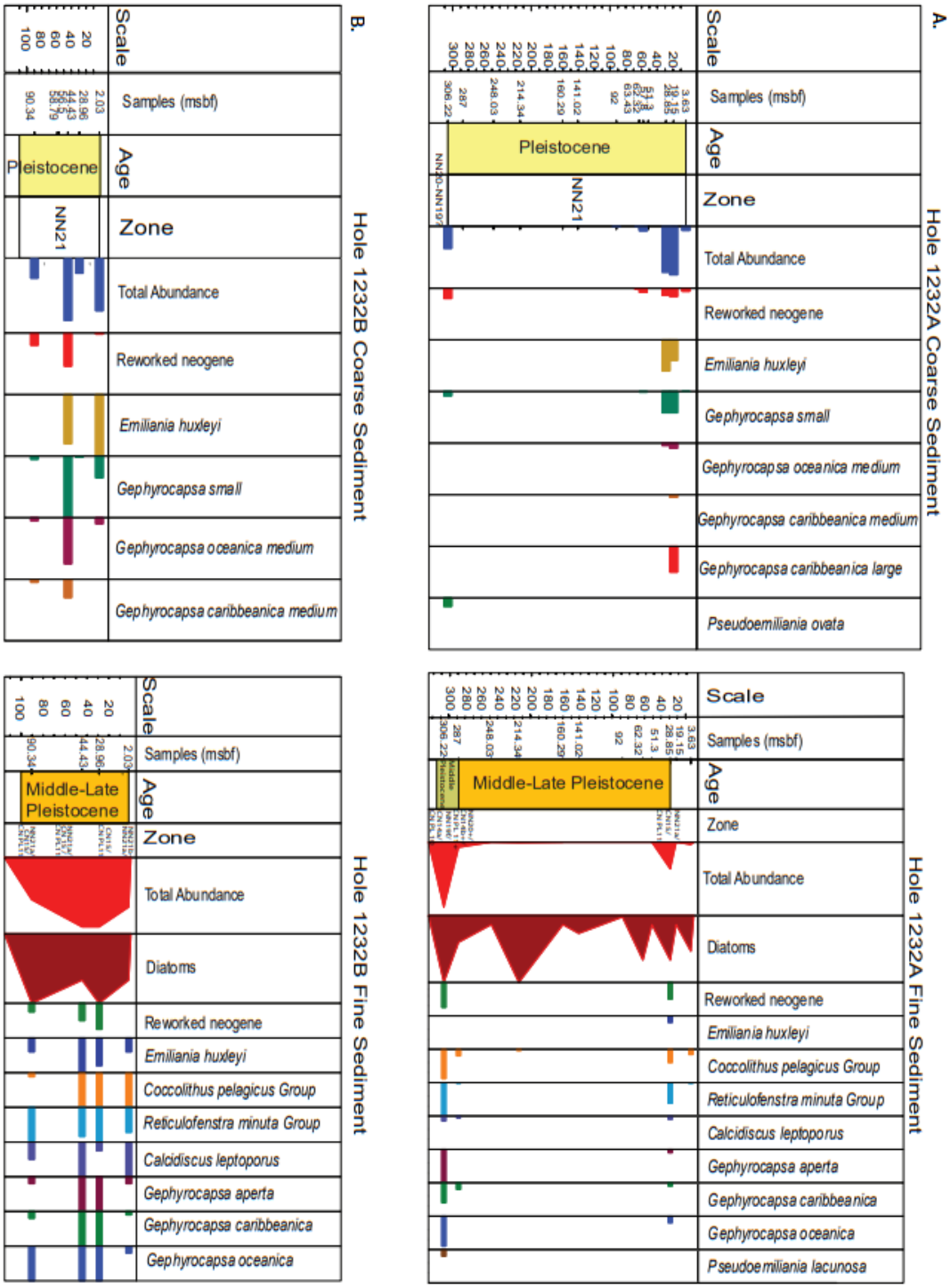

Figure 2.8: Calcareous nannofossil biostratigraphic correlation and age information. Completed by Bugware, Tampa Fl. http://www.bugware.com/default.html. Results from coarse (left) and fine (right) sediments from the same turbidite "packages" are shown. Hole 1232A is above and Hole 1232B is below.

2.4.1.2 Proportions of sediment particles

Turbidite layers in the upper 100 mbsf of both 1232A and 1232B yield large quantities (44-63%) of fresh volcanic glass. Felsic polymineralic (altered pumice) grains comprise the next largest proportion, 12.7-29.9% within the first 140 m and >99% below 214 m 1232A. Within the first 140 mbsf, clear minerals (primarily quartz and feldspar) range from 4.4-23.4%; polymineralic grains range from 2.3-8% and mafic minerals (non-clear monomineralic grains) from 1-10.1% of the composition (Table 1). At sample 1232A-16X-1W-41, at 140 mbsf, there is a marked decline in volcanic glass to 31%. The next sampled section (1232A-18X-1W-36) at 160 mbsf shows a further decline in volcanic glass with ~24% glass in the >149μ fraction and no glass present in the >249μ fraction. Samples below 214 mbsf depth show a marked change in appearance. Here, volcanic glass and monomineralic mineral grains are absent almost entirely, and samples are composed of >99% white, rounded altered pumice with embedded grains of quartz, feldspar, and magnetite. The shipboard party reports a distinct change in the thickness of coarse layers in the 1232A core below a depth of 200 mbsf, stating that very few layers were recovered that were thicker than 4cm, compared to thicknesses of .5-118cm found in the upper portion of the core (Mix et al., 2003). The decline in the thickness of coarse layers noted by the shipboard party does appear to correspond with the change in particle type from altered pumice to fresh unaltered glass discovered in this study.

2.4.2 Geochemistry of glass particles

2.4.2.1 Major elements

SEM-EDS analysis of glass grains (Table 2) reveals basaltic to rhyolitic glass compositions (Fig. 2.9a), with significant grain variation from individual intervals. The

analyzed glasses also show a high alkali content (basalt, basaltic andesite, basaltic trachy-andesite, andesite, trachy andesite, dacite and rhyolite after (Bas et al., 1986) and high MgO versus SiO_2 (Fig. 2.9b).

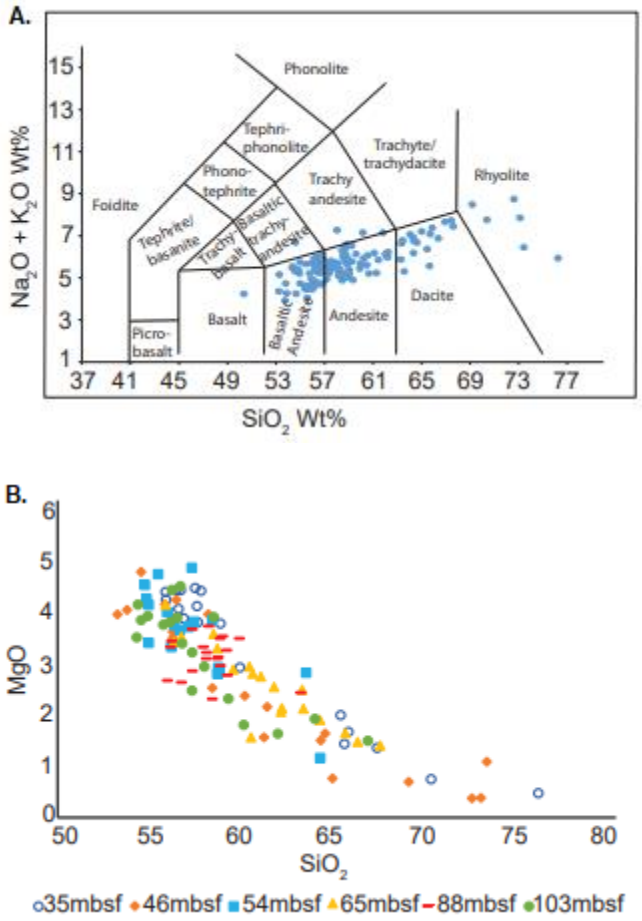

Figure 2.9a and 2.9b: a. Total alkali versus SiO_2 classification plot (Bas et al., 1986) for glasses separated from coarse sections of turbidites. Glass compositions fall in the calc-alkaline series and range from basaltic to rhyolitic. b. Plot of MgO content versus SiO_2 content of the Site 1232 volcanic glass grains. Data are from Table 2.

2.4.2.2 Trace elements

Grains analyzed by LA-ICPMS (Table 3; Fig. 2.10) yield broadly similar trace element abundance patterns when normalized to primitive mantle values. All glasses show enrichment in Rb, Ba, Th, Pb, and depletion in Nb and Ta compared with rare earth elements (Fig. 10) when normalized. This is a singular characteristic of rocks from

volcanic arcs formed by subduction and distinct from mid-ocean ridge basalts (MORB), oceanic island basalts (OIB), continental flood basalts (CFB), and their differentiated equivalents (Sun and McDonough, 1989).

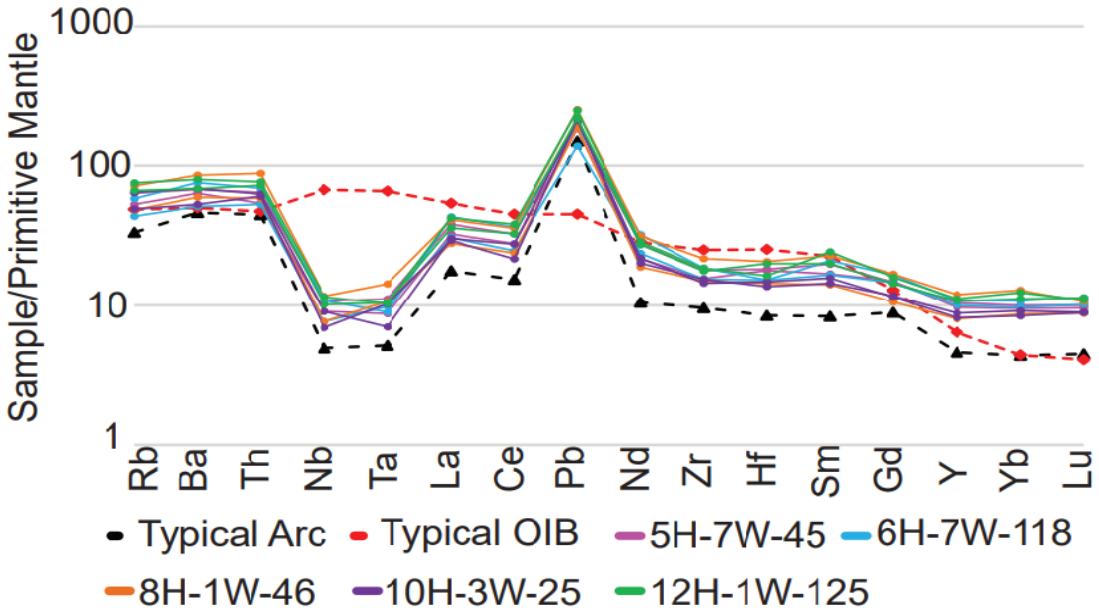

Figure 2.10: Abundances of trace elements in glass shards from Site 1232 (blue) normalized to a composition for the primitive mantle (Sun and McDonough, 1989). Data are from Table 3. Also plotted are patterns for typical OIB (red) and typical arc (black) volcanic rocks taken from (Sun and McDonough, 1989; López Escobar et al., 1995)

2.5 Discussion

2.5.1 Sources and depositional processes at ODP 1232

2.5.1.1 Origin of minerals, glass, microfossils and polymineralic particles

Petrographic and SEM major element analyses of minerals completed on sampled intervals show the presence of chlorite, quartz, biotite, garnet, feldspar, pyrite, magnetite, and pyroxene along with sedimentary and felsic lithic particles, and glasses, consistent with the findings of the Shipboard Party (Mix et al., 2003). Monomineralic grains are present consistently in all sampled intervals in the upper 214 m of the core and rare in samples below 214 m. Sedimentary lithic particles are rounded, having the appearance of

having been deposited and then undergoing transport that contributed to the rounding of the grains. The presence of garnet, chlorite, muscovite, biotite and hornblende show that samples contain constituents of metamorphic rocks that have not traveled a great distance from their source, likely the coastal metamorphic belt. Samples (>149μ, excluding microfossils) are predominantly composed of volcanic material (>80%), however, with the variety of minerals present, it is possible that the turbidites have sedimentary constituents that originated in various proportions from the three compositional belts (Coastal metamorphic, Central depression sediments, and Andean magmatic arc). However, the Andean magmatic arc has contributed the largest volume of the coarse particles in turbidites at Site 1232.

2.5.1.2 Age constraints from nannofossils

Refinement of the age of the section can be drawn from the nannofossil data. Site 1232A, the first sample with marker fossils was 1232A-4H-2W-31 (28.85 mbsf) and contained *Emiliania huxleyi* along with *Gephyrocapsa aperta, G. caribbaenica* and *G. oceanica*. The presence of *Emiliania huxleyi* gives an age of <0.275 Ma. The next event would be below the base of *Emiliania huxleyi* at 1232A-31X-3W-51 (288.19 mbsf), the *Gephyrocapsa* species were present, but there was no detection of *Emiliania huxleyi*. This would give an age of > 0.275 Ma. The last recognizable event was rare *Pseudoemiliania lacunosa* in sample 1232A-33X-2W-77 (306.22 mbsf). This would put the age > 0.424 Ma. Site 1232B. The first sample contained *Emiliania huxleyi* along with *Gephyrocapsa aperta, G.caribbaenica* and *G. oceanica*. The presence of *Emiliania huxleyi* gives an age of <0.275 Ma. There was a notable increase in *Gephyrocapsa* species at sample 1232B-4H-1W-87 (28.96mbsf), and the age could be considered 0.070-0.275 Ma (Bergen et al.,

2019), and an increase in *Gephyrocapsa* small would make the age > 0.070. *Emiliania huxleyi* was observed in every sample for this section down to 1232B-10H-7W-64 (90.34mbsf), so the age remains <0.275 Ma. In summary, the microfossil analysis refines the age range of the upper 288 m of the A core and the entirety of the B core of Site 1232 section to between 12.47 kyr and 275 kyr in age younger than the 0.78 Ma and 1.69 Ma maxima determined in prior work.

This dating shows an age of Mid to Late Pleistocene, a time spanning three glacial and three interglacial stages (Fig. 2.11). Using age data from Blumberg, 2008, giving an age of 138.16 kyr at a depth of 88mbsf and new data acquired from calcareous nannofossil biostratigraphy giving an age of 275 kyr at 288.96mbsf, assuming a constant sedimentation rate of 1.54 m/kyr from ~88mbsf to 288mbsf, the change of sediment type at 140-200mbsf that occurs within the core, relates to an age of ~ 195-220 kyr, right around the time of the shift from the Interglacial MIS 7 to the Glacial MIS 6 as sea level is dropping, temperatures are cooling, and glacial ice is increasing.

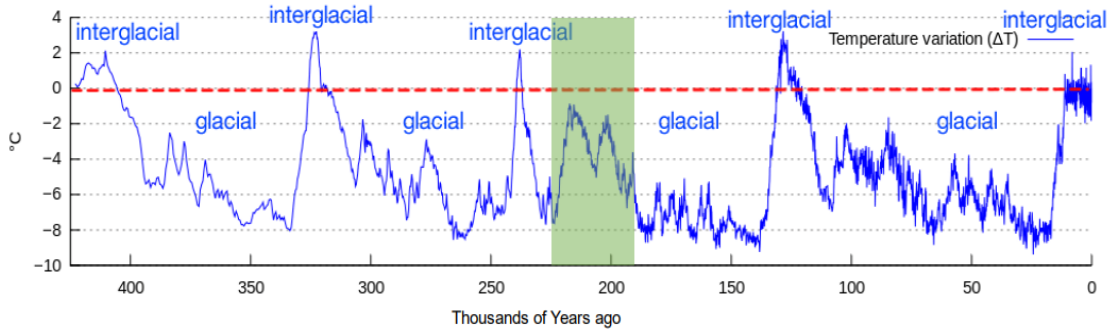

Figure 2.11: Glacial and interglacial stages shown on a temperature (°C) variation curve plotted against time. The green shaded area shows the estimated age of the change in sediment type (225-190 kyr) of the Site 1232 turbidites. The shift in sediment type overlaps with the change from MIS 7 (243-191 kyr) interglacial cycle to the MIS 6 (191-130 kyr) glacial cycle. Figure modified from Petit et al., 1999.

2.5.2 Origin of volcanic glass

Major and trace element analyses of the glasses are most consistent with an origin in a volcanic arc. The wide range of SiO_2 is typical of differentiated volcanic series, and the trace element fingerprint of consistent enrichment in Rb, Ba, Th, Pb, and depletion in Nb and Ta relative to rare earth element (REE) is a classic feature of subduction-related volcanic rocks, and they are clearly distinct from oceanic ridge, island, or seamount related volcanics (Hickey et al., 1986; Stern, 1991; Jacques et al., 2013). Given its proximity, an origin by erosion, transportation, and deposition of volcanic debris from the adjacent Southern Volcanic Zone is likely. Given the timing of activity of SVZ volcanoes, throughout the early Pleistocene to recent, this volcanic material could be incorporated into sediment on the continent and continental shelf by atmospheric deposition from explosive volcanic events or by glacial and stream erosion of volcanic edifices of varying ages, followed by stream, glacial or wind transport. Glasses within the samples vary in color, size of vesicles and vesicularity. The four textural varieties of glass are each present in all sampled intervals in the upper 200 m of the core (Scasso and Carey, 2005). Together with the wide range of SiO_2 contents within each coarse interval, this suggests that volcanic particles in each layer may have several volcanic sources, with mixing occurring during some part of the transport pathway. The presence of the volcanic sand terraces from 38°S - 40°S (Latorre et al., 2007; Vega et al., 2018) show that volcanic sediments were transported by rivers, then mixed and transported on the continental shelf, before the turbidite events. The angularity suggests that they have not been transported far or through a turbulent transport process that would have caused abrasion and rounding of the particles. It is possible that the chemical and textural

features of the glasses can be matched to a specific volcanic source or set of sources and therefore provide a specific geographic constraint on their mode of transport and deposition. Such an effort is beyond the scope of this paper but will be explored in future research.

2.5.3 Causes of downcore variations of sediment sources and depositional processes

Investigation into the variation in proportions of glass, minerals, multi-mineralic fragments and microfossils downcore was made to discern temporal changes throughout Site 1232. There is an overall consistency in the proportions of constituents throughout the upper 140 m of the core. The shipboard party reports two layers with very low quartz/feldspar ratios, one ~140-160 mbsf and the other ~250-260 mbsf, which could represent weathering of a drier climate, inhibiting the weathering of feldspar (Mix et al., 2003). The low quartz/feldspar ratios could also be representative of a mechanical/abrasive weathering scenario, where minerals are picked up and carried through glacial transport instead of chemical weathering, resulting in slower degradation of feldspar grains and resulting in a lower quartz/feldspar ratio. (Nesbitt et al., 1997). At depths below 140 m within the 1232A core, a decline in the quantity of volcanic glass is noted and an increase in altered pumice to about 214 mbsf, where the complete absence of volcanic glass is seen, and the samples are composed entirely of altered pumice coupled with a loss of angularity in grains. The shipboard party also reported a considerable change in the thickness of coarse layers below 200 m in the core (Mix et al., 2003).

These changes in sedimentary composition may represent fluctuations in volcanic activity and various paleoclimatic and sedimentological variables. Some possible scenarios for the sedimentological changes discovered within the Site 1232A core are:

1: A northward shift in global wind patterns

It is well known that during the LGM, global wind patterns in the Southern Hemisphere, such as the Southern Westerlies and Polar Easterlies, experienced a northward shift (McCulloch et al., 2000; Hulton et al., 2002b; Marchant, 2007). It is also a common occurrence that Southern Westerlies will experience a northward shift under El Nino Southern Oscillation conditions (Marchant, 2007). Based on this observation, there is the potential for the northward shifting of wind patterns throughout the glacial/interglacial cycles occurring in the Pleistocene, with a resulting change in the wind transport of volcanic ash. During glacial periods, as polar easterlies shift northward, glacial advances appear to correspond with the winds from the east (bringing material from the volcanic belt). Glacial retreats correspond with winds from the west (less volcanic material), like what is seen at present. Comparison of known geochemical data to new geochemical analyses performed on Site 1232 glasses would assist in determining if volcanic sediments are coming from a single source, multiple sources in close proximity to one another or multiple sources in different regions.

2: A change in sediment transport pathway or supply

Oxidation staining on the remnant pumice grains implies that they spent some period of time at or near surface before deposition as turbidite sediments. It is recognized in the Valdivia area that, even currently, pumice grains are commonly transported after eruption in rivers and deposited onto the continental shelf (Vega et al., 2018). The change from

altered pumice to fresh glass at 214 m, which appears to correspond with an interglacial period, could indicate transportation by river, while the volcanic glasses are deposited onto the Patagonian ice sheet, transported with little to no abrasion and deposited during periods of low sea level directly onto the edge of the continental shelf/slope as the ice sheet melts and recedes. This option would also explain the decrease in the thickness of coarse (turbidite) layers that the shipboard party noted below 200 m in the core and relate to the increase of sediment deposition during low sea level seen by Blumberg (2008). Although the change from altered pumice material to fresh glass material does not seem to follow a repetitive or cyclic trend, you would expect to see alternating layers of pumices and glasses as there is a shift from glacial to interglacial cycles. Alternatively, the altered pumice grains could be weathered material from the Interglacial Valdivian volcanic sand terraces with interbedded pumice layers (Latorre et al., 2007; Vega et al., 2018). This possibility, however, also seems to be an unlikely candidate. Although pumices are found throughout the different facies, the Valdivian deposits are suspected to be Late Pleistocene in age, younger than the suspected age of the pumice layers in this study (Vega et al., 2018). There is, however, the possibility that pumice accumulates during interglacial periods, and the Valdivian sand terraces are a younger example of these accumulations. Chemical composition of Site 1232 altered pumice grains could be more closely compared to pumices within the Valdivian Interglacial terraces and with river transported pumices to look for similarities.

3: A change in volcanic source or composition

A change in volcanic source or volcanic composition could also affect the dominant particle type within the 1232 core. This change would result in distinct physical and

chemical differences that would be detectable through time, which is seen in the 1232A core as a shift from the deposition of altered pumice at the base of the interval, followed by an increasing supply of fresh angular volcanic glass particles. If volcanic products originate from the same volcanic source, then a change in magma composition or volatile content would be expected. Geochemical variation along the SVZ has been well studied, and geochemical variations in proportions of major and trace elements can allow for the determination of source/source region (Hickey et al., 1984; Tormey et al., 1991; Hickey-Vargas et al., 2016). SVZ volcanoes with documented eruptions between 275-12 kyr include Antuco, Callaqui, Sierra Nevada, Llaima, Cerro Trautren, Cerro Maichin, Villarrica, Quinchilca, Mocho-Choshuenco, Cordon Caulle, Osorno, Calbuco, Cuernos de Diablo, and Hudson (Stern et al., 2007; Venzke, 2021). In-depth geochemical analyses of major and trace elements could be used to compare the glasses of the 1232 turbidites to known volcanic sources along the Chilean SVZ to determine the most likely source(s). These analyses could show if there are multiple sources/source regions or a single source that has fluctuated in chemistry (either throughout time or within an event). This is the most plausible option, although it does not appear to encompass the entirety of the sediment change. Most likely, a combination of these options at work resulted in the change in sediment deposition at Site 1232.

2.5.4 Depositional history of Site 1232

The depositional history of Site 1232 experienced marked changes during the Pleistocene -recent (Fig. 2.12). A significant increase in the thickness of turbidite layers (Mix et al., 2003; Blumberg et al., 2008) and change in sedimentary composition at a depth of 214 mbsf with a marked increase in fresh, angular volcanic glass, a normally

rare component of turbidites extending across a deep-sea trench. This means that a significant change in sediment supply or depositional pathway occurred between 12.47 kyr (Blumberg et al., 2008) and 275 kyr. The appearance of glasses at 214 m appears to be related to either a new sedimentary source or a new depositional pathway.

Glass compositions indicate that the glass fragments originated from the Andean magmatic arc, the geologic belt furthest from the coast. The predominant proportion of material in the turbidites is volcanic in origin. However, mineral and lithic particles deposited with the glass show the potential for origination within the other geographic belts, the Coastal metamorphic zone, and Central depression. Distinguishing the areas that are undergoing erosion can help to evaluate the likely sources of the silty-sand and sandy-silt (149–210μ) size fraction from the Site 1232 cores on the Nazca Plate adjacent to Southern Chile and reconstruct erosional patterns of the three source regions and potential sediment transport pathways to the continental slope. Due to the size and angular nature of the glass grains, the lack of plant detritus and absence of inverse-to-normal grading of the deposits is unlikely that the majority of the turbidite sediments at Site 1232 were transported by riverine hyperpycnal flow like those commonly found in lacustrine deposits on the continent adjacent to Site 1232 (Chapron et al., 2007; Zavala and Arcuri, 2016). The angularity of grains suggest that they have not traveled a great distance from the source or that their travel mechanism did not promote rounding. Possibly, glass fragments were transported to the continental shelf mainly in a glacial mode (ice rafting) as fine-grained sand, and sandy silt-sized particles that have been glacially transported tend to exhibit sharp and angular surfaces (Smith, 1987; W. Mahaney, 2002; Chapron et al., 2007). Other possibilities include wind transport; during

the glacial Pleistocene, it is known that the prevailing westerlies had a northward shift (Hulton et al., 2002b), a corresponding shift of the Polar easterlies into the SVZ is reasonable and would explain westward movement of ash sized volcanic ejecta; transport could also be due to a combination of wind and glacial transport. In summary, a possible depositional history for Site 1232 is airfall from one or more Pleistocene SVZ volcanic center was deposited onto the Patagonian ice sheet and traveled coastward, depositing onto the continental shelf as the ice sheet began to melt and recede.

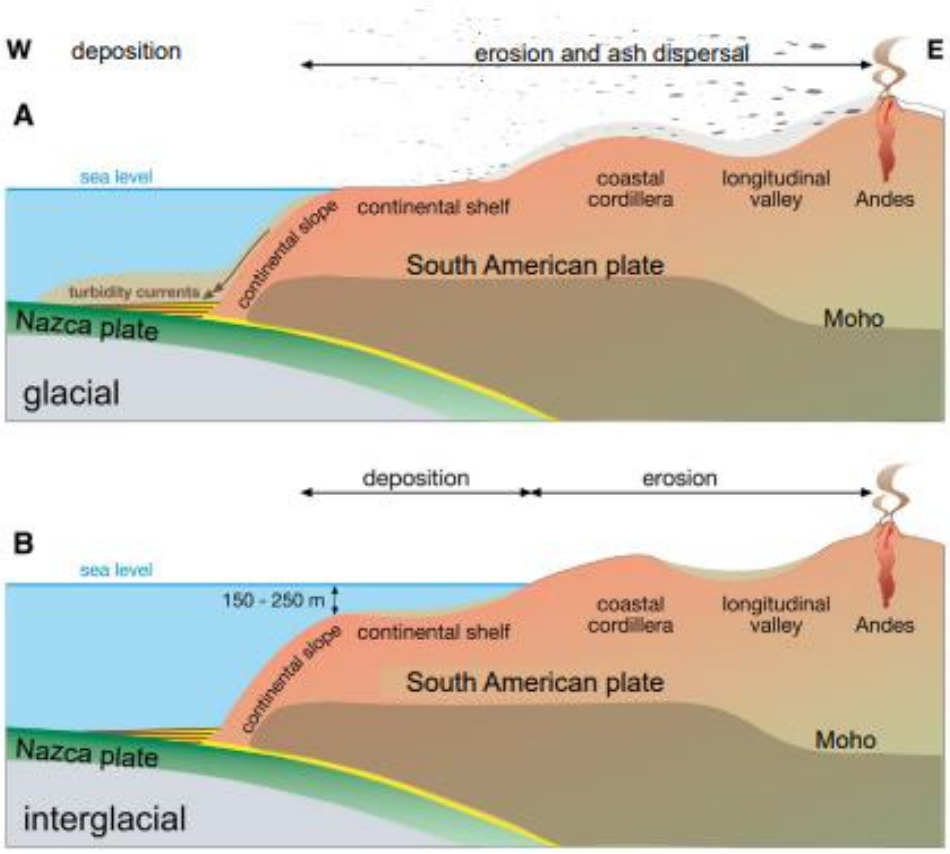

Figure 2.12: Schematic diagram of the coastline of South America near Site 1232 during a glacial and interglacial cycle. a. depicts a period of glaciation, where sea level is lower, the ice sheet extends to the coastline in some areas. Volcanic ejecta is deposited onto the ice sheet and is deposited directly onto the continental shelf and slope. b. depicts an interglacial period, with higher sea level and smaller ice mass. Volcanic debris is transported on melting glaciers and by streams through the central valley to the continental shelf. Figure adapted from (Blumberg et al., 2008).

2.6 Conclusions

1. This study recognizes a previously undocumented compositional change in sediments within the cored interval, evident in core 1232A at a depth of 214 mbsf. The timing in the change of sediment (calculated using new age data and estimated sedimentation rate) has been determined to be between 175-220 kyr. Even though the precise cause of the sedimentary shift is uncertain, due to the shift from Interglacial MIS 7 to the Glacial MIS 6 that occurs during the timeframe and the abrupt change in volcanic material type, this paper favors a combined change in volcanic source/composition and sediment transport due to glacial cycles.

2. The petrographic features and mineralogical composition suggest that the source for the upper 200 m of the core is primarily volcanic (glass and pumice), with minor proportions coming from sedimentary and metamorphic source regions.

3. New age constraints using nannofossil biostratigraphy place sediment ages of the upper 288 m of cored section between 12.47 kyr and 275 kyr. Further work is unlikely to provide better constraints due to an overall lack of microfossil biota, potentially due to the rapid accumulation of sediment in the area during the Pleistocene.

4. Turbidite deposits at Site 1232 show an abundance of fresh undevitrified volcanic glass. Glasses from the upper 200 m of the cored section have a geochemical signature consistent with origination in the Southern Volcanic Zone. Glasses precisely group into four distinct textural varieties, which may also be a critical factor in determining their volcanic source or sources. Further analysis could allow for correlation to known SVZ volcanic centers and their eruptive history.

Acknowledgements:

We gratefully acknowledge Dr. Kathleen Marsaglia for contributing the original samples from Site 1232. We thank Thomas Beasley of the Florida Center for Analytical Electron Microscopy (FCAEM) at FIU for assisting with SEM analyses and Sarah Jantzi of the Trace Evidence Analysis Facility (TEAF) at FIU for assisting with LA-ICPMS analyses.

Funding:

2019 GSA Graduate Student Research Grant Recipient, 2019 SEPM Student Research Grant Awardee

2.7 References

Angermann, D., J. Klotz, and C. Reigber, Space-geodetic estimation of the Nazca-South America angular velocity, Earth Planet. Sci. Lett., 171, 329– 334, 1999.

Bas, M.J.L., Maitre, R.W.L., Streckeisen, A., and Zanettin, B., 1986, A chemical classification of volcanic rocks based on the total alkali-silica diagram: Journal of Petrology, v. 27, doi:10.1093/petrology/27.3.745.

Bergen, J.A., Truax, S., de Kaenel, E., Blair, S., Browning, E., Lundquist, J., Boesiger, T., Bolivar, M., and Clark, K., 2019, BP Gulf of Mexico Neogene Astronomically-tuned Time Scale (BP GNATTS): Bulletin of the Geological Society of America, v. 131, doi:10.1130/B35062.1.

Bernhardt, A., Hebbeln, D., Regenberg, M., Lückge, A., and Strecker, M.R., 2016, Shelfal sediment transport by an undercurrent forces turbidity current activity during high sea level along the Chile continental margin: Geology, v. 44, doi:10.1130/G37594.1.

Bernhardt, A., Schwanghart, W., Hebbeln, D., Stuut, J.-B.W., and Strecker, M.R., 2017, Immediate propagation of deglacial environmental change to deep-marine turbidite systems along the Chile convergent margin: Earth and Planetary Science Letters, v. 473, p. 190–204, doi:10.1016/j.epsl.2017.05.017.

Blumberg, S., Lamy, F., Arz, H.W., Echtler, H.P., Wiedicke, M., Haug, G.H., and Oncken, O., 2008, Turbiditic trench deposits at the South-Chilean active margin: A Pleistocene–Holocene record of climate and tectonics: Earth and Planetary Science Letters, v. 268, p. 526–539, doi:10.1016/j.epsl.2008.02.007.

Chapron, E., Juvigné, E., Mulsow, S., Ariztegui, D., Magand, O., Bertrand, S., Pino, M., and Chapron, O., 2007, Recent clastic sedimentation processes in Lake Puyehue (Chilean Lake District, 40.5°S): Sedimentary Geology, v. 201, doi:10.1016/j.sedgeo.2007.07.006.

Dymond, J., 1981, Geochemistry of Nazca plate surface sediments: An evaluation of hydrothermal, biogenic, detrital, and hydrogenous sources, *in* p. 133–174, doi:10.1130/MEM154-p133.

Encinas, A., Finger, K.L., Buatois, L.A., and Peterson, D.E., 2012, Geological Society of America Bulletin Major forearc subsidence and deep-marine Miocene sedimentation in the present Coastal Cordillera and Longitudinal Depression of south-central Chile (38 o30'S-41 o45'S): Bulletin of the Geological Society of America, v. 124, doi:10.1130/B30567.1.

Encinas, A., Sagripanti, L., Rodríguez, M.P., Orts, D., Anavalón, A., Giroux, P., Otero, J., Echaurren, A., Zambrano, P., and Valencia, V., 2021, Tectonosedimentary evolution of the Coastal Cordillera and Central Depression of south-Central Chile (36°30′-42°S): Earth-Science Reviews, v. 213, doi:10.1016/j.earscirev.2020.103465.

Galli-Oliver, C., 1969, Climate: A Primary Control of Sedimentation in the Peru-Chile Trench: Geological Society of America Bulletin, v. 80, p. 1849.

Giorgetti, G., Talarico, F., Sandroni, S., and Zeoli, A., 2009, Provenance of Pleistocene sediments in the ANDRILL AND-1B drillcore: Clay and heavy mineral data: Global and Planetary Change, v. 69, p. 94–102, doi:10.1016/j.gloplacha.2009.03.018.

Glasser, N., and Jansson, K., 2008, The Glacial Map of southern South America: Journal of Maps, v. 4, p. 175–196, doi:10.4113/jom.2008.1020.

Griffin, W.L., Powell, W.J., Pearson, N.J., and O'Reilly, S.Y., 2008, GLITTER: Data reduction software for laser ablation ICP–MS: Laser Ablation–ICP–MS in the Earth Sciences CURRENT PRACTICES AND OUTSTANDING ISSUES, v. 40.

Hervé, F., Faundez, V., Calderón, M., Massonne, H.J., and Willner, A.P., 2007, Metamorphic and plutonic basement complexes: Geological Society Special Publication, doi:10.1144/goch.2.

Hickey, R.L., Frey, F.A., Gerlach, D.C., and Lopez-Escobar, L., 1986, Multiple sources for basaltic arc rocks from the southern volcanic zone of the Andes (34°–41°S): Trace element and isotopic evidence for contributions from subducted oceanic crust, mantle, and continental crust: Journal of Geophysical Research, v. 91, p. 5963, doi:10.1029/JB091iB06p05963.

Hickey, R.L., Gerlach, D.C., and Frey, F.A., 1984, Geochemical variation volcanic rocks central-south Chile (32-42S). Andean magmatism: chemical and isotopic constraints.

Hickey-Vargas, R., Holbik, S., Tormey, D., Frey, F.A., and Moreno Roa, H., 2016, Basaltic rocks from the Andean Southern Volcanic Zone: Insights from the comparison of along-strike and small-scale geochemical variations and their sources: Lithos, v. 258–259, p. 115–132, doi:10.1016/j.lithos.2016.04.014.

Hickey-Vargas, R., Sun, M., López-Escobar, L., Moreno-Roa, H., Reagan, M.K., Morris, J.D., and Ryan, J.G., 2002, Multiple subduction components in the mantle wedge: Evidence from eruptive centers in the Central Southern volcanic zone, Chile: Geology, v. 30, p. 199, doi:10.1130/0091-7613(2002)030<0199:MSCITM>2.0.CO;2.

Hulton, N.R.J., Purves, R.S., McCulloch, R.D., Sugden, D.E., and Bentley, M.J., 2002a, The Last Glacial Maximum and deglaciation in southern South America: Quaternary Science Reviews, v. 21, doi:10.1016/S0277-3791(01)00103-2.

Hulton, N.R.J., Purves, R.S., McCulloch, R.D., Sugden, D.E., and Bentley, M.J., 2002b, The Last Glacial Maximum and deglaciation in southern South America: Quaternary Science Reviews, v. 21, doi:10.1016/S0277-3791(01)00103-2.

Jenks, W.F., 1956, SELECTED GENERAL REFERENCES ON SOUTH AMERICAN GEOLOGY, *in* p. xi–xii, doi:10.1130/MEM65-pxi.

Lamy, F., Hebbeln, D., and Wefer, G., 1998, Terrigenous sediment supply along the Chilean continental margin: modern regional patterns of texture and composition: Geologische Rundschau, v. 87, p. 477–494, doi:10.1007/s005310050223.

Latorre, C., Moreno, P.I., Vargas, G., Maldonado, A., Villa-Martínez, R., Armesto, J.J., Villagrán, C., Pino, M., Núñez, L., and Grosjean, M., 2007, Late quaternary environments and palaeoclimate: Geological Society Special Publication, doi:10.1144/goch.12.

López Escobar, Á., Cembrano, J., and Moreno, H., 1995, Geochemistry and tectonics of the Chilean Southern Andes basaltic Quaternary volcanism (37-46°S): Revista geológica de Chile: An international journal on andean geology, v. 22, doi:10.5027/andgeoV22n2-a06.

Lopez-Escobar, L., Kilian, R., Kempton, P.D., and Tagiri, M., 1993, Petrography and geochemistry of Quaternary rocks from the Southern Volcanic Zone of the Andes between 41°30′ and 46°00′S, Chile: Revista Geologica de Chile, v. 20, doi:10.5027/andgeoV20n1-a04.

Marchant, M. et al., 2007, Marine geology, oceanography and climate: Geological Society Special Publication, doi:10.1144/goch.11.

Marchant, M., C.A., F.S., G.H., G.S., H.D., K.J., L.F., M.M., P.V., R.O., 2007, Marine geology, oceanography and climate, *in* Moreno, T. and Gibbons, W. eds., The Geology of Chile, Geological Society of London, London, The Geological Society, p. 289–309.

McCulloch, R.D., Bentley, M.J., Purves, R.S., Hulton, N.R.J., Sugden, D.E., and Clapperton, C.M., 2000, Climatic inferences from glacial and palaeoecological evidence at the last glacial termination, southern South America: Journal of Quaternary Science, v. 15, doi:10.1002/1099-1417(200005)15:4<409::aid-jqs539>3.0.co;2-%23.

Melnick, D., and Echtler, H.P., 2006, Inversion of forearc basins in south-central Chile caused by rapid glacial age trench fill: Geology, v. 34, p. 709, doi:10.1130/G22440.1.

Mix, A.C., Tiedemann, R., Blum, P., Lund, S.P., and Stoner, J.S., 2003, Proceedings of the Ocean Drilling Program, 202 Initial Reports: Ocean Drilling Program, Proceedings of the Ocean Drilling Program, doi:10.2973/odp.proc.ir.202.2003.

Muratli, J.M., Chase, Z., McManus, J., and Mix, A., 2010, Ice-sheet control of continental erosion in central and southern Chile (36°-41°S) over the last 30,000 years: Quaternary Science Reviews, v. 29, doi:10.1016/j.quascirev.2010.06.037.

Nesbitt, H.W., Fedo, C.M., and Young, G.M., 1997, Quartz and Feldspar Stability, Steady and Non Steady State Weathering, and Petrogenesis of Siliciclastic Sands and Muds: The Journal of Geology, v. 105, p. 173–192, doi:10.1086/515908.

Petit J.R., Jouzel J., Raynaud D., Barkov N.I.,Barnola J.M., Basile I., Bender M., Chappellaz J., Davis J., Delaygue G., Delmotte M., Kotlyakov V.M., Legrand M., Lipenkov V., Lorius C., Pépin L., Ritz C., Saltzman E., Stievenard M. (1999). Climate and Atmospheric History of the Past 420,000 years from the Vostok Ice Core, Antarctica, Nature, 399: 429-436.

Porter, S.C., 1981, Pleistocene glaciation in the southern Lake District of Chile: Quaternary Research, v. 16, doi:10.1016/0033-5894(81)90013-2.

Ramirez, S.G., and Milliken, K.L., 2016, Data report: atlas of lithic grain types at Site C0002; reference for petrographic provenance analysis in the Kumano Basin and upper Nankai accretionary prism, doi:10.2204/iodp.proc.338.204.2016.

Scasso, R.A., and Carey, S., 2005, Morphology and formation of glassy volcanic ash from the August 12-15, 1991 eruption of Hudson volcano, Chile: Latin American Journal of Sedimentology and Basin Analysis, v. 12.

Scholl, D.W., Christensen, M.N., Huene, R. v., and Marloe, M.S., 1970, Peru-Chile Trench Sediments and Sea-Floor Spreading: Geological Society of America Bulletin v. 81, p. 1339.

Schweller, W.J., Kulm, L.D., and Prince, R.A., 1981, Tectonics, structure, and sedimentary framework of the Peru-Chile Trench, *in* p. 323–350, doi:10.1130/MEM154-p323.

Servicio Nacional de Geología y Minería. Mapa geológico de Chile, 1982, Chile. Servicio Nacional de Geología y Minería. Mapa geológico de Chile. Santiago: Servicio Nacional de Geología y Minería, 2002. Scale 1:1,000,000; universal transverse Mercator proj. (W 76°--W 66°/S 18°--S 56).: https://lccn.loc.gov/2009578618,.

Smith, J. v., 1987, Clastic Particles: Scanning Electron Microscopy and Shape Analysis of Sedimentary and Volcanic Clasts. John R. Marshall: The Journal of Geology, v. 95, doi:10.1086/629185.

Stern, C.R., Moreno, H., López-Escobar, L., Clavero, J.E., Lara, L.E., Naranjo, J.A., Parada, M.A., and Skewes, M.A., 2007, Chilean volcanoes: Geological Society Special Publication, doi:10.1144/goch.5.

Sun, S. -s., and McDonough, W.F., 1989, Chemical and isotopic systematics of oceanic basalts: implications for mantle composition and processes: Geological Society, London, Special Publications, v. 42, p. 313–345, doi:10.1144/GSL.SP.1989.042.01.19.

Thornburg, T.M., and Kulm, L.D., 1987, Sedimentation in the Chile Trench: petrofacies and provenance.: Journal of Sedimentary Petrology, v. 57, doi:10.1306/212F8AA3-2B24-11D7-8648000102C1865D.

Todd M. Thornburg, L. D. Kulm, 1983, Depositional Environments and Sedimentary Processes in Chile Trench: ABSTRACT: AAPG Bulletin, v. 67, doi:10.1306/03b5b560-16d1-11d7-8645000102c1865d.

Tormey, D.R., Hickey-Vargas, R., Frey, F.A., and López-Escobar, L., 1991, Recent lavas from the Andean volcanic front (33 to 42°S); Interpretations of along-arc compositional variations, *in* p. 57–78, doi:10.1130/SPE265-p57.

Vega, R.M., Mella, M., Nielsen, S.N., and Pino, M., 2018, Stratigraphy and sedimentology of a late Pleistocene incised valley fill: a depositional and paleogeographic model for “Cancagua” deposits in north-western Patagonia, Chile: Andean Geology, v. 45, doi:10.5027/andgeoV45n2-3030.

Venzke, E. (ed.), 2021, Global Volcanism Program, 2013: Volcanoes of the World v. 4.9.4,.

Völker, D., Geersen, J., Contreras-Reyes, E., and Reichert, C., 2013, Sedimentary fill of the Chile Trench (32–46°S): volumetric distribution and causal factors: Journal of the Geological Society, v. 170, p. 723–736, doi:10.1144/jgs2012-119.

Völker, D., Reichel, T., Wiedicke, M., and Heubeck, C., 2008, Turbidites deposited on Southern Central Chilean seamounts: Evidence for energetic turbidity currents: Marine Geology, v. 251, p. 15–31, doi:10.1016/j.margeo.2008.01.008.

Völker, D., Wiedicke, M., Ladage, S., Gaedicke, C., Reichert, C., Rauch, K., Kramer, W., and Heubeck, C., 2006, Latitudinal Variation in Sedimentary Processes in the Peru-Chile Trench off Central Chile, *in* The Andes, doi:10.1007/978-3-540-48684-8_9.

Vostok Ice Core from Wikimedia, (Wikimedia, licensed under CC BY-NC-ND 2.0http://www.ngdc.noaa.gov/paleo/icecore/antarctica/vostok/vostok_data.html

W. Mahaney, 2002, Atlas of Sand Grain Surface Textures and Applications:

Zavala, C., and Arcuri, M., 2016, Intrabasinal and extrabasinal turbidites: Origin and distinctive characteristics: Sedimentary Geology, v. 337, p. 36–54, doi:10.1016/j.sedgeo.2016.03.008.

3. ORIGIN OF VOLCANIC GLASS IN TURBIDITES FROM ODP SITE 1232, NAZCA PLATE: INSIGHTS INTO PLEISTOCENE VOLCANISM IN SOUTHERN SOUTH AMERICA

Abstract

Volcanic glasses preserved in turbidite deposits in the Chile Basin provide a record of local glacial/interglacial eruption history. Geochemical data were used to link volcanic glass on the Nazca Plate to explosive eruptions within the Chilean Southern Volcanic Zone (SVZ). Pleistocene turbidites were recovered at Ocean Drilling Project (ODP) Site 1232 on the Nazca Plate seaward of the Peru-Chile Trench. The coarsest sediments within the turbidites contain anomalously large amounts (43-64%) of predominantly (~86%) basaltic andesite to andesitic fresh, angular volcanic glass fragments. Major and trace element concentrations of individual volcanic glass shards from cores from ODP Leg 202 were measured using scanning electron microscope (SEM) and laser ablation inductively coupled plasma mass spectrometry (La-ICP-MS). Glass compositional analyses indicate that the volcanic glasses within the Site 1232 turbidites originated from a single source. The Site 1232 glasses are present in pre-Holocene sediments, probably as old as 275 kyr. Glass geochemistry from these samples are compared to data from predominantly Holocene aged deposits from the Transitional, Central and Southern South volcanic zones. Geochemical analysis shows a strong correlation in incompatible trace element ratios, and the most likely potential source for the volcanic glasses is the Central Southern Volcanic Zone (specifically Puyehue-Cordon Caulle volcanic complex).

3.1 Introduction

Ocean Drilling Program (ODP) Site 1232 is located at 39°53.45', 75°54.08'W on the Nazca Plate across the trench from South-Central Chile, within the Chile Basin (Fig. 3.1). This site was one of 11 drilled on ODP Leg 202, which had the objective of investigating Pleistocene global climate and biota in the southeastern Pacific (Mix et al., 2003). While sites 1233, 1234, 1235, located on the adjacent South American continental shelf, encountered Pleistocene to Holocene hemipelagic sediments with rare volcanic ash layers, Site 1232 was characterized by an extremely high sedimentation rate with over 700 turbidite sequences within 300 m of drilled sediment (Mix et al., 2003). Detailed examination of the turbidites by Beck and Hickey-Vargas (in press, available online) revealed that volcanic glass particles were an abundant constituent of the coarse sediment fraction of the turbidites. Below 140 m depth, altered pumice fragments dominate the coarse fraction of the turbidites, while fresh-appearing, angular glass shards (45-63%) dominate the upper 140 m. Other phases in the coarse fractions are devitrified glass, lithic fragments, quartz, feldspar, pyroxene, chlorite, and biotite mica. Nannofossil biostratigraphy, Beck and Hickey-Vargas (in press, available online) indicates that the change from altered pumice to fresh angular glass fragments, occurred at about 175-220 kyr, overlapping the Marine Isotope Stage (MIS)-7 to MIS-6 interglacial to glacial transition.

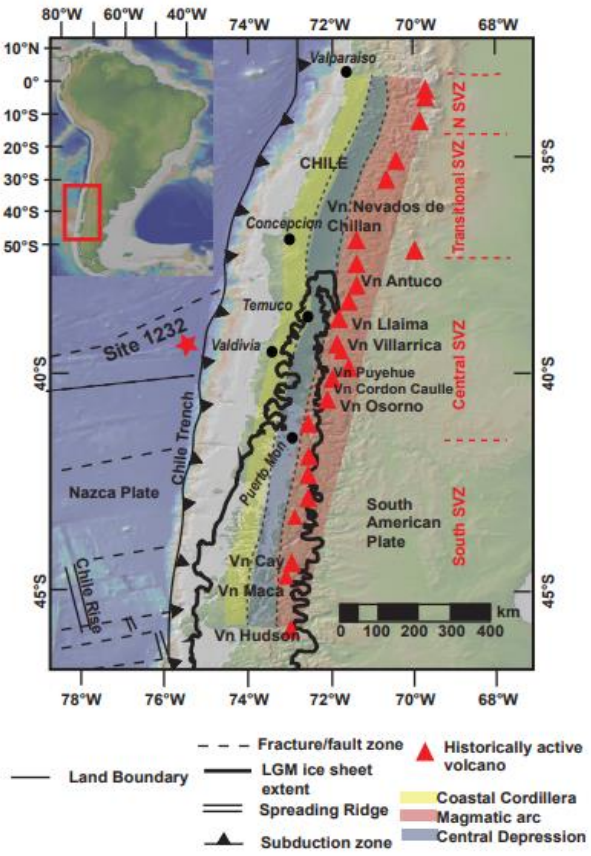

Figure 3.1: Figure modified from Beck and Hickey-Vargas (in press, available online), global multi-resolution topography (GMRT) map of southwest South America (South-central Chile) and adjacent Nazca plate ocean floor showing the location of ODP Site 1232. Figure made with GeoMapApp (www.geomapapp.org). Extent of the Patagonian Ice Sheet during the Pleistocene Glacial Maximum is represented by a thick solid and dashed line, after (Porter, 1981; McCulloch et al., 2000; Hulton et al., 2002b). Triangles represent volcanoes active during the Pleistocene in the SVZ (Stern et al., 2007; Venzke, 2021)

The purpose of this study is to determine the origin of coarse sediments from Pleistocene-Recent turbidites at ODP Site 1232, the methods of their emplacement on the Nazca plate, and their relationship to the past climatic environment. Basal layers of the turbidites include fresh angular glass shards, mineral grains, and fossils. Site 1232 is a rare example of turbidites extending across the trench and onto the downgoing plate. The high abundance of volcanic glass is also unusual, leading to questions about the mechanisms that enabled the sediments to travel from distant volcanic sources, traverse

the trench, while preserving the glass component. In this study the major and trace element geochemistry of glass shards from 29 turbidite intervals from Site 1232 were the main focus. The overall aim of this work is to contribute to the knowledge of Pleistocene volcanic activity and potential sedimentary transportation processes on the adjacent South American continent and continental shelf. Scanning electron microscopy (SEM) was used in conjunction with laser ablation inductively coupled mass spectrometry (LA-ICP-MS) to examine the chemical and physical properties of individual glass shards and determine:

1) Whether the volcanic glass shards from the Site 1232 turbidites come from multiple volcanic sources or from a single source, to help identify eruptive behavior of the source or sources.

2) Whether there is any type of recognizable temporal pattern to determine if there is a long-standing eruptive pattern; and

3) Whether the geochemical and physical characterization can constrain the Site 1232 glasses to a specific volcanic source or region, determination of source origin can allow for further understanding of transport processes involved in deposition.

Based on geography and preliminary analyses, the Chilean Southern Volcanic Zone (Fig. 3.2) is a likely source for the volcanic glasses (Beck and Hickey-Vargas, in press, available online). Although the Chilean SVZ is one of the most geologically active areas in the world, much is still unknown about the eruptive history throughout the Pleistocene due to its remoteness, high eruptive frequency, and landscape changes due to glaciation. Studies have shown that the major and trace element composition of volcanic glasses can be used with morphological characteristics in comparison with published data for known volcanic centers to establish their provenance (Haberle and Lumley, 1998;

Pearce et al., 1999) Glasses within turbidite deposits may also provide a record of the eruption frequency of source volcanoes and record the geochemical evolution of past eruptive products. Identifying the source of volcanic debris and its geochemical characteristics can significantly improve the understanding of volcanic eruption patterns, sediment transport pathways, and possibly allow for more refined forecasting of potential volcanic hazards (Albert et al., 2012)

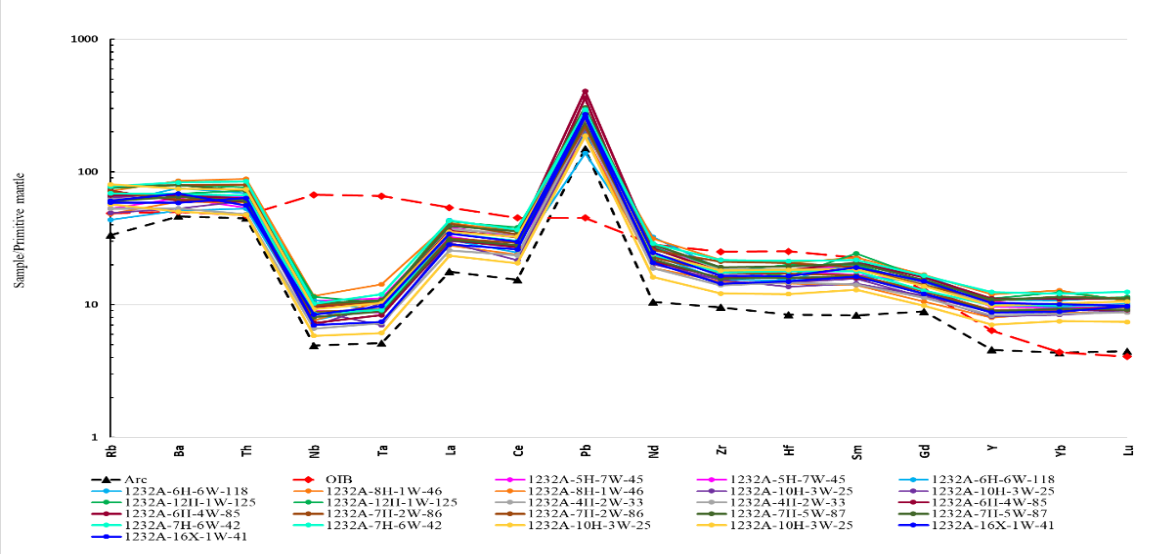

Figure 3.2: Abundances of trace elements in glass shards from Site 1232 normalized to a composition for the primitive mantle (Sun and McDonough, 1989). Two data points from each interval analyzed with LA_ICP_MS are represented. Also plotted are patterns for OIB (red) and arc (black) volcanic rocks taken from (Sun and McDonough, 1989; López Escobar et al., 1995

3.2 Study Region

3.2.1 Geologic history of the area

The continental coastline of Chile is one of the most geologically active continental margins, created by the subduction of the oceanic Nazca Plate and Antarctic Plates beneath the continental South American Plate. The oceanic Nazca and Antarctic Plates are located in the South Pacific Ocean, and separated by the Chile Ridge, the spreading center of the Antarctic and Nazca Plates. The Nazca Plate has a slightly

northeastward motion with respect to the Pacific Plate, driven by subduction of the South American Plate in the Peru-Chile Trench and the spreading of both the East Pacific Rise (EPR) and the Chile Ridge (Dymond, 1981, Merchant et al., 2007). The Chile Ridge is currently undergoing subduction into the Peru-Chile Trench at a latitude of approximately 46°S; the meeting of these three plates is known as the Chile triple junction (Dymond, 1981, Merchant et al., 2007). The Peru-Chile Trench extends along 5,900 km along the South American coastline and ranges between (~5.5-8km) in depth, (~10°-35°) angle of subduction, and amount of sedimentary infill (Scholl et al, 1968 and 1970, Schweller et al, Völker et al., 2008 and 2013, and Blumberg et al., 2008). A narrow continental shelf of varying widths, a high continental slope, and a deep-sea trench define the Chilean continental margin.

3.2.2 Southern Volcanic Zone and backarc

The SVZ is the result of the subduction of the Nazca plate beneath the South American plate, from 33°S to 46°S. The Andean arc contains several volcanic centers and has been active since the Miocene (Hickey et al., 1986, Tormey et al., 1991, López–Escobar et al., 1995, Stern, 2004, Hickey-Vargas et al., 2016). The SVZ is divided into four geochemically distinct zones: The Northern Southern Volcanic Zone (NSVZ), Transitional Southern Volcanic Zone (TSVZ), Central Southern Volcanic Zone (CSVZ), and Southern Southern Volcanic Zone (SSVZ), each producing a large variety of products with differing magmatic associations. (Hickey-Vargas et al., 2002). The NSVZ at the northernmost point of the SVZ between 33°S and 34.5°S is ~320km from the Peru-Chile Trench and is characterized by primarily andesitic volcanoes (Hickey-Vargas et al., 2016). The TSVZ spans 34.5°S to 37°S, ~320km from the Peru-Chile Trench, and is

represented by largely andesitic, dacitic and rhyolitic volcanoes (Hickey-Vargas et al., 2016). The CSVZ extends from 37°S to 41.5°S, ~280km from the trench, and is composed of predominantly basalt to basaltic andesite (Hickey-Vargas et al., 2016). The SSVZ, 41.5° to 46°, is located ~250km from the Peru-Chile Trench and is represented by volcanoes ranging in composition from rhyolite to basalt and dacite (Hickey et al., 1986). With the subduction of the Chile Ridge occurring at 46°S, the composition of the southernmost portion of the SSVZ is geochemically distinct from the other zones. The Southern Volcanic Zone (SVZ) of the Andean arc is centered on the latitude of Site 1232. Volcanic products erupted from centers within these segments range in composition from basalt to dacite and rhyolite, with specific geochemical signatures used to distinguish one center from another (Hickey et al., 1986; Tormey et al., 1991; Hickey-Vargas et al., 2016).

3.2.3 Major Pleistocene SVZ volcanic centers and the Pleistocene continental/shelf environment

Southern Chile is one of the most volcanically active areas globally, characterized by frequent, sometimes violent, volcanic eruptions. Although the tephra record of the Chilean Southern Volcanic Zone has been widely studied, very little is known about Pleistocene volcanism, due to its remoteness and highly active nature. SVZ volcanoes with documented eruptions in the Mid to Late Pleistocene include Descabezado-Quizapu-Azul, Calabozos, Nevado de Chillan, Antuco, Callaqui, Sierra Nevada, Llaima, Puyehue, Puyuhuapi, Tromen, Payun Matru, Caviahue, Cerro Velluda, Cerro Maichin, Villarrica, Quinchilca, Mocho-Choshuenco, Cordon Caulle, Osorno, Calbuco, Maca, Rio Ibanez and Hudson (Stern et al., 2007; Hickey et al., 2014, Venzke, 2021, Weller et al., 2019).

The Chilean continental shelf varies in width, generally increasing in width as you travel farther southward (Scholl et al., 1970, Thornburg and Kulm, 1987, Merchant et al., 2007). North of 33°S the width of the shelf does not exceed 5km, it steadily grows in width to 10 km at 35°S and widens to 40-60 km between 35°S and 37°S where there is a decrease in width to around 12 km, followed by a large increase in shelf width up to 100 km in width found at 46°S (Scholl et al., 1970, Thornburg and Kulm, 1987, Merchant et al., 2007). The shelf edge is generally at a depth of between 120-150 m (Scholl et al., 1970, Thornburg and Kulm, 1987, Merchant et al., 2007). Based on sediment distribution, the Peru-Chile trench can be separated into three general regions. The trench is only partially filled with sediments less than 1 km thick from 18°S to 27.5°S. The trench fill grows in density but still remaining less than 10 km wide from 27°S to 33°S and continues to increase in sediment infill up to 46°S, finally entirely burying the trench with sediments of 20 km or wider and 1.5-2.3 km in thickness (Scholl et al., 1970, Thornburg and Kulm, 1987, Merchant et al., 2007). It has been noted that between the Chile Ridge and the Juan Fernandez Ridge, there is a modest northward slope, forcing sediment to flow northward over a 650-kilometer-long twisting axial channel though the trench (Thornburg and Kulm, 1987, Merchant et al., 2007, Völker et al., 2008).

3.2.4 Site 1232

ODP Site 1232 is located on the Nazca Plate, 230 km off the coast of Valdivia, Chile. The trench adjacent to Site 1232 (39°S to 40°S) is infilled with ~2.5 km of sedimentary deposits includes abundant turbidites (Scholl et al., 1970; Schweller et al., 1981; Thornburg and Kulm, 1987). Sediment accumulation rates increase rapidly moving southward along the trench and sedimentation rate in and around Site 1232 ranges from

1,500 - 2,000 m/my (Schweller et al., 1981). The Nazca plate sediments are accumulated from varied sources, including hydrothermal, biogenic, detrital, and terrigenous (Dymond, 1981; Thornburg and Kulm, 1983). Transportation process, proximity to glacial extent, availability of terrigenous sediment, biologic productivity, and closeness to varying volcanic/hydrothermal sources can all play an important role in the sedimentological differences of the area.

The main purpose of Leg 202 was to explore the relationship between global climate and the biological cycle on a vast scale (Mix et al., 2003). The Nazca plate Site was chosen to evaluate long-term Neogene response to tectonic and climatic events. Site 1232 was chosen due to a predicted high rate of sedimentation, researchers expected to retrieve 300 m of hemipelagic sediments, but discovered a startling number of successive turbidite sequences. The expedition retrieved three cores from Site 1232: 1232A, 1232B and 1232C. Hole A, drilled on the seafloor with a starting depth of 4089 mbrf (meters below rig floor). An advanced piston corer (APC) was used to drill to a depth of 112.5 mbsf (meters below seafloor) and an extended core barrel (XCB) was used to continue from 112.5-371.3 mbsf (Mix et al., 2003). For Hole B, drilling began on the seafloor at a depth of 4075 mbrf; an APC was used to a depth of 90.1 mbsf where the hole was terminated (Mix et al., 2003). Hole C was drilled at a depth of 4079.8 mbrf, the shallowest recovery of the 3 cores, to a depth of only 33.2 mbsf using an APC (Mix et al., 2003). Using stratigraphic correlation and magnetic susceptibility, the shipboard party correlated the upper 42.58 m of the 1232A and 1232B cores into a composite section (Mix et al., 2003). The upper 288 m of the 1232A core is interpreted to be 12.47 kyr - 275 kyr (Blumberg et al., 2008, Beck and Hickey-Vargas, in press, available online).

3.3 Methods

3.3.1 Sample description and selection

Twenty-nine turbidite intervals from ODP Site 1232 Holes A and B were analyzed in this study. Eight initial samples were provided by Dr. K. Marsaglia and the remaining twenty-one samples were subsequently retrieved from the IODP Gulf Coast Repository, College Station, Texas. The turbidite intervals selected for this analysis were chosen throughout the depth of the core based on the overall thickness of coarse layers and grain size of the particles. The samples used in this study are predominantly sandy silt-sized particles or coarser in order to optimize the ability to analyze single grains (see methods). When possible, the thickness of the coarse layer that the sample was selected from was at least 4 cm in order to sample the most significant turbidite events. Visual inspection of the cores and core photos show a classic turbidite structure with coarser sandy-silt overlying a sharp basal contact which grades upward to silty clay.

Site 1232 cores consist of two main sedimentary facies, described in greater detail in Beck and Hickey-Vargas (in press, available online). Turbidite layers are found interbedded with the dominant clay facies and thin silt layers are present intermittently with insignificant sand content (Mix et al., 2003). According to Mix et al. (2003), there are 1328 coarse layers observed throughout the 1232 Site, with a total of 772 layers present in the 289 m of core recovered in 1232A and over 250 layers present in the 100 m of core recovered in 1232B (Mix et al., 2003). The coarse sediment layers range from 0.5cm to 52cm, with an overall average of 3.2cm in thickness. For this detailed provenance study, individual grain analysis of glass shards was chosen over bulk analytical methods because grains large enough for *in-situ* analysis were present, and

bulk coarse fractions contained identifiable foreign material such as microfossils, mineral and lithic fragments (polymineral grains) (Beck and Hickey-Vargas, in press, available online).

3.3.2 Analytical methods

Turbidite samples were wet sieved in deionized water to obtain the coarsest size fractions (>210 micron and > 149 micron) to isolate grains large enough for multiple LA-ICP-MS analyses. Samples were agitated in an ultrasonicator to remove adhering small particles and dried in an oven at 100°C oven overnight. Cleaned sediments were viewed under a binocular microscope to identify glassy grains and minerals. Grains with the appearance of glass were picked and examined under a petrographic microscope to verify isotropic properties. Cleaned and picked glass shards were then mounted on carbon tape disks, and color, vesicularity, and angularity was documented before Scanning Electron Microscope (SEM) analysis was performed at the Florida Center for Analytical Electron Microscopy (FCAEM) at Florida International University (FIU).

3.3.2.1 Scanning electron microscope (SEM)

Volcanic glass shards of both the >149µ size fraction and the 210µ size fraction were analyzed for major elements using SEM using energy dispersive spectroscopy (EDS). Although SEM-EDS analysis is semi-quantitative, this approach was selected rather than more precise electron probe microanalysis (EPMA) because, due to major element variations caused by magmatic differentiation processes, it was more likely that trace element patterns rather than major element criteria would be distinctive for identifying a specific volcanic source (Hickey-Vargas et al., 2016, and sources therein). The small and highly vesicular samples were preserved for later LA-ICPMS trace

element analysis. Preparing glasses for EPMA requires mounting in epoxy and surface polish which would have resulted in significant loss of material.

Secondary electron (SE) imaging was used to obtain high resolution images of glass shards and grains for examination of texture and backscatter electron imaging (BSE) was used to look for microcrystals and to assess homogeneity. Once identified, homogenous areas of glass were analyzed with the EDS. Grains were analyzed using a 39µm spot size under high vacuum with a 15kv accelerating voltage; an average of two to three spots were analyzed on each grain depending on grain size. Glass analyses were performed with reference materials Rhyolite (Smithsonian standard NMNH 72854, VG 568), and Hawaiian basaltic glass (BHVO-2) which were run at the beginning, middle and end of each analytical session. The average of three readings was taken for each reference material. Analytical precision, assessed during each analytical run using the EDS on the BHVO-2 glass is better than: SiO_2 (1.59%), Al_2O_3 (6.28%), FeO (6.85%), MgO (8.53%), CaO (7.12%), Na_2O (8.51%), and for Rhyolite better than: SiO_2 (0.94%), Al_2O_3 (4.06%), K_2O (9.48%).

3.3.2.2 Laser ablation inductively coupled plasma mass spectrometry (LA-ICP-MS)

After SEM with EDS analysis, 119 grains from the 210µ size fraction were analyzed for trace elements using the LA-ICP-MS (ELAN DRC ICP/MS and New Wave UP 213 nm laser ablation system) at the Trace Evidence Analysis Facility (TEAF), FIU. An additional 95 grains from the > 210µ fraction from both 1232A and 1232B were analyzed for trace elements using the Aligent Technologies 7700 Series LA-ICP-MS at TEAF, FIU. This size fraction was chosen in order to allow for the maximum surface for

repeat analyses. Glasses were analyzed for the trace elements Rb, Sr, Y, Zr, Nb, Ba, La, Ce, Nd, Sm, Eu, Gd, Dy, Er, Yb, Hf, Pb, Th, and U, as well as for the major element Ti, for comparison with SEM data.

Instrumentation parameters used during LA-ICP-MS glass analysis for both the ELAN and the Aligent laser ablation systems are as follows: a 55µm laser spot size with a repetition rate of 5hz and dwell time of 60 seconds. Ca was used as the internal standard, NIST (National Institute of Standards and Technology), SRM612 glass was used for calibration, and both NIST SRM 612 and BHVO-2 glass were used to monitor drift during analysis. At least two 55-micron spots were ablated on each grain whenever possible and the data for the two points averaged. In some cases grains were too small or not ideal to make a second ablation and a few grains had breakage during ablation resulting in poor signal collection; in those instances, only one ablation was used. Data reduction was performed using 'Glitter' software (Griffin et al., 2008) with the NIST SRM612 as a standard with the Ca data obtained from the individual glass grains by SEM entered manually.

3.4 Results

3.4.1 SEM images

Microscopic inspection using high resolution imaging on the SEM shows that the glass shards generally display well-preserved fresh, angular textures with no traces of abrasion. Four distinct textural varieties of glasses were observed. Elongate pipe vesicular shards, highly vesicular shards, poorly vesicular shards and dark brown to black blocky shards (Fig. 3.3) were all present in each interval containing glass.

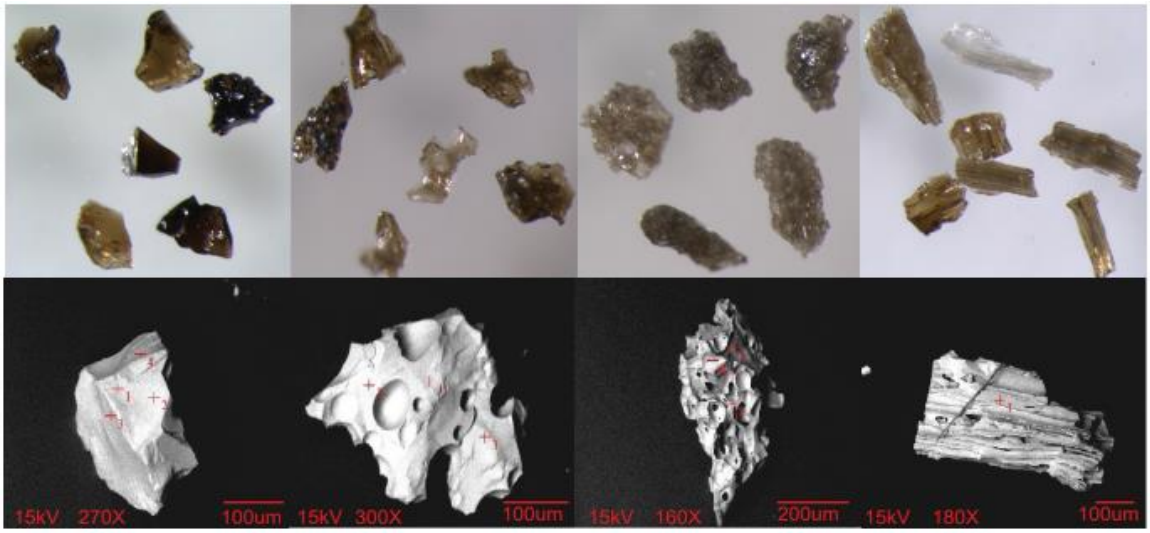

Figure 3.3: Figure modified from Beck and Hickey-Vargas (in press, available online), optical microscope (80x magnification) and high-resolution scanning electron microscope images (magnification and scale bar on image) of Site 1232 volcanic glasses. Four distinct varieties of glasses are present: Dark brown non-vesicular blocky shards, poorly vesicular shared, highly vesicular shards with spherical vesicles, and shards with pipe vesicles.

3.4.2 Major element analysis

For all analyzed turbidite intervals containing glass, there is no up-core change in the range of SiO_2 contents in glasses (Fig 3.4). The analyzed glasses range in composition from basalt (trachy-basalt) to rhyolite (49-79% SiO_2), with 5.4% of grains in the 45-52% SiO_2 (basalt/trachy-basalt) range, 57.5% of grains in the 52-57% SiO_2 (basaltic andesite/basaltic trachy-andesite) range, 26.4% of grains in the 57-63% SiO_2 (andesite/trachy-andesite) range, and 10.6% of grains in the >63% SiO_2 (dacite/rhyolite) range (Fig. 3.5). Samples show concentrations of FeO (3.3-16.5%), MgO (0.7-4.8%), TiO_2 (1.0-2.9%), Al_2O_3 (11.6-23.8%) and CaO (0.1-11.1%) versus SiO_2 (Fig. 3.6a-3.6e). On Harker variation diagrams, glasses exhibit well-defined trends of decreasing FeO, MgO, TiO_2 and CaO content with increasing SiO_2 as expected in series formed by magmatic differentiation by fractional crystallization. Samples have K_2O (0.88-3.2%) and Na_2O (3.4-7.6%) and generally plot in the medium-K field (Fig. 3.6f).

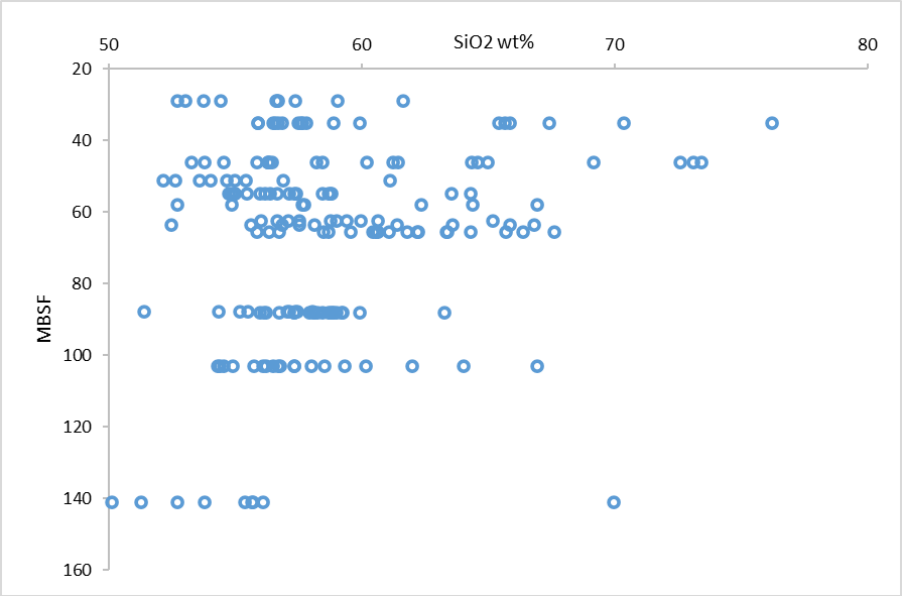

Figure 3.4: Plot of depth versus SiO_2 (wt%) content of glass shards in turbidite sediments of IODP Site 1232. Data are from Table 5.

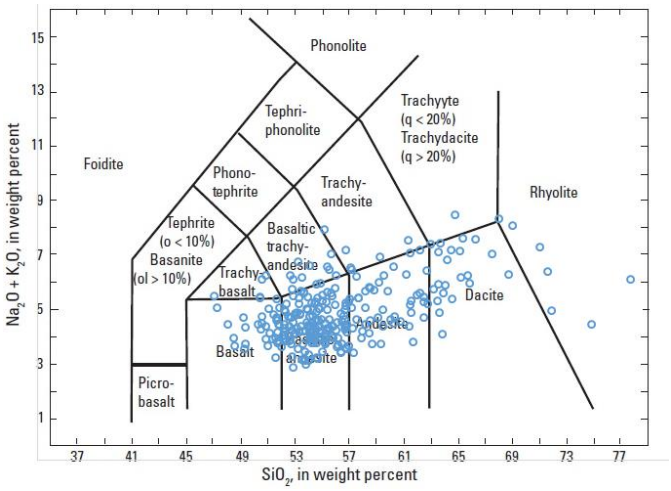

Figure 3.5: Total alkali versus SiO_2 (TAS) classification plot (Le Bas et al., 1986) for glasses separated from coarse sections of turbidites. Glass compositions range from basaltic to rhyolitic. Data are from Table 5.

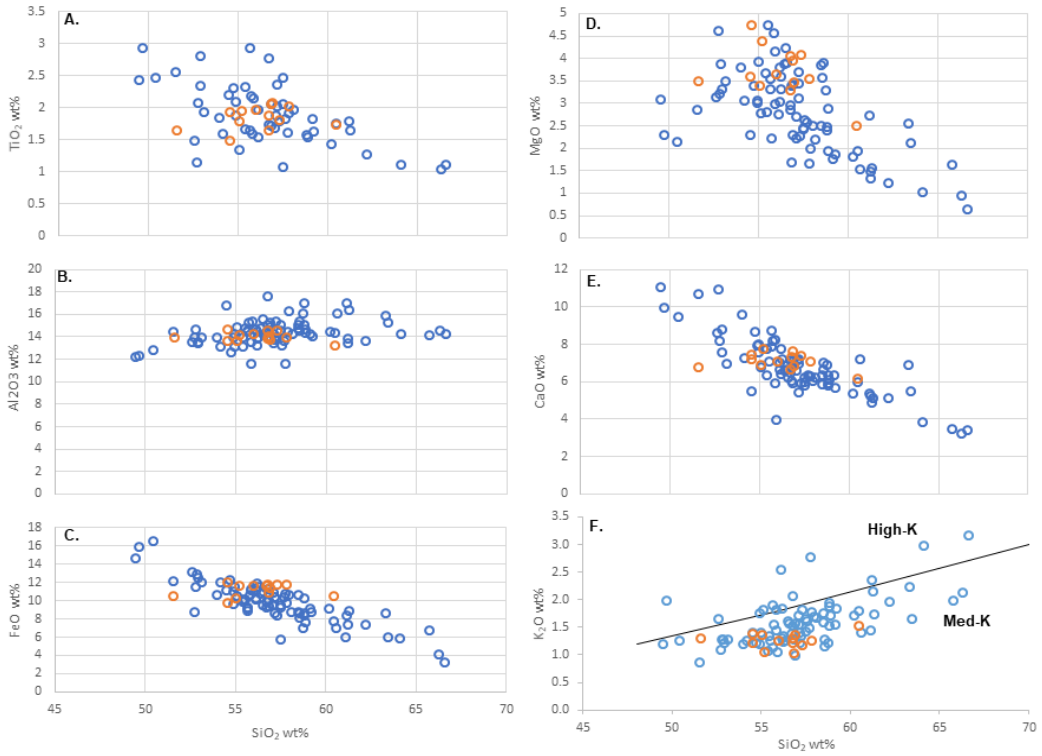

Figure 3.6 (a-f): a. Plot of TiO_2 versus SiO_2 content (wt%) of the Site 1232 volcanic glass grains (Ti in blue calculated using LA-ICP-MS, orange circles represent EPMA data); b. Plot of Al_2O_3 versus SiO_2 content (wt%) of the Site 1232 volcanic glass grains; c. Plot of FeO versus SiO_2 content (wt%) of the Site 1232 volcanic glass grains; d. Plot of MgO versus SiO_2 content (wt%) of the Site 1232 volcanic glass grains; e. Plot of CaO versus SiO_2 content (wt%) of the Site 1232 volcanic glass grains; f. plot of K_2O versus SiO_2 content (wt%) of the Site 1232 volcanic glass grains Geochemical classification line Medium K is from Ewart (1982). Data are from Tables 4 and 5.

3.4.3 Trace element analysis

Trace element data by LA-ICP-MS are given in Tables 4 and 5. Data normalized to primitive mantle (Sun and McDonough, 1989) are shown in Figure 3.2. The results exhibit subparallel trace element abundance patterns with no apparent systematic variation within or between intervals. Concentrations range from 5 to 500 times primitive mantle. All glass shards show enrichment in Rb, Ba, Th, Pb relative to rare earth elements (REE) (Fig. 3.2). The overall normalized incompatible element pattern is consistent with the distinctive pattern expected for subduction-related magmas and clearly dissimilar to mid-ocean ridge basalts (MORB), oceanic island basalts (OIB),

continental flood basalts (CFB), and their differentiated equivalents (Sun and McDonough, 1989; Rollinson, 1993).

Figures 3.7 a-e show trace element abundances plotted vs SiO_2 as a possible measure of magmatic differentiation. Compatible trace elements Sr, Sc, and V show higher concentrations in the basaltic samples with values decreasing with SiO_2. Other compatible element concentrations are Ni = 0.3 to 216.9 ppm and Cr = 0.9 to 151.2 ppm and are scattered, probably due to their low abundance. Abundances of incompatible elements La and Zr show a rough increasing trend with increasing SiO_2 (Figs. 3.7d and e), but significant scatter occurs for other incompatible trace elements such as Rb, Ba, Nb, Th, Sm, and Yb. Such scatter could be analytical, as some elements are close to their limit of detection, or related to incipient alteration of glass to clay, removing Si and adding Al, or by accidental inclusion of minute mineral crystals in the analysis. Ti contents increase to about 3% at a range of 55-60% SiO_2 and then decrease to .36% at >60% SiO_2 (Fig. 3.6).

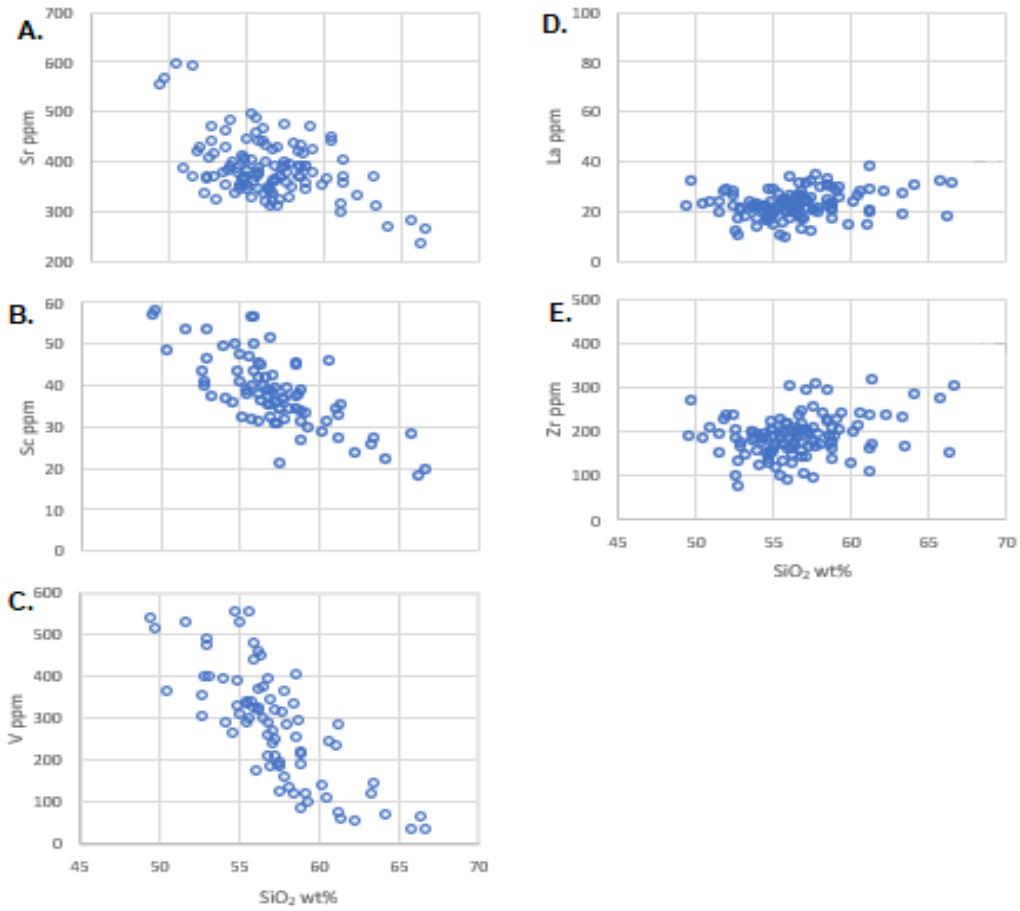

Figure 3.7 (a-e): LA-ICP-MS trace element data from individual glass shards (ppm) plotted against SEM major element data for SiO_2 (wt%). a. Sr (ppm) vs SiO_2 (wt%); b. Sc (ppm) vs SiO_2 (wt%); c. V (ppm) vs SiO_2 (wt%); d. La (ppm) vs SiO_2 (wt%); e. Zr (ppm) vs SiO_2 (wt%). Data are from Table 5

Plots of highly and moderately incompatible trace elements plotted versus each other are shown in Figs 3.8a to 3.8h. Plots of Rb, Ba, Th, La, Sm, Yb and Hf and Th vs Zr (Figs.3.8a-h) all show linear trends over the range of concentrations. Many of these extrapolate to 0, indicating little or no change during differentiation. Figure 3.9 shows REE abundances normalized to chondrites (McDonough and Sun, 1995). All glasses are LREE (light REE) enriched, with $(La/Sm)_N$ (La/Sm normalized to chondrites) = 2.27 to 3.67 and $(La/Yb)_N$ = 3.53 to 5.9.

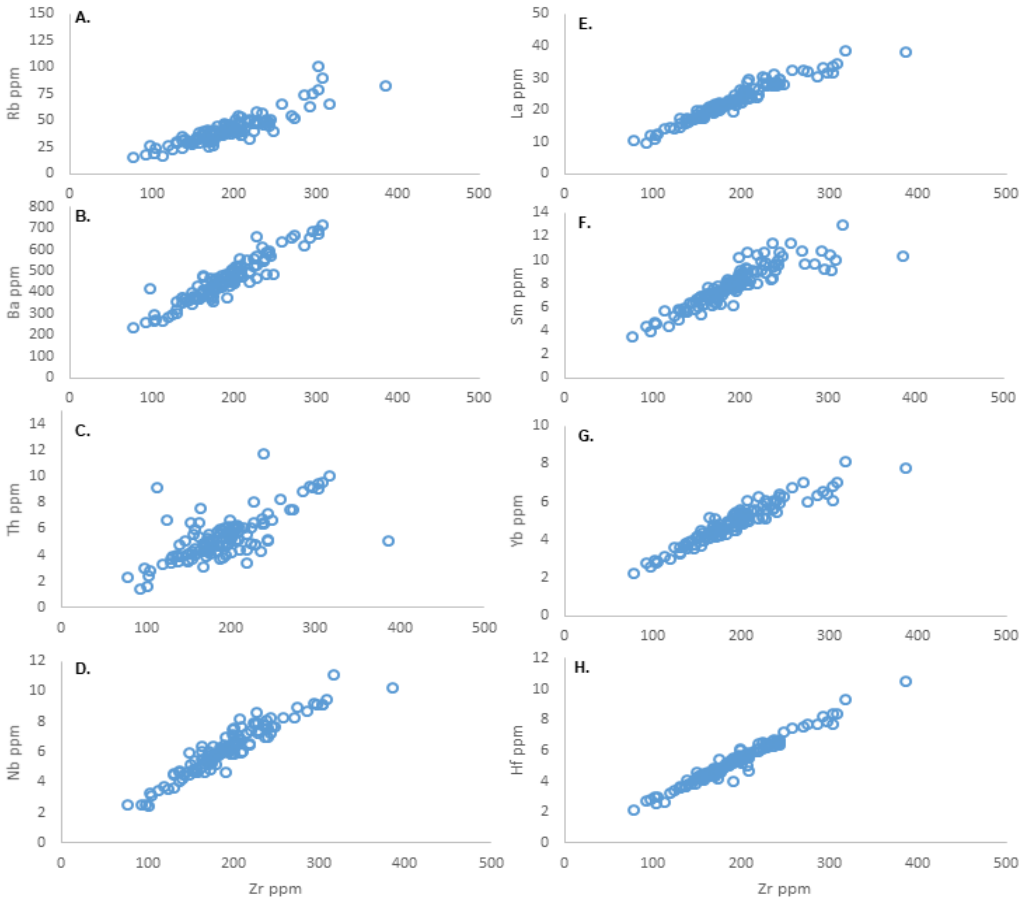

Figure 3.8 (a-g): LA-ICP-MS trace element bi-plots from individual glass shards (ppm) from Site 1232. a. Rb vs Zr; b. Ba vs Zr: c. Th vs Zr; d. Nb vs Zr; e. La vs Zr; f. Sm vs Zr; g. Yb vs Zr; and h. Hf vs Zr. The ratios are given in the Table 5.

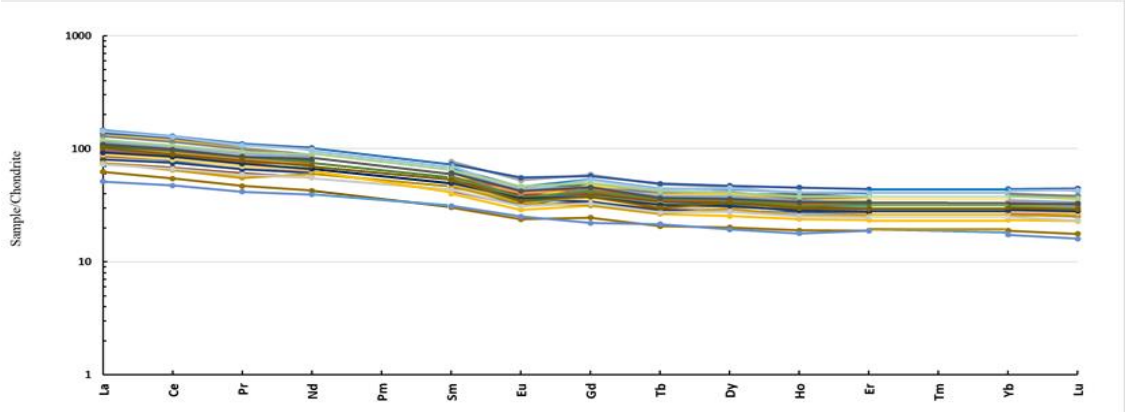

Figure 3.9: Abundances of Rare Earth Elements (REE) in glass shards from Site 1232 normalized to a composition for chondrites (Sun and McDonough, 1989). Data are from Table 5

3.5 Discussion

3.5.1 Distinguishing single vs. multiple sources, and methodology for comparison

Considering the numerous possible volcanic sources on the adjacent South American continent, one would expect the Site 1232 glasses to be derived from a range of volcanic sources. Mixing of different volcanic products could occur during turbidite initiation and deposition, with the turbidity current entraining products from different volcanic sources as it moves off the continental shelf and down the continental slope. On the continent, eruptive products could be mixed during transport by ice. Extensive ice sheets around SVZ during Pleistocene glacial periods may have received fallout from numerous eruptions and volcanic sources. With the repeated advance and retreat of glacial ice during the Pleistocene and shifting wind patterns during glacial maximums, ice sheets were subject to prolonged exposure to pyroclastic particle deposition from multiple volcanic sources. Melting of ice during glacial recession would result in a slow release of particles where further mixing would be inevitable. As evidence of this, mixed material deposits referred to as the Valdivian interglacial sand terraces are evident on the

Chilean coast Chile (38°S - 40°S) (Latorre et al., 2007). The sands are composed of volcanic sediments, ash, pumice, and kaolinite intermixed with metamorphic sediments and are deduced to be Late Pleistocene in age (Latorre et al., 2007). LaTorre et al., (2007) interpreted these sediments to have originated from a pre- Llanquihue (MIS 2) caldera forming eruption of Villarrica, with tephra transported by glacier and river and deposited fluvially along the coast in decreasing concentration from north to south.

Since the glasses and their sources are volcanic, shared magmatic processes can complicate the identification of sources and the determination of single or multi-source origin of glasses. In particular, magmatic differentiation through fractional crystallization, followed by processes such as zoning of the magma chamber and magma mixing, could affect a single magmatic source producing glassy tephra. Major and compatible element data (Figs. 3.6 and 3.7) for the turbidite glasses show typical evidence for magmatic differentiation, caused by crystal fractionation and partial melting. These are decreasing FeO, MgO, CaO and compatible element concentrations and increasing Na_2O and K_2O with increasing SiO_2. Since these trends are commonly found among continental volcanic sources, major and compatible elements are not ideal for use in distinguishing source variation.

In contrast, most incompatible trace elements in the glasses correspond with each other (Fig. 3.8), with trends that pass through the origin. This indicates that ratios of these elements were not affected by magmatic differentiation, despite the overall spread of element concentrations. Therefore, incompatible element ratios may be the most useful to fingerprint a specific volcanic source or sources. Typically, glasses originating from more than one volcanic source would yield multiple trend lines of different slopes or

recognizable clusters on incompatible vs. incompatible element plots (Figs. 3.10a and 3.10b). Samples originating from a single source would be expected to show linear compositional trends or clusters (Fig. 3.10c). The linear trends of incompatible trace elements in the Site 1232 glasses support but do not prove derivation of the glasses from a single volcanic source, as different volcanoes could have similar incompatible element features depending on their specific magma sources and evolution. However, the incompatible element ratios (Table 8) provide a differentiation-independent parameter that can be used to compare the glasses with known volcanic sources.

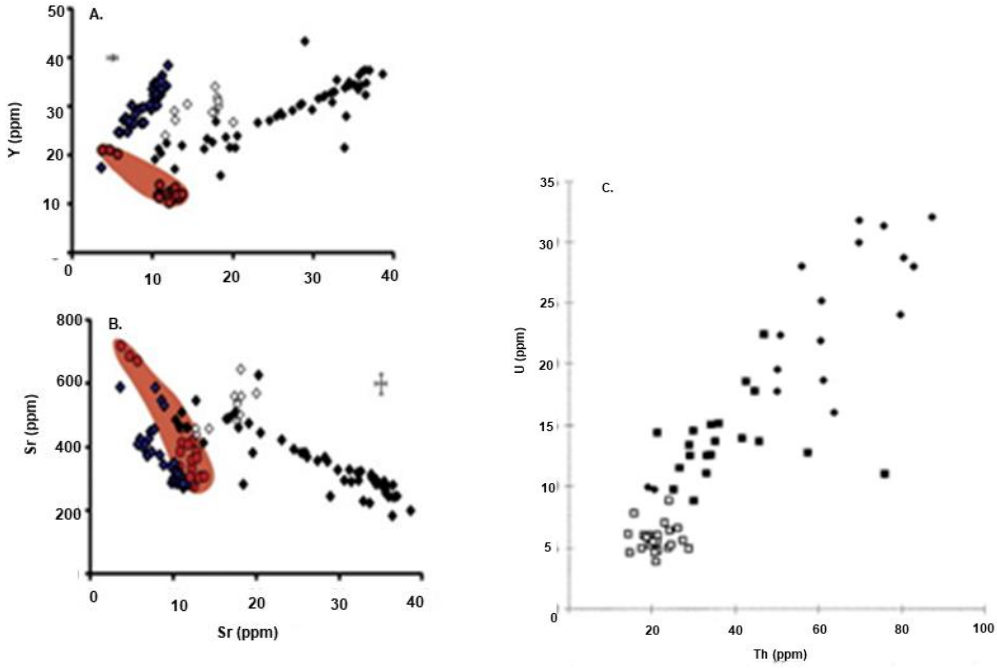

Figure 3.10a-3.10c: Plots for comparison of multi-source trace element data plotted on a variation diagram vs. single source trace element data. a. and b. are examples of geochemical data on samples from multiple sources, discernable here by multiple trend lines of differing slopes that do not extend through the origin (representing ratios of elements that are not constant) or recognizable clusters where sources plot together (seen above in blue) (Orazio et al., 2003). c. is an example of geochemical data from a single source (Pearce et al., 1999).

Another feature supporting a single source for the glasses is that there are no significant differences between the trace element patterns in glasses when comparing the

different turbidite layers to one another (Fig. 3.11). This suggests that not only are the glasses contained within the individual turbidite intervals from a single source, but all analyzed glasses from the upper 140 m of the Site 1232 core are from a single volcanic source.

To compare major and trace elements in glasses with potential volcanic sources which have differentiated, it is most useful to use a set of concentrations for a given SiO_2 or MgO, or other fixed measure of the extent of differentiation. This approach has been used widely for basaltic magmas (Klein and Langmuir, 1987; Plank and Langmuir, 1993). However, a prominent feature of the data is that the Site 1232 glasses display a strong compositional cluster in the basaltic andesite to andesite range, a better approach may be to use that predominant composition for comparison. For example, 75% of the glasses have SiO_2 between 52% and 60%. Using that range, averages of major and compatible and incompatible trace elements can be calculated, and then compared with potential volcanic sources. Averages of major and compatible element abundances for glasses in this SiO_2 range are given in Table 7, together with incompatible trace element ratios and other geochemical parameters than can be used to compare with potential sources.

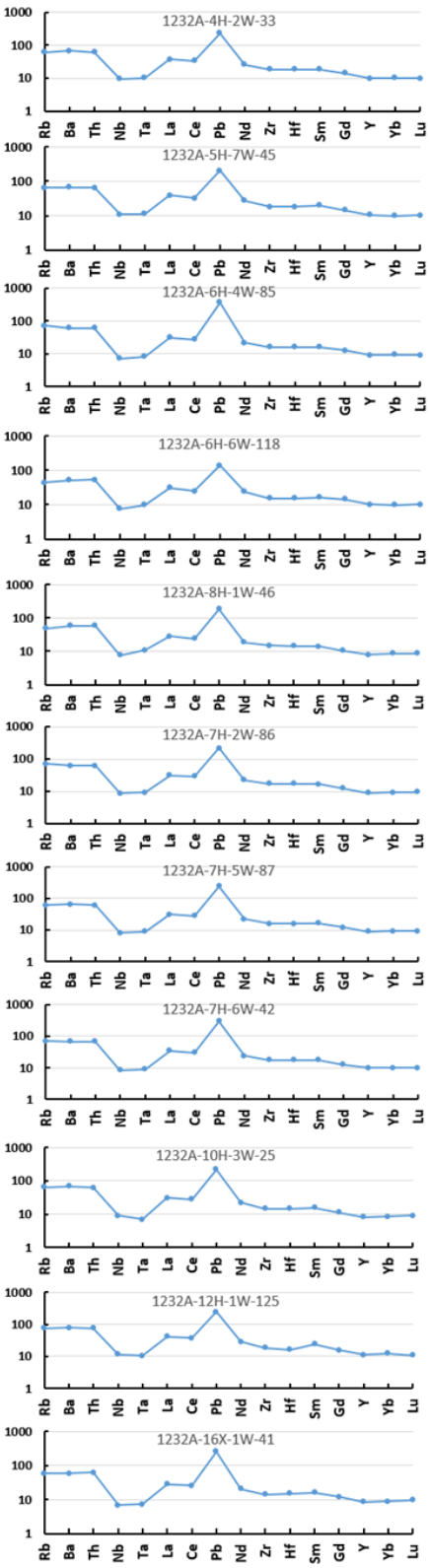

Figure 3.11: Abundances of trace elements in glass shards from Site 1232 normalized to a composition for the primitive mantle (Sun and McDonough, 1989). One plot from each interval downcore analyzed with LA-ICP-MS are represented.

3.5.2 Inferred major/trace element characteristics of the source(s)

The geochemical parameters of the Site 1232 glasses exhibit some potential fingerprints that are useful in the discrimination of source provenance. Considering major elements, Site 1232 displays a relatively high TiO_2 content (1.0-2.9%), somewhat high K_2O (.88-3.2%) compared with active SVZ volcanoes, whereas other major and compatible elements overlap. Incompatible element ratios are typical of subduction related volcanics, including the SVZ, but a specific source may be identified using all parameters together.

3.5.3 Comparison to geochemical data for SVZ volcanoes

Active volcanic areas in the region which could act as sources for the volcanic glasses include volcanoes from the southernmost TSVZ, CSVZ, SSVZ, pre-glacial volcanism, and the back arc that were active in the Pleistocene specifically between 275,000 - 12kyr, the age range determined for the upper 288 m of the Site 1232 (Blumberg et al., 2008, Beck and Hickey-Vargas, in press, available online). Since the glass shards form by rapid cooling of magma with minimal crystallization of mineral phases, its geochemical composition is considered representative of the bulk geochemistry of the magma (Haberle and Lumley, 1998; Pearce et al., 1999, Albert et al., 2012). Subsequently, the geochemistry of the glass shards within a single eruption are either homogeneous or they will define a distinct trend, allowing correlation of a source or source region (Haberle and Lumley, 1998; Pearce et al., 1999, Albert et al., 2012). To define the source area for the glasses in 1232 cores, the geochemical comparison of Site 1232 samples is compared to the chemical composition of different volcanic rock series from the SVZ.

3.5.3.1 Comparison of volcanic sources

Southernmost TSVZ

The TSVZ is characterized by volcanics ranging from basalt to dacite, ranging in SiO_2 from 50.4-71.98%, TiO_2 ranging from .33-1.36%, and K_2O ranging from .65-4.02% throughout some of the southernmost volcanic-front centers. The range of TiO_2 vs. SiO_2 falls much lower than the range of the Site 1232 glasses (Fig. 3.12a.) and while the K_2O plots (Fig. 3.13a) within the range of the K_2O values seen in the Site 1232 glasses, it falls predominantly on the lower end of the range. When compared the average values for Chillan and Site 1232 average values for HFSE (high field strength elements) Nb and Hf, LILE (large ion lithophile) Sr, and LREE (light rare Earth elements) La, Ce have comparable values (Table 7). When Descabezado-Quizapu-Azul average values are compared to the Site 1232 glasses average values similarities are seen in the LILE Ba, HFSE Ta and LREE La (Table 7). There is no association to HREE (heavy rare Earth elements) however avalible data is lacking. Trace element ratios for Zr/Hf, Hf/Rb, Th/Yb, Rb/Ba and La/Yb were compared to those of Site 1232, and while the plot for Zr/Hf showed similarities, the remaining plots were dissimilar (Figs. 3.14a-3.14e)

CSVZ

The volcanics of the CSVZ show ranges of SiO_2 (50.3-71.4%), low TiO_2 (0.36-1.9%), and K_2O (0.29-2.85%). The overall trend of the CSVZ TiO_2 content shows relatively low TiO_2 content. While some centers do show a slightly higher TiO_2 value (Llaima and Puyehue) (Fig. 3.12b), the CSVZ generally shows a trend of increasing TiO_2 with increasing SiO_2 to about 55-57% SiO_2 followed by a decrease of TiO_2 with increasing SiO_2 as SiO_2 >57%, where the Site 1232 glasses clearly show a consistent

trend of decreasing TiO_2 with increasing SiO_2. Most compared CSVZ samples plot well below the Site 1232 TiO_2 field. When K_2O values are compared (Fig. 3.13b) the CVZ fall within the range of the Site 1232 glasses, with some centers plotting in the lower range of K_2O. When comparing the average values of incompatible elements for the CSVZ and Site 1232, Puyehue-Cordon Caulle complex (PCCVC) shows the strongest correlation with moderately high TiO_2, K_2O and similar averages for the HFSEs Nb and Zr, LILEs Sr and Ba, HREEs Eu and Tb (Table 7), and overlap in the trace element ratio diagrams La/Yb, Ba/La and Ba/Th. Callaquen averages are similar for LILE Rb and LREE La (Table 7). Osorno is has comparable values to HFSE Sr, Sierra Velluda has a similar average for LILE Rb (Table 7). Trace element ratios for Zr/Hf, Hf/Rb, Th/Yb, Rb/Ba and La/Yb were compared to those of Site 1232, and all compared plots showed similarities and general overlap (Figs. 3.14a-3.14e).

Small eruptive centers (SECs)

Puyuhuapi, the SVZ small eruptive center, is characterized by basalt (48-49% SiO_2), moderately high TiO_2 (1.5-1.55%) but still plots well outside of the Site 1232 TiO_2 vs. SiO_2 range, with moderate TiO_2 concentrations but significantly lower SiO_2 concentrations (Fig 3.12c.). Puyuhuapi has high concentrations of K_2O (3.15-3.29%) but falls completely outside the field of Site 1232 glasses with high K_2O but lower SiO_2 values (Fig. 3.13c). The analyzed glasses from the Site 1232 core are inconsistent with data from the SVZ small eruptive centers, these centers show lower ranges of TiO_2 (1-3.5%), and SiO_2 (49-70%). With such a large range of geochemical differences, it is unlikely that the SVZ small eruptive centers are a potential source of the Site 1232 glasses. The averages of incompatible elements of the SECs Laguna Blanca and

Puyuhuapi were compared with the incompatible averages to the Site 1232 glasses (Table 7). Puyuhuapi showed similarities only with the LREEs La, Ce, and Nd. Laguna Blanca did not show any comparable averages to the Site 1232 glasses, however HREE data was lacking. Trace element ratios for Zr/Hf, Hf/Rb, Th/Yb, Rb/Ba and La/Yb were compared to those of Site 1232, and while the plots for Th/Yb and Hf/Rb showed similarities, the remaining plots were dissimilar (Figs. 3.14a-3.14e)

Select explosive back arc volcanoes

The Tromen, Payun Matru, and Caviahue volcanoes of the Andean back arc have major element compositions of SiO_2 (49.98-75.33%), TiO_2 (.13-2.21%), and K_2O (1.31-5.6%). When compared to the glasses found at Site 1232, the aforementioned back arc volcanoes follow the same general trend, decreasing TiO_2 content with rising SiO_2 content as the Site 1232 glasses and plot within the lower range of the SiO_2 vs TiO_2 field (Fig. 3.12d) When compared to the Site 1232 K_2O field, Payun Matru plots significantly higher and outside the 1232 field (Fig 3.13d), while Tromen and Caviahue plot within the field and some overlap is present, it is along the high end of K_2O values. When compared to the averages of Site 1232 incompatible elements (Table 7), Tromen shows similar values to the LREEs Ce and Nd and the LILE Cs. Caviahue has comparable averages for the LREEs La and Nd, and the LILE Hf, and Payun Matru is similar in average concentration to the LREE Sm.

SSVZ

The southernmost portion of the SVZ, the SSVZ, is compositionally distinct from the more northern zones. Chemically it is characterized by volcanoes that are distinctly higher in TiO_2 (.61-2.69%) and K_2O (.97-3.55%) with SiO_2 (50.86-69.88%). SSVZ

volcanoes TiO_2 vs SiO_2 values plot similarly to those of the Site 1232 glasses. Cay plots with the same trend of decreasing TiO_2 as SiO_2 increases, however the TiO_2 content is lower and falls outside 1232 range (Fig. 3.12e). Maca plots within the low TiO_2 end of the 1232 glass field but shows the same trend of increasing TiO_2 until SiO_2 of 55% and then begins to decrease in SiO_2 with increasing SiO_2 >55%. Hudson plots almost completely within the field of Site 1232 TiO_2 values and shows the same trend of decreasing with increasing SiO_2. The SSVZ plots very similarly to Site 1232 for K_2O vs. SiO_2 (Fig. 3.13e). When compared with the averages of Site 1232 incompatible elements, Cay showed no similarities, Maca showed a similar average for the LREE La, Rio Ibanez average for HFSE Ta is similar to Site 1232. Hudson showed similar values for LILEs Rb and Sr, HFSEs Hf, Th and U, LREEs La, Pr, Nd, and Sm, HREEs Gd, Tb, Dy, Ho, Er and Tm, but did not show a correlation in trace element ratio plots (Fig. 3.14).

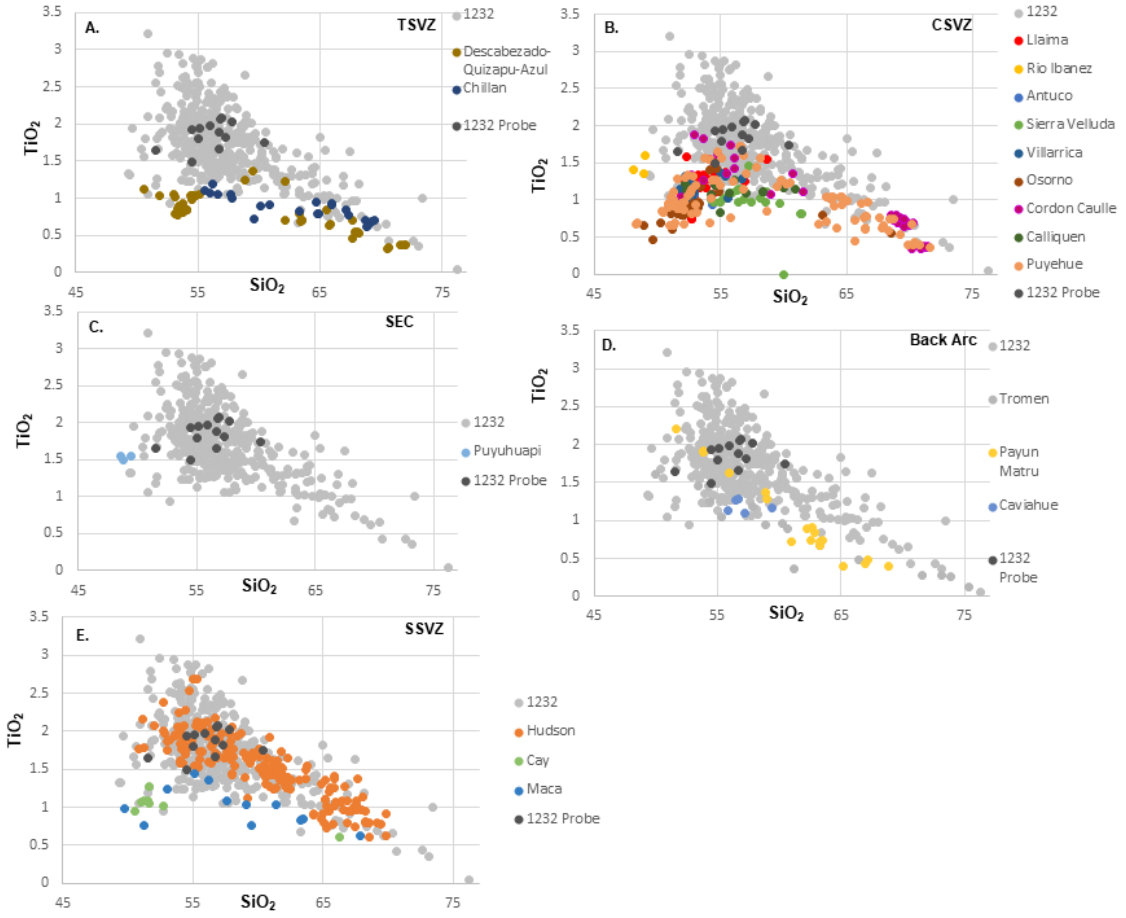

Figure 3.12: TiO_2 comparison of the Site 1232 glasses (data range shaded in grey, obtained by LA-ICP-MS) with: a. TSZV (Descabezado-Quizapu-Azul, and Nevado de Chillan), b. CSVZ (Antuco, Sierra Velluda, Calliquen, Llaima, Villarrica, Cordon Calle, Puyehue, and Osorno), c. SEC (Puyuhuapi), d. Back arc (Tromen, Payun Matru, and Caviahue), and e. SSVZ (Hudson, Maca, Cay and Rio Ibanez).

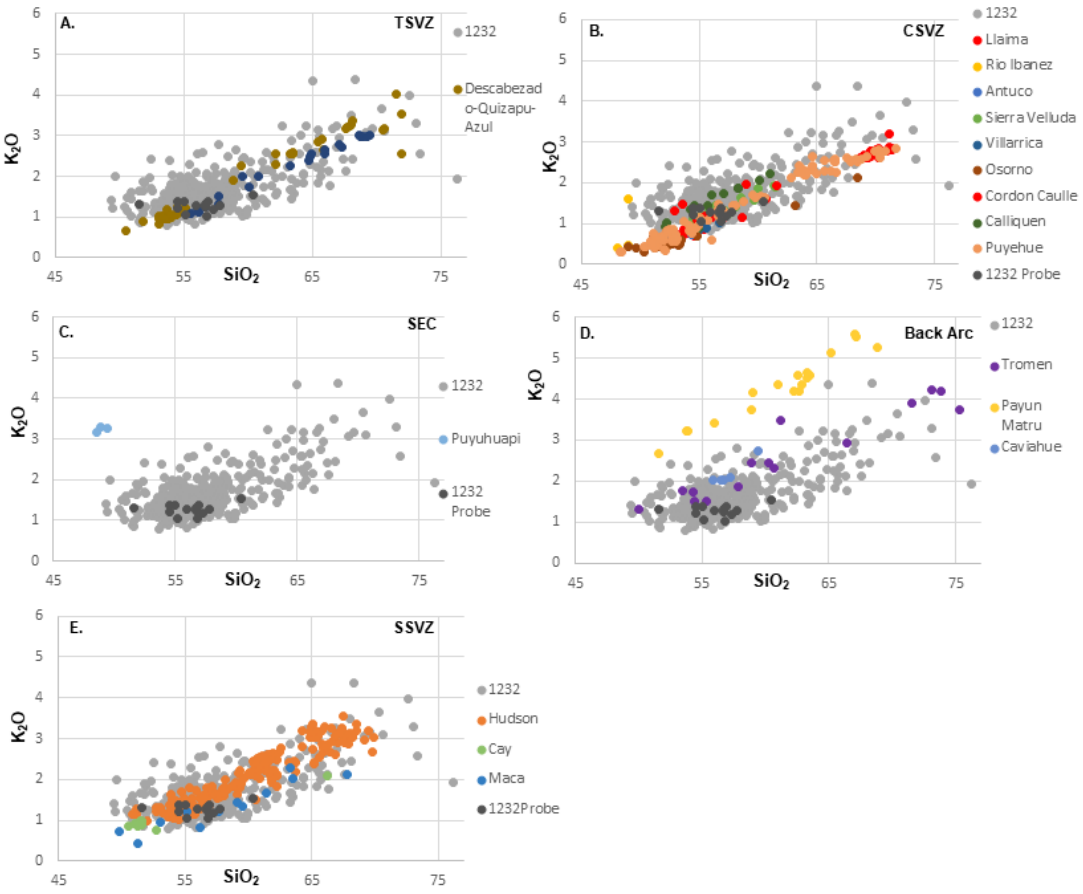

Figure 3.13: K_2O comparison of the Site 1232 glasses with: a. TSZV (Descabezado-Quizapu-Azul, and Nevado de Chillan), b. CSVZ (Antuco, Sierra Velluda, Calliquen, Llaima, Villarrica, Cordon Calle, Puyehue, and Osorno), c. SEC (Puyuhuapi), d. Back arc (Tromen, Payun Matru, and Caviahue), and e. SSVZ (Hudson, Maca, Cay and Rio Ibanez).

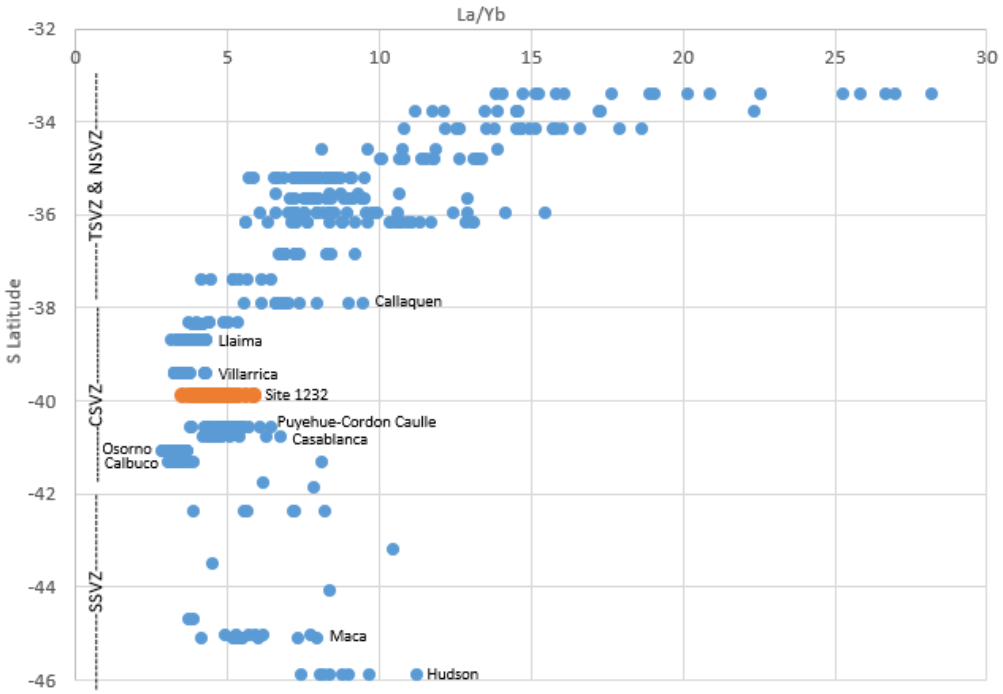
La/Yb
S Latitude
TSVZ & NSVZ
CSVZ
SSVZ
Callaquen
Llaima
Villarrica
Site 1232
Puyehue-Cordon Caulle
Casablanca
Osorno
Calbuco
Maca
Hudson

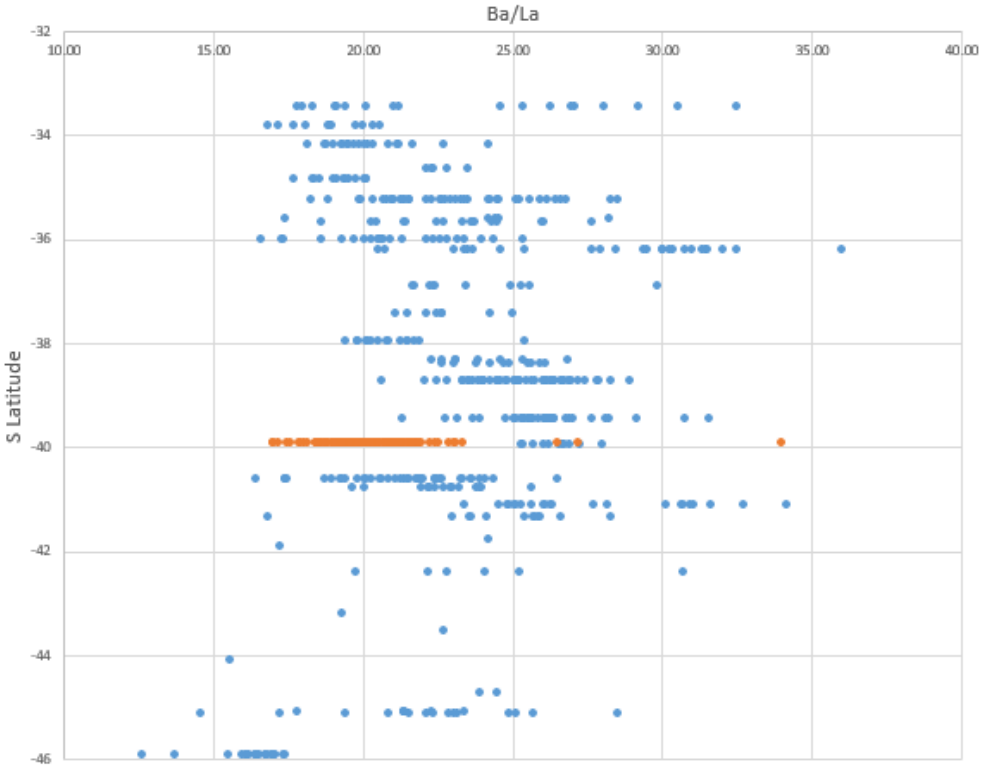
Ba/La
S Latitude

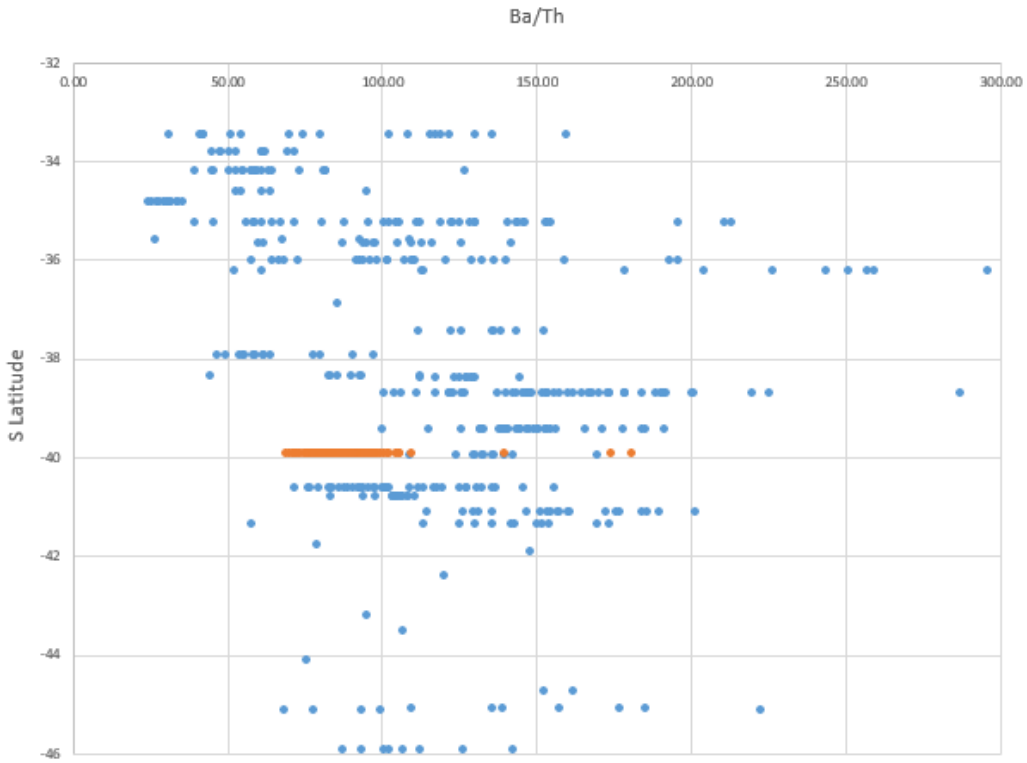

Figure 3.14: Comparison of the Site 1232 glasses with SVZ volcanic centers trace element ratios: a. La/Yb, b. Ba/La, c. Ba/Th.

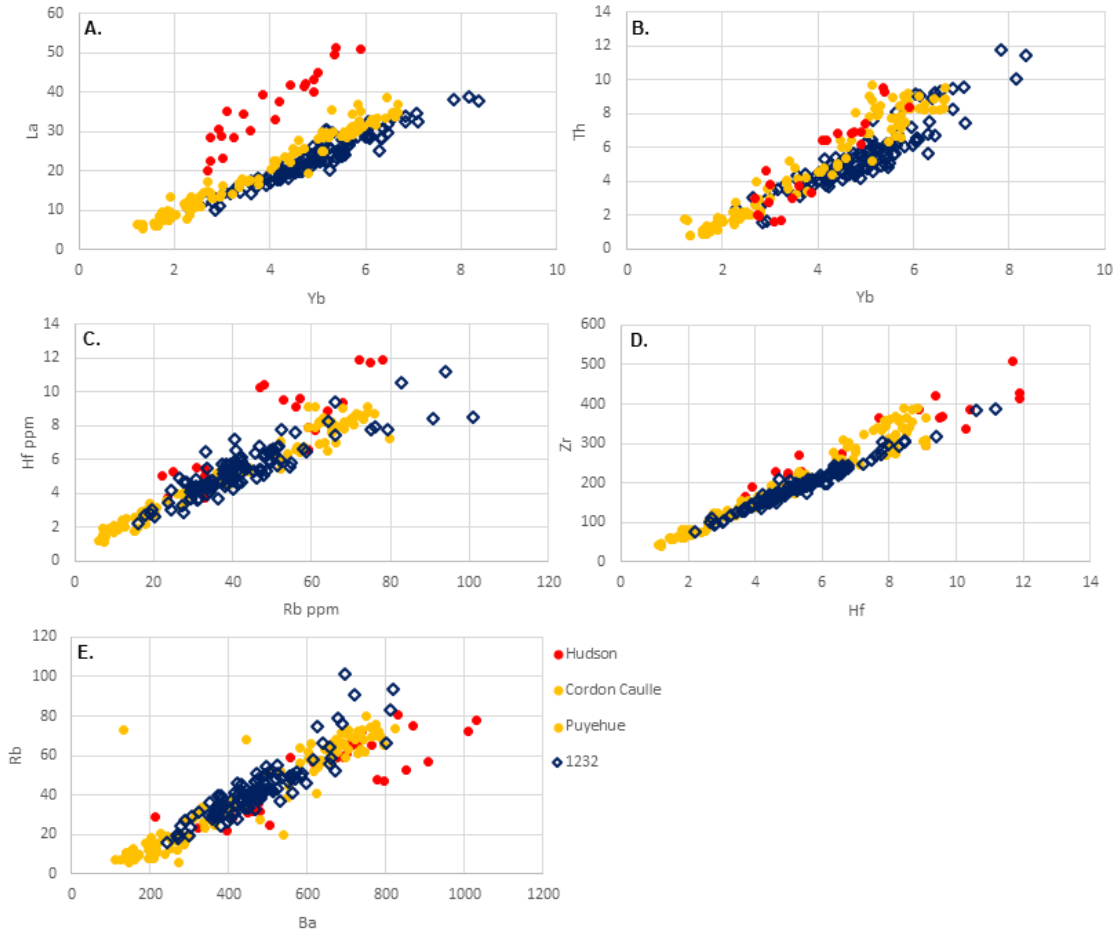

Figure 3.15: Comparison of the Site 1232 glasses with Puyehue-Cordon Caulle and Hudson Volcano: a. La/Yb, b. Th/Yb, c. Hf/Rb, d. Zr/Hf, and e. Rb/Ba.

3.5.3.2 Source (volcano/volcanic center)

Volcanic center

When comparing all investigated data to the Site 1232 glasses, they display a dominant basaltic andesite to andesitic component, with high concentration of TiO_2 and K_2O. With the much lower TiO_2 values, lower range of K_2O and lack of association of incompatible elements, it is unlikely that the TSVZ is the source of the Site 1232 glasses. Although they possess lower TiO_2, and generally lower K_2O content, the CSVZ (specifically the Puyehue-Cordon Caulle volcanic complex) does show some association

of incompatible element averages, and a strong comparison of trace element ratios La/Yb, Ba/La and Ba/Th. Considering these similarities, the adjacent CSVZ should be considered as a potential source for the Site 1232 glasses. With inconsistencies in SiO_2, TiO_2, K_2O and incompatible element averages, it is highly unlikely that the SEC Puyuhuapi could be considered as a source for the Site 1232 glasses. The Site 1232 glass shards are dissimilar to investigated back arc geochemical data, the back arc shows lower ranges of TiO_2 and overall higher ranges of K_2O, the backarc has averages of most incompatible trace elements which are inconsistent with those seen in the Site 1232 glasses, and it is therefore unlikely that the Site 1232 glasses originated from the back arc. With the similarities in SiO_2, TiO_2, and K_2O and incompatible element averages the SSVZ shows a comparison with the Site 1232 glasses. However, due to the lack of association of trace element ratios, which are unaffected by magma differentiation, and the distance from the source to Site 1232 SSVZ is not likely to be considered as a potential source. Geochemically the Site 1232 glasses compare most closely to CSVZ activity than the TSVZ, SECs, SSVZ or back arc.

Volcano

This study has analyzed the geochemical attributes and characterized glasses from the Site 1232 turbidite deposits. After geochemical analyses and comparison, I present these three options for potential source candidates, in order of most to least likely.

Option 1: Site 1232 glass shards show similarities in the incompatible element averages Nb, Zr, Sr, Ba, Eu and Tb, and a strong comparison of trace element ratios La/Yb, Ba/La and Ba/Th, which are not affected by differentiation. These coincide with published data from the CSVZ, more specifically the Puyehue-Cordon Caulle volcanic

complex (PCCVC). With the closeness in proximity (lying almost adjacent to the study site) at 40.5°S, 72.2°W and trace elemental similarities, based on the investigated parameters it is most likely that the 1232 glass shards are geochemically representative of the Puyehue/Cordon Caulle volcanic complex.

Option 2: the geochemical pattern of TiO_2, K_2O, and incompatible elements in the Site 1232 glass shards coincides with published data from SSVZ source region. Plots of SiO_2 vs. TiO_2 and SiO_2 vs. K_2O illustrate the similarity between the distribution of Hudson volcano reference data and the Site 1232 glasses. There are some similarities between Hudson volcano averages for incompatible elements and Site 1232 averages. Elemental comparisons do fall into the SSVZ Hudson volcano field as is observed for the major elements however, most trace element ratios fall outside of the published fields. Crystal fractionation of magma does not change the La/Yb, Ba/La and Ba/Th values as both elements in each ratio are incompatible in the major mineral phases. Due to the lack of similarity with trace element ratios and the vast distance (~800km) the fresh unaltered glass shards would have traveled, it is unlikely the 1232 glass shards are geochemically representative of the SSVZ Hudson volcano.

Option 3: a third possibility that cannot be discounted, is that the shards originated from an unknown that was active within the 275-12 kyr time frame of deposition for the Site 1232 glasses.

3.5.4 Implications

3.5.4.1 Implications for volcanic activity at SVZ center

CSVZ

The maximum TiO_2 content for Puyehue (Fig. 12) is not as high as Hudson or Site 1232 glasses. TiO_2 varies with differentiation and can change on a short timescale, typically increasing from basalt to andesite during differentiation, reaching a maximum and then decreases after titanomagnetite begins to crystallize. This could represent the crystallization of titanomagnetite earlier at active Puyehue than at active Hudson. Early crystallization of magnetite is a sign of high oxygen fugacity (f_{O2}) – the Fe is oxidized from Fe^{2+} to Fe^{3+} which stabilizes magnetite. Based on these observations it appears that the 1232 glasses are mainly from the middle to late Pleistocene precursors of Puyehue-Cordon Caulle and/or adjacent CSVZ volcanoes, but that crystallization conditions were different from the active volcanoes. The change in TiO_2 content of the PCCVC leads to questions such as, why were they different, can old rocks having this feature be found, and what caused the change in f_{O2}, to be explored in future research.

3.5.4.2 Implications for the mode and timing of sediment transport

If Site 1232 glasses originate from the PCCVC in the adjacent CSVZ, the change in sediment type from pumice to glass may be attributed to the older eruptions (>377 kyr and ~330 kyr) at Cordillera Nevada generating the pumice followed by a shift to the younger Cordon Caulle (300-70 kyr) or Puyehue (245-96 kyr) eruptions generating the volcanic glasses. With the positioning of glacial ice extending across the Lake District at south central latitudes, the volcanic material would have likely been deposited onto ice but would have required more than one transport process to reach the Nazca Plate.

3.6 Conclusions

1.) Volcanic glasses in the upper 140 m of the Site 1232 core likely originated from a single volcanic source.

2.) Geochemical characterization allowed for source region identification of the glasses found within the Site 1232 turbidite deposits. Geochemically the shards compare most closely with the Central SVZ.

3.) There is a good correlation between the geochemical composition (incompatible element ratios, LILE and HREEs) of the Site 1232 glasses to the adjacent Puyehue/Cordon Caulle volcanic complex (PCCVC) data.

4.) The 1232 shards are likely representative of either continuous activity at the Puyehue/Cordon Caulle volcanic complex, earlier activity than expected at another SVZ source, or the existence of a SVZ volcano that is previously unknown.

Acknowledgments:

We gratefully acknowledge Dr. Kathleen Marsaglia for contributing the original samples from Site 1232. We thank Thomas Beasley of the Florida Center for Analytical Electron Microscopy (FCAEM) at FIU for assisting with SEM analyses, Sarah Jantzi and Ping Jiang of the Trace Evidence Analysis Facility (TEAF) at FIU for assisting with LA-ICPMS analyses. Finally, we extend thanks to Dr. Eshita Samajpati for assisting with La-ICPMS data collection and Eduardo Fabelo for assisting with sample preparation.

Funding:

2019 GSA Graduate Student Research Grant Recipient, 2019 SEPM Student Research Grant Awardee

3.7 References

Albert, P.G., Tomlinson, E.L., Smith, V.C., di Roberto, A., Todman, A., Rosi, M., Marani, M., Muller, W., and Menzies, M.A., 2012, Marine-continental tephra correlations: Volcanic glass geochemistry from the Marsili Basin and the Aeolian Islands, Southern Tyrrhenian Sea, Italy: Journal of Volcanology and Geothermal Research, v. 229–230, doi:10.1016/j.jvolgeores.2012.03.009.

Angermann, D., J. Klotz, and C. Reigber, Space-geodetic estimation of the Nazca-South America angular velocity, Earth Planet. Sci. Lett., 171, 329– 334, 1999.

Beck, K., and Hickey-Vargas, R., 2022, Composition, age and origin of Pleistocene turbidite deposits at ODP site 1232, Nazca plate: Implications for volcanism and climate change in central south Chile: Journal of South American Earth Sciences, v. 118, https://doi.org/10.1016/j.jsames.2022.103908.

Blumberg, S., Lamy, F., Arz, H.W., Echtler, H.P., Wiedicke, M., Haug, G.H., and Oncken, O., 2008, Turbiditic trench deposits at the South-Chilean active margin: A Pleistocene–Holocene record of climate and tectonics: Earth and Planetary Science Letters, v. 268, p. 526–539, doi:10.1016/j.epsl.2008.02.007.

Daga, R., Ribeiro Guevara, S., Poire, D.G., and Arribére, M., 2014, Characterization of tephras dispersed by the recent eruptions of volcanoes Calbuco (1961), Chaitén (2008) and Cordón Caulle Complex (1960 and 2011), in Northern Patagonia: Journal of South American Earth Sciences, v. 49, doi:10.1016/j.jsames.2013.10.006.

Dymond, J., 1981, Geochemistry of Nazca plate surface sediments: An evaluation of hydrothermal, biogenic, detrital, and hydrogenous sources, *in* p. 133–174, doi:10.1130/MEM154-p133.

Ewart, A., 1982, The mineralogy and petrology of Tertiary-Recent orogenic volcanic rocks; With special reference to the andesitic-basaltic compositional range, in Andesites: Orogenic Andesites and Related Rocks, edited by R. S. Thorpe, pp. 25– 95, John Wiley, New York.

Griffin, W.L., Powell, W.J., Pearson, N.J., and O'Reilly, S.Y., 2008, GLITTER: Data reduction software for laser ablation ICP–MS: Laser Ablation–ICP–MS in the Earth Sciences CURRENT PRACTICES AND OUTSTANDING ISSUES, v. 40.

Gutiérrez, F., Gioncada, A., González Ferran, O., Lahsen, A., and Mazzuoli, R., 2005, The Hudson Volcano and surrounding monogenetic centres (Chilean Patagonia): An example of volcanism associated with ridge–trench collision environment: Journal of Volcanology and Geothermal Research, v. 145, p. 207–233, doi:10.1016/j.jvolgeores.2005.01.014.

Haberle, S.G., and Lumley, S.H., 1998, Age and origin of tephras recorded in postglacial lake sediments to the west of the southern Andes, 44°S to 47°S: Journal of Volcanology and Geothermal Research, v. 84, doi:10.1016/S0377-0273(98)00037-7.

Hartman, L.H. et al., 2019, Volcanic glass properties from 1459 C.E. volcanic event in South Pole ice core dismiss Kuwae caldera as a potential source: Scientific Reports, v. 9, p. 14437, doi:10.1038/s41598-019-50939-x.

Hickey, R.L., Gerlach, D.C., and Frey, F.A., 1984, Geochemical variations in volcanic rocks from central-south Chile (32-42oS): Andean magmatism: chemical and isotopic constraints.

Hickey, R.L., Frey, F.A., Gerlach, D.C., and Lopez-Escobar, L., 1986, Multiple sources for basaltic arc rocks from the southern volcanic zone of the Andes (34°–41°S): Trace element and isotopic evidence for contributions from subducted oceanic crust, mantle, and continental crust: Journal of Geophysical Research, v. 91, p. 5963, doi:10.1029/JB091iB06p05963.

Hickey-Vargas, R., Holbik, S., Tormey, D., Frey, F.A., and Moreno Roa, H., 2016, Basaltic rocks from the Andean Southern Volcanic Zone: Insights from the comparison of along-strike and small-scale geochemical variations and their sources: Lithos, v. 258–259, p. 115–132, doi:10.1016/j.lithos.2016.04.014.

Hickey-Vargas, R., Sun, M., López-Escobar, L., Moreno-Roa, H., Reagan, M.K., Morris, J.D., and Ryan, J.G., 2002, Multiple subduction components in the mantle wedge: Evidence from eruptive centers in the Central Southern volcanic zone, Chile: Geology, v. 30, p. 199, doi:10.1130/0091-7613(2002)030<0199:MSCITM>2.0.CO;2

Iverson, N.A., Kalteyer, D., Dunbar, N.W., Kurbatov, A., and Yates, M., 2017, Advancements and best practices for analysis and correlation of tephra and cryptotephra in ice: Quaternary Geochronology, v. 40, p. 45–55, doi:10.1016/j.quageo.2016.09.008.

Jacques, G., Hoernle, K., Gill, J., Hauff, F., Wehrmann, H., Garbe-Schönberg, D., van den Bogaard, P., Bindeman, I., and Lara, L.E., 2013, Across-arc geochemical variations in the Southern Volcanic Zone, Chile (34.5-38.0°S): Constraints on mantle wedge and slab input compositions: Geochimica et Cosmochimica Acta, v. 123, doi:10.1016/j.gca.2013.05.016.

Latorre, C., Moreno, P.I., Vargas, G., Maldonado, A., Villa-Martínez, R., Armesto, J.J., Villagrán, C., Pino, M., Núñez, L., and Grosjean, M., 2007, Late quaternary environments and palaeoclimate: Geological Society Special Publication, doi:10.1144/goch.12.

Le Bas, M. J., Le Maitre, R. W., Streckeisen, A., Zanettin, B., 1986, Subcommission on the Systematics of Igneous Rocks, A Chemical Classification of Volcanic Rocks Based

on the Total Alkali-Silica Diagram, Journal of Petrology, Volume 27, Issue 3, June 1986, Pages 745–750, https://doi.org/10.1093/petrology/27.3.745

López Escobar, Á., Cembrano, J., and Moreno, H., 1995, Geochemistry and tectonics of the Chilean Southern Andes basaltic Quaternary volcanism (37-46°S): Revista geológica de Chile: An international journal on andean geology, v. 22, doi:10.5027/andgeoV22n2-a06.

Lopez-Escobar, L., Kilian, R., Kempton, P.D., and Tagiri, M., 1993, Petrography and geochemistry of Quaternary rocks from the Southern Volcanic Zone of the Andes between 41°30′ and 46°00′S, Chile: Revista Geologica de Chile, v. 20, doi:10.5027/andgeoV20n1-a04.

Mix, A.C., Tiedemann, R., Blum, P., Lund, S.P., and Stoner, J.S., 2003, Proceedings of the Ocean Drilling Program, 202 Initial Reports: Ocean Drilling Program, Proceedings of the Ocean Drilling Program, doi:10.2973/odp.proc.ir.202.2003.

Orihashi, Y., Naranjo, J.A., Motoki, A., Sumino, H., Hirata, D., Anma, R., and Nagao, K., 2004, Quaternary volcanic activity of Hudson and Lautaro volcanoes, Chilean Patagonia: New constraints from K-Ar ages: Revista geológica de Chile, v. 31, doi:10.4067/S0716-02082004000200002.

Pearce, N.J.G., Westgate, J.A., Perkins, W.T., Eastwood, W.J., and Shane, P., 1999, The application of laser ablation ICP-MS to the analysis of volcanic glass shards from tephra deposits: bulk glass and single shard analysis: Global and Planetary Change, v. 21, p. 151–171, doi:10.1016/S0921-8181(99)00012-0.

Rollinson, H. R. (1993). *Using Geochemical Data: Evaluation, Presentation, and Interpretation*.

Scholl, D.W., Christensen, M.N., Huene, R. v., and Marloe, M.S., 1970, Peru-Chile Trench Sediments and Sea-Floor Spreading: Geological Society of America Bulletin, v. 81, p. 1339.

Schweller, W.J., Kulm, L.D., and Prince, R.A., 1981, Tectonics, structure, and sedimentary framework of the Peru-Chile Trench, *in* p. 323–350, doi:10.1130/MEM154-p323.

Stern, C.R., Moreno, H., López-Escobar, L., Clavero, J.E., Lara, L.E., Naranjo, J.A., Parada, M.A., and Skewes, M.A., 2007, Chilean volcanoes: Geological Society Special Publication, doi:10.1144/goch.5.

Sun, S., and McDonough, W.F., 1989, Chemical and isotopic systematics of oceanic basalts: implications for mantle composition and processes: Geological Society, London, Special Publications, v. 42, p. 313–345, doi:10.1144/GSL.SP.1989.042.01.19.

Suzuki, T., Kasahara, A., Nishizawa, F., and Saito, H., 2014, Chemical characterization of volcanic glass shards by energy dispersive X-ray spectrometry with EDAX Genesis APEX2 and JEOL JSM-6390: Geographical Reports of Tokyo Metropolitan University, v. 49, p. 1–12.

Thornburg, T.M., and Kulm, L.D., 1987, Sedimentation in the Chile Trench: petrofacies and provenance: Journal of Sedimentary Petrology, v. 57, doi:10.1306/212F8AA3-2B24-11D7-8648000102C1865D.

Todd M. Thornburg, L. D. Kulm, 1983, Depositional Environments and Sedimentary Processes in Chile Trench: ABSTRACT: AAPG Bulletin, v. 67, doi:10.1306/03b5b560-16d1-11d7-8645000102c1865d.

Tormey, D.R., Hickey-Vargas, R., Frey, F.A., and López-Escobar, L., 1991, Recent lavas from the Andean volcanic front (33 to 42°S); Interpretations of along-arc compositional variations, *in* p. 57–78, doi:10.1130/SPE265-p57.

Weller, D. J., Miranda, C. G., Moreno, P. I., Villa-Martínez, R., & Stern, C. R. (2015). Tephrochronology of the southernmost Andean Southern Volcanic Zone, Chile. *Bulletin of Volcanology*, *77*(12), 107. https://doi.org/10.1007/s00445-015-0991-2

Weller, D. J., de Porras, M. E., Maldonado, A., Méndez, C., & Stern, C. R. (2019). Petrology, geochemistry, and correlation of tephra deposits from a large early-Holocene eruption of Mentolat volcano, southern Chile. *Journal of South American Earth Sciences*, *90*. https://doi.org/10.1016/j.jsames.2018.12.020

Venzke, E. (ed.), 2021, Global Volcanism Program, 2013: Volcanoes of the World v. 4.9.4.

4. DISPERSAL PATTERNS AND SEDIMENT TRANSPORT PROCESSES OF VOLCANIC GLASSES OF ODP SITE 1232: A SOURCE TO SINK COMPARATIVE STUDY

Abstract

The goal of this work is to provide a complete review of the granulometric and mineralogical features of turbidite sediments from the Nazca Plate Site 1232, as well as to identify the source rocks and terrestrial sediment transport routes. The volume (30-63%) and lack of abrasion of the Pleistocene volcanic glasses found in the analyzed samples on the downgoing plate is abnormal and cannot be easily explained. Physical properties of particles, scanning electron microscope imaging and estimates of density were examined. With the lack of turbidite deposition in the Holocene despite constant sediment delivery to the continental shelf by adjacent rivers, is unlikely that the Site 1232 turbidites containing glass shards were deposited solely by river transport. With glacial shifts in wind patterns and ice distribution being the major change present during the time of deposition, they likely played a strong role in the dispersal and deposition of the glass shards. Of the scenarios presented within this chapter, the following scenarios are the most consistent with physical properties of Site 1232 glasses: 1) Primary ash fall of glasses onto the continental shelf, or 2) Farther extent of glacial ice than recorded during the last glacial stage transported volcanic glasses out to the coast where they were deposited during events of glacial recession. With either transport method to the continental shelf, the volcanic glasses were later remobilized within a turbidity flow, and the relative low density of the primarily basaltic andesite to andesitic shards allowed them to remain entrained in the near top dilute cloud layer (Paull et al., 2018). Transport

within this upper turbidite layer allowed for the abnormal concentration of glasses and helps to explain the lack of abrasion and disintegration during the transport from continental shelf onto the Nazca Plate.

4.1 Introduction

Data on sediment provenance are essential for evaluating paleogeographic reconstructions, mapping depositional systems, and determining the impact of climate change on sediment distribution. The south-central coastline of Chile is a mix of sediment transport processes. Currently, transport of continent-derived sediment to the Chilean continental margin is primarily by river drainage from South America, sediment funneling through submarine channels and erosion of the continental edge. Eroded sediments are transported downstream via river and generally deposited on the continental shelf or funneled into submarine channels leading to deposition. In Southern Chile during glacial maximums, the glacial ice extended out to the coastlines, resulting in sediment transportation directly onto the continental shelf in some areas. Deposition of volcanic ash and ejecta from frequent eruptions is common. There is evidence for sediment transport via underwater currents as well as lateral movement of sediments in a northward direction within the Peru-Chile trench. The dominant process acting on the sediments once they accumulate on the shelf is gravity flow, particularly that of turbidity currents, once the sediments either built up to the point of overload and failure or failure occurs due to seismic events. With the commencement of global warming following the last glacial (~12.5 kyr), Site 1232 reveals a marked drop in turbidite sedimentation. As a result, this argues that the turbiditic record is linked to the climate record, as Rauch (2005) and Völker (2006) have previously suggested.

The provenance of Pleistocene deep-sea turbidite glasses from Site 1232 (Fig 4.1) on the Nazca Plate have been investigated to better understand sediment sources and glacial influences on sedimentary routing, as well as the processes that determine sediment sources and delivery. This research looks at how several factors affect sediment routing and accumulation in a complex deep-sea environment over time. SEM, laser ablation inductively coupled plasma mass spectrometry (LA-ICP-MS), and manual point counts were used to conduct quantitative detrital analyses on 29 turbidite coarse sand intervals. This study determined that the volcanic glass shards in the Site 1232 turbidite deposits are coming from a single terrestrial volcanic source, most likely the CSVZ of the Andean magmatic arc.

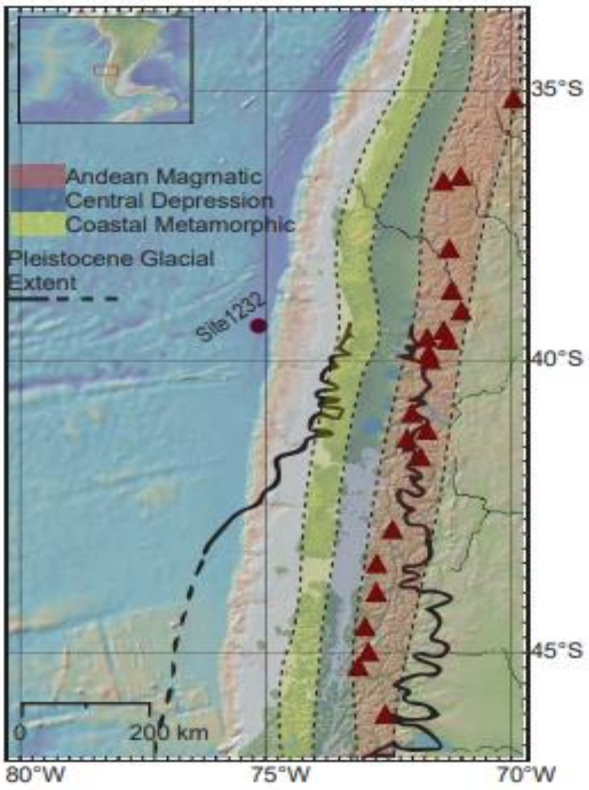

Figure 4.1 Global multi-resolution topography (GMRT) map of southwest South America (South-central Chile) and adjacent Nazca plate ocean floor showing the location of ODP Site 1232. Figure made with GeoMapApp (www.geomapapp.org). Geographic location of the 3 compositional belts of interest for sediment genesis are highlighted in yellow, blue and red. Extent of the Patagonian Ice Sheet during the Pleistocene Glacial Maximum is represented by a thick solid and dashed line, after (Porter, 1981; McCulloch et al., 2000; Hulton et al., 2002b). Triangles represent volcanoes active during the Pleistocene in the southern volcanic zone (Stern et al., 2007; Venzke, 2021)

4.2 Study Area

4.2.1 Geologic history of the area

The oceanic Nazca Plate subducting beneath the continental South American Plate has generated one of the most geologically active continental margins in the world. The Pacific, South American, Antarctic, Cocos, and Caribbean plates surround the oceanic Nazca Plate in the South Pacific Ocean. The Nazca Plate has a slightly northeastward direction in relation to the Pacific Plate, subduction is driven by the East Pacific Rise (EPR) coupled with the subduction of the Nazca plate beneath the South

American Plate (Angermann et al., 1999). With a convergence rate of ~8 cm/yr between 10°S and 40°S since ~26 Ma with the South American Plate terminating in the Peru-Chile Trench (Angermann et al., 1999). The Peru-Chile Trench stretches 5,900 km along the South American coast, with depths ranging from 5.5 to 8 km, angles of subduction ranging from 10 to 35 °, and sedimentary infill varying (Scholl et al, 1968 and 1970, Schweller et al, Völker et al., 2008 and 2013, and Blumberg et al., 2008).

Distal volcanic ash from big explosive eruptions is significant for reconstructing eruptive parameters such as erupted volume and eruption column height and crucial for comprehending the possible environmental implications of explosive eruptions beyond the local scale. Some of the most explosive recent eruptions have occurred in the SVZ (such as the Holocene eruptions of Llaima, Hudson, Villarrica and Cordon Caulle) and even larger eruptions are known to have occurred in the SVZ during the Pleistocene (Hildreth and Drake 1992, Stern 2004, Fontjin et al., 2014). However, there are no volume estimates for several prehistoric deposits and it is quite possible that the number of large explosive eruptions is significantly underestimated (Fontjin et al., 2014). The result volcanic ash fallout during and after significant volcanic eruptions deposited on terrestrial, lacustrine and continental shelf, allows potential for correlation and dating of recorded events (Fontjin et al., 2014).

4.2.2 Site 1232

The Nazca plate's Site 1232 was chosen as a high sedimentation rate site to investigate the long-term Neogene reaction to major climatic and tectonic events. The goal of Leg 202 was to examine the connections between climate and oceanographic changes, as well as biogeochemical cycles, in the southeast Pacific (Mix et al., 2003).

Instead of hemipelagic sediments, which were expected in this area, a >300 m series of Pleistocene turbidites was discovered (Mix et al., 2003). Gray to green silty clay interbedded with black to gray regularly graded sandy-silt to silty-sand layers was the most common sediment type recovered. Using stratigraphic correlation and magnetic susceptibility, the crew was able to link the upper 42.58 m of the 1232A and 1232B cores in a composite section (Mix et al., 2003). This research utilizes cores retrieved during ODP Expedition Leg 202. Site 1232 was determined to be of Pleistocene age, <0.78 Ma using paleomagnetic polarity measurements and 0.46-1.69 Ma using biostratigraphic analysis (Mix et al., 2003).

From Site 1232, the expedition recovered three cores: 1232A, 1232B, and 1232C. Recovery at hole 1232A, the deepest hole, was drilled on the seafloor at a starting depth of 4089 mbrf (meters below rig floor). A piston corer (APC) was initially deployed, drilling to a maximum depth of 112.5 mbsf (meters below seafloor), before being replaced with an extended core barrel (XCB), which continued the hole from 112.5 to 371.3 mbsf (Mix et al., 2003). Drilling for Hole B commenced at a depth of 4075 mbsf on the seafloor, and the hole was completed at a depth of 90.1 mbsf using a piston corer (Mix et al., 2003). Hole C was a shallow recovery hole drilled with a piston corer to a depth of 33.2 mbsf from a depth of 4079.8 mbrf (Mix et al., 2003).

4.2.3 Potential sediment transport pathways for glass shards

4.2.3.1 Air transport

There are potentially over 60 volcanoes that have been active in the Quaternary Andean SVZ (Stern, 2004). These volcanoes have been expelling volcanic ejecta for at least 1.1 million years. Volcaniclastic particles, such as volcanic glass fragments, can

travel in air for >1000 km depending on the size of the eruption. The eruption column of a volcanic eruption can reach heights of over 40 km, reaching into the stratosphere. Currently in in central and southern Chile, prevailing westerly winds do not favor deposition of volcanic sediments by aeolian transport, however primary ash fall of volcanic particles to the continental shelf could be considered as a potential method of transport (Marchant et al., 2007, Fontjin et al., 2014, Soto, 2018).

Global wind patterns in the Southern Hemisphere, such as the Southern Westerlies and Polar Easterlies, saw a northward shift during the Last Glacial Maximum (LGM) ~20 -12.5 kyr (McCulloch et al., 2000; Hulton et al., 2002; Marchant et al., 2007). Seasonality (up to 10° shift) and El Nino Southern Oscillation circumstances are still known to cause northward migration of Southern Westerlies (Marchant et al., 2007, Munoz et al., 2007). Based on this finding, it is quite possible that wind patterns would have shifted northward throughout the Pleistocene's glacial/interglacial cycles, resulting in a change in the wind transport of volcanic ash. Glacial advances appear to be linked to easterly winds during glacial times, when polar easterlies travel northward, bringing material from the volcanic belt (McCulloch et al., 2000; Hulton et al., 2002; Marchant et al., 2007). Glacial retreats are associated with winds from the west (less volcanic material), as is the case today (McCulloch et al., 2000; Hulton et al., 2002; Marchant et al., 2007).

4.2.3.2 Fluvial transport

Chiles CSVZ and SSVZ have over 9 major rivers (Fig. 4.2) that cut through the terrain and deliver sediments onto the continental shelf where precipitation is easily generated to runoff in the humid central and southern climates (Munoz et al., 2007). Due to the huge

volume of river systems generating a wide variety of terrestrial material in central and southern Chile, fluvial runoff can reach up to 21km^3/a. Seasonal to year-round precipitation in central and southern Chile permits perennial rivers to transfer massive sediment loads from the three parallel sediment zones to the continental slope consistently throughout the year (Lamy et al., 1999, Marchant et al., 2007, and Munoz et al., 2007). Riverine input would provide large quantities of plutonic and metamorphic varieties as well as the volcanic detritus that is seen in the Site 1232 turbidite deposits.

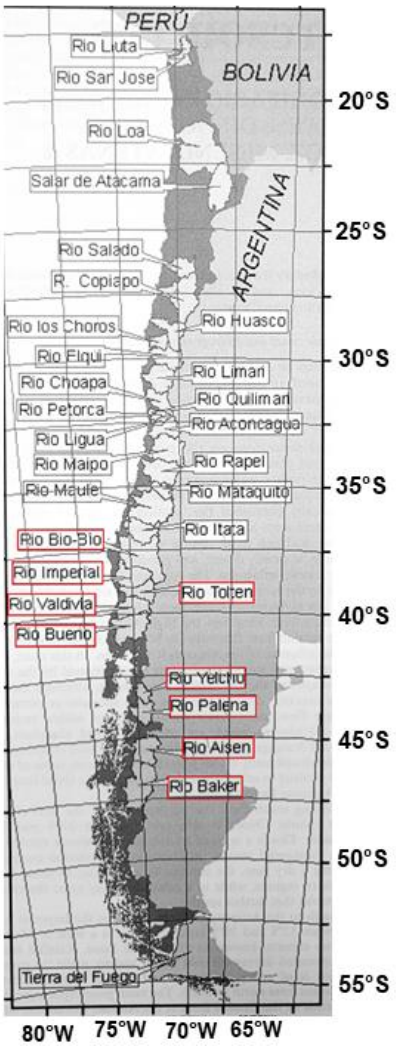

Figure 4.2 Map of river input onto the Chilean continental margin adapted from Munoz et al., 2007, Major rivers that fall in the CSVZ and SSVZ are marked with a red box.

4.2.3.3 Glacial transport

Glaciers are responsible for a huge amount of mixed sedimentary debris produced by severe erosion of the continental terrane. During the Quaternary, widespread glaciation was responsible for various geographic characteristics, such as erosion of the central depression in southern Chile and the deposition of glacial terraces throughout central and southern Chile (Jenks, 1956, and Marchant et al., 2007). Volcanic ejecta can also be deposited onto glaciers and that material deposited as ice melts and recedes. There were at least ten different glaciations that affected the Patagonian ice sheet of South America throughout the Pleistocene, according to certain estimates (Glasser and Jansson, 2008). During the Pleistocene in the Last Glacial Maximum (LGM), the Patagonian ice sheet nearly completely covered central and southern Chile (Glasser and Jansson, 2008). The ice sheet spread into the coastal cordillera beginning at 39°S, and south of 41°S, it reached past the Chilean shoreline, up to 40km in some areas (Fig. 4.1) (Melnick and Echtler, 2006, and Glasser and Jansson, 2008).

Ice rafting is a mode of transport that carries sand-size and larger material by floating ice, discharging it into an aquatic environment during warm periods; the ice works as a raft, providing buoyancy to any debris contained within or on its surface. Ice rafts and sea ice floating in marine areas commonly deposit debris but lake and river ice can also transport debris and release it into lakes or marine environments (Prueher and Rea, 2001).

4.2.3.4 Current transport

Ocean Currents

The northward-flowing Peru-Chile (or Humboldt) current dominates the surface ocean circulation in the eastern Pacific off the coast of Chile (Marchant et al., 2007). The poleward running Peru-Chile countercurrent, which is located 100-300km offshore and brings subtropical surface water to the south, can periodically split the Peru Chile current into an oceanic branch and a coastal branch near the Chilean coast, both of which flow northward (Fig. 4.3). The poleward flowing Gunther undercurrent is mostly present at water depths between 100m and 400m across the shelf and continental slope (Marchant et al., 2007). The Antarctic intermediate water, a deeper current which flows towards the equator at depths of 400m-1200m will intermittently rise to the surface during periods of intense upwelling (Marchant et al., 2007).

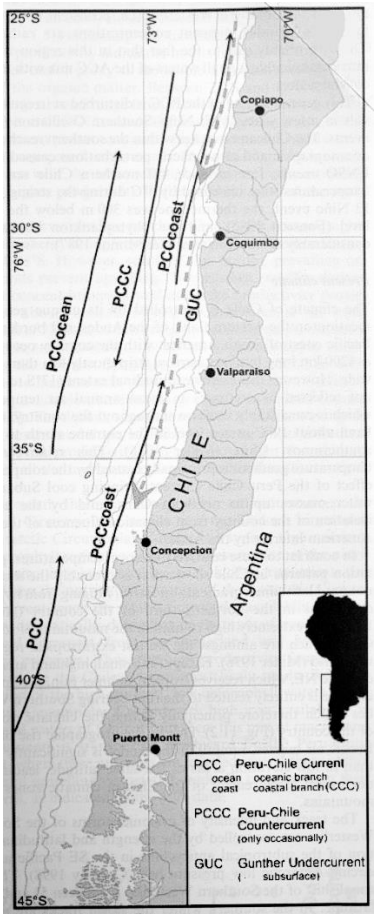

Figure 4.3a Schematic of ocean currents affecting the Chilean continental margin from Marchant et al., 2007

Turbidity Current

Turbidity currents that bridge the trench and axial channel and flow westward into the Nazca Plate, are caused by mass wasting episodes on the exposed continental slope. On the continental shelf, failure of the loosely packed sediment is the primary cause of turbidity currents. Turbidity currents are extremely common along the Chilean continental margin and are well documented as moving large quantities of sediments (Thornburg and Kulm, 1987; Mix et al., 2013, Völker et al., 2006, Marchant et al., 2007, Blumberg et al., 2008, Völker et al., 2008, Völker et al., 2013).

A relatively recent study conducted on the mechanics and density distribution of

turbidite flows conducted by Paull et al (2018) shows that turbidity flows show a layering structure during motion and lighter material is more likely to remain towards to top layer of the flow. The flow's frontal portion liquefies and mechanically erodes the sandy canyon floor, allowing the formation of a dense near-bed layer (Paull et al., 2018). The liquefaction forms a thick, fast-moving layer that accelerates downslope, resulting in a self-sustaining, rapid, and dense base layer that drives the flow (Fig.4.3b). Shear between the dense remobilized layer and the overlying water produces mixing, resulting in a dilute, turbulent sediment suspension overlaying the dense remobilized layer (Paull et al., 2018). The dilute turbulent sediment flow created by the initial near-bed layer can travel a great distance as the near-bed layer halts flow (Paull et al., 2018).

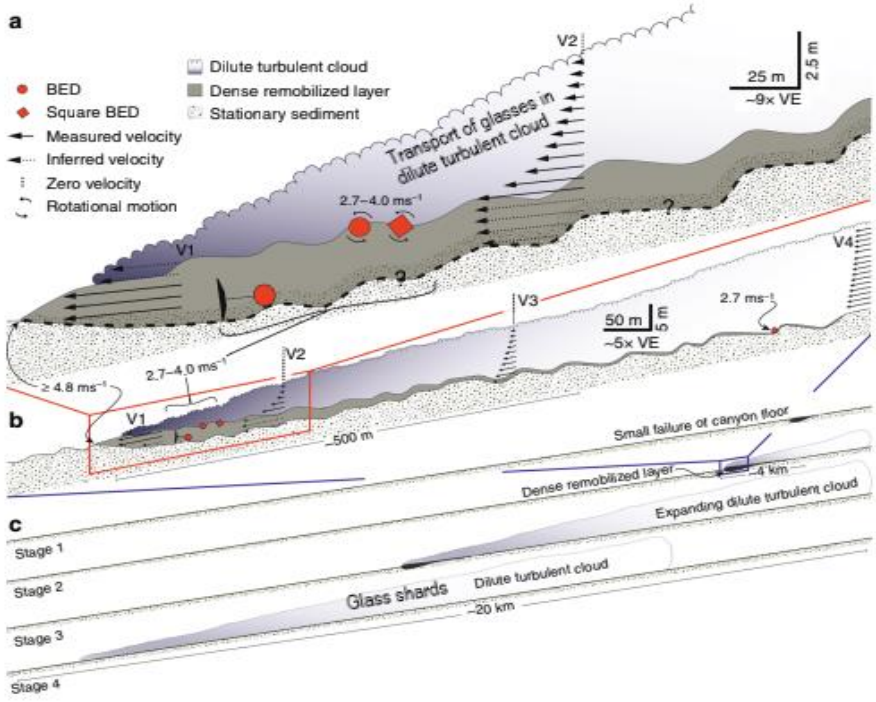

Figure 4.3b. Schematic of turbidity currents events, showing the change in velocities of the layers of flow and the stages of evolution of flow, adapted from Paull et al., 2018.

Trench axial channel

Beginning at Chile Ridge 45°S and extending to 33°S in the Juan Fernandez Ridge a 7–10 km wide, 150 m deep, somewhat winding axial channel is seen in the trench. (Thornburg and Kulm, 1987; Völker et al., 2006, Marchant et al., 2007, and Völker et al., 2008). The channel connects directly to the exits of the some of the largest submerged canyon systems, while other canyons are linked to this axial channel by a connecting feeder channel or by branching channels (Thornburg and Kulm, 1987; Völker et al., 2006, Marchant et al., 2007, and Völker et al., 2008). Between the Chile Ridge and the Juan Fernandez Ridge, the trench has a slight northward slope (~.12°), and the average trench depth increases from 3200 m at 46°S to 5950 m at 32°S, forcing sediment movement northward through the axial channel (Marchant et al., 2007, Völker et al., 2008, Völker et al., 2013 and sources therein). The normal course of turbidity currents to the west is redirected to the north upon entering the trench, and sediment-charged bottom currents will follow the natural northward slope (Thornberg et al., 1990, Völker et al., 2006, Herberer et al., 2010). Asymmetrical trench fan profiles also support this northward sediment movement trend (Thornberg et al., 1990, Völker et al., 2006, Herberer et al., 2010).

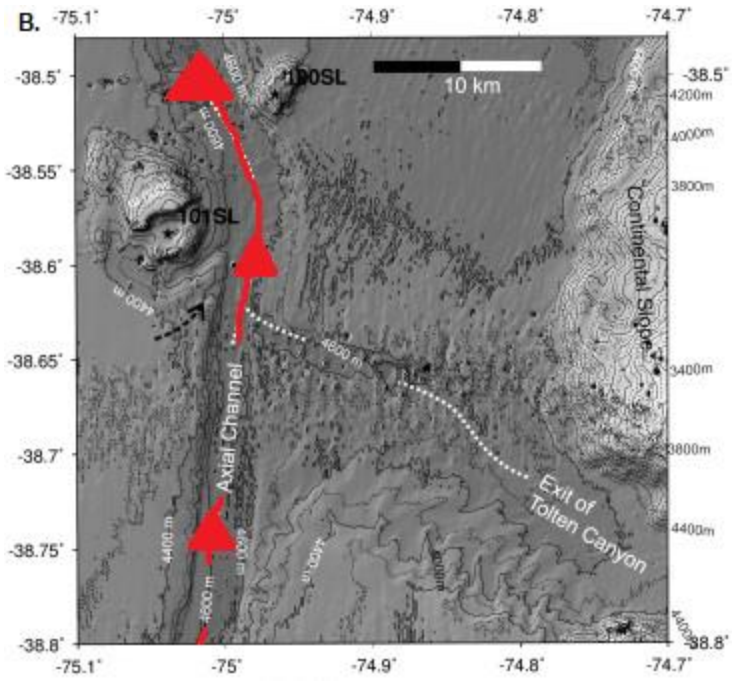

Figure 4.3c Schematic of a northern portion of the trench axial channel that flows northward from the Chile Ridge red arrows showing path of motion through the channel, adapted from Völker et al., 2008.

4.3 Methods

4.3.1 Sample description and selection

This study used a total of twenty-nine samples from ODP mission 202 Site 1232, all obtained from the Gulf Coast Repository. The sedimentary facies found in Site 1232 cores are divided into two categories (Mix et al., 2003). The major facies are classified as clay and silty clay with minimal sedimentary features. Light greenish-gray to faint gray to medium gray in hue, with light mottling and rare brown nodules (Mix et al., 2003). There are a few thin silt layers here and there, but the sand content is negligible (Mix et al., 2003). Interbedded with the predominant clay are turbidite strata. The turbidites are made up of coarser material, ranging from silty sand to sandy silt in most cases. The coarser sands overlie a sharp basal contact and grade upward to silty clay. There are a total of 1328 coarse layers found at the site, with 772 layers found in the 289 m of core retrieved

in 1232A. (Mix et al., 2003). The coarsest sediment layers range in thickness from 0.5 to 52 cm, with an average of 3.2 cm. Two key criteria were used to select the 29 coarse samples used for this study: 1) maximum grain size coarseness and 2) maximum coarse layer thickness. The sediments in the sample have a maximum coarseness of silty-sand-sized particles (4-250 microns), and all of the coarse layers examined are at least 4 cm thick. The core pictures reveal a fining upward structure with a sharp basal contact, which represents turbidites. Due to laser ablation requiring grains of at least 150 microns for repetition of analysis, coarseness was a significant consideration for sampling. Thicker layers of coarse sediment were favored over thin ones because they were more likely to include important events. To assess any sedimentological changes throughout time, turbidite sediments were chosen throughout the depth of the cores.

4.3.2 Analytical methods

Samples of turbidite material were wet sieved using deionized water through 75 mesh and 100 mesh sieves to separate grains into two size fractions, >149 microns and > 210 microns. Samples were agitated in an ultrasonicator to clean and loosen any silt, washed through each mesh sieve one final time and dried in an oven at 100°C oven overnight. A UV smear slide was made of each fraction by collecting sediments onto the tip of a single-use plastic spatula. Sediment was applied to a cleaned 12x12 grid slide in a drop of deionized water and dried on a hotplate. UV smear slides were utilized to complete point counts for most core samples. Grains with the appearance of glass were picked and observed under a petrographic microscope to check for optical isotropic. Characteristics of chosen glass shards, including size, color, vesicularity, angularity, and freshness, were documented.

Glass shards from both size fractions were picked and mounted on carbon tape disks for analysis. Samples were analyzed using the Scanning Electron Microscope (SEM) at the Florida Center for Analytical Microscopy (F.C.A.E.M) at Florida International University. Grains were analyzed using a 39µm spot size under high vacuum with a 15kv accelerating voltage. Secondary electron (SE) imaging was used to obtain high-resolution images of glass shards and grains for examination of texture and backscatter electron imaging (BSE) to determine homogeneity and look for microcrystals. Major element glass analyses were performed on Site 1232 glass shards and reference materials Rhyolite (Smithsonian standard NMNH 72854, VG 568), and Hawaiian basaltic glass (BHVO-2). At the Trace Evidence Analysis Facility (TEAF), FIU, 119 grains from the 210 micron size fraction were analyzed for trace elements using the LA-ICP-MS (ELAN DRC ICP/MS and New Wave UP 213 nm laser ablation system) after SEM with EDS analysis. A total of 95 grains from the > 210 micron fraction of both 1232A and 1232B were tested for trace elements at TEAF, FIU, using an Aligent Technologies 7700 Series LA-ICP-MS. For comparison with SEM results, glasses were tested for the trace elements Rb, Sr, Y, Zr, Nb, Ba, La, Ce, Nd, Sm, Eu, Gd, Dy, Er, Yb, Hf, Pb, Th, and U, as well as the significant element Ti.

4.4 Results

4.4.1 Prior Results

In total at Site 1232A, 371.3 m was drilled with a total recovery of 288.8 m of sediment was recovered from the hole (Mix et al., 2003). Unit 1 contains the fine grained pelagic sediments in the upper 0.6 mcd of the core and in the upper portions of the turbidite layers, color of Unit 1 ranges from light greenish gray to light gray to medium

gray, and most color transitions are gradual (Mix et al., 2003). A second more dominant lithology (Unit 2 is interbedded with the dominant silty clay and clay throughout Unit I. It consists of coarser sediment, typically silty sand or sandy silt, overlying a sharp basal contact and grading upward over several centimeters to silty clay predominantly gray to dark gray to black in color. A total of 772 coarse layers are present in the 289 m of core recovered in Hole 1232A. From 235-293 mcd (217.3-275.0 mbsf) no coarse-grained layers thicker than 4 cm are present (Mix et al., 2003).

The dominant particle type (Fig. 4.4) found in the coarsest layers of the Unit 2 turbidite layers according to smear slide examinations of the turbidite fractions of Site 1232 is volcanic glass. Mineral phases are present throughout the coarsest sediment and include quartz, feldspar (clear minerals), pyroxene, magnetite, muscovite, chlorite, biotite, and in minor concentrations hornblende, augite, pyrite, and garnet. The sedimentology of the 1232B core and the top two-thirds of the 1232A core is generally constant throughout. The dominant particle size varies from clayey silt to silty clay, with sandy silt to silty sand-sized particles constituting the coarsest turbidite intervals (4-250 microns).

In the 1232A core there is a distinct shift in sediment proportions starting 160 mbsf, grains become more subangular to rounded appearance. The coarsest fraction (>210 microns) is composed entirely of large crystals of anhydrite encased in the white felsic polymineralic material. Samples below 214 mbsf are composed entirely of comprised primarily of felsic polymineralic particles and sedimentary lithic fragments. Felsic polymineralic particles are white to reddish-orange in appearance with distinct feldspar laths, quartz grains, and magnetite grains embedded, some containing anhydrite

grains, in a fine-grained clay matrix. Particles are magnetic, sub-rounded, to rounded in appearance. These grains have the overall appearance and composition of altered pumice.

Based on geochemical analysis completed in the previous chapter, there are strong similarities in incompatible trace element ratios, incompatible element averages, and some overlap in the TiO_2, K_2O and SiO_2 content, of the Site 1232 glasses and the CSVZ. Geochemically the Site 1232 glasses compare more closely to CSVZ activity than the TSVZ, SSVZ, SECs or back arc.

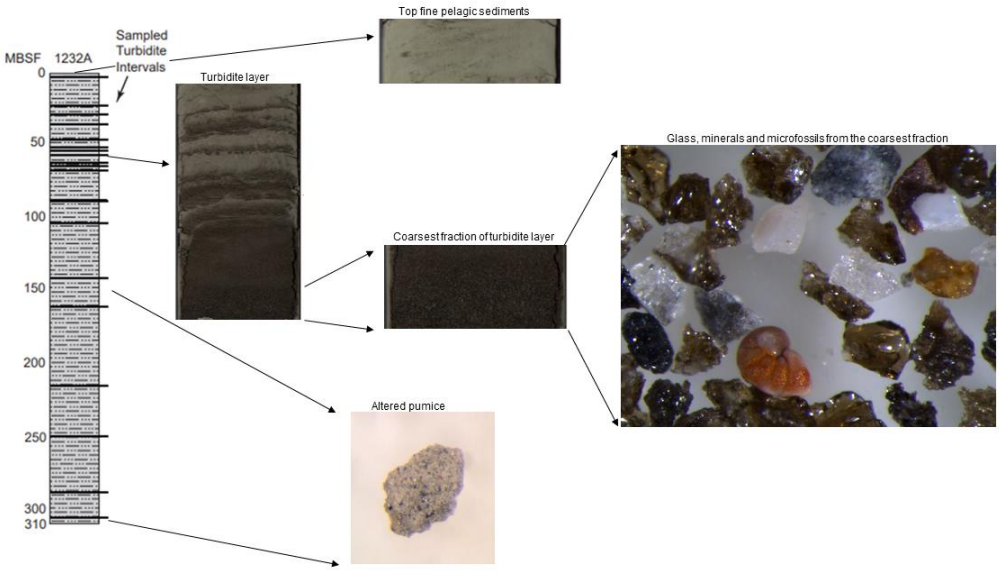

Figure 4.4: Schematic of Core 1232A depicting the stratigraphic units, and a photographic breakdown of a typical turbidite layer and the pumice that becomes more dominant below 140 m (Mix et al., 2013, Beck and Hickey-Vargas, in press, available online)

4.4.2 Morphology, geochemistry, and density of glass

Glass grains are relatively unaltered, fresh, and angular. Glass shards from both size fractions (149µ and 210µ) were mounted on carbon disk tape and viewed under high resolution imaging using a scanning electron microscope. Grains surfaces were viewed under high magnification to look for evidence of rounding of abrading (see photos in

appendix). Edges of glass fragments are irregular and sharp, with little to no evidence of rounding. One glass shard was randomly selected from 39 fractions (22 total intervals, with 15 from the 1232A core and 7 from the 1232B core) and compared to a visual silhouette chart (Krumbein, 1941 and Powers, 1953). This visual comparison of angularity was used to determine the degree of roundness/angularity (Krumbein, 1941 and Powers, 1953). The average angularity of Site 1232 glass shards was 0.167, based on the Powers (1953) scale of angularity. The majority of the shards (X%) are determined to be in the "very angular" category which ranges from 0.012 to 0.017, Y% are angular and Z% are sub-angular (Table 10). Four distinct textural varieties of glasses are observed in the Site 1232 turbidite sediments. Elongate pipe vesicular shards, highly vesicular shards, poorly vesicular shards and dark brown to black blocky shards were present in each interval containing glass. Colors range from black/dark brown to light tan/clear. Glass shards make up the predominant amount of sediment, between 45-63%, of the samples in the upper 140 mbsf of the 1232A core (Fig 4.5).

There is no regular variation in the range of SiO_2 contents in glass grains across all turbidite intervals studied. The analyzed glasses range in composition from basalt (trachy-basalt) to rhyolite (49-79% SiO_2), with 5.4% of grains in the 45-52% SiO_2 range (basalt/trachy-basalt), 57.5% in the 52-57% SiO_2 range (basaltic andesite/basaltic trachy-andesite), 26.4% in the 57-63% SiO_2 (andesite/trachy-andesite). The density of basaltic andesite to andesite glass (the predominance of what is found in the Site 1232 samples, >80%) is estimated to be between 2.1 – 2.8 g/cc (Yamada and Shoji 1990, and Malfait et al., 2018). However, water content of the glasses and degree of vesicularity can affect the movement of glasses within water.

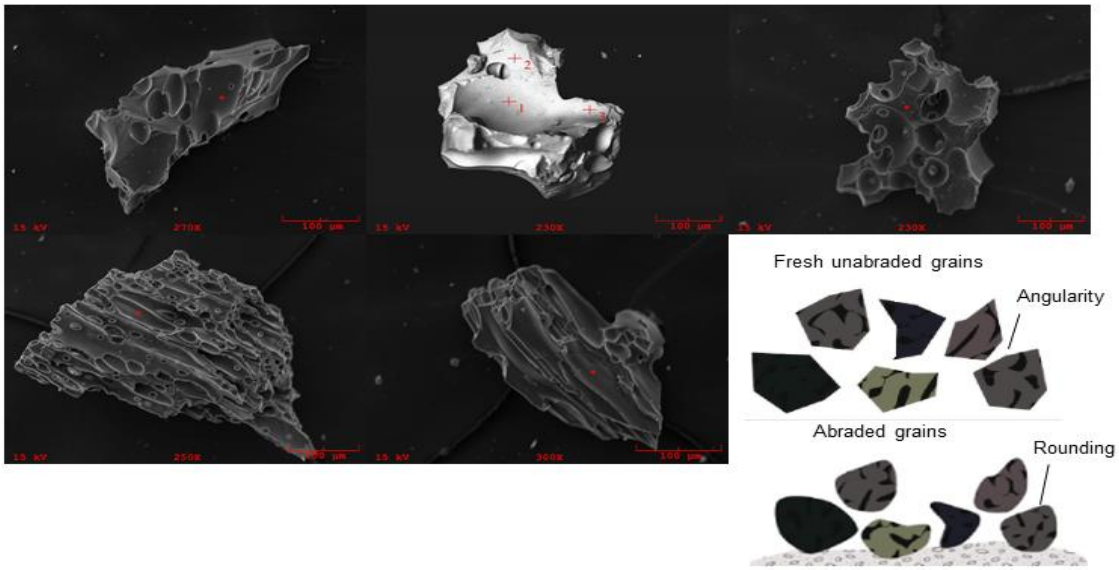

Figure 4.5: SEM high resolution images of Site 1232 glass shards pictured alongside a schematic depicting the rounding you would expect to see on abraded grains vs. the angularity of unaltered/unabraded grains. Schematic image modified from Buckland et al., (2018).

4.5 Discussion

4.5.1 Textural and chemical variations downcore (Changes in Sediment Input?)

To determine temporal variations throughout Site 1232, the proportions of glass, minerals, multi-mineral grains, and geochemical data of glasses downcore were investigated. The proportions of elements are quite consistent between 306 - 214 mbsf and throughout the upper 140 m of the core. The shipboard party reported two layers with extremely low quartz/feldspar ratios, one at 140-160 mbsf and the other at 250-260 mbsf (Mix et al., 2003). Between 306 - 214 mbsf samples are made up entirely of altered pumice with a rounded appearance, volcanic glass appears (making up 24%) at 180 mbsf within the core in the 149 micron size fraction and then shows a significant increase in abundance (30-63%) from 140 mbsf to 20 mbsf. A significant change in the thickness of coarse strata below 200 m in the core was also noticed by the shipboard party, with very

few coarse layers thicker than 4 cm below 200 m (Mix et al., 2003). The linear patterns of incompatible trace elements in the upper 160 mbsf of Site 1232 suggest, that the glasses were derived from a single volcanic source and there are no substantial differences in trace element patterns in glasses downcore.

The shift from altered pumice to glass occurs at an inferred age of 220 kyr – 190 kyr (Beck and Hickey-Vargas, in press, available online). This timeframe seems to correspond with the older volcanism at eruptions (>377 kyr and ~330 kyr) at Cordillera Nevada (Lagabrielle et al., 2000, and Gutierrez et al., 2005). The change in sediment type noted in the 1232A core from altered pumice shifting to fresh volcanic glass may be due to the changing chemistry of shifting from the older Cordillera Nevada (producing pumice) to younger Cordon Caulle/Puyehue (producing glass).

4.5.2 Transport and deposition of glasses

Predominantly, the same river systems that were active during the Pleistocene, are still active today. The rivers and subsequent submarine canyons in the SVZ are still in areas that experience high volumes of precipitation, runoff and sediment load transport creating high volume of sediment transport both onto the continental shelf as well as into the submarine channels. Volcanic eruptions are still occurring in the Holocene and the volcanic ejecta created by these eruptions is still being put into the atmosphere. Data even suggests a higher input of Andean material delivered fluvially to the continental shelf in the Holocene (Lamy et al., 2001, and Marchant et al., 2007). However, Site 1232 has not experienced deposition of volcanic turbidites in the last 12 kyr. Site 1232 reveals an obvious drop in turbidite deposition coinciding with the start of global warming following the last glacial.

It is highly unlikely that with the overall sharpness, angularity, and lack of abrasion of the mineral grains and glass shards, coupled with the lack of recent (Holocene) deposition that fluvial transport was the sole mode of transport for the deposition of the turbidites at Site 1232. The lack of sedimentation cannot be explained by a change in fluvial supply or a lack of volcanic sediments, therefore other possible scenarios must be explored. Considering the possible distance from the source (up to 800 km), it is extremely likely that a combination of multiple processes must be considered.

It is not unheard of for turbidites to travel over great distances (>1000 km) and to climb great heights (>2400 m) to deposition sites, examples have been seen in the Hawaiian Arch, Tiburon Rise and Aleutian Trench to name a few (Völker et al., 2008). With the relatively low density of basaltic andesite to andesitic glasses (2.1 – 2.8 g/cc), size (<210 microns) and the vesicularity of the shards, travel at or near the top of the turbidity current (Fig. 4.3b) in the dilute cloud layer (Paull et al., 2018). Travel in the dilute turbulent cloud layer would enable a much longer-lived mode of transport, allowing the grains to travel for great distances and potentially explaining the accumulation of such large quantities of lower density angular glass shards. Below are four scenarios for transport of the Site 1232 glass shards to the Nazca Plate, in order of most to least likely.

Proposed scenarios for transport from CSVZ

1.) Glasses were transported directly to the continental shelf as a primary ash deposit, as seen in ODP Sites 1233, 1234 and 1235 (continental shelf core sites from Leg 202) noted by Soto (2018), then transported to the Nazca Plate Site 1232 by turbidity current. This transport scenario is most reasonable explanation for the

pristine and unabraded nature of the glasses. There are records of PCCVC ash fall deposits on the continental shelf and it would explain the abundance of volcanic glasses compared to terrestrial material within the samples. This method would suggest multiple episodes of volcanic explosive eruptivity to feed the >700 turbidite layers found in the 1232A core alone.

2.) New biostratigraphic dating places deposition starting at ~275 kyr, at least two glacial stages before the LGM. The extent of glacial ice during these advances is not well documented, particularly in areas now covered with LGM glacial deposits. With glacial ice potentially extending to the coast as it did farther south during the LGM, volcanic glasses may have been erupted onto the glacial ice and deposited onto the shelf during the melt and recession of the ice sheet and farther transported to Site 1232 through turbidity current. This method would account for the pristine nature of the glasses and their arrival to Site 1232 without abrasion, however, without knowledge of earlier glacial extent it draws on a certain degree of speculation.

3.) Glasses erupt onto an icesheet whose maximum was similar to that of the LGM covering the full extent of Lagos Puyehue and Ranco which are current catchment basins for PCCVC volcanic debris. As glacial ice melted, the glass shards were deposited directly into either Rio Pilmaiquen (Lago Ranco) which turns into Rio Bueno, or directly into Rio Bueno (Lago Puyehue) where it is transported roughly ~100-120 km to the continental shelf and deposited. Glasses would then be deposited at Site 1232 through turbidity current. This scenario corresponds well to a volcanic source originating in the PCCVC, and river transport is the current

predominant mode of transport onto the continental shelf in the CSVZ. It is difficult to believe the glass shards were able to withstand 100-120 km of fluvial transport without showing any signs of abrasion. However, particles are very small (generally <250 microns), have relatively low density and a large proportion are vesicular so there is the potential that these factors allowed for transport suspended in water, reducing risk of abrasion. With three active (geochemically distinct) volcanoes in the PCCVC alone, one would expect to see some source variation within the samples. Most importantly, with 100-120 km of riverine transport, one would expect a higher proportion of terrigenous material.

4.) Transport of vesicular volcanic glasses by ice rafting. Assuming the potential of glacial ice extending to the coast in previous glacial events, as warming occurs ice cleaving off transporting the volcanic glasses in a slightly north-westward direction along the Peru-Chile coastal current and deposition on continental shelf occurs with melting. With glacial extent similar to that of the LGM, ice rafts could have travelled down river to reach the continental shelf with their sediment load (or partial load) still entrained. Deposited glasses and debris are moved in turbidity currents to the Nazca plate. This process is commonly seen with pumices and could be a potential pathway for the glasses. It would explain the angularity and lack of abrasion of the volcanic glasses, however at generally >210 microns, material is finer than expected for ice rafted debris and one would expect to also encounter coarser material as well. The lack of coarse material could be explained by the distance traveled from the continental shelf within the turbidity current. It seems an unlikely method considering the quantity of material transported.

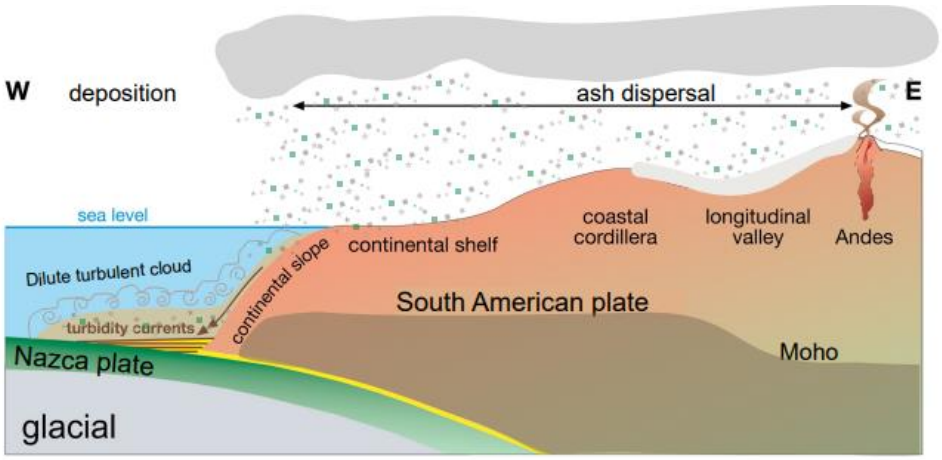

Figure 4.6 Schematic of potential turbidite glass transport from PCCVC by a glacial shift in wind patterns (adapted from Blumberg et al., 2008) and deposited directly onto continental shelf/slope and then transported within a dilute turbulent cloud (the uppermost portion) of a turbidity current across the trench to Site 1232.

4.6 Conclusions

1.) With the distance that was traveled (>250 km) from the likely source of the CSVZ, Site 1232 turbidites likely experienced complex transport involving multiple methods including ash fall, river, glacial transport, and turbidity current.

2.) The distinct change in sediment type noted in the 1232A core from altered pumice shifting to fresh volcanic glass above 140 m occurring between 220 kyr – 175 kyr may correspond to the older eruptions (>377 kyr and ~330 kyr) at Cordillera Nevada generating the pumice followed by a shift to the younger Cordon Caulle (300-70 kyr) or Puyehue (245-96 kyr) eruptions generating the volcanic glasses.

3.) With lack of Holocene deposition of volcanic turbidites at the Nazca Plate Site 1232, and no discernable change in fluvial sediment supply and pathways, it is unlikely that the Site 1232 turbidites containing glass shards were deposited exclusively through fluvial deposition.

4.) The abundance of glass in the Site 1232 turbidites can likely be explained by the

turbidity model put forth by Paull et al., (2018). With the lower density of the glasses, during the mobilization of the turbidite, the glasses which are relatively light, are suspended in the upper "dilute cloud layer" while the larger and heavier particles are contained in lower "near-bed layers". The upper dilute cloud layer travels greater distances due to the difference in the vertical density profile. This vertical separation may also play a role in the Site 1232 turbidity currents acquiring additional volcanic material from other sources *en route* to the Nazca Plate.

5.) The largest difference from today experienced in the Southern Chile area during the Late Pleistocene was widespread glaciation. With glaciers advancing and retreating in some areas to the coast and shifts in prevailing wind patterns, in a timeframe linked to increased sedimentary deposition of turbidite deposits, it is very likely that there is a connection. Glacial shifting of wind patterns or explosive volcanism are strong candidates for deposition of the glasses onto the continental shelf by primary ash fall. Glacial extent of the Patagonian ice sheet would have allowed for deposition of glasses either directly onto the shelf or rafting may have allowed the shards to travel down river to the shelf.

4.7 References

Angermann, D., J. Klotz, and C. Reigber, Space-geodetic estimation of the Nazca-South America angular velocity, Earth Planet. Sci. Lett., 171, 329– 334, 1999.

Beck, K., and Hickey-Vargas, R., 2022, Composition, age and origin of Pleistocene turbidite deposits at ODP site 1232, Nazca plate: Implications for volcanism and climate change in central south Chile: Journal of South American Earth Sciences, v. 118, https://doi.org/10.1016/j.jsames.2022.103908.

Blumberg, S., Lamy, F., Arz, H.W., Echtler, H.P., Wiedicke, M., Haug, G.H., and Oncken, O., 2008, Turbiditic trench deposits at the South-Chilean active margin: A

Pleistocene–Holocene record of climate and tectonics: Earth and Planetary Science Letters, v. 268, p. 526–539, doi:10.1016/j.epsl.2008.02.007.

Buckland, H.M., Eychenne, J., Rust, A.C., Cashman, K.V., 2018, Relating the physical properties of volcanic rocks to the characteristics of ash generated by experimental abrasion: J. Volcanol. Geotherm. Res., 349, pp. 335-350, 10.1016/j.jvolgeores.2017.11.017

Dymond, J. (1981). Geochemistry of Nazca plate surface sediments: An evaluation of hydrothermal, biogenic, detrital, and hydrogenous sources (pp. 133–174). https://doi.org/10.1130/MEM154-p133

Fontijn, K., Lachowycz, S. M., Rawson, H., Pyle, D. M., Mather, T. A., Naranjo, J. A., & Moreno-Roa, H. (2014). Late Quaternary tephrostratigraphy of southern Chile and Argentina. Quaternary Science Reviews, 89, 70-84.

Glasser, N., & Jansson, K. (2008). The Glacial Map of southern South America. *Journal of Maps*, *4*(1), 175–196. https://doi.org/10.4113/jom.2008.1020

Glasser, N., & Jansson, K. (2008). The Glacial Map of southern South America. *Journal of Maps*, *4*(1), 175–196. https://doi.org/10.4113/jom.2008.1020

Griffin, W. L., Powell, W. J., Pearson, N. J., & O'Reilly, S. Y. (2008). GLITTER: Data reduction software for laser ablation ICP–MS. *Laser Ablation–ICP–MS in the Earth Sciences CURRENT PRACTICES AND OUTSTANDING ISSUES*, *40*.

Gutiérrez, F., Gioncada, A., González Ferran, O., Lahsen, A., & Mazzuoli, R. (2005). The Hudson Volcano and surrounding monogenetic centres (Chilean Patagonia): An example of volcanism associated with ridge–trench collision environment. *Journal of Volcanology and Geothermal Research*, *145*(3–4), 207–233. https://doi.org/10.1016/j.jvolgeores.2005.01.014

Hildreth, W., Drake, R.E. Volcán Quizapu, Chilean Andes. Bull Volcanol 54, 93–125 (1992). https://doi.org/10.1007/BF00278002

Hulton, N. R. J., Purves, R. S., McCulloch, R. D., Sugden, D. E., & Bentley, M. J. (2002). The Last Glacial Maximum and deglaciation in southern South America. *Quaternary Science Reviews*, *21*(1–3). https://doi.org/10.1016/S0277-3791(01)00103-2

Jenks, W. F. (1956). *SELECTED GENERAL REFERENCES ON SOUTH AMERICAN GEOLOGY* (pp. xi–xii). https://doi.org/10.1130/MEM65-pxi

Krumbein, W.C. and Pettijohn, F.J. (1938) Manual of Sedimentary Petrography. D. Appleton-Century Company, Inc., New York, 549 p.

Lagabrielle, Y., Guivel, C., Maury, R. C., Bourgois, J., Fourcade, S., & Martin, H. (2000). Magmatic–tectonic effects of high thermal regime at the site of active ridge subduction: the Chile Triple Junction model. *Tectonophysics*, *326*(3–4), 255–268. https://doi.org/10.1016/S0040-1951(00)00124-4

Lamy, F., Hebbeln, D., & Wefer, G. (1999). High-Resolution Marine Record of Climatic Change in Mid-latitude Chile during the Last 28,000 Years Based on Terrigenous Sediment Parameters. *Quaternary Research*, *51*(1), 83–93. https://doi.org/10.1006/qres.1998.2010

Lamy, F., Hebbeln, D., Röhl, U., & Wefer, G. (2001). Holocene rainfall variability in southern Chile: a marine record of latitudinal shifts of the Southern Westerlies. *Earth and Planetary Science Letters*, *185*(3–4), 369–382. https://doi.org/10.1016/S0012-821X(00)00381-2

Malfait, W.J., Seifert, R., Petitgirard, S., Mezouar, M., Sanchez-Valle, C. (2014). The density of andesitic melts and the compressibility of dissolved water in silicate melts at crustal and upper mantle conditions. Earth Planet. Sci. Lett., 393 (2014), pp. 31-38

Marchant, M., Cecioni, A., Figueroa, S., González, H., Giglio, S., Hebbeln, D., Kaiser, J., Lamy, F., Mohtadi, M., Pineda, V., & Romero, O. (2007). Marine geology, oceanography and climate. In *Geological Society Special Publication*. https://doi.org/10.1144/goch.11

McCulloch, R. D., Bentley, M. J., Purves, R. S., Hulton, N. R. J., Sugden, D. E., & Clapperton, C. M. (2000). Climatic inferences from glacial and palaeoecological evidence at the last glacial termination, southern South America. *Journal of Quaternary Science*, *15*(4). https://doi.org/10.1002/1099-1417(200005)15:4<409

Melnick, D., & Echtler, H. P. (2006). Inversion of forearc basins in south-central Chile caused by rapid glacial age trench fill. *Geology*, *34*(9), 709. https://doi.org/10.1130/G22440.1

Mix, A. C., Tiedemann, R., Blum, P., Lund, S. P., & Stoner, J. S. (2003). *Proceedings of the Ocean Drilling Program, 202 Initial Reports*. Ocean Drilling Program. https://doi.org/10.2973/odp.proc.ir.202.2003

Muñoz, J. F. , F. B. , V. E. , P. P. , G. D. , R. P. , & G. W. (2007). Chilean water resources. In *The geology of Chile* (pp. 215–230).

Powers, M.C. (1953) A new roundness scale for sedimentary particles. J. Sediment. Petrol. 23, 117– 119.

Prueher, L., Rea, D., (2001). Volcanic triggering of late Pliocene glaciation: evidence from the flux of volcanic glass and ice-rafted debris to the North Pacific Ocean Palaeogeogr. Palaeoclimatol. Palaeoecol., 173 (2001), pp. 215-230

Rollinson, H. R. (1993). *Using Geochemical Data: Evaluation, Presentation, Interpretation*.

Scholl, D. W., Christensen, M. N., Huene, R. v., & Marloe, M. S. (1970). Peru-Chile Trench Sediments and Sea-Floor Spreading. *Geological Society of America Bulletin* , *81*, 1339.

Soto, Emmanuel, "Identifying the Origins of Volcanic Ash Deposits Using Their Chemical and Physical Compositions" (2018). FIU Electronic Theses and Dissertations. 3650. DOI 10.25148/etd.FIDC006542. https://digitalcommons.fiu.edu/etd/3650

Stern, C. R. (2004). Active Andean volcanism: Its geologic and tectonic setting. In *Revista Geologica de Chile* (Vol. 31, Issue 2). https://doi.org/10.4067/S0716-02082004000200001

Sun, S. -s., & McDonough, W. F. (1989). Chemical and isotopic systematics of oceanic basalts: implications for mantle composition and processes. *Geological Society, London, Special Publications*, *42*(1), 313–345. https://doi.org/10.1144/GSL.SP.1989.042.01.19

Thornburg, T. M., & Kulm, L. D. (1987). Sedimentation in the Chile Trench: petrofacies and provenance. *Journal of Sedimentary Petrology*, *57*(1). https://doi.org/10.1306/212F8AA3-2B24-11D7-8648000102C1865D

Völker, D., Wiedicke, M., Ladage, S., Gaedicke, C., Reichert, C., Rauch, K., Kramer, W., & Heubeck, C. (2006). Latitudinal Variation in Sedimentary Processes in the Peru-Chile Trench off Central Chile. In *The Andes*. https://doi.org/10.1007/978-3-540-48684-8_9

Völker, D., Geersen, J., Contreras-Reyes, E., and Reichert, C., 2013, Sedimentary fill of the Chile Trench (32–46°S): volumetric distribution and causal factors: Journal of the Geological Society, v. 170, p. 723–736, doi: 10.1144/jgs2012-119.

Yamada, I., & Shoji, S., (1990). Heavy solution method for determination of volcanic glass content in tephras and tephra-derived soils, Soil Science and Plant Nutrition, 36:3, 505-509, DOI: 10.1080/00380768.1990.10416920

5. Conclusions

5.1 Geochemical and source identification

Turbidite deposits at Site 1232 show an abundance of fresh undevitrified volcanic glass. Geochemical characterization allowed for source region identification of the glasses found within the Site 1232 turbidite deposits. Glasses from the upper 200 m of the cored section have a geochemical signature consistent with origination in the Southern Volcanic Zone. Based on major and trace elemental analyses compared throughout the core, the volcanic glasses in investigated turbidite intervals in the upper 140 m of the Site 1232 core likely originate from a single volcanic source.

Geochemically the shards compare most closely with the Central SVZ and the Southern SVZ. There is a good connection between the geochemical composition of the Site 1232 glasses to the adjacent Puyehue/Cordon Caulle volcanic complex data. The 1232 shards are likely representative of either continuous activity at the Puyehue/Cordon Caulle volcanic complex, earlier activity than expected at another SVZ source, or the existence of a SVZ volcano that is not yet known.

The petrographic features and mineralogical composition suggest that the source for the upper 200 m of the sediments is primarily volcanic (glass and pumice), with minor proportions coming from sedimentary and metamorphic source regions. New age constraints using nannofossil biostratigraphy place the upper 288 m of cored section between 12.47 kyr and 275 kyr. Further work is unlikely to provide better constraints due to an overall scarcity of microfossil biota, potentially due to the rapid accumulation of sediment in the area during the Pleistocene.

5.2 Changes in sediment type and deposition

This study recognizes a previously undocumented compositional change in sediments within the cored interval from altered pumice a depth of 214 mbsf and below shifting to fresh volcanic glass above 140 mbsf, evident in core 1232A. The timing in the change of sediment (calculated using new age data and estimated sedimentation rate) has been determined to be between 175-220 kyr. Even though the precise cause of the sedimentary shift is uncertain, due to the shift from Interglacial MIS 7 to the Glacial MIS 6 that occurs during the timeframe and the abrupt change in volcanic material type.

The distinct change in sediment type noted in the 1232A core from altered pumice shifting to fresh volcanic glass above 140 m occurring between 220 kyr – 175 kyr may be due to: older eruptions (>377 kyr and ~330 kyr) at Cordillera Nevada generating the pumice followed by a shift to the younger Cordon Caulle (300-70 kyr) or Puyehue (245-96 kyr) eruptions generating the volcanic glasses, if Site 1232 glasses originate from the PCCVC in the adjacent CSVZ.

Complex transport processes combined to enable the emplacement of the glass shards at Site 1232 on the Nazca plate. With the great distance that was traveled (>250 m) from the likely source of the CSVZ the Site 1232 turbidites likely experienced complex transport involving multiple methods. Lack of Holocene deposition of volcanic turbidites at the Nazca Plate Site 1232, and no significant change in fluvial sediment supply and pathways, show that it is unlikely that the Site 1232 turbidites containing glass shards were deposited through a predominantly fluvial mode. The abundance of glass in the Site 1232 turbidites can likely be explained by the turbidity model put forth by Paull et al., 2018. With the lower density of the glasses, during the mobilization of the

turbidite, the lighter glasses are suspended in the upper “dilute cloud layer” while the larger and heavier particles are contained in lower “near bed layers”. The upper dilute cloud layer travels greater distances due to the difference in the vertical density profile. This vertical separation may also play a role in the Site 1232 turbidite deposits not picking up volcanic material from other sources enroute to the Nazca Plate. It is highly likely that glacial ice played an extensive role in the deposition of the 1232 turbidite glass shards.

Due to the limited data available for the chemical composition of distinct eruption locations, studying volcanic activity in the Southern Volcanic Zone is critical. Despite the fact that the active margins of Chile have been widely investigated, there are still significant gaps in knowledge. Many volcanic eruptions in the Andes have not been geochemically recorded over time, and more recent glacial events have potentially erased the footprints of the full extent of past glacial events, resulting in vast gaps in the literature. This makes determining the transport methods of volcanic glasses more difficult. The goal of this project has been to offer a substantial amount of petrographical and geochemical data, identify the source of the volcanic glass shards, and provide the most possible and plausible scenarios for transport that may be used in future investigations.

5.3 Future work

- More high-resolution sampling, taking more turbidite intervals especially between 160 mbsf and 214 mbsf to determine the exact depth of the material shift from pumice to unaltered glass.

- Sediments could be collected from local rivers (Rio Pilmaiquen and Rio Bueno), lakes (Lago Ranco and Lago Puyehue) and catchment basins (Chronos Archipelagio, Chiloe Island, and sample sites in the central depression near ~40°S and ~46°S. Samples can be petrographically and geochemically compared to the Site 1232 samples to further narrow down source and transport mechanism.
- Get a better, more confined age constraint for the time of evolution using mineral dating. Dating biotite grains in the sediments from Site 1232 ash layer or zircons within glasses can help to define the timing of events.
- Collect more samples for calcareous nannofossil biostratigraphical analysis to refine the age of the core potentially further.
- Preform bulk geochemistry on pumice pieces using Solution Inductively Coupled Plasma Mass Spectrometer (ICP-MS) to help identify a potential source and a reason for the shift in sediment type.
- Explore the change in TiO_2 content of the PCCVC from Pleistocene to recent if the glasses are originating there. Why is the Ti different, can old rocks having this feature be found, and what caused the change in f_{O2}?
- Use Monte Carlo simulations to help trace the provenance and transport pathways of distal turbidite deposits using geochemical tracers.

APPENDIX

Table 1 - Individual point count data for each examined interval

Table 1 Point Counts													
Sample	C	G	P	Fp	M	Tot		Sample	%G	%P	%Fp	%M	%C
1232A-4H-2W-38 >149	77	185	22	45	25	354		1232A-4H-2W-38 >149	52.26	6.21	12.71	7.06	21.75
1232A-4H-6W-45 >149	47	191	23	82	8	351		1232A-4H-6W-45 >149	54.42	6.55	23.36	2.28	13.39
1232A-5H-7W-45 >210	64	160	25	97	6	352		1232A-5H-7W-45 >210	45.45	7.10	27.56	1.70	18.18
1232A-6H-4W-85 >149	58	177	18	76	14	342		1232A-6H-4W-85 >149	51.75	5.26	22.22	4.09	16.96
1232A-6H-6W-118 >149	79	164	15	74	6	338		1232A-6H-6W-118 >149	48.52	4.44	21.89	1.78	23.37
1232A-6H-6W-118 >210	29	174	16	102	20	341		1232A-6H-6W-118 >210	51.03	4.69	29.91	5.87	8.50
1232A-7H-2W-86 >149	77	177	23	61	10	348		1232A-7H-2W-86 >149	50.86	6.61	17.53	2.87	22.13
1232A-7H-5W-87 >149	60	153	26	71	15	325		1232A-7H-5W-87 >149	47.08	8.00	21.85	4.62	18.46
1232A-7H-6W-42 >149	73	177	21	85	16	372		1232A-7H-6W-42 >149	47.58	5.65	22.85	4.30	19.62
1232A-8H-1W-46 >149	16	228	11	91	14	360		1232A-8H-1W-46 >149	63.33	3.06	25.28	3.89	4.44
1232A-10H-3W-25 >149	28	214	12	58	35	347		1232A-10H-3W-25 >149	61.67	3.46	16.71	10.09	8.07
1232A-12H-1W-125 >149	55	198	11	76	20	360		1232A-12H-1W-125 >149	55.00	3.06	21.11	5.56	15.28
1232A-16X-1W-41 >149	62	108	13	128	29	340		1232A-16X-1W-41 >149	31.76	3.82	37.65	8.53	18.24
1232A-18X-1W-36 >149*	31	52	10	103	21	216		1232A-18X-1W-36 >149*	24.07	4.63	47.69	9.72	14.35
1232A-23X-5W-62 >149*								1232A-23X-5W-62 >149*	0.00	0.00	99.00	1.00	0.00
1232A-27X-2W-42 >149	0	0	0	307	0	307		1232A-27X-2W-42 >149	0.00	0.00	100.00	0.00	0.00
1232A-31X-3W-54 >149	0	0	0	338	2	340		1232A-31X-3W-54 >149	0.00	0.00	99.41	0.59	0.00
1232B-3H-6W-26 >149	59	170	14	71	16	330		1232B-3H-6W-26 >149	51.52	4.24	21.52	4.85	17.88
1232B-4H-1W-89 >149	75	166	25	50	6	322		1232B-4H-1W-89 >149	51.55	7.76	15.53	1.86	23.29
1232B-5H-5W-80 >149	51	189	10	61	13	324		1232B-5H-5W-80 >149	58.33	3.09	18.83	4.01	15.74
1232B-6H-7W-33 >149	71	158	16	100	9	354		1232B-6H-7W-33 >149	44.63	4.52	28.25	2.54	20.06
1232B-6H-7W-33 >210	27	165	0	113	3	310		1232B-6H-7W-33 >210	53.23	0.00	36.45	0.97	8.71
1232B-7H-2W-68 >149	57	164	13	69	10	313		1232B-7H-2W-68 >149	52.40	4.15	22.04	3.19	18.21
1232B-7H-2W-68 >210	24	180	0	81	21	306		1232B-7H-2W-68 >210	58.82	0.00	26.47	6.86	7.84
1232B-7H-3W-90 >149	58	194	11	56	6	325		1232B-7H-3W-90 >149	59.69	3.38	17.23	1.85	17.85
1232B-9H-2W-69 >149	25	213	11	85	6	340		1232B-9H-2W-69 >149	62.65	3.24	25.00	1.76	7.35
1232B-10H-7W-23 >149	68	171	8	72	23	342		1232B-10H-7W-23 >149	50.00	2.34	21.05	6.73	19.88
C - clear minerals, G - glass, P - polymineralic grains, Fp - felsic polymineralic grains, M - metamorphic grains, Tot - total													

Table 2 – Select major element data for glass in ODP Site 1232 turbidites. SEM data for USGS standard BHVO-2g and Smithsonian standard (NMNH 72854, VG 568) run with samples are given with analytical precision.

Table 2 SEM Major Element Analysis						
		Oxide (wt%)	SiO_2	MgO	Na_2O	K_2O
1232A-4H-6W-45>149	G2		65.45	1.99	4.53	1.84
	G4		65.87	1.67	5.02	2.35
	G5		57.61	4.13	4.39	1.39
	G6		57.83	4.43	4.42	1.09
	G7		55.91	4.26	3.25	1.69
	G8		67.44	1.35	5.32	2.42
	G9		57.51	4.49	4.63	1.15
	G10		55.90	4.41	3.83	0.81
1232A-4H-6W-45 >210	G1		70.39	0.74	4.11	3.65
	G2		56.88	3.89	4.55	1.35
	G3		65.65	1.43	3.40	2.17
	G4		58.90	3.79	4.16	1.48
	G5		59.95	2.93	4.49	1.18
	G6		56.72	4.44	4.06	1.18
	G7		57.65	3.81	4.42	1.34
	G8		56.50	4.45	4.73	0.92
	G9		76.25	0.46	4.02	1.92
	G10		56.61	4.08	4.05	1.43
1232A-5H-7W-45 >149	G1		53.26	3.97	3.82	1.34
	G2		73.42	1.08	3.89	2.56
	G3		53.80	4.06	3.44	1.29
	G4		65.00	0.75	2.86	4.35
	G5		69.17	0.69	5.42	3.07
	G6		54.56	4.80	4.28	1.05
	G7		56.29	3.63	4.25	1.14
	G8		60.22	2.37	4.40	1.53
	G9		58.23	3.97	3.81	1.39
	G10		61.44	2.16	4.50	1.36
1232A-5H-7W-45 >210	G1		56.48	4.26	3.81	1.62
	G2		58.45	2.53	3.40	1.48
	G3		73.11	0.37	4.55	3.31
	G4		64.61	1.63	3.97	2.72
	G5		55.86	4.16	3.56	1.07
	G6		56.29	3.51	4.26	1.42
	G7		64.36	1.50	4.69	2.07
	G8		72.61	0.36	4.76	3.98
	G9		56.35	3.89	4.25	1.27
	G10		61.27	1.56	3.50	1.74
1232A-6H-6W-118 >149	G1		56.38	3.76	4.15	1.11
	G2		54.98	4.15	4.52	1.22
	G3		54.86	4.27	4.05	1.32
	G4		58.72	2.80	3.80	1.97
	G5		63.57	2.83	3.73	1.57
	G6		57.33	4.88	4.31	1.09
	G7		58.76	2.92	4.91	1.55
	G8		57.44	3.82	4.32	1.40
	G9		55.98	4.01	4.18	1.51
	G10		54.98	3.41	3.11	1.63
1232A-6H-6W-118 >210	G2		56.68	3.67	4.37	1.42
	G4		58.81	2.90	4.71	1.89
	G5		56.21	3.33	3.49	1.34
	G6		64.33	1.15	4.16	2.03
	G7		57.16	3.72	3.70	1.23
	G8		55.49	4.76	4.39	1.27
	G9		58.44	3.86	4.55	1.77
	G10		54.77	4.55	4.31	1.02
1232A-8H-1W-46>149	G1		66.37	1.47	5.11	1.77
	G2		62.24	2.13	4.62	1.61
	G3		60.47	2.95	4.10	1.52
	G4		67.61	1.40	5.34	2.12
	G5		55.88	4.16	3.47	1.17
	G6		59.59	2.89	5.10	1.04
	G7		62.20	2.06	4.43	1.55
	G8		56.75	3.53	3.76	1.78
	G9		60.65	2.81	3.93	1.28
1232A-8H-1W-46 >210	G1		61.81	2.55	5.40	1.76
	G2		63.42	2.12	5.11	1.67
	G3		58.52	3.58	4.77	1.29
	G4		58.72	3.30	4.90	1.23
	G5		56.35	3.43	4.89	1.09
	G6		64.32	1.90	5.09	1.83
	G7		61.09	2.75	4.73	1.46
	G8		65.71	1.64	5.08	2.00
	G9		63.35	2.49	5.22	1.43
	G10		60.56	1.56	4.67	1.41
1232A-10H-3W-25 >149	G1		59.24	3.27	5.04	1.49
	G2		59.02	3.54	3.52	1.65
	G3		57.36	2.86	3.87	1.42
	G4		58.86	3.50	4.58	1.37
	G5		58.12	3.11	4.45	1.26
	G6		58.89	2.96	3.65	1.38
	G7		59.27	2.78	4.64	1.15
	G8		59.92	3.50	4.28	1.16
	G9		58.15	3.22	3.41	1.71
	G10		58.27	3.74	4.22	1.21
1232A-10H-3W-25 >210	G1		58.77	3.13	3.67	1.41
	G2		58.44	2.31	3.53	1.42
	G3		57.36	3.68	4.14	1.08
	G4		56.22	3.45	4.07	1.36
	G5		63.28	2.44	4.21	1.67
	G6		56.75	2.64	4.48	1.63
	G7		57.94	3.33	4.30	1.14
	G8		55.99	2.67	3.29	1.20
	G9		56.17	3.33	3.02	1.61
	G10		58.71	3.11	4.55	1.37
1232A-12H-1W-125 >149	G1		54.32	3.52	3.85	1.64
	G2		62.02	1.63	3.76	2.37
	G3		58.01	2.95	5.65	1.62
	G4		57.35	3.22	3.91	1.70
	G5		56.71	4.52	3.58	1.15
	G6		55.77	3.76	3.59	1.64
	G7		66.94	1.49	4.93	2.73
	G8		64.04	1.92	4.52	2.55
	G9		60.16	1.80	4.78	2.37
	G10		56.24	4.45	4.72	1.18
1232A-12H-1W-125 >210	G1		54.92	3.94	3.81	1.40
	G2		54.38	4.16	3.68	1.85
	G3		56.12	3.81	4.22	1.69
	G4		58.53	3.92	4.06	1.16
	G5		56.52	3.90	4.34	1.58
	G6		57.34	2.47	3.64	1.88
	G7		59.33	2.32	3.03	1.88
	G8		56.80	3.40	3.42	1.28
	G10		54.57	3.86	5.65	1.04
BHVO meas avg			45.03	7.59	2.86	
Sdev%			0.47	2.40	4.91	
Rhyolite meas avg			72.00		4.26	8.11
Sdev%			0.37		2.72	1.72

Sdev - standard deviation, BHVO - Basalt, Hawaiian Volcanic Observatory, meas - measured, avg - average, Wt% - weight percent, SEM - scanning electron microscope

Table 3 – Select trace element data for glass in ODP Site 1232 turbidites. LA-ICPMS data for USGS standard BHVO-2g and Smithsonian standard (NMNH 72854, VG 568) run with samples are given with analytical precision.

Table 3 LA-ICP-MS Trace Elemental Data												
	1232A-5H-7W-45		1232A-6H-6W-118		1232A-8H-1W-46		1232A-10H-3W-25		1232A-12H-1W-			
Trace Element (ppm)	G1	G9	G4	G8	G2	G10	G7	G9	G1	G5	BHVO meas avg	Std dev %
Rb	40	34	37	27.7	30.6	46	31.1	41	48	42	7.1	2.79
Ba	470	440	520	350	410	590	370	470	550	470	120	2.65
Th	5.5	4.6	5.9	4.5	5.0	7.5	5.2	5.3	6.5	6.2	1.20	2.53
Nb	7.6	6.4	7.8	5.4	5.4	8.3	4.9	6.4	8.2	7.2	17.0	2.59
Ta	0.46	0.36	0.37	0.40	0.44	0.59	0.42	0.287	0.42	0.43	1.17	2.77
La	26.3	22.4	29.7	21.1	19.1	28.3	20.1	20.8	29.1	24.7	15.0	3.05
Ce	58	49	65	44	42	64	38	49	68	58	34	3.32
Pb	14.4	13.1	13.7	9.8	13.3	17.8	15.1	15.4	17.6	15.4	1.36	5.41
Nd	37	29	44	32	26	43	27	30	39	37	24	4.46
Zr	201	175	207	173	167	243	172	162	207	198	148	2.58
Hf	5.6	5.5	4.7	4.7	4.5	6.4	4.2	4.6	5.1	6.2	4.0	6.38
Sm	8.8	7.5	9.3	7.4	6.2	10.1	6.4	7.0	10.8	8.9	5.8	3.27
Gd	8.7	8.9	9.9	8.7	6.3	10.0	7.0	6.8	9.5	8.6	5.6	5.08
Y	48	44	49	46	36	54	40	37	51	49	22.8	2.93
Yb	4.9	4.7	5.3	4.8	4.3	6.3	4.5	4.1	6.1	5.5	2.04	4.64
Lu	0.74	0.71	0.84	0.75	0.65	0.79	0.66	0.66	0.81	0.84	0.27	6.53

meas - measured, avg - average, ppm - parts per million, LA-ICP-MS - laser ablation inductively coupled mass spectrometer, Std - standard, dev- deviation, BHVO -

Table 4: All SEM major element data for >149 micron glass in ODP Site 1232 turbidites.

Major Oxide	1232A-1H-3W-61 >149										1232A-3H-3W-64 >149								
	G1	G2	G3	G4	G5	G6	G7	G8	G9	G10	G1	G2	G3	G4	G5	G6	G7	G8	G9
wt%	54.91	63.35	55.22	59.53	53.70	54.10	53.65	56.74	70.63	79.03	54.80	65.37	56.01	59.71	54.43	57.33	50.88	55.05	55.00
TiO_2	1.76	1.30	1.30	1.84	1.24	1.23	1.99	1.65	0.43	0.09	1.92	1.04	1.62	1.87	1.46	1.61	1.05	2.55	1.13
Al_2O_3	14.60	13.94	14.44	13.74	14.59	14.38	14.43	14.96	14.00	11.97	15.30	14.64	15.30	14.07	15.12	16.69	25.57	15.27	17.80
FeO	8.85	6.72	9.55	8.88	10.78	9.85	11.55	8.52	2.99	1.04	8.74	6.21	8.33	8.42	9.36	7.95	6.34	12.44	9.27
MgO	4.06	1.08	3.82	2.24	5.07	4.25	4.01	2.98	0.39	0.13	4.24	1.00	4.33	1.87	5.03	3.41	1.47	2.23	2.62
CaO	9.10	4.44	9.03	5.06	8.10	10.04	8.34	7.07	1.83	0.17	8.77	3.48	7.56	5.91	8.12	6.50	8.98	6.05	6.09
Na_2O	4.79	5.66	4.91	5.28	5.50	4.55	4.29	5.74	6.45	2.71	4.51	4.80	4.97	4.46	4.75	4.77	4.44	4.25	5.57
K_2O	1.39	2.87	1.41	2.42	0.79	1.35	1.12	1.67	3.10	4.87	1.37	2.59	1.54	2.44	0.89	1.19	1.01	1.76	1.66

Major Oxide	1232A-4H-2W-33 >149									1232A-4H-6W-45 >149							
	G1	G2	G3	G4	G5	G6	G7	G8	G9	G2	G4	G5	G6	G7	G8	G9	G10
wt%	55.47	66.87	55.38	56.42	56.27	60.81	59.01	53.44	55.06	65.45	65.87	57.61	57.83	55.91	67.44	57.51	55.90
TiO_2	1.89	1.17	1.77	1.49	1.96	1.72	2.02	1.79	1.80	1.01	1.02	1.83	1.46	1.37	1.63	1.48	1.90
Al_2O_3	14.67	14.91	14.76	15.44	14.16	14.68	14.62	14.73	15.13	14.86	15.39	15.63	15.22	14.99	14.97	15.39	15.67
FeO	9.86	3.29	10.41	10.11	10.16	7.65	8.57	10.56	10.41	6.31	4.94	8.25	8.53	10.38	3.25	8.46	9.90
MgO	3.75	0.75	3.83	2.75	2.77	1.68	2.04	4.28	3.78	1.99	1.67	4.13	4.43	4.26	1.35	4.49	4.41
CaO	6.65	3.30	7.20	6.01	6.14	5.23	5.37	9.14	6.59	4.01	3.73	6.77	7.01	8.15	3.62	6.88	7.58
Na_2O	5.16	5.37	4.35	5.19	6.31	5.13	4.93	4.40	5.53	4.53	5.02	4.39	4.42	3.25	5.32	4.63	3.83
K_2O	1.73	3.25	1.45	1.54	1.79	2.05	1.83	1.20	1.43	1.84	2.35	1.39	1.09	1.69	2.42	1.15	0.81

Major Oxide	1232A-5H-7W-45 >149										1232A-6H-4W-85 >149								
	G1	G2	G3	G4	G5	G6	G7	G8	G9	G10	G1	G2	G3	G4	G5	G6	G7	G8	G9
wt%	53.26	73.42	53.80	65.00	69.17	54.56	56.29	60.22	58.23	61.44	67.10	55.40	58.77	54.48	58.16	53.91	55.17	56.56	55.20
TiO_2	1.60	1.00	2.48	1.83	0.69	1.65	1.89	1.62	1.39	1.56	0.91	1.59	1.35	2.25	2.20	1.81	2.50	1.70	2.16
Al_2O_3	19.42	12.14	16.16	14.11	13.75	15.27	15.85	15.34	14.92	16.07	14.84	14.71	15.08	14.13	14.70	14.31	13.60	14.81	13.92
FeO	9.53	3.38	11.83	7.51	4.59	11.12	10.10	9.48	9.14	7.81	4.38	9.72	9.18	11.18	9.12	10.73	11.80	10.38	11.14
MgO	3.97	1.08	4.06	0.75	0.69	4.80	3.63	2.37	3.97	2.16	0.91	3.53	2.48	3.66	2.40	4.47	2.90	2.92	2.98
CaO	7.06	2.51	6.94	3.59	2.63	7.27	6.86	5.03	7.14	5.11	2.34	8.84	6.41	6.99	6.52	8.31	6.94	7.79	6.69
Na_2O	3.82	3.89	3.44	2.86	5.42	4.28	4.25	4.40	3.81	4.50	6.12	3.39	4.11	5.02	4.19	4.68	3.91	3.84	4.52
K_2O	1.34	2.56	1.29	4.35	3.07	1.05	1.14	1.53	1.39	1.36	2.95	1.67	1.73	1.39	1.83	1.40	1.67	1.43	1.74

Major Oxide	1232A-6H-6W-118 >149										1232A-7H-2W-86 >149								
	G1	G2	G3	G4	G5	G6	G7	G8	G9	G10	G1	G2	G3	G4	G5	G6	G7	G8	G9
wt%	56.38	54.98	54.86	58.72	63.57	57.33	58.76	57.44	55.98	54.98	55.24	54.45	64.53	60.55	63.41	56.22	53.37	56.90	57.74
TiO_2	1.79	2.06	1.90	2.00	1.03	1.06	1.78	1.58	2.15	2.82	1.84	1.99	1.42	1.89	1.32	1.64	1.73	1.51	1.06
Al_2O_3	15.68	14.59	14.08	13.68	15.21	15.33	14.79	14.21	13.25	13.15	13.87	15.53	14.89	14.11	14.43	14.90	16.44	15.08	15.91
FeO	10.38	11.28	11.82	10.89	6.57	8.51	9.55	10.30	12.30	12.49	11.10	9.33	5.75	8.04	7.14	9.62	9.25	8.44	8.21
MgO	3.76	4.15	4.27	2.80	2.83	4.88	2.92	3.82	4.01	3.41	3.76	4.36	1.17	2.09	1.71	3.79	4.29	3.86	3.12
CaO	6.75	7.20	7.70	6.14	5.49	7.49	5.72	6.94	6.62	8.42	8.24	7.78	3.81	5.09	4.81	7.51	8.42	6.99	6.64
Na_2O	4.15	4.52	4.05	3.80	3.73	4.31	4.91	4.32	4.18	3.11	3.75	4.51	4.69	5.25	4.42	4.17	5.40	5.17	5.55
K_2O	1.11	1.22	1.32	1.97	1.57	1.09	1.55	1.40	1.51	1.63	1.86	1.29	3.23	1.99	1.94	1.48	1.10	1.34	1.52

Major Oxide	1232A-7H-5W-87 >149									1232A-7H-6W-42 >149									
	G1	G2	G3	G4	G5	G6	G7	G8	G9	G1	G2	G3	G4	G5	G6	G7	G8	G9	
wt%	66.01	56.61	65.30	52.82	56.32	63.12	59.68	54.43	56.06	63.84	54.37	56.98	68.02	62.70	58.70	53.93	54.06	65.54	
TiO_2	0.84	1.31	0.99	1.92	2.05	1.61	1.48	1.70	1.27	1.32	1.24	1.88	0.97	1.38	1.83	1.36	2.44	1.25	
Al_2O_3	14.89	13.99	15.82	14.67	14.13	15.38	16.24	14.27	15.36	16.96	16.31	14.16	15.63	16.24	14.86	14.18	16.51	14.90	
FeO	5.52	12.64	5.26	11.33	10.28	5.12	7.03	11.83	9.15	4.95	10.52	10.63	3.20	6.01	7.77	11.46	10.92	4.43	
MgO	0.89	2.07	1.27	4.84	2.69	1.21	1.38	3.88	4.50	1.36	3.90	2.95	0.59	1.79	2.68	4.75	3.26	1.00	
CaO	3.36	5.78	4.25	8.15	7.52	4.31	6.70	7.34	7.57	4.03	8.03	7.11	2.26	4.84	6.92	8.91	6.93	3.30	
Na_2O	5.65	5.02	4.20	4.59	4.10	5.52	5.13	4.64	4.82	5.16	4.43	4.01	5.55	4.06	4.28	4.44	4.41	5.91	
K_2O	2.64	1.66	2.59	1.17	1.75	2.24	1.77	1.30	1.19	1.85	0.97	1.46	3.50	2.00	1.99	0.87	0.94	2.97	

Major Oxide	1232A-8H-1W-46>149									1232A-10H-3W-25 >149									
	G1	G2	G3	G4	G5	G6	G7	G8	G9	G1	G2	G3	G4	G5	G6	G7	G8	G9	
wt%	66.37	62.24	60.47	67.61	55.88	59.59	62.20	56.75	60.65	56.27	55.49	56.27	56.37	61.41	57.89	56.83	55.56	56.30	
TiO_2	1.01	1.16	1.50	0.97	1.72	1.24	1.29	2.29	1.42	1.45	2.08	1.64	1.95	1.55	2.36	1.41	1.81	1.88	
Al_2O_3	15.99	15.94	15.80	15.01	15.29	15.47	14.95	14.76	14.87	16.30	14.23	14.96	14.92	13.18	14.20	14.80	14.36	13.75	
FeO	4.69	7.43	6.87	4.36	10.18	9.37	7.77	10.28	8.29	8.95	11.06	9.55	10.17	9.87	10.63	8.60	11.06	12.15	
MgO	1.47	2.13	2.95	1.40	4.16	2.89	2.06	3.53	2.81	3.45	3.16	3.42	3.51	1.34	2.36	2.65	2.81	1.94	
CaO	3.58	4.87	6.79	3.19	8.14	5.31	5.76	6.85	6.75	6.97	6.23	7.07	6.75	5.19	5.65	8.34	6.65	6.81	
Na_2O	5.11	4.62	4.10	5.34	3.47	5.10	4.43	3.76	3.93	4.84	4.82	4.59	4.20	3.88	4.17	5.36	4.46	3.76	
K_2O	1.77	1.61	1.52	2.12	1.17	1.04	1.55	1.78	1.28	1.38	1.87	1.64	1.26	2.60	1.71	1.53	1.87	1.74	

Major oxide (wt.%)	1232A-10H-3W-25 >149										1232A-12H-1W-125 +149									
	G1	G2	G3	G4	G5	G6	G7	G8	G9	G10	G1	G2	G3	G4	G5	G6	G7	G8	G9	G10
SiO_2	59.24	59.02	57.36	58.86	58.12	58.89	59.27	59.92	58.15	58.27	54.32	62.02	58.01	57.35	56.71	55.77	66.94	64.04	60.16	56.24
TiO_2	1.65	1.82	2.40	1.31	2.23	2.04	1.79	1.44	1.74	1.09	2.51	1.06	1.80	2.09	1.83	2.76	1.30	1.56	1.72	2.08
Al_2O_3	15.46	15.27	14.54	15.17	14.78	14.18	14.82	15.70	14.68	16.50	14.55	14.05	14.71	14.49	14.22	13.61	13.20	13.76	12.74	14.53
FeO	8.37	8.42	10.51	9.08	9.90	10.41	9.54	7.39	9.98	7.73	12.83	9.80	9.65	10.40	10.60	11.60	5.74	7.53	11.99	9.74
MgO	3.27	3.54	2.86	3.50	3.11	2.96	2.78	3.50	3.22	3.74	3.52	1.63	2.95	3.22	4.52	3.76	1.49	1.92	1.80	4.45
CaO	5.48	6.75	7.04	6.13	6.15	6.48	6.02	6.62	7.11	7.25	6.77	5.31	5.61	6.83	7.38	7.26	3.66	4.12	4.44	7.07
Na_2O	5.04	3.52	3.87	4.58	4.45	3.65	4.64	4.28	3.41	4.22	3.85	3.76	5.65	3.91	3.58	3.59	4.93	4.52	4.78	4.72
K_2O	1.49	1.65	1.42	1.37	1.26	1.38	1.15	1.16	1.71	1.21	1.64	2.37	1.62	1.70	1.15	1.64	2.73	2.55	2.37	1.18

Major Oxide	1232A-16X-1W-41 >149									1232A-18X-1W-36 >149								
	G1	G2	G3	G4	G5	G6	G7	G8	G9	G1	G2	G3	G4	G5	G6	G7	G8	G9
wt%	53.88	53.15	54.23	53.15	50.93	57.66	55.72	55.79	53.98	59.16	51.64	53.96	51.63	55.52	56.49	55.03	53.80	57.50
TiO_2	2.07	1.92	1.37	1.75	3.21	1.26	2.76	1.59	1.61	1.25	1.26	1.89	1.80	1.74	1.81	1.74	2.09	1.72
Al_2O_3	13.99	14.24	14.30	13.38	12.60	14.20	13.85	15.73	14.01	15.44	13.93	12.92	13.82	13.85	13.75	14.31	14.54	13.87
FeO	11.09	11.69	11.76	12.58	13.81	8.55	9.44	9.92	11.61	7.07	10.64	13.42	11.48	11.24	11.21	12.04	11.32	11.45
MgO	4.87	5.18	3.98	4.12	3.99	3.14	3.90	3.87	4.70	1.92	5.53	3.15	5.58	3.89	3.19	3.39	3.72	2.31
CaO	7.58	8.27	8.16	8.34	8.61	6.86	8.54	6.77	8.00	6.23	10.78	7.82	9.89	7.05	6.70	7.68	7.91	5.50
Na_2O	4.97	4.30	3.92	4.55	3.68	6.62	3.07	4.63	4.38	5.95	4.98	4.46	4.04	4.99	4.71	3.35	4.30	4.65
K_2O	1.22	1.11	1.19	1.30	1.45	1.30	1.59	1.05	1.29	2.04	0.85	1.71	0.99	1.29	1.56	1.02	1.14	1.82

Major Oxide	1232B-1H-2W-56 >149						1232B-4H-1W-89 >149									
	G5	G6	G7	G8	G9	G10	G1	G2	G3	G4	G5	G6	G7	G8	G9	G10
wt%	49.34	55.01	61.90	50.66	54.17	54.54	59.66	61.93	54.74	59.09	54.34	54.12	54.99	58.91	58.12	53.83
TiO_2	1.33	1.60	1.67	1.80	1.98	1.57	1.79	1.15	2.11	2.01	2.18	1.77	1.86	2.05	1.88	1.78
Al_2O_3	24.53	17.43	14.98	23.11	15.13	17.96	13.85	13.84	14.10	13.76	14.03	14.97	14.59	14.48	12.45	14.46
FeO	8.86	9.57	8.31	8.86	11.13	9.76	8.64	7.90	11.67	8.41	11.14	10.19	10.83	9.69	11.85	11.28
MgO	2.35	3.21	1.28	2.70	3.09	3.22	1.76	1.37	3.21	1.65	4.14	4.01	3.97	2.28	1.69	3.89
CaO	6.37	6.95	4.89	6.64	7.92	6.78	5.50	5.01	8.96	5.66	7.94	9.40	7.82	5.96	6.56	7.47
Na_2O	5.12	4.74	4.03	4.16	4.47	4.26	4.95	5.30	3.27	5.49	4.36	4.09	4.27	4.81	3.91	5.09
K_2O	1.40	1.16	2.13	1.49	1.46	1.45	2.44	2.48	1.01	2.65	1.38	1.13	1.12	1.71	2.09	1.31

Major Oxide	1232B-5H-5W-80 >149										1232B-6H-7W-33 >149									
	G1	G2	G3	G4	G5	G6	G7	G8	G9	G10	G1	G2	G3	G4	G5	G6	G7	G8	G9	G10
wt%	62.63	55.70	55.25	51.82	65.49	52.08	56.07	55.74	56.39	55.41	56.52	56.63	55.31	53.49	56.24	55.65	55.24	52.75	57.60	53.59
TiO_2	1.30	1.90	2.87	1.86	1.02	1.89	2.28	1.52	1.78	1.66	2.13	1.86	1.83	2.94	1.87	1.51	1.24	2.10	1.61	2.01
Al_2O_3	14.02	15.69	14.14	20.38	19.75	17.63	14.25	14.62	14.65	17.15	13.38	14.87	13.86	13.57	13.78	15.64	14.64	13.99	14.21	14.40
FeO	8.27	9.25	10.94	10.15	2.00	9.56	9.92	10.87	9.84	10.52	12.49	9.82	11.36	11.45	11.39	9.67	9.61	11.66	9.80	10.71
MgO	1.19	3.92	2.56	2.67	0.50	3.88	3.42	3.35	3.05	2.11	1.69	3.29	3.95	3.90	2.89	3.18	4.89	4.09	2.35	4.68
CaO	4.88	6.79	6.79	7.41	1.96	9.21	7.71	8.41	6.75	6.03	7.27	7.48	7.49	7.86	7.46	8.09	9.56	8.40	6.95	7.66
Na_2O	3.98	5.09	4.95	3.43	5.82	3.73	3.97	3.42	5.29	3.96	3.20	4.12	4.62	4.83	4.35	4.53	3.62	4.67	4.89	5.18
K_2O	3.23	1.26	1.83	1.63	3.15	1.25	1.68	1.54	1.63	2.29	2.59	1.44	1.28	1.28	1.48	1.35	0.95	1.34	1.70	1.07

Major Oxide	1232B-7H-2W-68 >149										1232B-7H-3W-90 >149									
	G1	G2	G3	G4	G5	G6	G7	G8	G9	G10	G1	G2	G3	G4	G5	G6	G7	G8	G9	G10
wt%	54.12	58.28	55.68	53.52	54.89	58.46	53.73	54.34	53.28	54.87	55.93	55.00	54.16	68.17	58.99	55.67	57.27	53.99	58.65	56.82
TiO_2	2.57	1.89	2.29	2.50	2.30	1.28	1.98	2.12	2.51	2.56	2.42	1.98	2.02	1.19	2.12	1.78	1.39	2.46	1.47	2.36
Al_2O_3	13.24	14.34	13.54	13.68	13.39	14.56	13.31	13.71	13.68	13.37	11.98	13.16	13.99	15.23	13.73	14.73	13.88	12.90	14.31	13.83
FeO	12.37	10.23	10.47	12.38	11.43	8.88	12.70	11.89	12.16	11.81	13.25	12.15	11.29	4.76	9.84	10.01	10.25	13.04	9.35	9.89
MgO	3.51	2.33	2.78	4.02	3.41	2.62	3.46	3.92	3.64	3.41	2.35	3.03	3.70	0.93	2.49	3.89	2.92	3.62	2.43	2.81
CaO	8.00	6.65	6.89	7.67	7.43	7.19	7.87	7.34	7.75	7.47	6.70	7.18	8.69	2.75	6.12	7.35	7.17	7.69	6.87	6.47
Na_2O	3.95	3.11	5.68	4.43	4.90	4.87	4.47	4.65	4.93	4.32	3.94	5.51	4.79	4.44	3.54	4.82	4.49	4.07	4.41	4.62
K_2O	1.45	1.92	1.86	1.40	1.64	1.59	1.53	1.42	1.38	1.53	2.09	1.50	0.97	2.44	2.13	1.13	1.83	1.33	1.73	2.01

Major Oxide	1232B-10H-7W-23 >149									
	G1	G2	G3	G4	G5	G6	G7	G8	G9	G10
wt%	55.46	51.88	53.76	50.61	55.08	53.74	54.69	53.77	54.48	53.51
TiO_2	1.78	2.08	2.63	1.56	1.75	2.01	2.43	2.02	2.02	1.55
Al_2O_3	15.02	19.13	15.30	12.63	13.92	13.80	16.69	14.92	13.44	15.55
FeO	10.54	11.23	10.66	15.79	11.95	12.14	10.47	10.97	11.87	11.68
MgO	3.90	3.31	3.54	3.79	4.14	3.57	3.60	4.23	3.40	3.87
CaO	7.63	6.93	7.60	10.27	7.09	8.43	7.29	7.88	8.41	7.79
Na_2O	4.47	3.94	4.44	3.70	4.28	4.37	3.30	4.56	4.04	4.41
K_2O	0.91	1.09	1.44	1.16	1.41	1.33	1.07	1.19	1.54	1.25

Table 5: Table 5: All SEM and EPMA major and LA-ICP-MS trace element data for >210 micron glass and pumice particles in ODP Site 1232 turbidites

	1232A-4H-2W-33 >210									
Major oxide (wt.%)										
	G1	G2	G3	G4	G5	G6	G7	G8	G9	G10
SiO_2	54.04	61.49	58.97	57.72	56.33	52.77	53.17	57.23	54.18	56.84
TiO_2 LA-ICP-MS	1.86	1.23	1.55	2.08	2.75	2.35	1.93	2.07	2.29	2.81
TiO_2 SEM	1.70	1.23	1.30	2.21	1.97	1.83	1.87	2.31	1.34	2.38
Al_2O_3	14.06	14.77	14.39	14.66	14.44	13.43	14.06	15.00	12.51	13.32
FeO	10.71	6.40	7.70	9.64	9.83	12.53	12.03	10.19	12.22	11.68
MgO	3.82	2.32	1.95	2.48	2.85	3.31	3.52	2.33	3.38	2.40
CaO	9.65	5.49	6.15	6.05	6.46	8.79	6.97	6.00	8.64	6.26
Na_2O	4.05	5.53	6.95	5.34	5.33	5.00	6.43	4.98	4.95	4.46
K_2O	1.21	2.18	1.73	1.44	1.39	1.22	1.28	1.59	1.22	1.62
Trace element (ppm)										
Sc	49.59		26.68	34.61	38.84	53.55	37.65	32.23	50.11	
Ti	11108.05		9282.90	12390.66	16610.27	14094.83	11574.77	12330.09	13835.06	
V	396.85		85.36	195.36	211.25	491.34	402.80	188.47	555.54	
Cr	65.26		28.27	4.74	6.41	39.01	36.88	2.64	29.70	
Fe	58142.74		37394.55	46887.27	58063.68	62255.25	49742.65	46726.75	63718.63	
Ni	22.60		0.78	0.33	2.78	13.47	23.49	0.32	17.19	
Cs	2.39		2.65	2.30	3.23	2.05	1.96	2.49	2.00	
Rb	33.63		38.68	37.42	46.87	30.69	30.07	39.35	29.63	
Ba	370.39		469.06	473.40	549.87	409.46	346.61	474.63	387.35	
Th	4.08		5.32	5.25	6.47	4.19	3.56	5.17	3.69	
U	1.15		1.48	1.37	1.72	1.15	1.07	1.47	1.11	
Nb	4.71		6.19	6.85	7.76	5.54	4.54	6.92	5.24	
Ta	0.30		0.37	0.41	0.52	0.35	0.28	0.42	0.29	
La	17.64		23.49	25.52	31.57	21.34	17.75	25.60	19.02	
Ce	41.73		54.09	58.53	74.39	49.27	40.64	60.14	46.00	
Pb	15.65		18.62	14.81	18.83	14.00	13.12	16.28	13.52	
Pr	5.61		7.35	7.82	9.88	6.68	5.42	7.87	6.11	
Sr	483.97		391.77	392.83	362.11	414.95	325.62	392.14	413.40	
Nd	25.46		33.25	34.82	46.96	30.12	25.40	35.58	27.94	
Sm	6.29		7.97	7.98	11.46	7.89	5.90	8.32	6.74	
Zr	157.05		189.44	207.54	236.25	174.42	147.83	205.58	149.17	
Hf	4.54		5.23	5.69	6.78	4.85	3.90	5.70	4.23	
Eu	1.77		2.12	2.29	2.96	2.17	1.63	2.20	2.01	
Gd	6.73		7.84	8.57	11.73	8.30	6.26	8.52	6.79	
Tb	1.05		1.21	1.23	1.75	1.24	0.96	1.27	1.01	
Dy	6.89		8.46	8.79	11.36	8.14	6.26	8.42	6.99	
Y	37.70		45.10	46.84	59.49	44.64	34.82	45.62	36.68	
Ho	1.45		1.70	1.77	2.19	1.68	1.31	1.74	1.47	
Er	4.23		4.81	5.16	6.60	4.88	3.75	5.07	4.08	
Yb	4.21		4.72	5.11	6.10	4.89	3.77	5.02	4.22	
Lu	0.65		0.74	0.77	0.93	0.76	0.56	0.73	0.62	
Ba/La	21.00		19.97	18.55	17.42	19.19	19.53	18.54	20.37	
La/Sm	2.81		2.95	3.20	2.75	2.70	3.01	3.08	2.82	
La/Yb	4.19		4.98	5.00	5.18	4.37	4.71	5.10	4.51	
La/Nb	3.75		3.79	3.72	4.07	3.85	3.91	3.70	3.63	
Zr/Nb	33.38		30.60	30.30	30.44	31.51	32.56	29.71	28.49	
Zr/Hf	34.63		36.26	36.47	34.85	35.96	37.90	36.10	35.26	
Ba/Th	90.78		88.17	90.17	84.99	97.84	97.50	91.80	105.11	
Rb/Ba	0.09		0.08	0.08	0.09	0.07	0.09	0.08	0.08	
Nb/Yb	1.12		1.31	1.34	1.27	1.13	1.21	1.38	1.24	
Ba/Yb	88.08		99.38	92.73	90.14	83.82	92.06	94.55	91.79	
Th/Yb	0.97		1.13	1.03	1.06	0.86	0.94	1.03	0.87	
Th/La	0.20		0.27	0.26	0.32	0.21	0.18	0.26	0.18	

	1232A-5H-7W-45 >210									
Major oxide (wt.%)										
	G1	G2	G3	G4	G5	G6	G7	G8	G9	G10
SiO_2	56.14	58.10	72.67	64.22	55.53	55.95	63.98	72.18	56.01	60.90
TiO_2 LA-ICP-MS	1.96	1.74	0.36	1.21	2.33	2.33	1.32	0.43	1.96	1.34
TiO_2 SEM	1.98	1.75	0.36	1.22	2.35	2.35	1.33	0.43	1.97	1.35
Al_2O_3	15.54	19.08	13.79	15.34	14.53	16.13	14.03	13.68	14.68	16.35
FeO	9.48	7.57	2.73	6.36	11.09	9.66	7.00	2.65	10.81	8.95
MgO	4.23	2.51	0.37	1.62	4.14	3.48	1.49	0.36	3.86	1.55
CaO	6.65	5.54	1.67	3.99	7.18	6.19	4.87	1.41	6.59	5.11
Na_2O	3.79	3.38	4.53	3.94	3.54	4.24	4.66	4.74	4.23	3.48
K_2O	1.61	1.47	3.29	2.70	1.06	1.41	2.06	3.96	1.26	1.73
Trace element (ppm)										
Sc	39.86			56.89					45.05	35.72
Ti										
V	302.57			481.28					449.46	59.12
Cr	28.60			10.08					14.69	12.83
Fe										
Ni	22.31			14.24					17.07	1.58
Cs	2.86			2.32					2.22	4.36
Rb	40.50			33.19					33.58	66.01
Ba	472.08			449.10					443.70	800.46
Th	5.47			5.67					4.58	10.06
U	1.38			1.12					1.13	2.37
Nb	7.65			6.55					6.43	11.15
Ta	0.46			0.43					0.36	0.82
La	26.27			25.12					22.36	38.68
Ce	57.70			51.52					49.38	86.94
Pb	14.41			12.09					13.09	24.33
Pr	8.25			7.61					6.80	11.57
Sr	343.59			375.64					344.39	403.98
Nd	37.39			36.25					29.19	51.93
Sm	8.78			10.51					7.49	12.99
Zr	200.64			218.43					174.84	316.70
Hf	5.63			6.47					5.52	9.41
Eu	2.28			2.36					2.37	3.14
Gd	8.68			10.76					8.87	11.64
Tb	1.34			1.49					1.21	1.91
Dy	8.84			10.41					7.65	12.26
Y	47.55			53.07					43.93	70.44
Ho	1.78			2.01					1.65	2.40
Er	4.88			6.27					4.91	7.01
Yb	4.91			6.29					4.68	8.15
Lu	0.74			0.87					0.71	1.06
Ba/La	17.97			17.88					19.84	20.69
La/Sm	2.99			2.39					2.99	2.98
La/Yb	5.35			3.99					4.78	4.75
La/Nb	3.44			3.84					3.48	3.47
Zr/Nb	26.24			33.37					27.19	28.42
Zr/Hf	35.64			33.76					31.67	33.66
Ba/Th	86.30			79.21					96.88	79.57
Rb/Ba	0.09			0.07					0.08	0.08
Nb/Yb	1.56			1.04					1.37	1.37
Ba/Yb	96.15			71.40					94.81	98.22
Th/Yb	1.11			0.90					0.98	1.23
Th/La	0.27			0.28					0.23	0.50

	1232A-6H-4W-85 >210								
Major oxide (wt.%)									
	G1	G2	G3	G4	G5	G6	G7	G8	G9
SiO_2	53.12	57.08	54.09	55.20	54.91	55.03	52.96	55.35	61.46
TiO_2 LA-ICP-MS	2.81	1.88	2.12	1.35	1.62	2.91	1.51	2.11	1.80
TiO_2 SEM	2.16	1.58	2.11	1.51	2.54	1.55	2.18	2.77	1.62
Al_2O_3	13.62	13.51	12.55	14.98	13.42	14.43	13.70	13.31	13.59
FeO	12.96	10.92	13.34	10.65	12.26	9.06	13.36	11.15	8.43
MgO	3.90	2.72	2.69	2.79	3.13	3.53	3.17	3.11	1.34
CaO	7.62	7.16	7.71	6.82	7.42	8.66	8.72	8.12	5.28
Na_2O	4.71	4.58	4.51	5.76	5.35	3.89	4.32	4.46	5.11
K_2O	1.30	1.55	2.39	1.83	1.28	1.90	1.67	1.79	2.38
Trace element (ppm)									
Sc	46.48	38.69		32.37	37.15	56.69	43.69	40.80	32.98
Ti	16864.52	11262.70		8096.59	9542.87	17648.01	8992.38	12542.81	10743.50
V	476.39	271.22		311.17	292.49	556.14	354.26	333.28	286.05
Cr	8.63	1.60		24.44	20.83	6.94	78.69	16.77	1.92
Fe	65387.85	54426.67		39581.95	51487.11	76897.97	49157.85	60679.21	48120.73
Ni	11.47	3.62		6.91	4.36	11.43	22.74	15.15	5.18
Cs	2.49	5.16		1.89	3.03	2.76	1.46	3.57	2.30
Rb	35.01	76.19		27.24	45.95	42.20	20.34	49.56	34.96
Ba	382.72	687.43		288.52	422.73	464.63	271.59	488.30	415.67
Th	4.31	9.23		3.41	5.13	5.34	2.48	6.01	4.41
U	1.22	2.67		0.96	1.36	1.49	0.68	1.71	1.23
Nb	5.62	9.15		3.81	5.20	6.81	3.37	6.66	5.59
Ta	0.36	0.59		0.24	0.34	0.43	0.16	0.43	0.34
La	20.45	31.95		14.79	21.14	24.80	12.15	23.99	21.07
Ce	49.04	73.90		33.37	48.20	57.27	28.96	56.24	49.71
Pb	13.86	25.40		11.67	25.63	28.94	12.83	20.50	14.34
Pr	6.64	9.38		4.36	6.54	7.79	3.87	7.48	6.59
Sr	369.91	430.93		346.37	402.18	459.82	407.43	410.34	299.90
Nd	30.72	40.37		19.46	28.77	35.89	18.03	33.59	29.95
Sm	7.68	9.33		4.47	7.07	9.21	4.63	8.35	7.14
Zr	169.46	295.92		118.62	178.74	200.11	102.32	205.71	162.72
Hf	4.76	7.97		3.27	4.91	5.63	2.65	5.84	4.39
Eu	2.19	2.36		1.34	1.81	2.62	1.41	2.29	2.01
Gd	7.96	9.70		4.89	7.65	9.55	4.38	8.58	7.37
Tb	1.23	1.43		0.74	1.16	1.43	0.78	1.30	1.11
Dy	8.21	9.88		4.96	7.98	9.65	4.76	9.01	7.00
Y	43.51	55.35		26.82	40.70	50.66	25.60	47.46	38.40
Ho	1.68	2.14		1.03	1.51	1.92	0.97	1.79	1.44
Er	4.67	6.00		3.02	4.41	5.54	3.01	5.28	4.16
Yb	4.60	6.45		3.04	4.57	5.43	2.79	5.44	4.14
Lu	0.69	0.94		0.43	0.67	0.81	0.39	0.81	0.64
Ba/La	18.71	21.52		19.51	20.00	18.74	22.35	20.35	19.73
La/Sm	2.66	3.42		3.31	2.99	2.69	2.63	2.87	2.95
La/Yb	4.45	4.95		4.87	4.63	4.57	4.35	4.41	5.10
La/Nb	3.64	3.49		3.89	4.07	3.64	3.61	3.60	3.77
Zr/Nb	30.15	32.36		31.17	34.41	29.41	30.41	30.89	29.11
Zr/Hf	35.60	37.15		36.33	36.44	35.54	38.61	35.22	37.07
Ba/Th	88.90	74.48		84.61	82.40	87.09	109.51	81.32	94.36
Rb/Ba	0.09	0.11		0.09	0.11	0.09	0.07	0.10	0.08
Nb/Yb	1.22	1.42		1.25	1.14	1.25	1.21	1.22	1.35
Ba/Yb	83.20	106.58		94.91	92.60	85.57	97.34	89.76	100.52
Th/Yb	0.94	1.43		1.12	1.12	0.98	0.89	1.10	1.07
Th/La	0.22	0.46		0.17	0.26	0.27	0.12	0.30	0.22

	1232A-6H-6W-118 >210							
Major oxide (wt.%)								
	G2	G4	G5	G6	G7	G8	G9	G10
SiO_2	56.34	58.46	55.87	63.94	56.82	55.15	58.09	54.44
TiO_2 LA-ICP-MS	2.09	2.65	2.80	1.40	2.47	1.95	1.78	2.35
TiO_2 SEM	2.10	2.66	2.82	1.41	2.48	1.96	1.79	2.37
Al_2O_3	14.58	14.67	13.91	16.02	13.95	14.77	14.72	14.01
FeO	10.06	8.37	11.49	6.09	10.36	10.09	8.81	11.72
MgO	3.65	2.89	3.31	1.15	3.70	4.73	3.84	4.52
CaO	6.93	5.80	7.21	4.65	7.21	7.08	5.88	7.06
Na_2O	4.34	4.68	3.47	4.13	3.68	4.37	4.52	4.28
K_2O	1.41	1.88	1.33	2.02	1.23	1.26	1.76	1.01
Trace element (ppm)								
Sc		39.06	36.59		39.71	46.99	45.01	
Ti								
V		220.78	326.42		318.74	341.26	337.40	
Cr		8.50	11.59		7.07	24.47	14.21	
Fe								
Ni		2.09	3.29		4.27	9.40	5.95	
Cs		2.21	1.89		1.68	1.89	2.37	
Rb		36.98	28.30		26.61	27.69	40.93	
Ba		529.39	404.97		396.27	357.82	562.84	
Th		5.87	4.13		4.38	4.50	6.13	
U		1.36	0.95		0.99	0.96	1.56	
Nb		7.75	6.03		5.81	5.43	7.91	
Ta		0.37	0.36		0.36	0.40	0.42	
La		29.67	20.14		21.56	21.11	30.55	
Ce		64.75	46.04		44.03	43.79	64.11	
Pb		13.71	10.20		10.57	9.82	14.94	
Pr		8.84	6.19		6.37	6.46	8.53	
Sr		359.44	320.44		322.46	363.99	392.32	
Nd		43.65	28.64		32.43	32.06	38.88	
Sm		9.29	6.58		7.10	7.35	9.20	
Zr		207.47	148.38		168.34	173.19	223.93	
Hf		4.71	4.63		4.90	4.70	6.57	
Eu		2.59	2.09		2.13	2.17	2.65	
Gd		9.87	7.25		7.44	8.66	10.28	
Tb		1.41	1.06		1.17	1.23	1.49	
Dy		11.07	7.11		7.54	8.40	9.29	
Y		49.33	36.71		41.80	45.69	52.56	
Ho		1.92	1.38		1.62	1.68	1.94	
Er		6.02	4.17		4.67	4.93	6.00	
Yb		5.30	4.20		4.78	4.76	5.19	
Lu		0.84	0.53		0.64	0.75	0.77	
Ba/La		17.85	20.11		18.38	16.95	18.42	
La/Sm		3.19	3.06		3.04	2.87	3.32	
La/Yb		5.60	4.80		4.51	4.44	5.89	
La/Nb		3.83	3.34		3.71	3.89	3.86	
Zr/Nb		26.77	24.61		28.97	31.90	28.33	
Zr/Hf		44.05	32.08		34.39	36.89	34.11	
Ba/Th		90.26	98.05		90.57	79.51	91.82	
Rb/Ba		0.07	0.07		0.07	0.08	0.07	
Nb/Yb		1.46	1.44		1.22	1.14	1.52	
Ba/Yb		99.98	96.54		82.99	75.25	108.55	
Th/Yb		1.11	0.98		0.92	0.95	1.18	
Th/La		0.29	0.21		0.22	0.23	0.31	

	1232A-7H-2W-86 >210								
Major oxide (wt.%)									
	G1	G2	G3	G4	G5	G6	G7	G8	G9
SiO_2	66.61	52.84	57.81	49.43	49.10	64.34	54.99	58.40	62.42
TiO_2 LA-ICP-MS	1.11	1.17	1.92	2.93	2.42	1.12	1.88	1.64	1.28
TiO_2 SEM	0.73	0.94	1.74	1.95	1.32	1.03	1.92	1.34	1.07
Al_2O_3	14.32	14.01	14.52	12.34	12.20	14.33	14.05	11.78	13.76
FeO	3.32	8.78	9.82	15.92	14.62	6.00	9.68	10.89	7.42
MgO	0.67	4.63	2.02	2.31	3.09	1.04	3.03	1.70	1.26
CaO	3.43	11.01	6.35	9.94	11.03	3.89	8.02	6.39	5.20
Na_2O	6.77	5.84	5.19	4.54	5.73	5.66	6.54	5.79	6.07
K_2O	3.17	1.11	1.79	1.99	1.20	3.01	1.21	2.82	1.99
Trace element (ppm)									
Sc	19.84	41.23	37.21	58.25	56.96	22.20	43.64	31.82	23.64
Ti	6666.57	6966.51	11484.07	17622.47	14612.15	6709.51	11255.98	9697.19	7650.38
V	36.80	306.56	364.75	516.73	542.81	71.75	391.48	160.64	55.63
Cr	10.81	151.18	11.51	3.72	26.73	3.89	30.76	5.71	45.73
Fe	28017.49	50762.42	57251.62	83162.98	80587.13	30886.87	59810.33	47160.97	35714.58
Ni	0.91	48.81	7.62	11.43	12.38	0.54	11.01	4.27	1.54
Cs	4.91	0.99	3.02	3.78	2.82	4.71	2.45	5.52	3.19
Rb	79.07	16.01	45.34	55.69	40.93	74.88	34.12	90.74	49.32
Ba	677.45	241.64	431.85	656.47	472.89	623.76	369.56	720.99	556.06
Th	9.08	2.41	5.36	7.49	4.89	8.92	3.80	9.57	6.80
U	2.51	0.58	1.55	2.12	1.41	2.42	1.05	2.77	1.79
Nb	9.16	2.57	6.29	8.35	6.24	8.73	4.89	9.48	7.02
Ta	0.58	0.16	0.38	0.56	0.36	0.54	0.30	0.60	0.42
La	31.85	10.57	21.64	32.59	22.29	30.61	17.73	34.57	27.99
Ce	72.72	24.56	52.04	76.61	52.93	70.46	39.74	79.11	59.84
Pb	30.65	7.47	15.72	24.19	16.52	24.31	17.52	30.40	19.51
Pr	9.26	3.21	6.68	10.28	7.06	9.18	5.12	10.28	7.81
Sr	265.14	470.95	327.73	567.45	555.87	268.90	403.66	396.20	334.34
Nd	39.76	14.71	30.71	46.35	33.10	39.30	27.42	44.63	34.84
Sm	9.21	3.58	7.37	10.80	8.18	9.68	6.88	10.08	8.48
Zr	303.17	76.88	194.09	269.47	190.14	284.83	153.19	308.19	236.31
Hf	7.80	2.19	5.29	7.61	5.56	7.79	4.10	8.46	6.37
Eu	1.99	1.17	1.86	3.13	2.47	1.96	1.85	2.60	2.09
Gd	9.49	3.67	7.53	11.44	8.47	8.88	6.27	10.70	8.35
Tb	1.43	0.57	1.17	1.78	1.33	1.49	0.97	1.60	1.30
Dy	9.74	3.82	7.56	11.59	8.74	10.20	7.25	10.82	8.73
Y	53.47	20.31	41.31	63.86	47.70	54.48	37.58	59.74	48.74
Ho	1.98	0.78	1.57	2.48	1.79	2.00	1.39	2.25	1.72
Er	5.59	2.32	4.45	7.02	5.40	6.01	4.13	6.46	5.14
Yb	6.13	2.30	4.55	7.09	5.33	6.38	4.16	7.05	5.67
Lu	0.88	0.32	0.71	1.10	0.79	0.94	0.63	1.05	0.82
Ba/La	21.27	22.86	19.96	20.15	21.22	20.38	20.84	20.86	19.87
La/Sm	3.46	2.95	2.94	3.02	2.72	3.16	2.58	3.43	3.30
La/Yb	5.20	4.61	4.76	4.60	4.18	4.80	4.26	4.90	4.94
La/Nb	3.48	4.11	3.44	3.90	3.57	3.51	3.63	3.65	3.99
Zr/Nb	33.10	29.91	30.86	32.27	30.47	32.63	31.33	32.53	33.66
Zr/Hf	38.87	35.19	36.69	35.43	34.23	36.59	37.36	36.45	37.10
Ba/Th	74.65	100.47	80.64	87.70	96.80	69.93	97.25	75.38	81.77
Rb/Ba	0.12	0.07	0.10	0.08	0.09	0.12	0.09	0.13	0.09
Nb/Yb	1.50	1.12	1.38	1.18	1.17	1.37	1.18	1.34	1.24
Ba/Yb	110.60	105.29	95.02	92.59	88.81	97.84	88.84	102.27	98.16
Th/Yb	1.48	1.05	1.18	1.06	0.92	1.40	0.91	1.36	1.20
Th/La	0.45	0.12	0.27	0.37	0.24	0.45	0.19	0.48	0.34

	1232A-7H-5W-87 >210									
Major oxide (wt.%)										
	G1	G2	G3	G4	G5	G6	G7	G8	G9	G10
SiO_2	60.32	58.01	57.27	56.74	56.29	59.14	58.81	59.29	60.43	64.91
TiO_2 LA-ICP-MS	1.75	1.85	1.70	1.74	1.55	1.84	1.59	1.64	1.45	1.01
TiO_2 SEM	1.13	2.03	1.52	1.69	1.58	1.48	1.55	1.22	1.54	1.01
Al_2O_3	14.37	13.81	14.38	15.09	14.81	14.28	15.12	14.15	14.52	14.70
FeO	7.77	10.56	9.65	9.29	10.34	9.14	8.69	8.79	9.18	6.14
MgO	1.95	2.60	2.26	2.96	2.77	1.78	2.49	1.87	1.82	0.70
CaO	5.97	6.40	6.68	7.19	6.69	6.38	5.99	5.69	5.43	3.07
Na_2O	5.47	4.65	5.72	4.85	4.38	5.30	5.19	6.11	4.83	6.59
K_2O	1.80	1.51	1.74	1.54	2.57	1.56	1.53	1.85	1.74	2.28
Trace element (ppm)										
Sc	31.28	37.15	42.66	37.58	31.50	33.39	31.40	29.69	28.82	
Ti	10526.16	11022.18	10175.27	10421.37	9263.40	10993.41	9531.74	9814.60	8647.15	
V	113.04	318.47	239.82	289.59	175.41	122.00	191.37	102.19	142.63	
Cr	3.88	0.88	4.00	9.31	1.69	1.38	3.57	7.31	9.57	
Fe	50116.22	54041.95	50175.17	55073.83	48476.05	53909.79	47589.51	46977.10	43591.31	
Ni	0.30	6.86	1.39	5.31	3.17	0.59	2.45	0.53	3.31	
Cs	3.43	2.36	2.06	2.65	5.35	3.37	2.84	2.87	3.12	
Rb	49.27	34.59	30.12	38.26	101.05	48.00	39.21	42.93	42.55	
Ba	556.16	421.27	357.85	455.32	696.40	570.46	467.36	522.71	510.36	
Th	6.13	4.85	3.99	5.11	9.53	6.52	5.27	5.87	5.65	
U	1.67	1.35	1.13	1.47	2.66	1.82	1.50	1.60	1.58	
Nb	7.30	5.59	4.55	5.74	9.18	7.30	5.88	6.61	6.28	
Ta	0.44	0.35	0.28	0.36	0.62	0.46	0.37	0.41	0.36	
La	26.86	20.98	17.21	21.19	33.90	28.27	21.92	25.97	24.09	
Ce	63.42	49.30	40.79	49.65	78.21	65.37	51.94	60.52	54.72	
Pb	21.75	15.25	12.95	17.05	27.29	22.87	16.62	18.44	22.39	
Pr	8.34	6.51	5.49	6.52	9.96	8.72	6.85	7.91	7.35	
Sr	443.33	357.89	311.79	426.92	440.81	470.05	389.69	424.11	365.29	
Nd	38.45	29.44	25.58	29.81	45.19	40.89	30.23	37.09	32.35	
Sm	9.13	7.30	6.41	7.25	10.46	9.60	7.34	9.03	7.84	
Zr	214.44	168.05	141.91	175.84	302.32	227.20	177.71	202.85	199.50	
Hf	5.98	4.75	3.93	4.92	8.47	6.30	5.00	5.53	5.64	
Eu	2.53	1.97	1.75	2.06	2.40	2.61	2.05	2.38	1.93	
Gd	9.13	7.51	6.51	7.21	10.59	9.90	7.47	9.05	7.55	
Tb	1.38	1.12	0.99	1.11	1.59	1.53	1.15	1.32	1.08	
Dy	9.31	7.55	6.81	7.62	11.07	10.04	7.66	8.87	8.26	
Y	49.62	40.14	35.76	40.58	59.63	54.56	40.90	48.25	43.54	
Ho	1.88	1.57	1.38	1.58	2.26	2.06	1.55	1.84	1.62	
Er	5.40	4.34	3.96	4.51	6.65	6.03	4.43	5.38	4.70	
Yb	5.64	4.42	4.01	4.60	6.84	6.09	4.62	5.24	4.87	
Lu	0.82	0.66	0.57	0.68	1.06	0.90	0.69	0.80	0.72	
Ba/La	20.71	20.08	20.79	21.49	20.55	20.18	21.32	20.13	21.19	
La/Sm	2.94	2.88	2.69	2.92	3.24	2.94	2.99	2.88	3.07	
La/Yb	4.76	4.75	4.30	4.61	4.96	4.65	4.74	4.96	4.95	
La/Nb	3.68	3.75	3.79	3.69	3.69	3.87	3.73	3.93	3.84	
Zr/Nb	29.40	30.06	31.22	30.63	32.95	31.14	30.25	30.69	31.77	
Zr/Hf	35.86	35.38	36.16	35.74	35.71	36.06	35.58	36.71	35.37	
Ba/Th	90.73	86.95	89.63	89.19	73.07	87.49	88.77	89.12	90.33	
Rb/Ba	0.09	0.08	0.08	0.08	0.15	0.08	0.08	0.08	0.08	
Nb/Yb	1.29	1.26	1.13	1.25	1.34	1.20	1.27	1.26	1.29	
Ba/Yb	98.61	95.31	89.35	99.09	101.89	93.75	101.16	99.85	104.80	
Th/Yb	1.09	1.10	1.00	1.11	1.39	1.07	1.14	1.12	1.16	
Th/La	0.31	0.24	0.20	0.26	0.48	0.33	0.26	0.29	0.28	

	1232A-7H-6W-42 >210								
Major oxide (wt.%)									
	G1	G2	G3	G4	G5	G6	G7	G8	G9
SiO_2	61.40	56.78	57.40	55.23	66.51	58.07	52.74	65.64	63.37
TiO_2 LA-ICP-MS	1.66	1.72	1.80	2.17	1.05	1.98	2.09	1.66	0.67
TiO_2 SEM	1.32	1.44	1.36	1.25	0.81	1.56	1.95	1.65	0.67
Al_2O_3	13.99	15.31	14.06	15.23	14.69	14.29	14.67	16.24	14.33
FeO	7.46	9.38	8.48	8.81	4.18	8.87	11.56	3.57	6.07
MgO	1.51	3.43	2.29	2.22	0.98	2.22	3.23	0.61	1.32
CaO	4.96	6.96	5.97	8.13	3.30	6.24	8.19	3.09	4.62
Na_2O	6.26	4.83	7.58	6.06	6.54	6.05	5.63	6.35	6.54
K_2O	2.16	0.99	1.83	1.54	2.15	1.68	1.28	2.25	2.47
Trace element (ppm)									
Sc	27.37	35.25	31.17	39.87	18.39	34.42	39.93		
Ti	9941.23	10300.20	10738.63	13118.23	6291.71	11875.47	12511.59		
V	78.06	348.03	188.97	339.01	66.52	134.99	399.66		
Cr	31.41	21.14	12.14	12.00	12.54	17.88	13.71		
Fe	42820.67	52074.38	49959.85	62554.08	28503.20	51924.35	62391.44		
Ni	1.07	8.15	3.64	6.15	0.90	0.78	8.73		
Cs	3.35	1.59	3.23	2.99	2.32	3.30	2.19		
Rb	51.16	24.28	43.75	43.27	33.80	49.37	31.54		
Ba	588.13	276.63	477.54	505.91	384.15	582.11	376.24		
Th	6.51	2.87	5.66	5.51	4.39	7.21	3.93		
U	1.70	0.76	1.44	1.56	1.15	1.79	1.16		
Nb	7.05	3.18	6.09	6.22	4.71	7.25	4.69		
Ta	0.45	0.22	0.37	0.39	0.28	0.49	0.29		
La	28.85	12.78	23.63	23.49	18.05	29.63	17.33		
Ce	62.34	29.35	53.67	54.54	39.97	65.17	41.28		
Pb	21.69	11.76	20.96	20.08	14.24	20.37	14.63		
Pr	8.37	4.06	6.92	7.00	5.25	8.72	5.45		
Sr	370.99	362.44	389.46	486.86	237.13	436.95	440.35		
Nd	36.57	18.21	32.38	32.13	23.17	39.05	24.61		
Sm	9.19	4.67	7.95	7.74	5.48	9.63	5.93		
Zr	238.67	103.77	195.64	196.16	153.89	242.94	136.20		
Hf	6.68	3.05	5.52	5.49	4.35	6.59	3.71		
Eu	2.12	1.43	2.05	2.29	1.47	2.60	1.81		
Gd	9.83	4.65	7.60	7.98	5.53	9.87	6.08		
Tb	1.36	0.73	1.15	1.22	0.83	1.55	0.89		
Dy	8.73	5.14	8.05	8.36	6.03	10.05	6.42		
Y	51.90	26.62	44.84	45.12	33.42	56.66	33.84		
Ho	1.88	0.97	1.69	1.69	1.24	2.03	1.26		
Er	5.35	2.97	4.87	4.85	3.61	5.99	3.70		
Yb	6.08	2.89	4.89	4.99	3.74	5.97	3.85		
Lu	1.02	0.46	0.73	0.76	0.58	0.93	0.58		
Ba/La	20.39	21.65	20.21	21.54	21.28	19.65	21.71		
La/Sm	3.14	2.74	2.97	3.04	3.29	3.08	2.92		
La/Yb	4.75	4.42	4.83	4.71	4.83	4.97	4.51		
La/Nb	4.09	4.02	3.88	3.78	3.84	4.09	3.70		
Zr/Nb	33.85	32.63	32.12	31.54	32.71	33.53	29.07		
Zr/Hf	35.73	34.02	35.47	35.76	35.38	36.89	36.76		
Ba/Th	90.34	96.55	84.37	91.90	87.51	80.79	95.86		
Rb/Ba	0.09	0.09	0.09	0.09	0.09	0.08	0.08		
Nb/Yb	1.16	1.10	1.25	1.25	1.26	1.21	1.22		
Ba/Yb	96.73	95.72	97.66	101.38	102.71	97.59	97.85		
Th/Yb	1.07	0.99	1.16	1.10	1.17	1.21	1.02		
Th/La	0.33	0.14	0.28	0.28	0.22	0.36	0.20		

	1232A-8H-1W-46 >210									
Major oxide (wt.%)										
	G1	G2	G3	G4	G5	G6	G7	G8	G9	G10
SiO_2	61.44	63.04	58.16	58.37	56.02	63.93	60.73	65.31	62.97	60.20
TiO_2 LA-ICP-MS	1.29	0.84	1.53	1.72	1.80	1.19	1.37	1.02	1.05	1.42
TiO_2 SEM	1.30	0.84	1.53	1.73	1.81	1.20	1.38	1.03	1.06	1.43
Al_2O_3	15.72	15.20	15.29	16.00	16.11	14.98	16.98	14.10	15.61	16.05
FeO	6.70	5.97	8.18	7.03	9.08	6.01	6.07	6.80	5.76	6.97
MgO	2.53	2.11	3.56	3.28	3.41	1.89	2.73	1.63	2.48	1.55
CaO	4.61	5.50	6.66	6.90	7.04	4.51	5.36	3.48	4.93	7.17
Na_2O	5.36	5.08	4.74	4.87	4.86	5.06	4.70	5.05	5.18	4.64
K_2O	1.75	1.66	1.28	1.23	1.09	1.82	1.45	1.99	1.42	1.40
Trace element (ppm)										
Sc		27.50	37.29	38.08			34.47	28.24		45.88
Ti										
V		144.76	257.37	294.75			235.06	36.08		246.33
Cr		11.08	14.02	11.23			10.30	21.85		88.46
Fe										
Ni		2.16	3.97	4.85			5.16	2.42		3.54
Cs		1.97	2.27	1.84			1.15	3.19		3.18
Rb		30.64	32.59	24.23			17.79	52.37		45.69
Ba		415.68	468.56	379.85			270.65	670.74		598.17
Th		4.98	4.60	3.98			3.52	9.19		7.51
U		1.05	1.35	1.00			0.68	1.90		1.76
Nb		5.44	6.06	4.82			3.55	8.97		8.29
Ta		0.44	0.37	0.21			0.23	0.64		0.59
La		19.15	22.22	17.44			14.41	32.37		28.32
Ce		42.17	51.05	39.78			28.30	71.42		63.59
Pb		13.32	13.14	9.44			7.30	20.01		17.83
Pr		6.13	6.53	5.35			4.05	9.57		8.38
Sr		313.55	433.75	418.75			315.18	282.80		449.94
Nd		25.56	31.97	24.84			21.62	46.40		42.62
Sm		6.25	6.90	5.63			5.78	9.73		10.09
Zr		167.41	170.06	137.08			112.72	273.60		242.76
Hf		4.45	4.43	4.17			2.69	7.78		6.38
Eu		1.64	2.22	1.59			1.46	2.45		2.59
Gd		6.29	7.36	5.94			5.26	10.22		10.01
Tb		1.08	1.03	1.08			0.72	1.56		1.45
Dy		6.68	7.25	5.86			4.83	11.24		9.73
Y		36.23	41.95	33.74			27.54	55.65		54.44
Ho		1.24	1.50	1.37			1.09	2.04		2.06
Er		4.15	4.64	3.65			2.65	5.75		6.06
Yb		4.28	5.15	3.60			3.16	6.05		6.34
Lu		0.65	0.57	0.56			0.50	0.97		0.79
Ba/La		21.71	21.09	21.78			18.78	20.72		21.13
La/Sm		3.07	3.22	3.10			2.49	3.33		2.81
La/Yb		4.48	4.32	4.84			4.56	5.35		4.47
La/Nb		3.52	3.67	3.62			4.06	3.61		3.42
Zr/Nb		30.77	28.09	28.47			31.80	30.52		29.30
Zr/Hf		37.62	38.39	32.87			41.98	35.19		38.08
Ba/Th		83.47	101.86	95.44			77.00	73.03		79.65
Rb/Ba		0.07	0.07	0.06			0.07	0.08		0.08
Nb/Yb		1.27	1.18	1.34			1.12	1.48		1.31
Ba/Yb		97.23	91.07	105.51			85.65	110.87		94.42
Th/Yb		1.16	0.89	1.11			1.11	1.52		1.19
Th/La		0.25	0.23	0.20			0.18	0.46		0.38

	1232A-10H-3W-25 >210								
Major oxide (wt.%)									
	G1	G2	G3	G4	G5	G6	G7	G8	G9
SiO_2	57.13	54.36	55.42	57.12	57.66	57.22	55.71	58.25	51.86
TiO_2 LA-ICP-MS	2.37	2.20	2.34	2.02	1.08	2.46	1.66	1.79	1.68
TiO_2 SEM	1.85	1.77	2.19	1.85	1.36	1.41	1.44	1.79	1.67
Al_2O_3	13.74	16.83	14.03	15.44	15.22	13.26	14.57	15.57	15.46
FeO	10.36	10.66	11.61	9.73	8.68	11.27	10.77	8.62	11.95
MgO	2.42	2.52	2.64	2.22	2.57	1.70	2.51	2.48	3.63
CaO	6.36	6.39	6.97	6.07	6.13	6.41	7.03	5.99	9.57
Na_2O	5.07	4.84	4.66	5.08	5.81	5.02	5.46	5.24	4.01
K_2O	1.94	1.60	1.73	1.72	2.24	2.06	1.71	1.45	1.25
Trace element (ppm)									
Sc	35.83	35.97	37.95	30.93	21.54	34.49	32.19		
Ti	14224.80	13219.76	13996.70	12119.47	6466.66	14791.91	9915.17		
V	251.02	264.62	291.33	208.94	187.26	125.01	300.40		
Cr	10.57	2.83	11.14	0.99	14.06	2.61	19.02		
Fe	63077.26	61038.61	62747.47	52562.22	32239.02	64689.74	48692.42		
Ni	5.64	2.15	4.06	0.56	9.96	0.85	10.00		
Cs	3.69	3.39	3.15	3.52	1.83	4.57	2.45		
Rb	54.85	48.38	46.74	51.22	27.51	66.03	36.17		
Ba	522.29	474.74	489.94	521.86	423.28	638.12	351.19		
Th	6.20	5.72	5.90	6.28	3.04	8.30	4.02		
U	1.79	1.61	1.62	1.81	1.44	2.27	1.10		
Nb	6.73	6.23	6.52	6.61	2.61	8.35	4.16		
Ta	0.41	0.35	0.40	0.42	0.17	0.51	0.25		
La	25.29	22.33	22.62	24.30	12.47	32.57	16.04		
Ce	60.25	52.54	52.61	57.76	28.44	76.69	36.49		
Pb	19.33	19.88	21.01	18.08	11.84	25.16	13.20		
Pr	7.94	6.91	6.96	7.32	3.68	10.06	4.84		
Sr	371.48	379.86	405.36	371.81	475.47	398.07	371.54		
Nd	35.51	31.41	31.12	32.96	16.57	46.73	21.90		
Sm	8.90	7.83	8.31	8.19	4.05	11.53	5.74		
Zr	205.18	186.86	189.41	202.05	96.88	257.51	136.03		
Hf	5.80	5.33	5.41	5.65	2.84	7.48	3.71		
Eu	2.27	2.08	2.13	2.13	1.17	2.87	1.51		
Gd	9.35	8.21	8.39	8.20	4.09	12.11	5.85		
Tb	1.40	1.25	1.23	1.21	0.64	1.75	0.86		
Dy	9.28	8.46	7.83	8.45	4.17	11.48	5.78		
Y	49.04	44.57	44.94	44.59	23.16	62.62	32.09		
Ho	1.94	1.70	1.71	1.69	0.87	2.44	1.23		
Er	5.50	4.86	5.05	4.97	2.45	6.81	3.47		
Yb	5.43	5.04	5.19	5.04	2.65	6.83	3.71		
Lu	0.78	0.76	0.80	0.78	0.37	1.00	0.55		
Ba/La	20.65	21.26	21.66	21.48	33.96	19.59	21.89		
La/Sm	2.84	2.85	2.72	2.97	3.08	2.82	2.80		
La/Yb	4.66	4.43	4.36	4.83	4.70	4.77	4.32		
La/Nb	3.76	3.58	3.47	3.68	4.79	3.90	3.86		
Zr/Nb	30.51	29.99	29.07	30.57	37.19	30.84	32.74		
Zr/Hf	35.38	35.09	35.01	35.76	34.17	34.45	36.67		
Ba/Th	84.24	83.07	83.04	83.10	139.24	76.93	87.47		
Rb/Ba	0.11	0.10	0.10	0.10	0.06	0.10	0.10		
Nb/Yb	1.24	1.24	1.26	1.31	0.98	1.22	1.12		
Ba/Yb	96.19	94.29	94.49	103.65	159.73	93.50	94.66		
Th/Yb	1.14	1.14	1.14	1.25	1.15	1.22	1.08		
Th/La	0.31	0.29	0.30	0.31	0.15	0.41	0.20		

	1232A-10H-3W-25 >210									
Major oxide (wt.%)										
	G1	G2	G3	G4	G5	G6	G7	G8	G9	G10
SiO_2	58.42	58.09	57.01	55.88	62.90	56.41	57.59	55.65	55.83	58.36
TiO_2 LA-ICP-MS	1.72	1.61	1.90	1.97	1.11	1.67	1.48	2.32	1.36	1.96
TiO_2 SEM	1.73	1.62	1.92	1.98	1.12	1.68	1.49	2.33	1.37	1.97
Al_2O_3	16.95	15.06	14.93	15.82	15.85	17.56	16.21	14.04	14.45	15.50
FeO	8.67	11.08	9.93	10.38	5.83	9.26	9.20	13.07	11.96	8.79
MgO	3.11	2.30	3.66	3.43	2.42	2.62	3.31	2.66	3.31	3.09
CaO	5.48	6.34	6.77	6.53	5.45	5.80	6.20	7.20	7.88	5.83
Na_2O	3.65	3.51	4.12	4.04	4.19	4.45	4.27	3.27	3.00	4.52
K_2O	1.40	1.41	1.07	1.35	1.66	1.62	1.13	1.19	1.60	1.36
Trace element (ppm)										
Sc	33.75	34.36			25.84	35.27	39.65		42.05	
Ti										
V	218.41	123.26			122.33	261.94	285.55		370.02	
Cr	7.20	10.00			16.82	18.79	16.53		28.97	
Fe										
Ni	1.09	1.37			3.12	8.46	5.81		16.43	
Cs	2.62	3.99			4.00	2.36	2.06		2.63	
Rb	37.87	58.60			57.96	30.18	31.10		41.00	
Ba	474.42	661.91			613.91	368.95	370.64		478.81	
Th	5.21	7.61			8.08	4.36	5.16		5.34	
U	1.46	2.12			2.02	1.00	1.01		1.34	
Nb	6.10	8.65			7.86	4.72	4.93		6.43	
Ta	0.31	0.52			0.56	0.44	0.42		0.29	
La	20.36	30.36			27.67	17.18	20.14		20.79	
Ce	49.61	74.86			58.98	36.27	38.40		49.02	
Pb	13.14	21.82			19.60	10.56	15.05		15.41	
Pr	6.62	9.83			8.00	5.13	5.04		6.53	
Sr	346.36	422.87			368.87	320.45	351.00		434.16	
Nd	30.19	43.00			35.84	23.92	27.25		29.63	
Sm	7.76	10.77			8.43	6.45	6.39		6.97	
Zr	162.73	226.71			234.29	145.19	172.33		162.09	
Hf	4.44	6.50			6.65	4.15	4.23		4.57	
Eu	1.94	2.52			2.15	1.82	1.80		2.14	
Gd	7.06	9.84			7.62	5.63	6.98		6.81	
Tb	1.09	1.65			1.24	0.83	0.90		1.14	
Dy	7.12	10.65			8.32	6.65	7.53		7.07	
Y	39.47	53.06			45.39	33.91	39.82		37.11	
Ho	1.49	1.95			1.82	1.14	1.58		1.39	
Er	4.28	5.96			5.28	3.36	4.62		4.32	
Yb	5.25	5.15			5.63	3.56	4.49		4.14	
Lu	0.57	0.93			0.85	0.53	0.66		0.66	
Ba/La	23.30	21.80			22.19	21.48	18.40		23.04	
La/Sm	2.63	2.82			3.28	2.66	3.15		2.98	
La/Yb	3.88	5.90			4.91	4.83	4.49		5.02	
La/Nb	3.34	3.51			3.52	3.64	4.09		3.23	
Zr/Nb	26.68	26.22			29.81	30.79	34.99		25.21	
Zr/Hf	36.69	34.91			35.23	35.03	40.79		35.51	
Ba/Th	91.15	86.98			75.98	84.72	71.90		89.66	
Rb/Ba	0.08	0.09			0.09	0.08	0.08		0.09	
Nb/Yb	1.16	1.68			1.40	1.32	1.10		1.55	
Ba/Yb	90.45	128.65			109.04	103.64	82.64		115.65	
Th/Yb	0.99	1.48			1.44	1.22	1.15		1.29	
Th/La	0.26	0.38			0.40	0.22	0.26		0.27	

	1232A-12H-1W-125 +210								
Major oxide (wt.%)									
	G1	G2	G3	G4	G5	G6	G7	G8	G10
SiO_2	54.60	54.06	55.78	58.17	56.18	56.99	58.97	56.46	54.24
TiO_2 LA-ICP-MS	2.40	1.72	2.53	1.90	2.19	2.35	1.99	2.43	1.95
TiO_2 SEM	2.41	1.73	2.55	1.91	2.20	2.37	2.01	2.44	1.96
Al_2O_3	14.21	14.13	13.25	14.56	14.10	13.58	14.23	14.57	15.53
FeO	11.52	12.67	11.18	8.67	10.96	12.14	11.09	10.80	8.84
MgO	3.91	4.14	3.79	3.89	3.88	2.46	2.30	3.38	3.84
CaO	7.58	7.19	7.00	7.00	6.20	6.39	5.94	7.10	8.36
Na_2O	3.78	3.66	4.19	4.04	4.32	3.62	3.01	3.40	5.61
K_2O	1.40	1.83	1.68	1.15	1.57	1.87	1.87	1.27	1.03
Trace element (ppm)									
Sc	47.48		45.53	45.45	41.98			51.87	
Ti									
V	531.81		462.91	406.67	376.49			395.30	
Cr	8.87		11.83	19.49	13.28			16.52	
Fe									
Ni	18.70		14.92	8.66	13.16			19.98	
Cs	3.31		2.77	2.82	2.74			2.80	
Rb	47.93		41.74	43.09	42.11			40.62	
Ba	557.63		512.37	483.39	479.22			484.83	
Th	6.52		6.36	5.65	6.16			6.78	
U	1.72		1.49	1.42	1.41			1.46	
Nb	8.20		7.55	7.02	7.23			7.73	
Ta	0.42		0.48	0.48	0.43			0.49	
La	29.09		26.48	25.04	24.67			28.32	
Ce	67.80		62.87	58.04	57.87			56.49	
Pb	17.58		15.63	17.72	15.43			15.38	
Pr	8.69		8.64	7.95	8.23			7.98	
Sr	368.65		337.06	369.51	312.97			362.64	
Nd	38.69		36.91	34.82	37.06			37.93	
Sm	10.77		10.33	8.09	8.88			10.43	
Zr	206.65		198.56	191.04	198.23			247.74	
Hf	5.05		6.06	5.47	6.16			7.23	
Eu	2.66		2.50	2.39	2.36			2.45	
Gd	9.49		9.46	8.56	8.55			10.23	
Tb	1.39		1.48	1.31	1.38			1.58	
Dy	9.22		9.12	8.61	9.34			9.93	
Y	50.64		50.02	46.66	48.85			58.44	
Ho	1.94		2.06	1.84	1.86			2.26	
Er	5.37		5.29	4.69	5.41			6.71	
Yb	6.09		5.66	5.43	5.49			6.32	
Lu	0.81		0.80	0.81	0.84			1.03	
Ba/La	19.17		19.35	19.30	19.43			17.12	
La/Sm	2.70		2.56	3.10	2.78			2.72	
La/Yb	4.78		4.68	4.62	4.50			4.48	
La/Nb	3.55		3.51	3.57	3.41			3.67	
Zr/Nb	25.20		26.32	27.21	27.44			32.07	
Zr/Hf	40.92		32.77	34.96	32.18			34.27	
Ba/Th	85.59		80.56	85.55	77.80			71.56	
Rb/Ba	0.09		0.08	0.09	0.09			0.08	
Nb/Yb	1.35		1.33	1.29	1.32			1.22	
Ba/Yb	91.64		90.60	89.10	87.37			76.77	
Th/Yb	1.07		1.12	1.04	1.12			1.07	
Th/La	0.33		0.32	0.28	0.31			0.34	

	1232A-16X-1W-41 >210								
Major oxide (wt.%)									
	G1	G2	G3	G4	G5	G6	G7	G8	G9
SiO_2	56.06	55.84	50.91	55.44	55.81	69.62	50.18	54.01	52.99
TiO_2 LA-ICP-MS	1.97	2.15	2.54	1.68	1.60	0.62	2.46	1.92	1.57
TiO_2 SEM	1.60	1.55	1.18	1.31	1.68	0.62	1.67	1.92	1.57
Al_2O_3	13.92	11.68	14.35	13.22	13.63	12.65	12.82	14.09	14.80
FeO	10.18	11.37	12.07	10.24	10.74	4.65	16.45	11.47	10.00
MgO	3.04	2.99	2.84	2.82	4.59	0.13	2.14	3.85	2.94
CaO	7.75	8.30	10.59	7.77	5.92	1.93	9.44	8.14	9.50
Na_2O	5.18	5.24	5.23	6.87	5.65	6.62	4.65	4.80	6.36
K_2O	1.30	1.84	0.87	1.36	1.46	3.17	1.25	1.13	1.23
Trace element (ppm)									
Sc	38.03	50.09	53.56	39.08	43.54	16.12	48.60		
Ti	11844.92	12913.46	15387.62	10070.73	9560.16	2522.69	14805.10		
V	322.83	443.02	530.25	337.76	323.83	1.57	365.67		
Cr	3.79	47.88	6.29	43.98	76.72	2.04	10.29		
Fe	60146.02	72984.61	82196.56	52428.26	141059.81	23682.01	74029.06		
Ni	4.49	38.42	9.43	7.53	216.98	3.34	1.52		
Cs	1.94	2.84	2.39	1.49	1.41	6.55	2.67		
Rb	29.32	37.31	34.20	19.39	19.17	93.78	38.46		
Ba	363.03	409.30	434.88	297.58	265.81	817.26	480.14		
Th	3.48	5.40	4.12	1.65	1.53	11.45	4.75		
U	1.03	1.64	1.24	0.50	0.52	3.12	1.36		
Nb	4.60	4.99	5.47	2.52	2.59	10.85	6.02		
Ta	0.29	0.31	0.34	0.18	0.15	0.73	0.40		
La	17.55	19.49	19.97	10.96	10.04	37.64	23.50		
Ce	40.59	46.28	47.22	26.59	25.75	84.60	52.94		
Pb	12.40	18.39	15.49	11.67	9.42	30.42	19.32		
Pr	5.38	6.04	6.32	3.65	3.35	10.85	6.98		
Sr	465.96	442.45	593.17	495.32	346.40	164.45	597.10		
Nd	24.53	28.10	28.80	17.88	16.72	47.34	33.41		
Sm	5.87	7.23	6.97	4.79	4.43	11.15	8.46		
Zr	129.34	161.13	154.26	101.30	92.20	387.03	184.78		
Hf	3.65	4.63	4.49	3.04	2.79	11.19	5.08		
Eu	1.87	1.90	2.28	1.52	1.34	2.07	2.33		
Gd	6.04	7.19	7.22	5.18	4.79	11.06	8.94		
Tb	0.96	1.13	1.15	0.76	0.72	1.80	1.36		
Dy	6.47	7.40	7.50	5.15	4.71	12.61	8.52		
Y	33.67	39.65	40.49	28.01	24.75	69.79	46.78		
Ho	1.30	1.53	1.64	1.11	0.97	2.69	1.79		
Er	3.70	4.48	4.55	3.15	2.67	7.81	5.26		
Yb	3.68	4.37	4.51	2.94	2.85	8.35	4.96		
Lu	0.54	0.72	0.69	0.46	0.40	1.30	0.73		
Ba/La	20.69	21.01	21.78	27.15	26.48	21.71	20.44		
La/Sm	2.99	2.70	2.87	2.29	2.27	3.38	2.78		
La/Yb	4.77	4.46	4.43	3.73	3.53	4.51	4.74		
La/Nb	3.81	3.90	3.65	4.35	3.88	3.47	3.91		
Zr/Nb	28.12	32.29	28.23	40.20	35.67	35.69	30.72		
Zr/Hf	35.48	34.80	34.39	33.32	33.04	34.60	36.37		
Ba/Th	104.47	75.80	105.55	180.73	173.90	71.38	101.19		
Rb/Ba	0.08	0.09	0.08	0.07	0.07	0.11	0.08		
Nb/Yb	1.25	1.14	1.21	0.86	0.91	1.30	1.21		
Ba/Yb	98.78	93.77	96.53	101.39	93.43	97.87	96.90		
Th/Yb	0.95	1.24	0.91	0.56	0.54	1.37	0.96		
Th/La	0.17	0.27	0.21	0.08	0.08	0.57	0.24		

	1232B-4H-1W-89 >210			1232B-5H-5W-80 >210						
Major oxide (wt.%)										
	G1	G2	G3	G2	G3	G4	G5	G6	G7	G8
SiO_2	51.47	52.02	59.40	55.64	56.60	53.96	55.42	55.63	53.36	55.19
TiO_2 LA-ICP-MS	1.90	3.51	1.97	1.86	1.83	2.16	2.46	1.87	2.23	1.95
TiO_2 SEM	2.10	2.43	1.92	1.49	1.64	2.27	1.86	1.52	1.90	1.64
Al_2O_3	14.18	13.19	13.62	16.05	16.96	13.78	15.42	15.22	15.72	14.20
FeO	16.83	13.40	9.49	9.16	9.17	11.95	9.93	9.45	10.12	10.51
MgO	2.43	3.07	1.89	3.09	2.96	3.34	2.65	3.09	3.63	3.41
CaO	6.94	8.46	6.12	7.37	6.55	9.65	5.89	7.86	9.04	7.93
Na_2O	4.05	3.91	4.39	4.34	4.08	3.09	5.62	4.84	3.90	4.54
K_2O	1.61	1.85	2.51	1.90	1.25	1.47	2.01	1.44	1.40	1.66
Trace element (ppm)										
Sc	33.07	53.90	32.37	37.49	32.70	47.30	32.56	41.16	49.64	39.74
Ti	11245.74	21025.30	11626.50	11044.45	10989.73	12888.59	14739.49	11226.67	13456.48	11676.87
V	286.92	647.38	169.60	327.80	302.02	382.88	229.07	319.64	411.94	315.28
Cr	23.73	2.49	4.15	68.47	12.23	77.01	16.65	65.40	88.98	66.39
Fe	57342.67	84649.56	53681.71	54847.88	55321.64	65469.61	55491.95	55191.23	67674.70	62085.35
Ni	6.62	11.38	1.97	17.69	9.76	28.05	3.10	22.21	24.14	23.18
Cs	3.72	3.39	4.30	2.77	2.67	2.62	3.44	2.33	2.95	2.70
Rb	54.38	50.33	64.19	39.72	40.01	38.36	50.76	33.81	42.31	38.50
Ba	494.56	562.97	656.54	378.30	371.08	431.05	469.67	387.20	447.52	382.41
Th	6.28	6.43	9.30	4.51	4.38	4.83	5.69	4.30	5.17	4.10
U	1.63	1.91	2.53	1.31	1.25	1.33	1.54	1.14	1.47	1.18
Nb	6.01	8.16	9.30	4.69	4.97	5.80	7.42	5.32	5.88	5.38
Ta	0.41	0.47	0.57	0.27	0.33	0.33	0.46	0.32	0.37	0.34
La	23.79	28.72	33.60	19.48	18.19	21.53	27.67	20.22	22.67	19.84
Ce	54.20	68.09	78.67	44.41	42.63	50.29	62.99	45.22	52.72	44.97
Pb	22.86	20.51	23.61	16.72	16.78	18.27	23.31	14.69	22.96	18.31
Pr	7.18	8.97	10.22	6.16	5.77	6.31	8.42	6.03	6.77	6.09
Sr	387.40	429.30	370.56	355.59	337.12	464.49	328.83	388.17	430.84	384.69
Nd	31.04	40.36	45.37	26.13	24.70	28.72	38.37	27.04	31.61	28.39
Sm	7.98	9.49	10.88	6.74	6.26	7.45	8.93	6.82	7.99	6.74
Zr	208.21	237.94	292.57	190.80	156.83	182.04	227.74	173.98	199.43	171.72
Hf	5.56	6.63	8.29	5.02	4.28	5.24	6.27	4.67	5.21	4.61
Eu	2.01	2.65	2.42	1.70	1.69	2.02	2.33	1.75	2.24	1.74
Gd	7.41	10.23	10.42	6.17	6.49	7.29	10.05	7.16	8.05	6.72
Tb	1.15	1.51	1.60	1.16	0.97	1.12	1.50	1.09	1.37	0.99
Dy	7.92	10.32	10.47	6.54	6.50	7.80	9.37	7.02	7.94	7.18
Y	43.80	53.97	58.35	39.34	36.21	41.64	53.06	39.08	46.76	39.29
Ho	1.59	2.10	2.19	1.42	1.35	1.54	1.93	1.45	1.77	1.48
Er	4.74	5.98	6.46	4.40	3.89	4.37	5.62	4.22	4.92	4.29
Yb	5.00	6.04	6.58	4.52	3.96	4.34	5.61	4.25	5.05	4.16
Lu	0.73	0.93	1.00	0.63	0.56	0.69	0.80	0.60	0.74	0.63
Ba/La	20.79	19.61	19.54	19.42	20.41	20.02	16.98	19.15	19.74	19.27
La/Sm	2.98	3.03	3.09	2.89	2.91	2.89	3.10	2.96	2.84	2.94
La/Yb	4.76	4.76	5.11	4.31	4.59	4.97	4.94	4.76	4.49	4.77
La/Nb	3.96	3.52	3.61	4.16	3.66	3.71	3.73	3.80	3.86	3.69
Zr/Nb	34.64	29.16	31.46	40.73	31.59	31.39	30.69	32.70	33.95	31.92
Zr/Hf	37.45	35.91	35.31	38.05	36.69	34.74	36.32	37.25	38.32	37.29
Ba/Th	78.75	87.62	70.63	83.88	84.72	89.34	82.62	90.15	86.64	93.27
Rb/Ba	0.11	0.09	0.10	0.10	0.11	0.09	0.11	0.09	0.09	0.10
Nb/Yb	1.20	1.35	1.41	1.04	1.25	1.34	1.32	1.25	1.16	1.29
Ba/Yb	98.91	93.28	99.85	83.69	93.71	99.43	83.79	91.21	88.62	91.92
Th/Yb	1.26	1.06	1.41	1.00	1.11	1.11	1.01	1.01	1.02	0.99
Th/La	0.31	0.32	0.46	0.23	0.22	0.24	0.28	0.21	0.26	0.21

	1232B-6H-7W-33 >210									
Major oxide (wt.%)										
	G1	G2	G3	G4	G5	G6	G7	G8	G9	G10
SiO_2	51.65	51.81	53.24	52.56	56.12	57.86	53.67	58.36	54.02	60.49
TiO_2 LA-ICP-MS	2.90	3.32	2.46	2.91	1.83	1.76	2.90	1.15	2.37	1.60
TiO_2 SEM	2.55	2.69	2.25	2.96	1.63	1.89	2.17	1.15	2.37	1.60
Al_2O_3	12.55	11.98	14.93	12.95	14.71	14.96	12.55	14.94	13.63	14.21
FeO	15.24	15.40	13.23	13.67	10.36	9.51	13.21	9.49	11.50	7.84
MgO	3.33	2.70	2.30	3.44	2.71	2.30	3.50	2.61	3.44	1.69
CaO	7.82	8.60	5.99	7.76	6.99	6.46	8.05	7.28	8.13	5.60
Na_2O	4.25	3.71	4.81	4.41	5.01	4.90	3.93	4.19	4.27	5.86
K_2O	1.66	1.88	2.44	1.70	1.66	1.66	1.58	1.39	2.04	2.11
Trace element (ppm)										
Sc	51.08	55.40	33.77	49.36	37.02	33.97	54.38			
Ti	17367.54	19902.45	14549.22	17408.05	11026.42	10480.68	17445.04			
V	572.34	640.64	181.33	552.31	320.66	261.41	578.21			
Cr	8.67	24.71	2.17	7.73	5.67	2.79	13.21			
Fe	81057.99	91591.14	57188.26	78808.97	58031.15	53210.32	82228.59			
Ni	20.84	25.69	0.51	18.04	6.03	3.29	22.77			
Cs	2.87	3.33	2.93	2.74	2.62	2.75	2.75			
Rb	41.33	49.10	42.28	38.81	40.10	42.18	38.54			
Ba	451.79	532.95	496.11	447.58	424.91	428.42	450.11			
Th	4.86	6.11	5.88	4.77	4.80	4.96	5.00			
U	1.38	1.75	1.61	1.37	1.32	1.38	1.36			
Nb	6.36	7.96	7.09	6.37	5.22	5.57	5.94			
Ta	0.40	0.49	0.41	0.37	0.32	0.31	0.41			
La	23.62	28.48	26.22	22.76	19.65	20.28	23.45			
Ce	54.96	67.44	61.42	55.00	45.38	46.43	54.42			
Pb	16.63	17.89	17.26	14.87	16.08	15.39	15.15			
Pr	7.56	9.03	8.13	7.27	5.92	6.24	7.37			
Sr	369.31	420.08	369.82	368.55	399.03	380.77	384.18			
Nd	33.52	41.09	37.32	33.32	26.77	27.84	34.93			
Sm	8.39	9.84	9.39	8.01	6.45	6.34	8.43			
Zr	194.00	227.80	205.79	184.01	170.18	176.22	196.61			
Hf	5.29	6.40	5.89	5.07	4.75	4.68	5.71			
Eu	2.27	2.72	2.39	2.37	1.77	1.77	2.33			
Gd	8.82	10.24	9.13	8.50	6.84	7.24	9.10			
Tb	1.36	1.58	1.37	1.33	1.06	1.11	1.36			
Dy	9.07	10.18	9.28	8.62	7.07	6.97	9.55			
Y	48.62	55.37	49.84	45.92	38.23	39.04	50.55			
Ho	1.84	2.17	1.86	1.76	1.45	1.51	1.92			
Er	5.28	6.08	5.53	4.97	4.10	4.37	5.50			
Yb	5.47	5.99	5.23	5.05	4.42	4.26	5.40			
Lu	0.78	0.89	0.81	0.75	0.65	0.71	0.81			
Ba/La	19.13	18.72	18.92	19.67	21.63	21.13	19.19			
La/Sm	2.82	2.90	2.79	2.84	3.05	3.20	2.78			
La/Yb	4.32	4.75	5.01	4.51	4.44	4.77	4.35			
La/Nb	3.72	3.58	3.70	3.57	3.76	3.64	3.95			
Zr/Nb	30.53	28.62	29.02	28.89	32.60	31.64	33.13			
Zr/Hf	36.67	35.62	34.97	36.33	35.86	37.69	34.43			
Ba/Th	92.96	87.30	84.44	93.93	88.62	86.38	90.11			
Rb/Ba	0.09	0.09	0.09	0.09	0.09	0.10	0.09			
Nb/Yb	1.16	1.33	1.36	1.26	1.18	1.31	1.10			
Ba/Yb	82.67	88.97	94.86	88.72	96.13	100.69	83.43			
Th/Yb	0.89	1.02	1.12	0.94	1.08	1.17	0.93			
Th/La	0.24	0.31	0.29	0.24	0.24	0.25	0.25			

	1232B-7H-2W-68 >210									
Major oxide (wt.%)										
	G1	G2	G3	G4	G5	G6	G7	G8	G9	G10
SiO_2	54.93	53.83	54.04	58.50	53.17	68.73	52.77	55.93	54.26	54.99
TiO_2 LA-ICP-MS	2.83	2.58	2.77	1.96	2.89	0.64	2.53	2.30	2.01	2.79
TiO_2 SEM	2.25	2.03	2.82	1.99	2.01	0.75	2.20	2.30	2.00	2.78
Al_2O_3	13.60	14.61	12.65	15.01	13.35	12.54	18.63	14.90	13.58	13.54
FeO	11.71	10.52	14.48	9.57	13.07	5.39	10.87	10.96	13.16	12.45
MgO	2.86	4.05	3.13	2.15	3.53	0.29	2.17	3.03	3.70	3.18
CaO	6.76	7.17	7.44	6.79	7.77	2.04	5.90	7.31	6.94	7.02
Na_2O	4.69	5.25	3.37	3.78	4.07	5.36	4.56	3.54	4.27	3.94
K_2O	2.01	1.40	1.51	1.65	1.55	4.40	1.98	1.43	1.48	1.50
Trace element (ppm)										
Sc	43.03	47.79	48.78	36.93	51.62	17.94	34.72			
Ti	16927.36	15544.15	16526.30	11747.73	17465.20	3840.77	15037.33			
V	283.07	493.18	525.57	287.23	548.84	1.24	239.27			
Cr	2.61	11.25	9.09	8.46	7.32	4.99	6.07			
Fe	73349.01	72279.85	76953.88	60645.83	81625.66	28301.29	59213.48			
Ni	4.46	17.91	17.61	5.79	19.22	0.60	1.42			
Cs	3.37	2.61	2.53	3.23	2.80	5.45	3.38			
Rb	47.93	37.52	37.66	47.01	40.15	82.85	49.99			
Ba	521.13	434.68	424.30	465.55	452.40	810.68	490.26			
Th	6.04	4.86	4.71	5.62	5.11	11.82	6.08			
U	1.70	1.28	1.26	1.51	1.40	2.94	1.67			
Nb	7.96	6.02	6.07	6.47	6.53	10.32	7.59			
Ta	0.47	0.38	0.37	0.35	0.40	0.64	0.45			
La	28.75	22.43	22.19	23.08	23.87	38.25	27.97			
Ce	67.84	52.44	52.33	53.27	55.99	83.45	63.36			
Pb	18.03	14.38	14.99	21.31	15.19	28.85	21.29			
Pr	9.04	7.11	7.16	6.97	7.49	10.51	8.86			
Sr	354.61	339.07	354.69	392.25	377.85	184.03	336.33			
Nd	41.58	32.65	32.68	32.23	35.04	44.81	39.12			
Sm	9.91	8.22	8.14	7.61	8.58	10.41	9.71			
Zr	223.15	186.42	183.93	192.92	199.10	385.03	238.83			
Hf	6.21	5.37	5.13	5.30	5.59	10.58	6.44			
Eu	2.67	2.17	2.26	2.08	2.40	1.99	2.28			
Gd	10.58	7.93	8.51	7.64	9.07	10.40	10.37			
Tb	1.57	1.21	1.28	1.12	1.38	1.68	1.54			
Dy	10.15	8.73	8.45	7.78	9.24	11.41	10.19			
Y	55.00	46.29	46.00	43.35	50.50	64.68	53.13			
Ho	2.10	1.84	1.77	1.69	1.95	2.45	2.05			
Er	5.80	5.09	5.16	4.60	5.47	7.37	5.85			
Yb	5.82	4.95	4.83	4.74	5.50	7.85	5.50			
Lu	0.87	0.77	0.76	0.76	0.82	1.24	0.89			
Ba/La	18.13	19.38	19.13	20.18	18.96	21.19	17.53			
La/Sm	2.90	2.73	2.73	3.03	2.78	3.67	2.88			
La/Yb	4.94	4.54	4.59	4.87	4.34	4.88	5.08			
La/Nb	3.61	3.73	3.65	3.57	3.65	3.71	3.68			
Zr/Nb	28.03	30.99	30.30	29.84	30.49	37.31	31.47			
Zr/Hf	35.96	34.71	35.85	36.40	35.65	36.39	37.11			
Ba/Th	86.28	89.53	90.08	82.84	88.53	68.59	80.63			
Rb/Ba	0.09	0.09	0.09	0.10	0.09	0.10	0.10			
Nb/Yb	1.37	1.22	1.26	1.36	1.19	1.32	1.38			
Ba/Yb	89.54	87.90	87.85	98.22	82.25	103.34	89.14			
Th/Yb	1.04	0.98	0.98	1.19	0.93	1.51	1.11			
Th/La	0.30	0.24	0.24	0.28	0.26	0.59	0.30			

	1232B-7H-3W-90 >210								
Major oxide (wt.%)									
	G1	G2	G3	G4	G5	G6	G7	G8	G9
SiO_2	54.99	57.13	54.36	54.94	56.61	59.97	53.75	56.36	54.29
TiO_2 LA-ICP-MS	2.00	1.96	1.93	1.57	2.11	1.88	1.65	1.81	2.65
TiO_2 SEM	2.01	1.71	1.56	1.49	1.71	1.73	1.66	1.81	2.63
Al_2O_3	14.19	14.82	14.39	15.07	13.96	13.90	14.72	13.99	13.48
FeO	11.58	9.57	10.11	10.34	11.19	10.10	10.75	11.63	12.31
MgO	2.99	2.38	3.96	3.65	2.46	1.40	4.35	2.40	3.07
CaO	7.49	6.37	7.35	7.37	6.32	5.46	8.38	7.41	7.26
Na_2O	4.45	5.08	5.84	4.81	5.05	4.71	4.58	4.07	4.54
K_2O	1.72	2.08	1.46	1.66	1.70	1.97	1.22	1.73	1.80
Trace element (ppm)									
Sc	39.98	31.53	42.24	33.70	35.05	34.64	47.18		
Ti	11974.25	11662.01	11576.48	9352.50	12627.52	11147.34	9942.53		
V	391.13	165.94	379.20	258.48	330.87	33.51	358.23		
Cr	13.58	14.32	52.74	53.10	5.34	3.48	94.38		
Fe	62416.86	52782.10	62112.36	51549.52	61261.25	63092.72	60601.45		
Ni	17.82	5.40	20.36	15.39	9.50	0.61	23.90		
Cs	2.01	3.48	2.17	1.99	2.84	3.67	1.53		
Rb	29.34	51.87	32.61	31.09	41.76	51.55	23.72		
Ba	373.12	502.05	378.65	322.79	458.94	573.06	301.08		
Th	4.50	6.50	3.98	3.74	5.13	6.73	3.14		
U	1.19	1.83	1.11	1.06	1.55	1.86	0.84		
Nb	4.95	7.50	4.77	4.57	6.08	7.71	3.62		
Ta	0.31	0.46	0.31	0.28	0.39	0.44	0.23		
La	19.09	26.37	18.19	16.16	22.12	29.75	14.31		
Ce	43.99	62.24	42.00	38.55	53.22	69.67	33.09		
Pb	15.81	18.04	12.98	10.78	15.91	20.22	11.81		
Pr	6.00	8.27	5.68	5.00	6.92	9.52	4.38		
Sr	445.83	364.89	353.68	365.23	341.85	378.02	391.73		
Nd	26.35	36.53	25.79	23.04	31.87	42.99	21.41		
Sm	6.65	9.10	6.09	5.72	7.65	10.77	5.32		
Zr	156.69	218.93	151.11	129.93	185.98	243.39	123.61		
Hf	4.12	5.96	4.41	3.62	5.20	6.77	3.44		
Eu	1.87	2.10	1.82	1.50	2.07	2.59	1.54		
Gd	6.74	8.97	6.49	5.69	7.85	10.87	5.49		
Tb	1.02	1.34	1.00	0.83	1.18	1.67	0.82		
Dy	6.55	8.83	6.97	5.56	8.14	10.92	5.75		
Y	37.21	47.37	36.97	29.33	42.51	59.17	32.45		
Ho	1.40	1.79	1.41	1.15	1.67	2.15	1.23		
Er	4.16	5.15	4.12	3.28	4.75	6.45	3.51		
Yb	4.01	5.12	4.23	3.30	4.94	6.45	3.61		
Lu	0.60	0.79	0.62	0.49	0.72	0.98	0.53		
Ba/La	19.55	19.04	20.82	19.97	20.75	19.27	21.05		
La/Sm	2.87	2.90	2.99	2.83	2.89	2.76	2.69		
La/Yb	4.76	5.15	4.30	4.90	4.48	4.62	3.96		
La/Nb	3.86	3.52	3.82	3.54	3.64	3.86	3.95		
Zr/Nb	31.65	29.21	31.71	28.43	30.59	31.59	34.15		
Zr/Hf	38.08	36.73	34.30	35.89	35.80	35.95	35.99		
Ba/Th	83.01	77.30	95.26	86.42	89.55	85.15	95.89		
Rb/Ba	0.08	0.10	0.09	0.10	0.09	0.09	0.08		
Nb/Yb	1.23	1.46	1.13	1.38	1.23	1.20	1.00		
Ba/Yb	93.05	98.06	89.52	97.81	93.00	88.91	83.40		
Th/Yb	1.12	1.27	0.94	1.13	1.04	1.04	0.87		
Th/La	0.22	0.32	0.20	0.19	0.26	0.34	0.16		

	1232B-10H-7W-23 >210									
Major oxide (wt.%)										
	G1	G2	G3	G4	G5	G6	G7	G8	G9	G10
SiO_2	55.10	51.91	55.27	55.87	54.62	60.89	54.93	59.88	56.02	54.32
TiO_2 LA-ICP-MS	1.96	2.79	2.45	2.47	2.29	1.73	2.06	1.56	2.45	2.48
TiO_2 SEM	1.96	2.78	2.69	1.61	2.00	1.38	2.88	1.26	2.05	2.18
Al_2O_3	13.82	13.28	12.93	12.92	13.91	14.23	14.53	14.62	12.36	13.45
FeO	11.40	13.54	12.12	11.50	12.55	9.20	11.07	9.96	12.83	12.49
MgO	3.41	3.25	3.14	3.37	3.24	1.76	3.82	2.42	2.49	3.13
CaO	8.56	8.60	7.84	7.45	7.39	5.26	7.37	6.48	7.38	8.32
Na_2O	3.94	4.74	4.20	4.35	4.11	4.91	4.40	3.45	4.05	3.89
K_2O	1.20	1.28	1.46	1.46	1.29	1.40	1.23	1.04	1.82	1.32
Trace element (ppm)										
Sc			49.20	47.60	45.60	31.48	43.87	34.60	45.64	47.73
Ti			14639.45	14979.97	13769.61	10463.79	12246.61	9370.86	14622.42	14902.23
V			487.59	459.87	466.97	139.82	428.23	304.24	391.66	449.88
Cr			49.54	55.82	7.27	9.14	39.85	23.33	15.77	16.15
Fe			75303.45	75045.91	71400.23	55546.22	68417.47	55190.01	74878.88	77432.16
Ni			17.20	22.85	13.29	1.00	19.52	3.71	8.24	10.85
Cs			3.10	3.08	2.53	2.83	2.42	2.12	3.65	3.27
Rb			41.40	40.40	34.78	40.12	33.41	29.25	50.40	47.05
Ba			413.56	476.58	374.00	458.62	372.25	306.94	496.56	468.00
Th			4.43	5.61	4.32	4.89	3.75	3.49	6.25	5.45
U			1.51	1.43	1.19	1.06	1.03	0.91	1.74	1.61
Nb			4.69	6.08	4.84	5.41	4.26	3.71	6.63	5.95
Ta			0.31	0.45	0.32	0.29	0.27	0.25	0.41	0.38
La			19.71	24.08	18.29	19.88	16.54	14.56	24.29	22.38
Ce			43.33	51.75	43.20	45.46	36.32	31.98	55.54	51.27
Pb			23.64	20.57	15.08	18.43	22.21	12.92	24.37	25.61
Pr			5.68	6.97	5.92	6.15	4.96	4.29	7.52	6.93
Sr			385.33	350.28	362.34	358.07	346.73	352.53	378.29	389.17
Nd			28.02	33.06	26.49	27.64	23.04	19.11	34.94	32.24
Sm			6.83	8.34	6.98	7.17	5.61	4.95	8.07	7.89
Zr			166.36	210.65	154.71	171.67	138.96	129.38	217.93	197.42
Hf			4.59	5.91	4.37	4.90	3.90	3.69	6.18	5.43
Eu			2.06	2.09	1.74	2.01	1.77	1.39	2.25	2.07
Gd			7.33	7.75	7.13	7.82	7.03	5.26	9.45	8.55
Tb			1.08	1.40	1.10	1.11	0.92	0.81	1.30	1.25
Dy			7.86	9.38	7.21	7.46	6.45	5.58	9.35	8.83
Y			42.97	49.92	39.14	42.54	36.52	30.77	50.19	46.92
Ho			1.57	1.83	1.57	1.55	1.42	1.16	1.86	1.78
Er			4.52	5.45	4.14	4.62	3.99	3.31	5.69	5.08
Yb			4.66	5.58	4.37	4.61	3.91	3.36	5.53	5.20
Lu			0.77	0.79	0.62	0.70	0.58	0.50	0.81	0.79
Ba/La			20.98	19.79	20.45	23.07	22.51	21.08	20.45	20.91
La/Sm			2.89	2.89	2.62	2.77	2.95	2.94	3.01	2.84
La/Yb			4.23	4.32	4.18	4.32	4.24	4.33	4.39	4.30
La/Nb			4.20	3.96	3.78	3.67	3.88	3.92	3.66	3.76
Zr/Nb			35.47	34.67	32.00	31.73	32.62	34.87	32.87	33.18
Zr/Hf			36.24	35.67	35.44	35.07	35.68	35.06	35.26	36.39
Ba/Th			93.46	85.03	86.67	93.88	99.40	88.07	79.51	85.83
Rb/Ba			0.10	0.08	0.09	0.09	0.09	0.10	0.10	0.10
Nb/Yb			1.01	1.09	1.11	1.17	1.09	1.10	1.20	1.14
Ba/Yb			88.84	85.49	85.58	99.59	95.33	91.35	89.79	90.00
Th/Yb			0.95	1.01	0.99	1.06	0.96	1.04	1.13	1.05
Th/La			0.22	0.28	0.22	0.24	0.19	0.17	0.31	0.27

		Probe data												
	Sample	1232A-6H-6W-118 +210												
		1P	2P	3P	4P	5P	6P	7P	8P	9P	10P	11P	12P	13P
Oxide wt%														
SiO_2		53.747	55.5705	53.247	55.5045	55.951	53.247	55.410	54.647	56.4525	59.027	50.356	53.886	55.398
TiO_2		1.791	2.069	1.922	2.048	1.809	1.483	1.654	1.970	2.013	1.736	1.640	1.939	1.878
Al_2O_3		13.435	13.550	13.397	13.8475	14.3255	14.4105	14.3475	14.033	13.7075	13.034	13.765	13.9745	13.622
FeO		10.280	11.440	12.117	10.9025	11.8425	9.829	11.862	11.712	11.795	10.5535	10.5415	11.732	11.733
MgO		3.326	3.399	3.525	3.880	4.008	4.653	3.973	3.584	3.475	2.470	3.439	4.317	3.227
CaO		6.903	6.868	7.229	7.620	7.403	7.466	7.340	7.109	7.125	6.186	6.797	7.755	6.699
Na_2O		2.641	2.776	3.263	3.558	3.437	3.123	3.355	3.098	3.580	3.992	3.037	3.340	3.454
K_2O		1.381	1.372	1.222	1.036	1.181	1.386	1.234	1.268	1.270	1.539	1.318	1.058	1.315

	Altered pumice													
Oxide	1232A-23X-5W-62			1232A-23X-5W-62		1232A-27X-2W-42			1232A-27X-2W-42		1232A-31X-3W-54		1232A-31X-3W-54		
(wt%)	G3	G4	G5	G6	G7	G8	G9	G10	G11	G12	G13	G14	G15	G16	G17
SiO_2	54.12	56.73	52.52	60.50	39.17	60.49	44.99	34.44	61.04	60.70	56.13	54.21	56.16	60.65	56.97
Al2O3	25.90	24.13	29.57	19.73	14.60	19.76	18.04	12.78	20.74	19.23	22.49	28.18	24.37	19.81	18.33
FeO	11.28	9.45	8.62	10.96	40.52	10.82	29.41	47.64	9.12	12.10	11.38	8.66	9.82	10.05	15.57
MgO	3.30	4.06	4.22	3.43	2.32	3.41	2.60	1.94	3.14	2.41	4.34	4.05	4.43	4.46	3.86
Na_2O	3.42	3.33	3.12	3.41	2.29	3.18	3.03	2.21	3.88	3.64	3.78	3.23	3.27	3.11	3.65
K_2O	1.98	2.30	1.94	1.98	1.09	2.34	1.92	0.98	2.07	1.92	1.87	1.67	1.95	1.91	1.62

Table 6: Table 6: SEM, EPMA and LA-ICPMS data for USGS standard BHVO-2g and Smithsonian standard (NMNH 72854, VG 568) run with samples are given with analytical precision and correction factors used for data in Table 5

EDS 5/19/2021	**BHVO Rec**	BHVO meas avg	Bias %	Sdev%	Correction Factor	Avg/best correction factor	Avg correction factor values
		USGS BHVO-2 Glass					
SiO2	49.9	49.05	-1.71	0.74	1.02	1.000	1.000
TiO2	2.73	3.08	12.97	14.19	0.89	0.885	0.885
Al2O3	13.5	13.22	-2.06	1.50	1.02	1.017	1.017
FeO	11.1	11.49	3.48	3.44	0.97	0.966	0.966
MgO	7.23	7.30	1.04	2.30	0.99	0.990	0.990
CaO	11.4	12.20	7.05	6.49	0.93	0.934	0.934
Na2O	2.22	2.53	13.99	3.42	0.88	1.167	1.167
K2O	0.52	0.57	9.40	9.69	0.91	0.930	0.930
MnO		0.36		24.94			
P2O5	0.27	0.189604	-29.78	63.85	1.42	1.42	1.42
Total							
	Rhyolite Rec	Rhyolite meas avg	Bias %	relative Sdev%	Correction Factor		
		USNM 72854 VG-568					
SiO2	76.71	78.02	1.70	0.48	0.98		
TiO2	0.12	0.10	-19.29	134.01	1.24		
Al2O3	12.06	11.90	-1.33	4.06	1.01		
FeO	0.8	1.36	69.57	17.63	0.59		
MgO	0	0.03		103.23	0.00		
CaO	0.5	0.43	-14.56	22.97	1.17		
Na2O	3.75	2.57	-31.39	8.01	1.46		
K2O	4.89	5.16	5.60	9.48	0.95		
MnO	0.03	0.40	1230.88	42.02	0.08		
P2O5	0	0.03939	#DIV/0!	127.04	0.00		
Total							

EDS 5/21/2021	**BHVO Rec**	BHVO meas avg	Bias %	Sdev%	Correction Factor	Avg/best correction factor	Avg correction factor values
		USGS BHVO-2 Glass					
SiO2	49.9	49.90	0.00	1.41	1.00	0.993	0.993
TiO2	2.73	2.80	2.60	9.08	0.97	0.975	0.975
Al2O3	13.5	13.76	1.89	2.06	0.98	0.980	0.980
FeO	11.1	11.02	-0.71	6.56	1.01	1.007	1.007
MgO	7.23	7.34	1.56	2.29	0.98	0.985	0.985
CaO	11.4	12.32	8.04	6.68	0.93	0.926	0.926
Na2O	2.22	2.18	-1.87	8.51	1.02	1.019	1.019
K2O	0.52	0.52	0.85	9.49	0.99	1.001	1.001
MnO		0.06		66.07			
P2O5	0.27	0.103348	-61.72	79.52	2.61	2.61	2.61
Total							
	Rhyolite Rec	Rhyolite meas avg	Bias %	relative Sdev%	Correction Factor		
		USNM 72854 VG-568					
SiO2	76.71	77.72	1.32	0.59	0.99		
TiO2	0.12	0.04	-69.97	108.96	3.33		
Al2O3	12.06	12.32	2.18	2.80	0.98		
FeO	0.8	1.06	32.57	29.56	0.75		
MgO	0	0.07		75.69	0.00		
CaO	0.5	0.48	-3.78	24.17	1.04		
Na2O	3.75	3.43	-8.62	13.88	1.09		
K2O	4.89	4.84	-1.00	6.41	1.01		
MnO	0.03	0.01	-83.28	181.49	5.98		
P2O5		0.03533		155.22			
Total							

EDS 5/24/2021	BHVO Rec	BHVO meas avg	Bias %	Sdev%	Correction Factor	Avg/best correction factor	Avg correction factor values
		USGS BHVO-2 Glass					
SiO2	49.9	49.42	-0.97	1.35	1.01	0.998	0.998
TiO2	2.73	3.06	12.21	10.82	0.89	0.891	0.891
Al2O3	13.5	13.70	1.48	1.64	0.99	0.988	0.988
FeO	11.1	11.47	3.35	6.65	0.97	0.968	0.968
MgO	7.23	7.23	-0.02	2.73	1.00	1.000	1.000
CaO	11.4	12.22	7.15	4.70	0.93	0.933	0.933
Na2O	2.22	2.08	-6.28	3.99	1.07	1.108	1.108
K2O	0.52	0.57	10.31	9.19	0.91	0.943	0.943
MnO		0.11		54.28			
P2O5	0.27	0.1362393	-49.54	76.02	1.98	1.98	1.98
Total							
	Rhyolite Rec	Rhyolite meas avg	Bias %	relative Sdev%	Correction Factor		
		USNM 72854 VG-568					
SiO2	76.71	77.74	1.35	0.94	0.99		
TiO2	0.12	0.09	-25.74	122.22	1.35		
Al2O3	12.06	12.17	0.91	1.71	0.99		
FeO	0.8	1.19	49.08	18.81	0.67		
MgO	0	0.04		89.49	0.00		
CaO	0.5	0.42	-16.57	25.74	1.20		
Na2O	3.75	3.26	-12.98	8.60	1.15		
K2O	4.89	4.99	2.10	4.51	0.98		
MnO	0.03	0.02	-20.86	138.11	1.26		
P2O5		0.0702431		119.74			
Total							

EDS 5/25/2021	BHVO Rec	BHVO meas avg	Bias %	Sdev%	Correction Factor	Avg/best correction factor	Avg correction factor values
		USGS BHVO-2 Glass					
SiO2	49.9	49.27	-1.26	1.59	1.01	0.999	0.999
TiO2	2.73	3.17	16.17	9.65	0.86	0.861	0.861
Al2O3	13.5	13.31	-1.42	6.28	1.01	1.010	1.010
FeO	11.1	11.61	4.64	6.31	0.96	0.956	0.956
MgO	7.23	7.08	-2.10	8.53	1.02	1.021	1.021
CaO	11.4	12.52	9.83	7.12	0.91	0.911	0.911
Na2O	2.22	2.17	-2.41	7.53	1.02	1.057	1.057
K2O	0.52	0.55	6.01	9.45	0.94	0.971	0.971
MnO		0.22		105.60	0.00		
P2O5	0.27	0.103434	-61.69	124.63	2.61	2.61	2.61
Total							
	Rhyolite Rec	Rhyolite meas avg	Bias %	relative Sdev%	Correction Factor		
		USNM 72854 VG-568					
SiO2	76.71	77.91	1.57	0.75	0.98		
TiO2	0.12	0.05	-55.26	146.48	2.24		
Al2O3	12.06	12.00	-0.49	3.97	1.00		
FeO	0.8	1.07	34.10	22.83	0.75		
MgO	0	0.05		88.90	0.00		
CaO	0.5	0.50	0.22	15.63	1.00		
Na2O	3.75	3.44	-8.22	6.28	1.09		
K2O	4.89	4.90	0.16	6.25	1.00		
MnO	0.03	0.05	61.90	144.50	0.62		
P2O5		0.026555		138.40			
Total							

IXRF EDS 6/12 & 13/2017	BHVO Rec	BHVO meas avg	Bias %	Sdev%	Correction Factor	Avg/best correction factor	Avg correction factor values
		USGS BHVO-1 Glass					
SiO2	49.9	45.03	-9.77	0.47	1.11	1.087	1.087
TiO2	2.73	2.90	6.17	4.49	0.94	0.942	0.942
Al2O3	13.5	13.68	1.35	0.61	0.99	0.974	0.974
FeO	11.1	13.31	19.92	1.68	0.83	0.834	0.834
MgO	7.23	7.59	4.97	2.40	0.95	0.953	0.953
CaO	11.4	13.60	19.28	2.20	0.84	0.838	0.838
Na2O	2.22	2.86	29.01	4.91	0.78	0.827	0.827
K2O	0.52	0.77	47.50	11.85	0.68	0.603	0.603
MnO		0.30		19.20			
P2O5							
Total							
	Rhyolite Rec	Rhyolite meas avg	Bias %	relative Sdev%	Correction Factor		
		USNM 72854 VG-568					
SiO2	76.71	72.00	-6.14	0.37	1.07		
TiO2	0.12	0.18	51.20	18.81	0.66		
Al2O3	12.06	12.55	4.09	0.94	0.96		
FeO	0.8	1.68	110.26	6.56	0.48		
MgO	0	0.36		25.01	0.00		
CaO	0.5	0.68	36.40	14.35	0.73		
Na2O	3.75	4.26	13.69	2.72	0.88		
K2O	4.89	8.11	65.78	1.72	0.60		
MnO	0.03	0.17	468.15	31.79	0.18		
P2O5							
Total							

IXRF EDS 11/7/18	BHVO meas avg	Bias %	Sdev%	Correction Factor	Avg/best correction factor	Avg correction factor values
SiO2	45.00	-9.82	0.37	1.11	1.08	1.08
TiO2	2.88	5.62	3.66	0.95	0.95	0.95
Al2O3	13.08	-3.11	0.57	1.03	1.02	1.02
FeO	13.99	26.03	0.90	0.79	0.79	0.79
MgO	7.04	-2.64	0.99	1.03	1.03	1.03
CaO	14.07	23.45	1.51	0.81	0.81	0.81
Na2O	2.67	20.17	2.42	0.83	0.94	0.94
K2O	0.85	63.49	8.15	0.61	0.58	0.58
MnO	0.34		28.00	0.00		
P2O5	0.08		31.51	0.00		
Total						
Rhyolite meas avg	Average	Bias	std dev %			
SiO2	72.91	-4.95	0.24	1.05		
TiO2	0.21	72.08	15.04	0.58		
Al2O3	12.02	-0.32	0.93	1.00		
FeO	1.68	109.50	7.90	0.48		
MgO	0.43		29.52	0.00		
CaO	0.51	1.87	14.96	0.98		
Na2O	3.61	-3.87	3.61	1.04		
K2O	8.40	71.82	2.47	0.58		
MnO	0.15	385.00	40.17	0.21		
P2O5	0.09		33.42	0.00		
Total	100.00					

Oxide Probe 3/28/18	Average	Std dev	std dev %	BHVO Rec	Bias
SiO2	48.74	0.50	1.03	49.90	-2.32
TiO2	2.72	0.09	3.23	2.73	-0.50
Al2O3	13.24	0.15	1.10	13.50	-1.91
FeO	11.10	0.27	2.47	11.10	0.03
MgO	7.08	0.21	2.94	7.23	-2.12
CaO	11.37	0.18	1.56	11.40	-0.24
Na2O	2.30	0.35	15.00	2.22	3.64
K2O	0.52	0.08	16.27	0.52	-0.08
MnO	0.17	0.01	6.33		
P2O5					
Total	97.26				

Trace elements LA-ICPMS 4/16/21-4/23/21	BHVO-2G Recommended Value	Average	Bias %	std dev %
Ca42	81800	81475.91	-0.39778	1.06E-05
Ca43	81800	81903.56	0.12644	0.894777
Sc45	34	31.88319	-6.63926	1.669725
Ti49	1650	18054.12	90.86081	4.594813
V51	317	329.5013	3.793999	0.876038
Cr52	291	313.4706	7.168339	1.234435
Fe57	83700	59694.63	-40.2136	7.111542
Ni60	110	124.1604	11.40494	3.8734
Cs133		0.108549		26.57773
Rb85	8.9	9.438085	5.701211	2.362598
Ba137	125	126.0811	0.857436	1.35582
Th232	1.19	1.151532	-3.3406	3.050935
U238	0.42	0.439532	4.443799	10.18936
Nb93	20	17.25021	-15.9406	1.573308
Ta181		1.124681		3.376351
La139	15.2	14.73191	-3.17735	1.113588
Ce140	36.6	37.30553	1.891226	1.046098
Pb208	1.5	1.877255	20.09611	7.035074
Pr141		5.044681		1.191374
Nd146	24.9	23.3083	-6.82891	1.738287
Sr88	393	382.574	-2.72521	0.51786
Zr90	163	146.4696	-11.2859	1.448914
Hf178		3.885319		3.051755
Sm147	6.19	5.702979	-8.53977	3.54385
Eu153	2.07	1.960298	-5.5962	2.641089
Gd160	6.03	5.59234	-7.82605	2.664608
Tb159	0.9	0.808	-11.3861	3.02509
Dy163	5.22	4.945319	-5.55436	3.11478
Ho165	1.01	0.892787	-13.1289	2.965719
Y89	26	22.5134	-15.4868	1.719356
Yb174	2.09	1.923255	-8.66992	3.374968
Lu175	0.28	0.261128	-7.22725	6.074909

Trace elements LA-ICPMS 4/16/21-4/23/21	NIST 612 Recommended Value	Average	Bias %	std dev %
Ca42		85262.51		1.32E-05
Ca43		85268.22		0.790179
Sc45		41.04688		1.216333
Ti49	50.1	48.32625	-3.67037	10.09988
V51		39.23333		1.323312
Cr52	35	39.88729	12.25275	1.373316
Fe57	51	58.93792	13.46827	24.25031
Ni60	38.8	38.44146	-0.9327	2.757031
Cs133		41.66729		1.195351
Rb85	31.4	31.64542	0.77552	1.257289
Ba137	38.6	37.74813	-2.25673	1.467511
Th232	37.79	37.235	-1.49053	1.2139
U238	37.38	37.16625	-0.57512	1.07638
Nb93		38.06125		0.939874
Ta181		39.76896		1.221737
La139	36	35.77125	-0.63948	0.819667
Ce140	39	38.3525	-1.68829	0.817846
Pb208	38.57	38.98354	1.060811	1.436394
Pr141		37.16396		0.844899
Nd146	36	35.24958	-2.12887	1.525428
Sr88	78.4	76.15	-2.95469	0.761409
Zr90		35.99313		1.277986
Hf178		34.77333		1.2983
Sm147	39	36.72333	-6.19951	1.273395
Eu153	36	34.44313	-4.52013	0.874084
Gd160	39	36.95208	-5.54209	1.462917
Tb159		35.91625		1.061699
Dy163	35	35.97	2.696692	1.296972
Ho165		37.86958		1.212432
Y89		38.25083		1.235283
Yb174	42	39.94396	-5.14732	1.196716
Lu175		37.71063		1.214537

Trace elements LA-ICPMS 6/22/17-7/10/17	BHVO-2G Recommended Value	Average	Bias %	std dev %
Ca42	81800	80833.91	-1.18104	0.457323
Ca43	81800	81475.9	-0.39621	1.08E-05
Sc45	34	32.17797	-5.35891	1.435866
Ti49	1650	6968.469	322.3314	95.04814
V51	317	258.9188	-18.3221	2.015901
Cr52	291	195.2923	-32.8893	1.185559
Fe57	83700	76204.66	-8.95501	2.216307
Ni60	110	92.93411	-15.5144	1.785022
Cs133		0.087592		11.39063
Rb85	8.9	7.061444	-20.6579	2.792735
Ba137	125	120.1456	-3.88349	2.654547
Th232	1.19	1.199639	0.809991	2.529587
U238	0.42	0.338731	-19.3499	4.466953
Nb93	20	16.98275	-15.0863	2.585975
Ta181		1.166722		2.772544
La139	15.2	15.00772	-1.26499	3.045736
Ce140	36.6	33.83397	-7.55745	3.324821
Pb208	1.5	1.357972	-9.46852	5.408461
Pr141		5.071972		3.76809
Nd146	24.9	24.11322	-3.15975	4.463982
Sr88	393	370.8994	-5.62356	1.09454
Zr90	163	147.8277	-9.30816	2.584828
Hf178		4.003611		6.375569
Sm147	6.19	5.788778	-6.48178	3.268989
Eu153	2.07	1.959583	-5.33414	4.667301
Gd160	6.03	5.64825	-6.33085	5.07835
Tb159	0.9	0.841989	-6.44568	2.300381
Dy163	5.22	5.175361	-0.85515	4.852816
Ho165	1.01	0.915606	-9.34598	1.639312
Y89	26	22.82036	-12.2294	2.925148
Yb174	2.09	2.037194	-2.52658	4.640073
Lu175	0.28	0.266517	-4.81548	6.534004

Table 7: Averages of select elements for Site 1232 glasses (analyzed with LA-ICP-MS and SEM)

Average chemical characteristics of Site 1232 turbidite glasses				
		Average	STD DEV	
Weight percent	SiO_2	56.0	1.8	
	TiO_2	1.9	0.4	
	Al_2O_3	14.5	1.2	
	FeO	10.6	1.5	
	MgO	3.1	0.7	
	CaO	7.1	1.0	
	Na_2O	4.7	0.8	
	K_2O	1.6	0.3	
Parts per million	Sc	39.8	6.8	
	Ti	12254.5	2527.4	
	V	320.9	118.1	
	Cr	22.5	25.7	
	Ni	12.7	23.0	
	Sr	386.3	43.3	
	Cs	2.7	0.8	
	Rb	40.3	13.0	
	Ba	446.6	94.8	
	Th	5.1	1.5	
	U	1.4	0.4	
	Pb	16.9	4.6	
	Nb	6.0	1.5	
	Ta	0.4	0.1	
	Zr	182.9	44.1	
	Hf	5.1	1.2	
	Y	43.2	8.9	
	La	22.2	5.4	
	Ce	51.2	12.4	
	Pr	6.8	1.6	
	Nd	31.3	7.2	
	Sm	7.6	1.7	
	Eu	2.1	0.4	
	Gd	7.9	1.7	
	Tb	1.2	0.3	
	Dy	8.0	1.7	
	Ho	1.6	0.3	
	Er	4.7	1.0	
	Yb	4.8	1.0	
	Lu	0.7	0.2	
Useful Ratios	Ba/La	20.4	2.0	
	La/Sm	2.9	0.2	
	La/Yb	4.7	0.4	
	La/Nb	3.7	0.2	
	Zr/Nb	31.1	2.7	
	Ba/Th	88.9	14.8	
	Rb/Ba	0.09	0.01	
	Nb/Yb	1.3	0.1	
	Ba/Yb	94.9	9.9	
	Th/Yb	1.1	0.2	
	Th/La	0.3	0.1	

Table 8: Ratios of select elements for Site 1232 glasses (analyzed with LA-ICP-MS) and comparison data from SVZ

Ratios		SSVZ				1232	CSVZ									TSVZ	SEC		Back Arc		
Eruption																		Laguna Blanca/			
Material	Maca	Hudson	Hudson	Cay	1232	Puyehue	Cordon Caulle	Llaima	Callaqui	Antuco	Osorno	Rio Ibanez	Villarrica	Sierra Velluda	Descabezo	Chillan	Puyuhuapi	Zapaleri	El Tromen	Payun Matru	Caviahue
Zr/Nb	22.68	21.12	22.15	49.48	30.64	34.55	36.92	40.42		38.93	41.04	30.68	39.85	41.99	36.39	46.47			13.83	9.41	28.03
Zr/Hf	42.86	43.43	47.65	46.73	35.83	44.14	43.81	36.58		50.19	34.32	46.49	39.50	38.26	33.49	48.34		40.38	39.77	47.07	44.61
Rb/Ba	0.06	0.08	0.09	0.07	0.09	0.08	0.10	0.06	0.12	0.08	0.09	0.14	0.08	0.13	0.13	0.16	0.36	0.33	0.16	0.23	0.13
Nb/Yb	3.41	4.19	3.70	1.22	1.26	1.54	1.60	0.93		1.18	0.96	1.79	1.12	1.44	1.86	2.24			6.97	16.19	3.12
Ba/Yb	152.17	174.16	145.70	145.86	93.94	126.06	118.25	91.84	134.83	116.29	88.68	30.98	93.70	138.78	195.97	188.80	31.80	217.33	298.59	149.35	200.56
Th/Yb	1.24	1.51	1.31	0.96	1.08	1.20	1.40	0.56	2.23	1.02	0.96	0.48	0.67	1.66		3.78	2.14	7.18	5.75	5.17	3.51
La/Yb	9.63	9.80	8.99	7.34	4.67	5.04	5.22	3.74	7.00	5.18	3.34	3.56	3.64	6.08	8.69	7.84	13.69	15.25	13.43	13.34	10.78
La/Sm	3.90	4.50	4.27	3.26	2.91	3.12	3.69	2.43	3.16	3.26	2.24	2.09	2.35	3.02	4.47	3.75	4.66	37.34	2.36	6.46	4.35
La/Nb	2.82	2.34	2.43	6.00	3.72	3.28	3.26	4.00		4.38	3.49	1.99	3.24	4.23	4.67	3.50			1.93	0.82	3.46
Ba/La	15.81	17.78	16.20	19.88	20.10	25.01	22.66	24.58	19.27	22.45	26.55	8.69	25.74	22.83	22.55	24.07	2.32	14.25	22.24	11.20	18.60
Ba/Th	122.71	115.52	110.83	151.23	87.05	105.47	84.38	163.89	60.55	114.22	92.37	65.02	140.86	83.58		49.90	14.83	30.27	51.89	28.89	57.11

Table 9: Correlation coefficient matrix of trace element ratios

	Rb	*Zr*	Analytical precision
Rb	1		2.79%
Zr	0.897603	1	2.58%
	Ba	*Zr*	
Ba	1		2.65%
Zr	0.941708	1	2.58%
	Th	*Zr*	
Th	1		3.05%
Zr	0.681218	1	2.58%
	Nb	*Zr*	
Nb	1		2.58%
Zr	0.599913	1	2.58%
	La	*Zr*	
La	1		3.04%
Zr	0.964101	1	2.58%
	Sm	*Zr*	
Sm	1		3.54%
Zr	0.881718	1	2.58%
	Yb	*Zr*	
Yb	1		4.64%
Zr	0.946128	1	2.58%
	Hf	*Zr*	
Hf	1		6.37%
Zr	0.786984	1	2.58%
	Ba	*Th*	
Ba	1		2.65%
Th	0.670774	1	3.05%
	Ba	*La*	
Ba	1		2.65%
La	0.949849	1	3.04%
	La	*Yb*	
La	1		3.04%
Yb	0.953595	1	4.64%

Table 10: Angularity of glass grains based on visual comparison chart for determination from Krumbein (1941) and scored using Powers (1953) scoring chart, both below

Sample		Grain	Grade
1232A	1H-3W-61 >149	G3	0.10
	3H-3W-64>149	G6	0.20
	4H-2W-33>149	G3	0.10
	4H-2W-33>210	G1	0.20
	4H-6W-45>149	G7	0.30
	4H-6W-45>210	G4	0.10
	5H-7W-45>149	G5	0.20
	5H-7W-45>210	G5	0.20
	6H-4W-85>149	G4	0.10
	6H-4W-85>210	G8	0.10
	6H-6W-118>149	G1	0.10
	6H-6W-118>210	G6	0.10
	7H-2W-86>149	G7	0.20
	7H-2W-86>210	G8	0.30
	7H-5W-87>149	G3	0.20
	7H-5W-87>210	G3	0.10
	7H-6W-42>149	G5	0.20
	7H-6W-42>210	G2	0.10
	8H-1W-46>149	G5	0.10
	8H-1W-46>210	G2	0.10
	10H-3W-25>149	G4	0.20
	10H-3W-25>210	G6	0.20
	12H-1W-125>149	G8	0.10
	12H-1W-125>210	G7	0.30
	16X-1W-41>149	G4	0.10
	16X-1W-41>210	G8	0.10
	18X-1W-36>149	G7	0.30
1232B	1H-2W-56>149	G4	0.10
	4H-1W-89>149	G1	0.20
	5H-5W-80>149	G2	0.10
	5H-5W-80>210	G3	0.10
	6H-1W-33>149	G4	0.20
	6H-1W-33>210	G1	0.20
	7H-2W-68>149	G8	0.30
	7H-2W-68>210	G4	0.20
	7H-3W-70>149	G9	0.10
	7H-3W-70>210	G6	0.20
	10H-7W-23>149	G7	0.10
	10H-7W-23>210	G10	0.30
Average angularity grade of 1232			0.166667

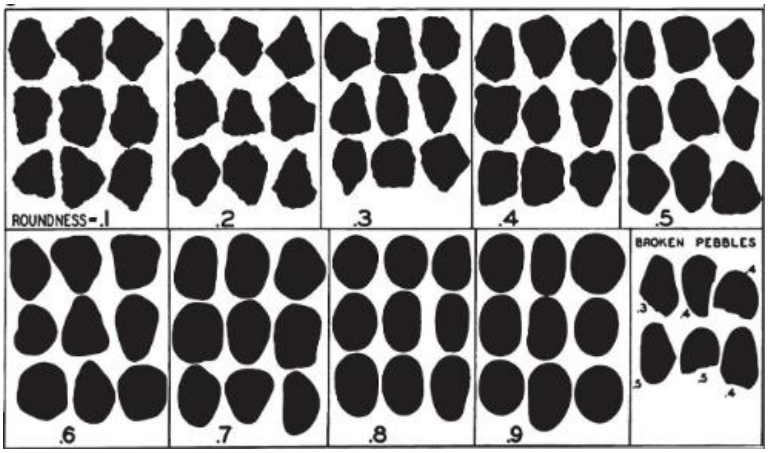

Grade Terms	Class limits (Powers, 1953)
Very angular	0.12 to 0.17
Angular	0.17 to 0.25
Sub-angular	0.25 to 0.35
Sub-rounded	0.35 to 0.49
Rounded	0.49 to 0.70
Well-rounded	0.70 to 1.00

High resolution backscatter images of Site 1232A glass shards, taken using SEM
1232A-1H-3W-61 >149µ

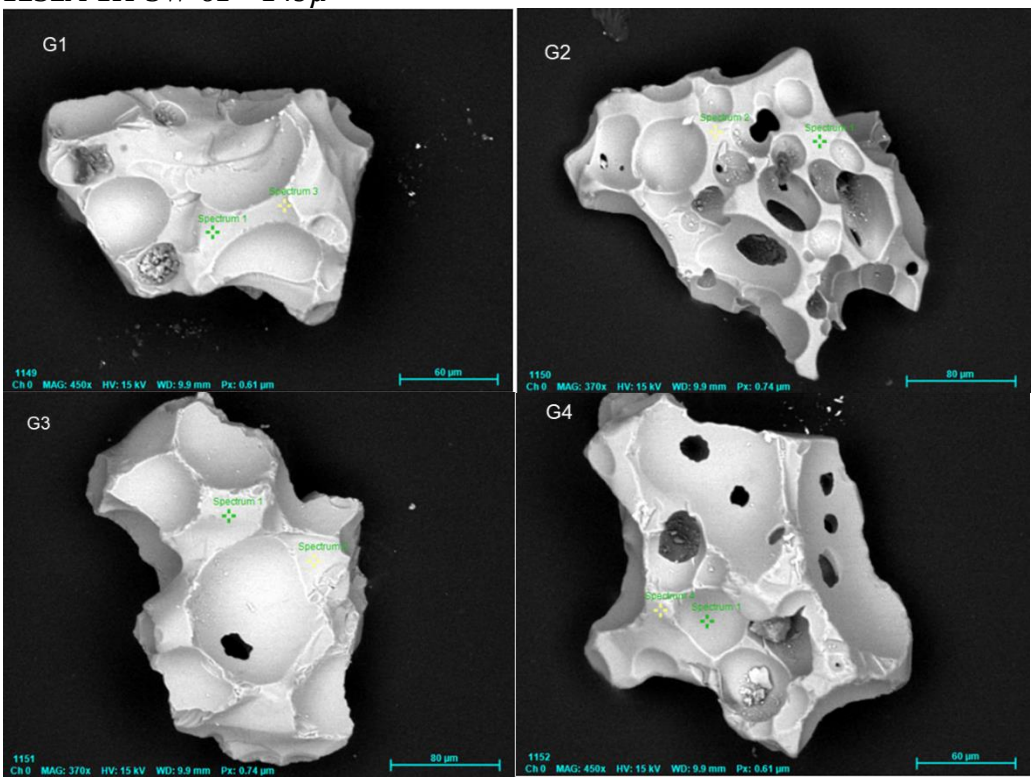

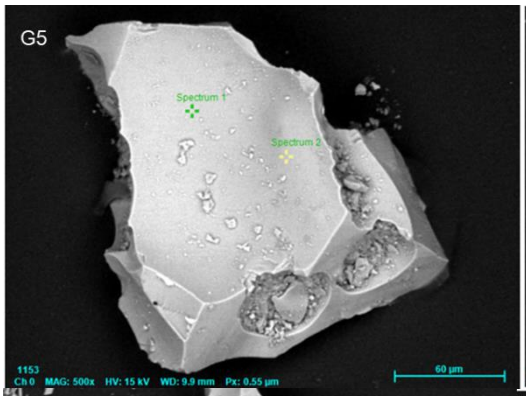

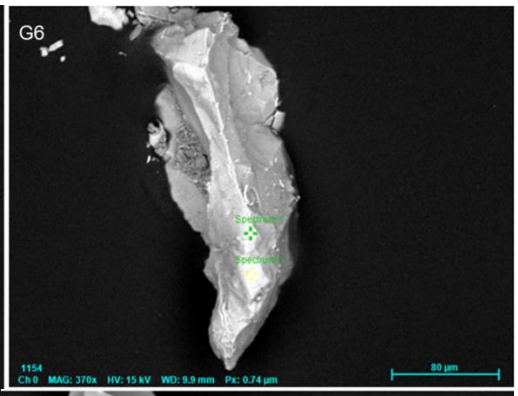

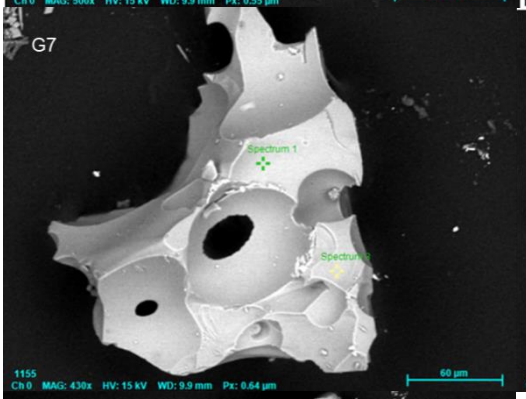

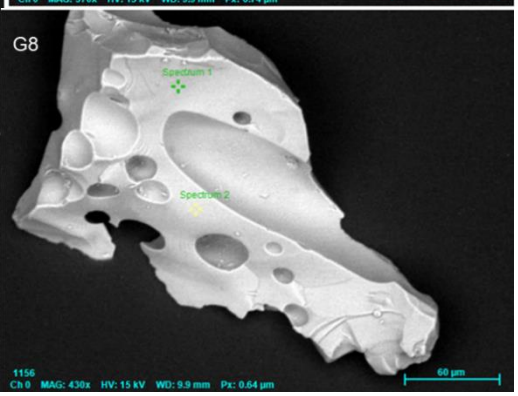

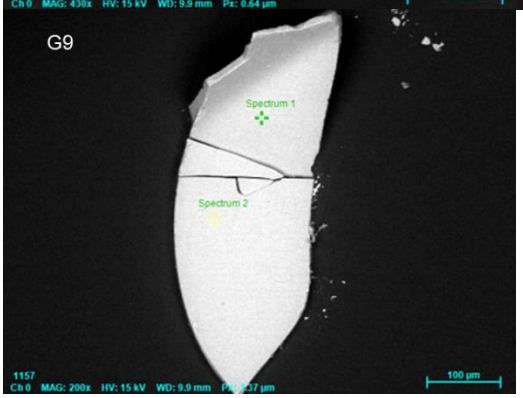

1232A-3H-3W-64 >149µ

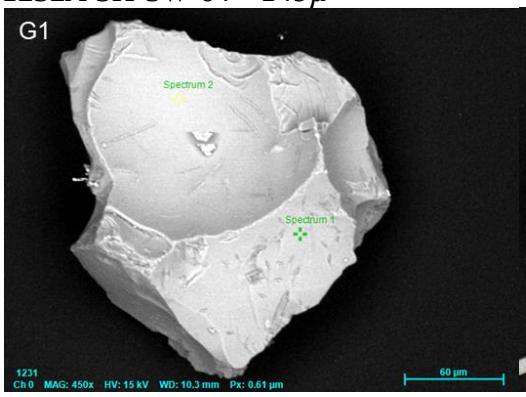

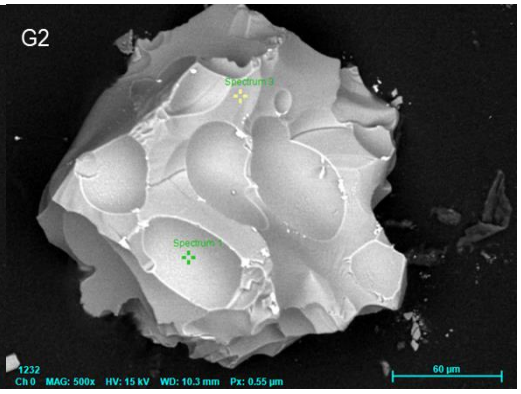

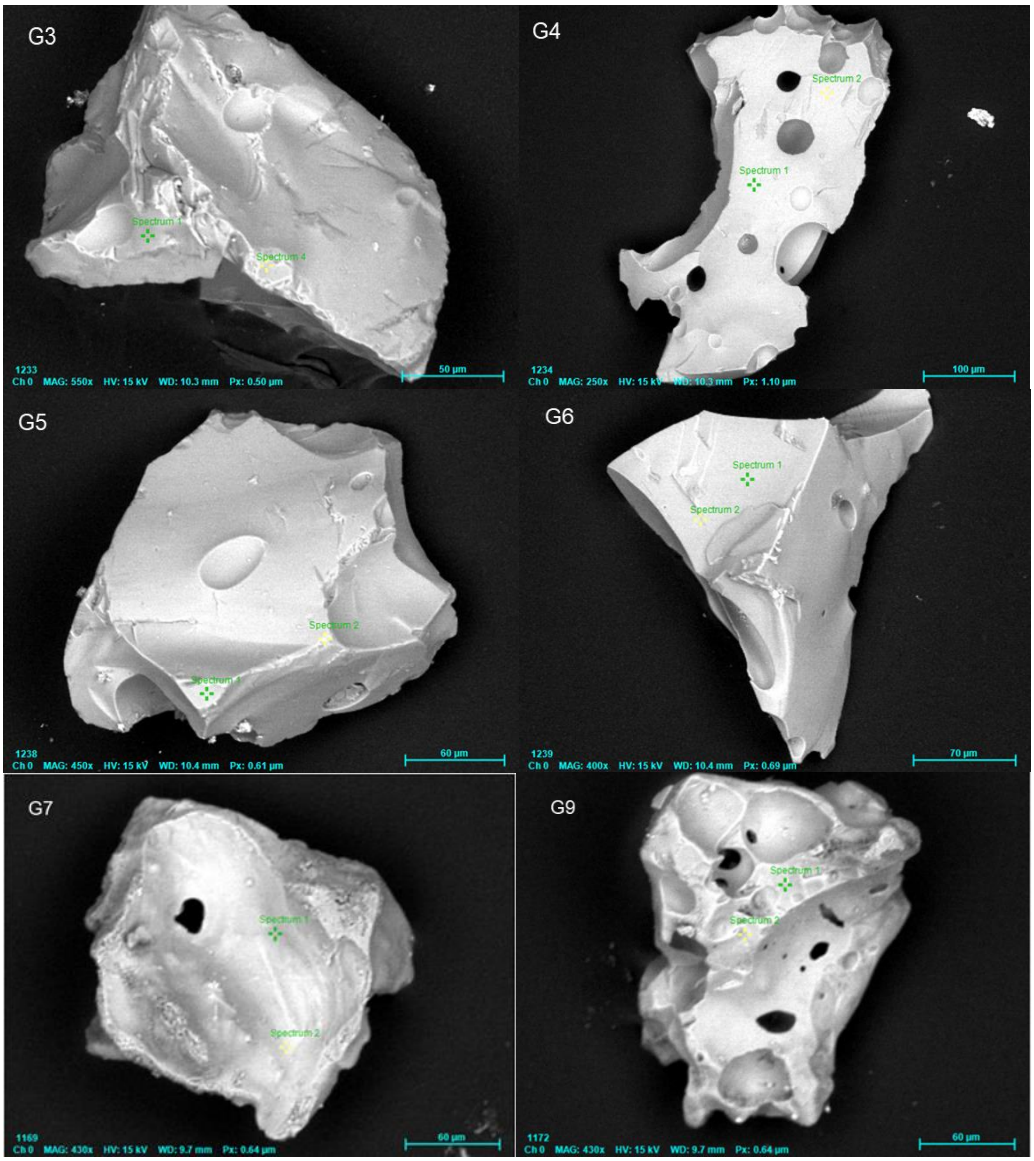

1232A-4H-2W-33 >149µ

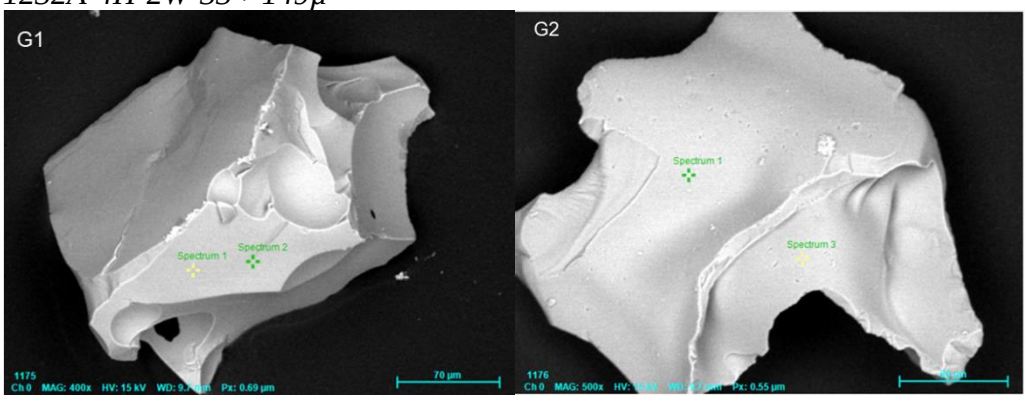

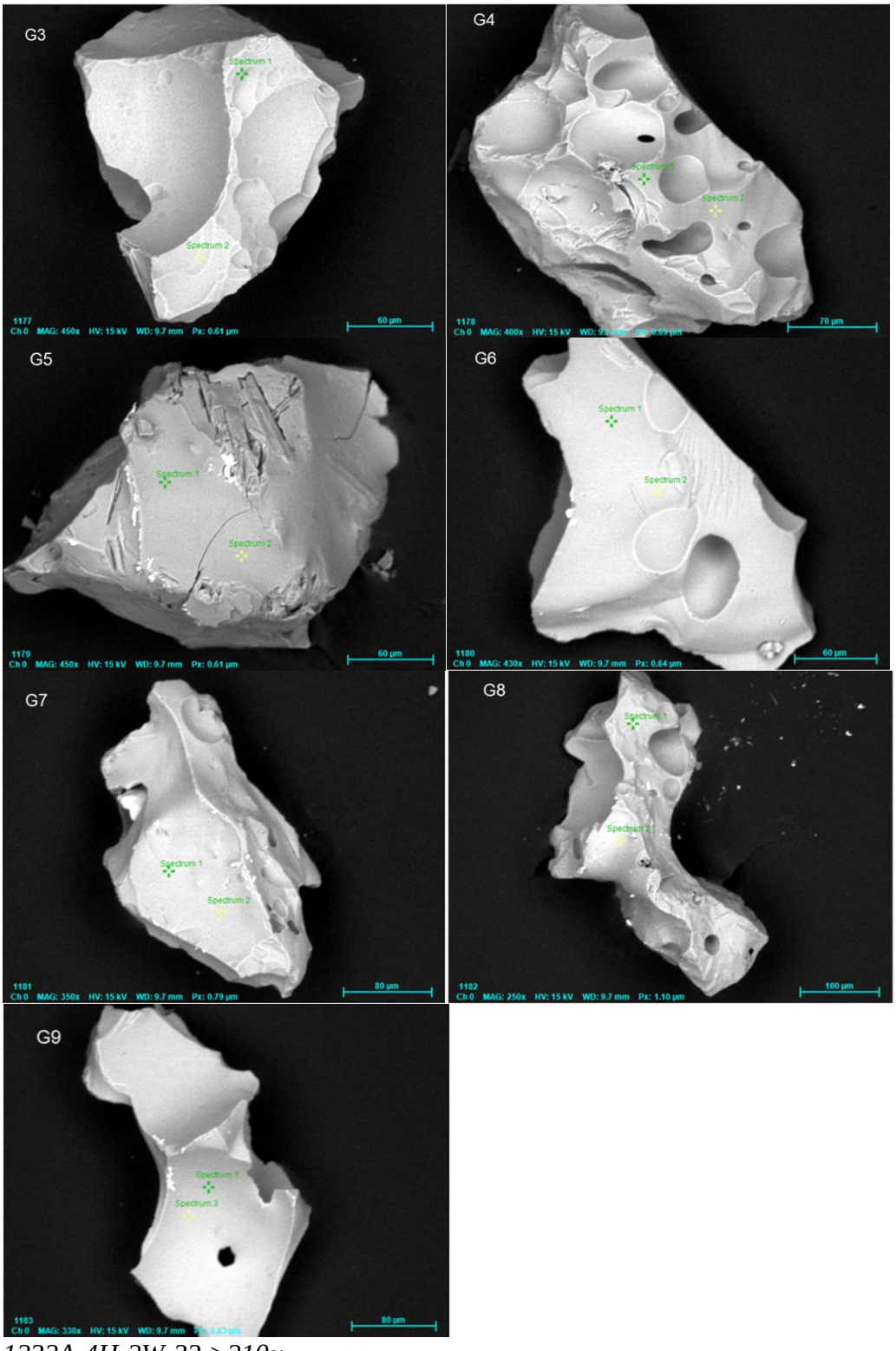

1232A-4H-2W-33 >210µ

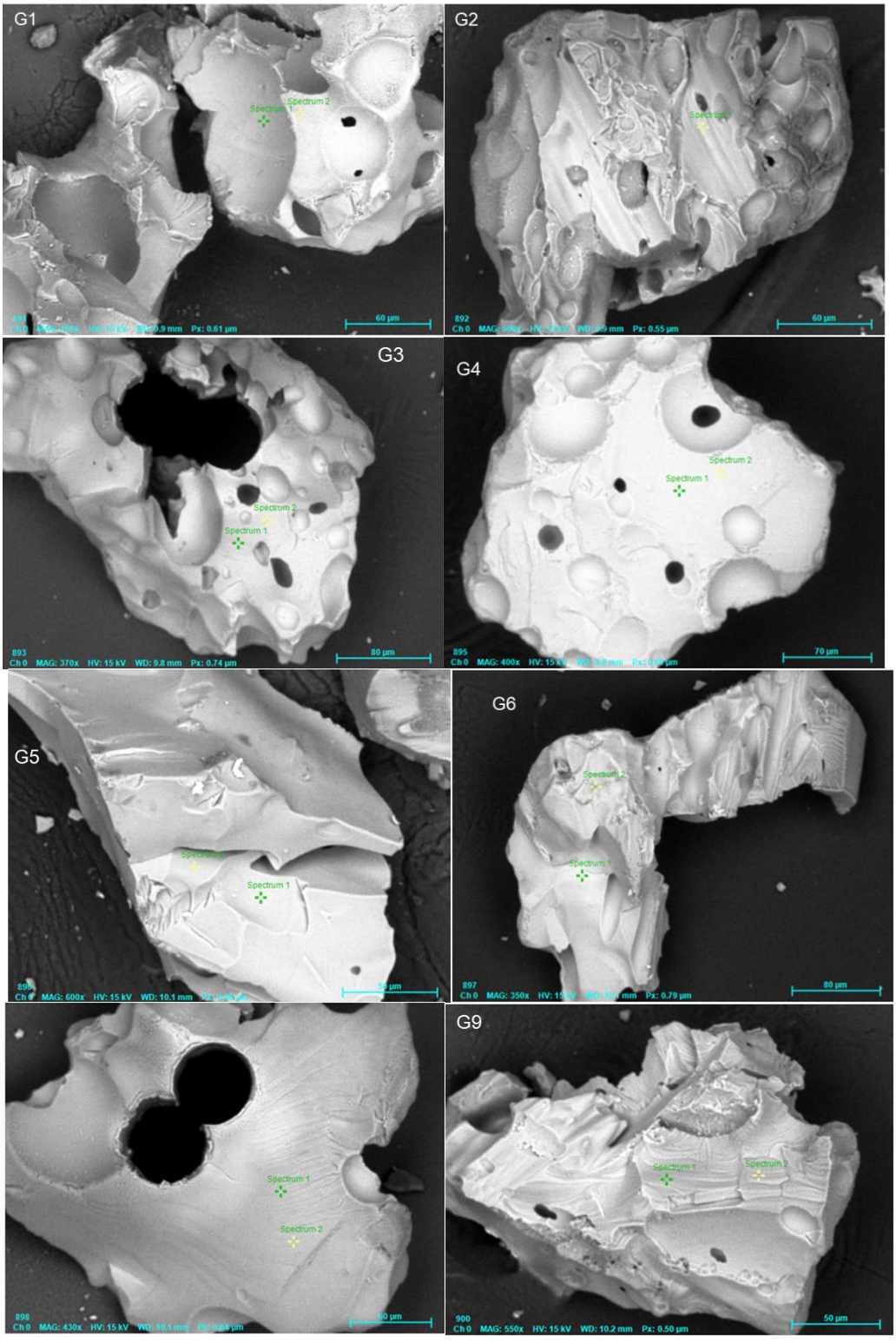
G1
Spectrum 1
Spectrum 2
60 µm
G2
Spectrum 1
60 µm
G3
Spectrum 2
Spectrum 1
80 µm
G4
Spectrum 2
Spectrum 1
70 µm
G5
Spectrum 1
50 µm
G6
Spectrum 2
Spectrum 1
80 µm
Spectrum 1
Spectrum 2
50 µm
G9
Spectrum 1
Spectrum 2
50 µm

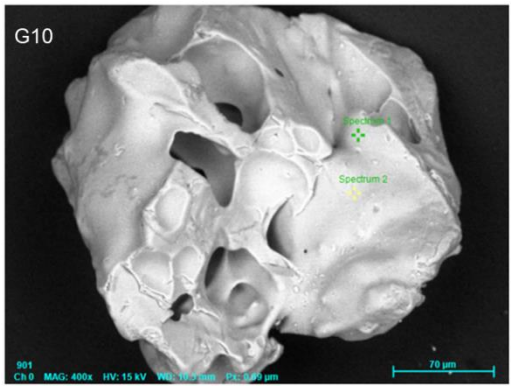

1232A-4H-6W-45 >149µ

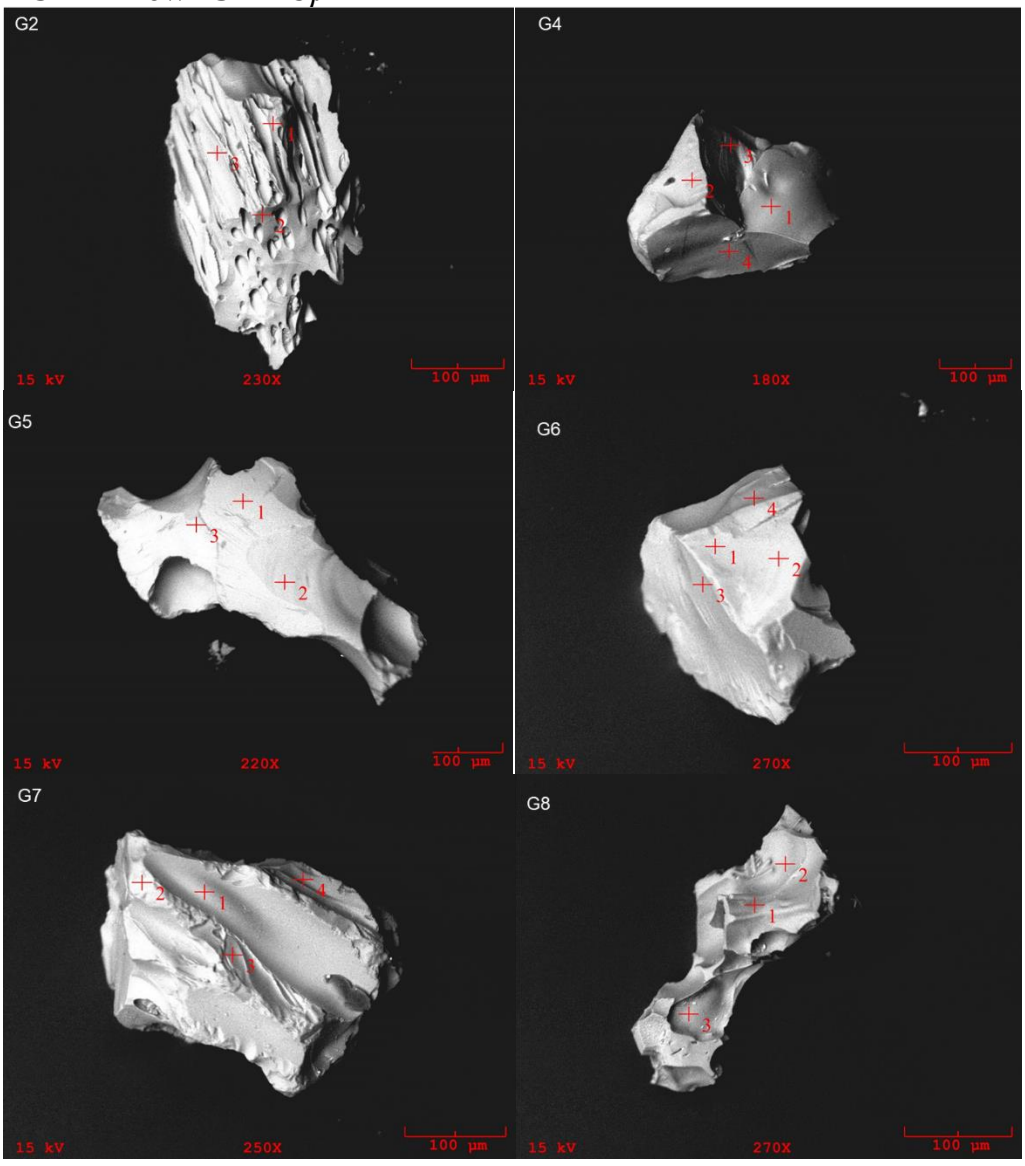

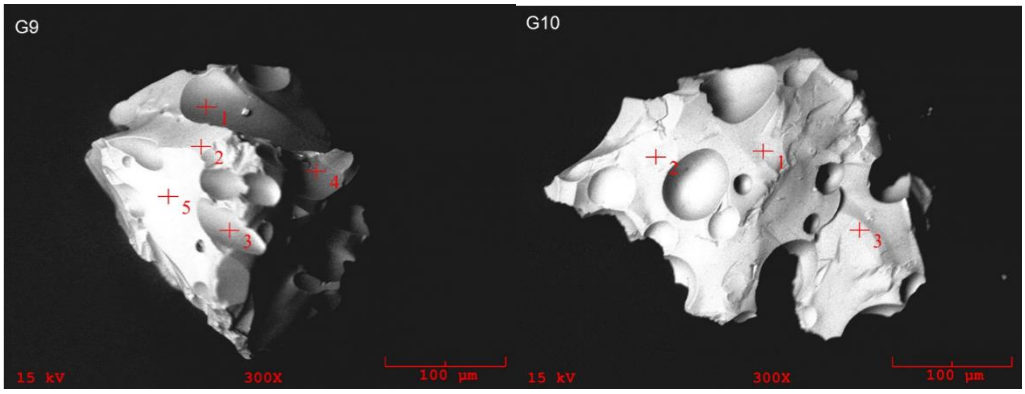

1232A-4H-6W-45 >210µ

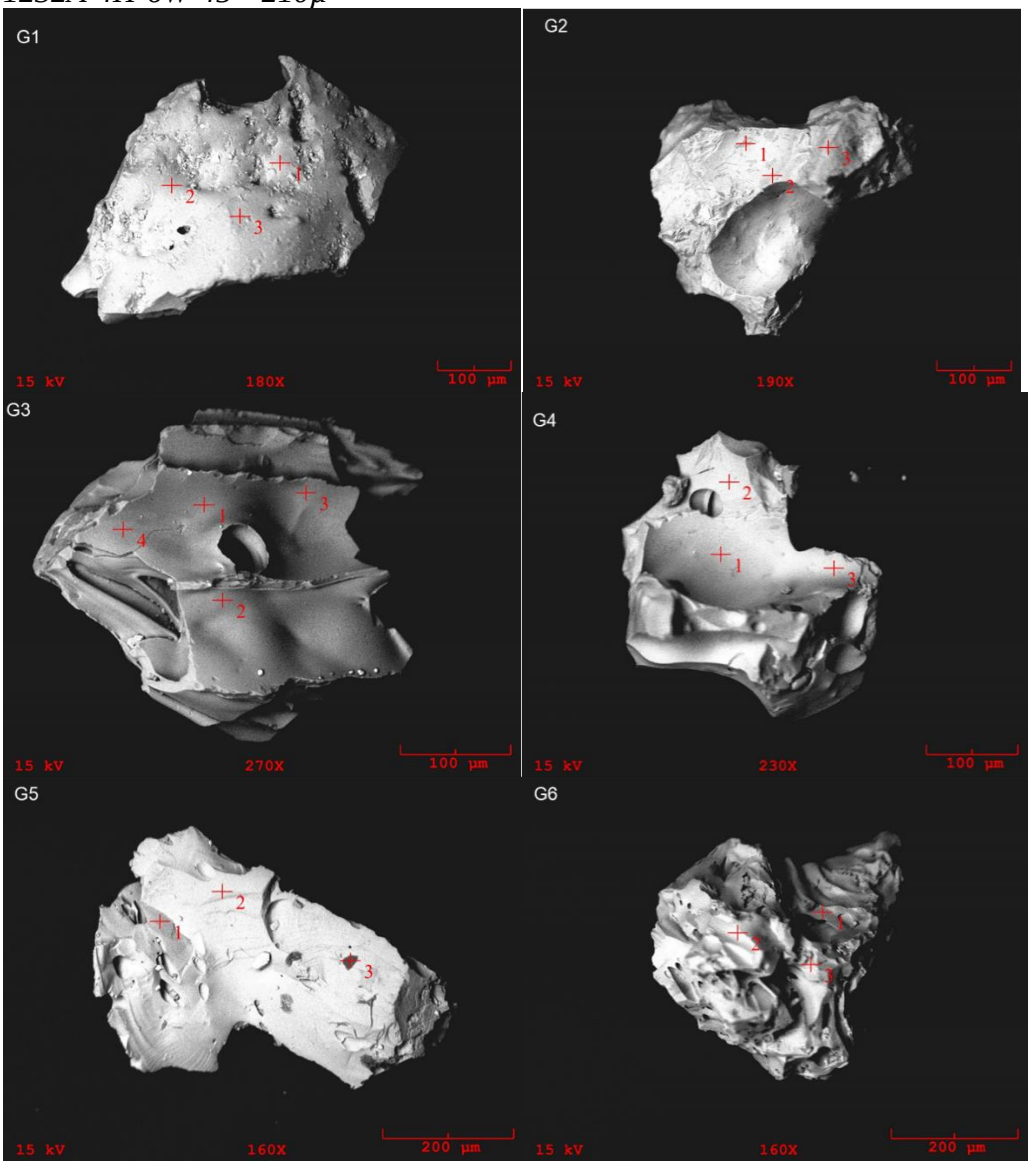

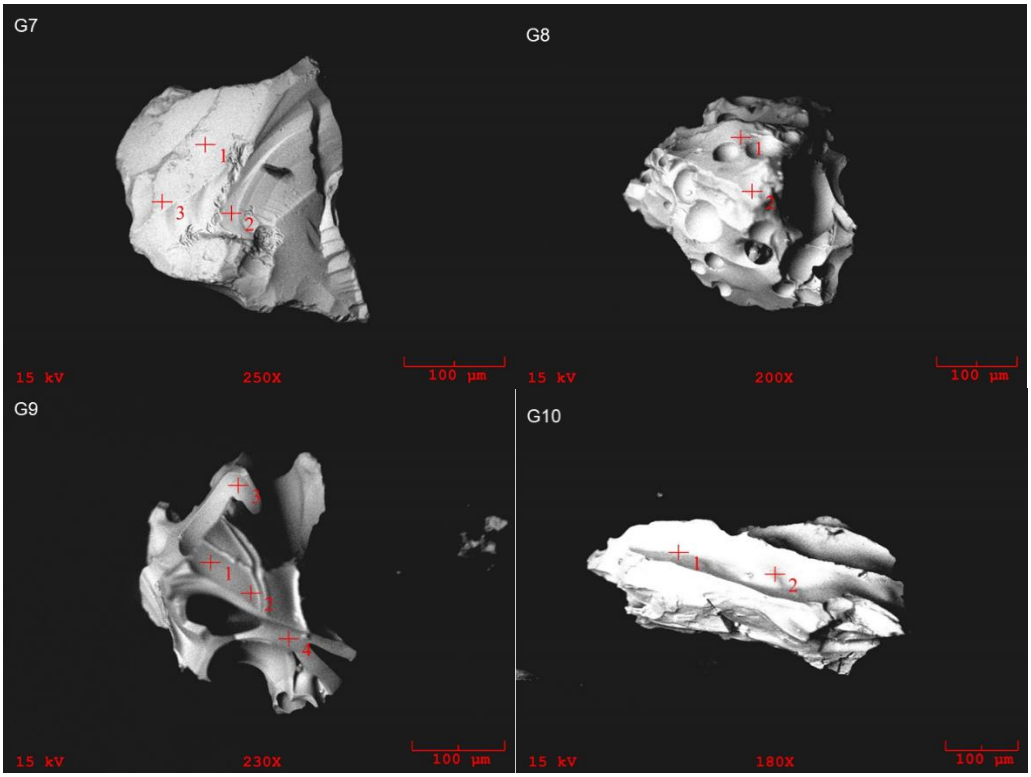

1232A-5H-7W-45 >149µ

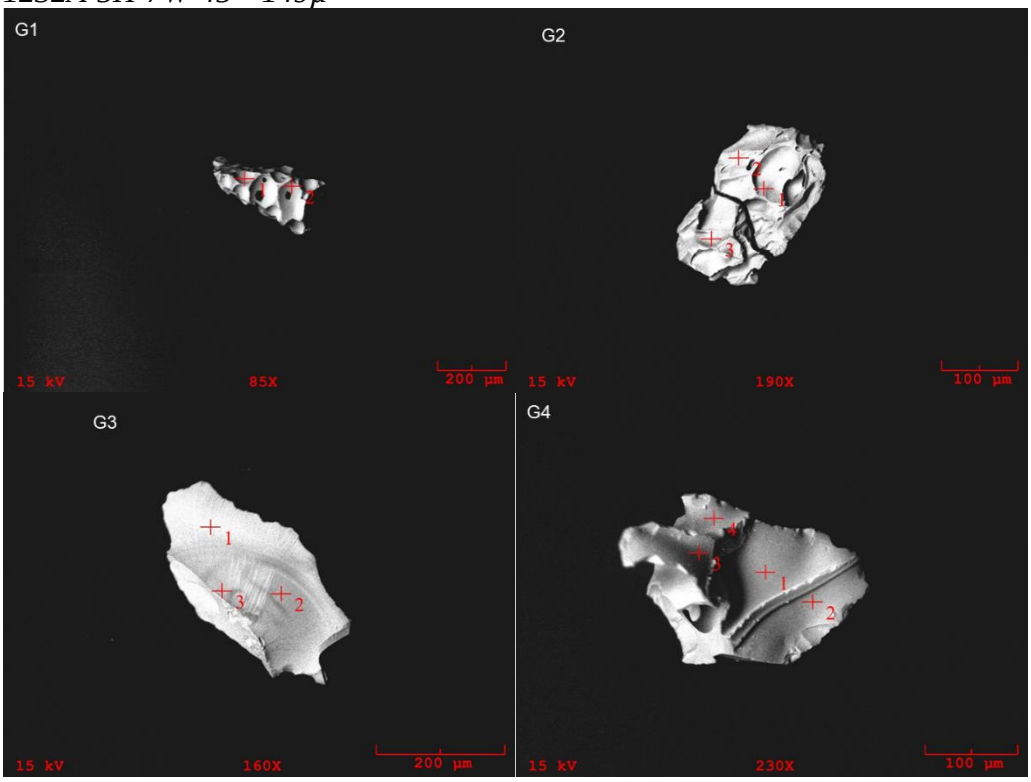

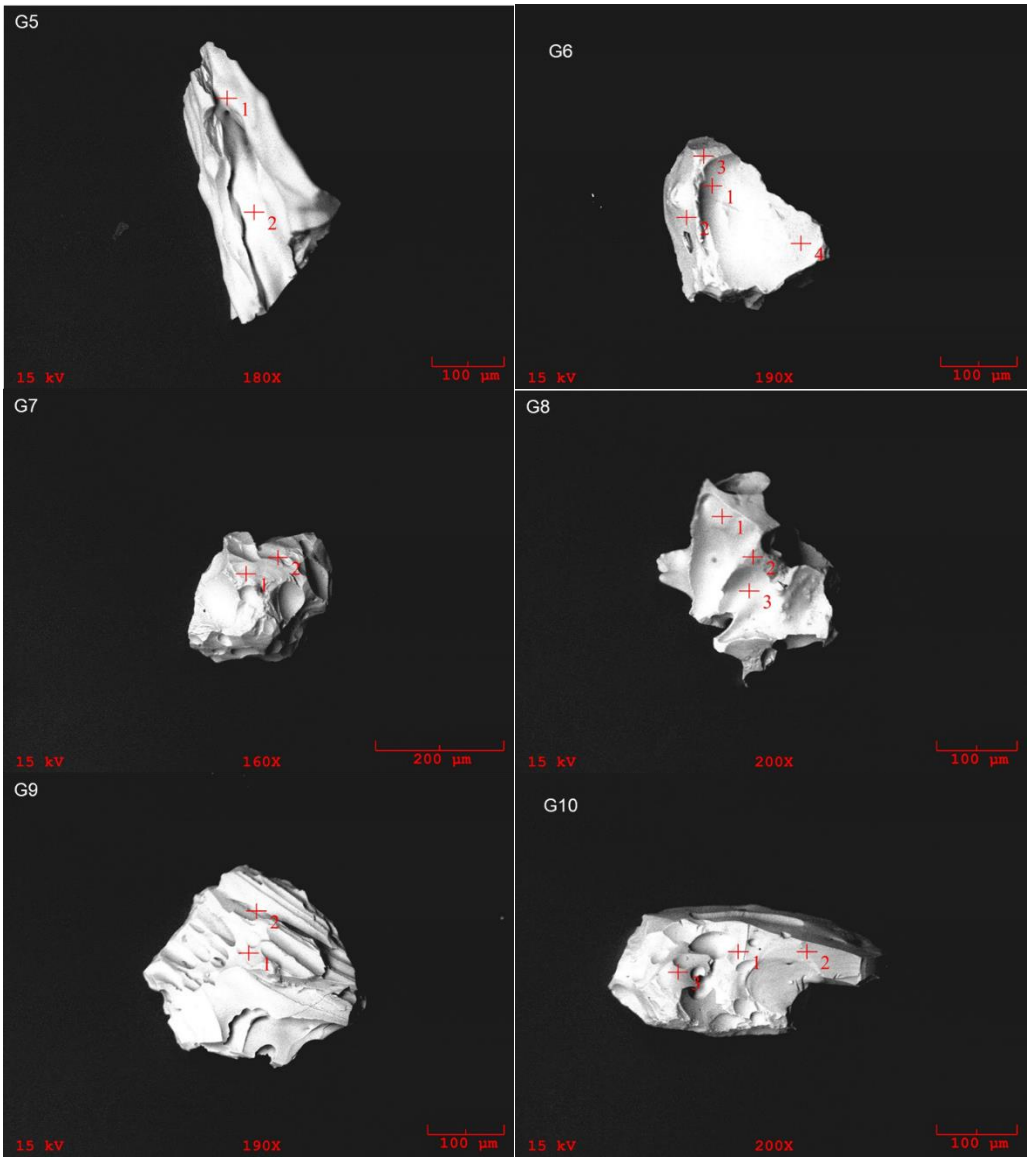

1232A-5H-7W-45 >210µ

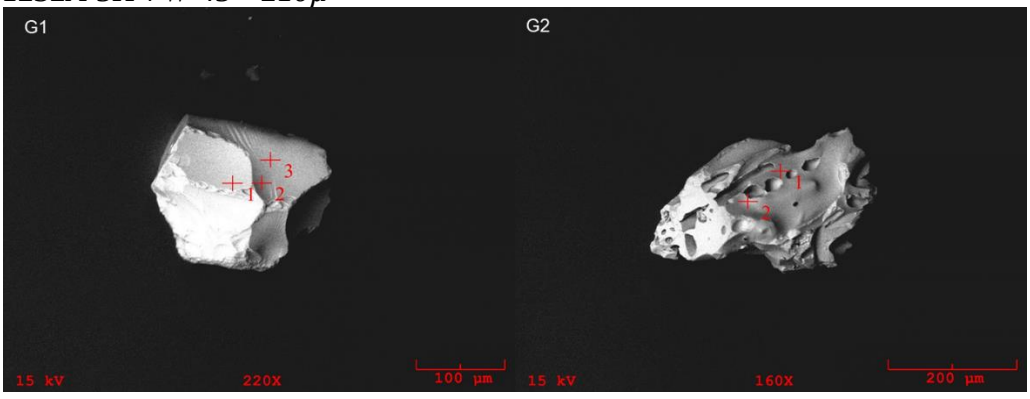

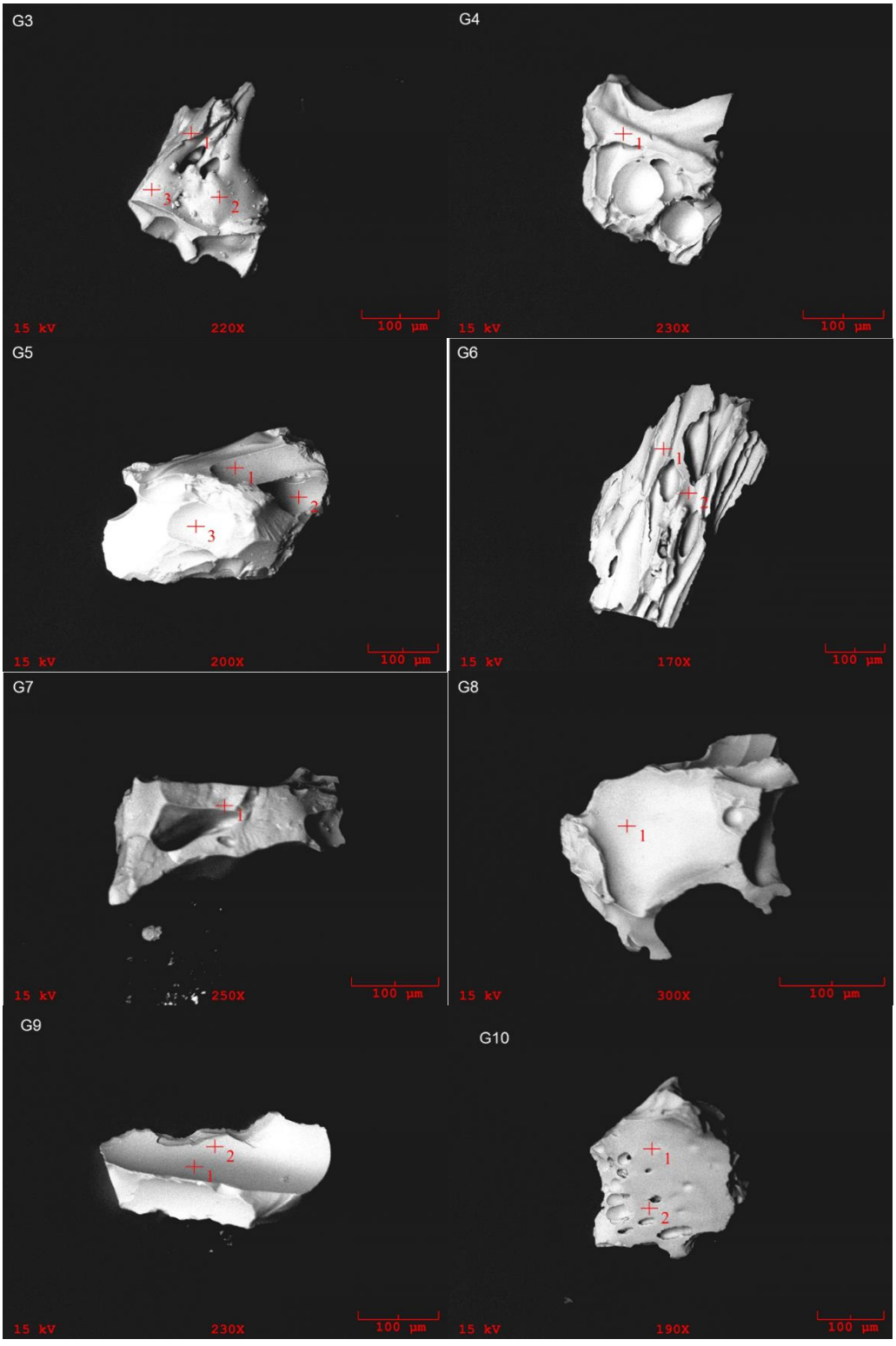

1232A-6H-4W-85 >149µ

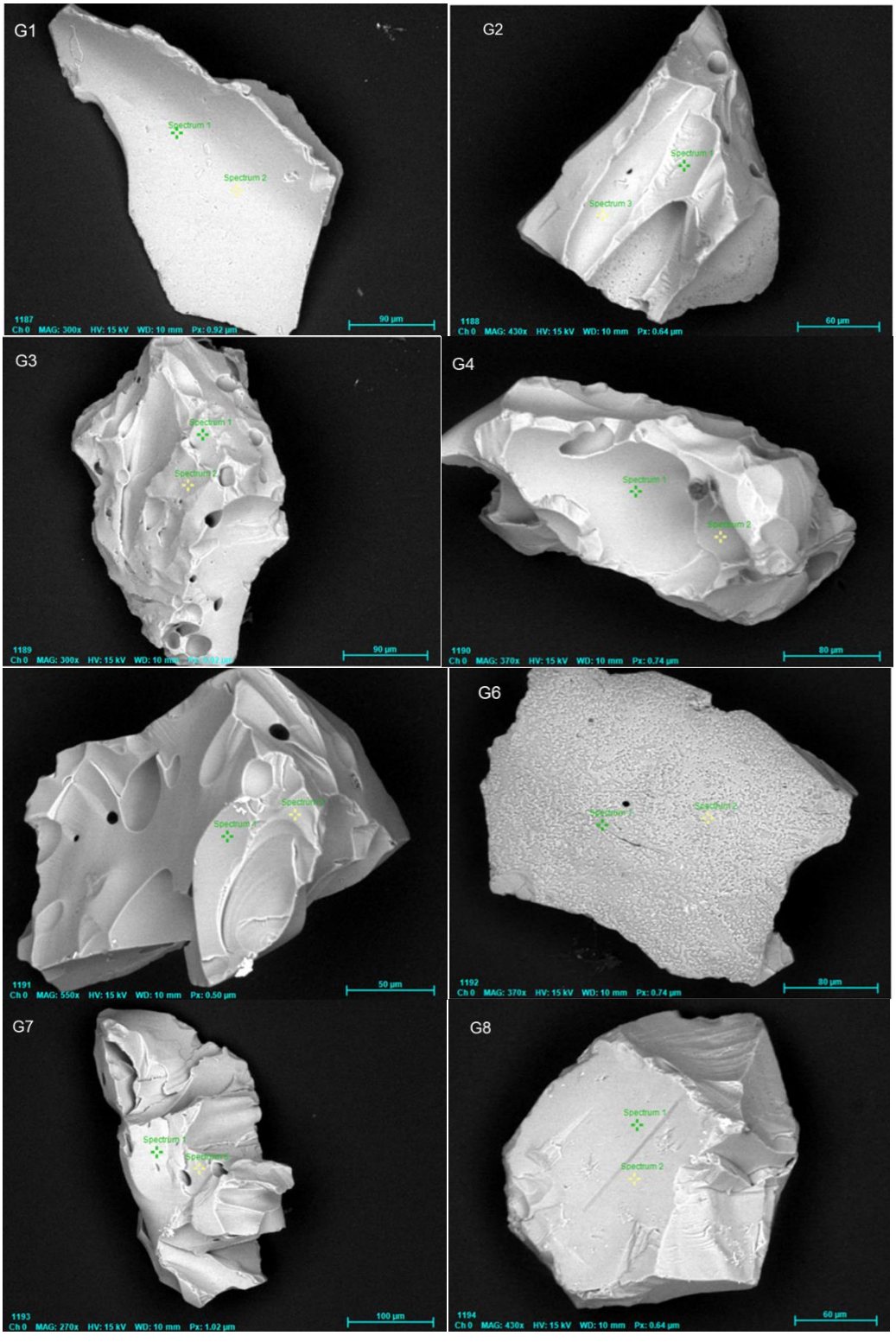
G1
Spectrum 1
Spectrum 2
1187
Ch 0 MAG: 300x HV: 15 kV WD: 10 mm Px: 0.92 µm
90 µm
G2
Spectrum 1
Spectrum 3
1188
Ch 0 MAG: 430x HV: 15 kV WD: 10 mm Px: 0.64 µm
60 µm
G3
Spectrum 1
Spectrum 2
1189
Ch 0 MAG: 300x HV: 15 kV WD: 10 mm
90 µm
G4
Spectrum 1
Spectrum 2
1190
Ch 0 MAG: 370x HV: 15 kV WD: 10 mm Px: 0.74 µm
80 µm
Spectrum 1
1191
Ch 0 MAG: 550x HV: 15 kV WD: 10 mm Px: 0.50 µm
50 µm
G6
Spectrum 1
Spectrum 2
1192
Ch 0 MAG: 370x HV: 15 kV WD: 10 mm Px: 0.74 µm
80 µm
G7
Spectrum 1
1193
Ch 0 MAG: 270x HV: 15 kV WD: 10 mm Px: 1.02 µm
100 µm
G8
Spectrum 1
Spectrum 2
1194
Ch 0 MAG: 430x HV: 15 kV WD: 10 mm Px: 0.64 µm
60 µm

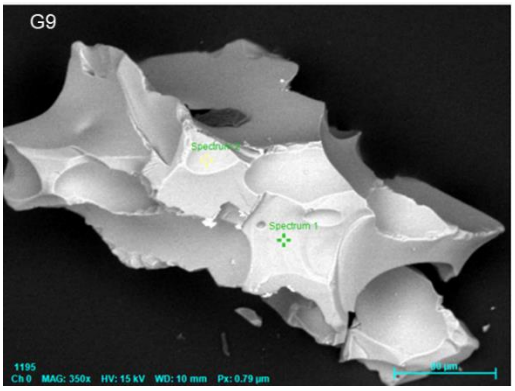

1232A-6H-4W-85 >210µ

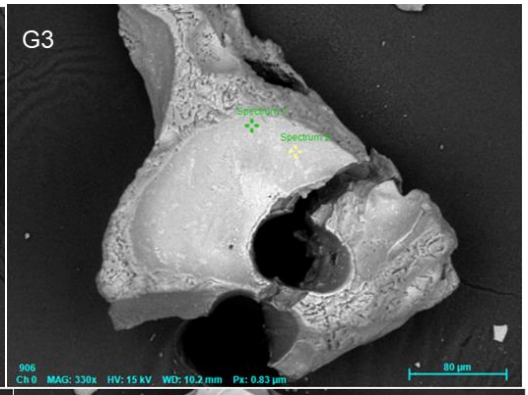

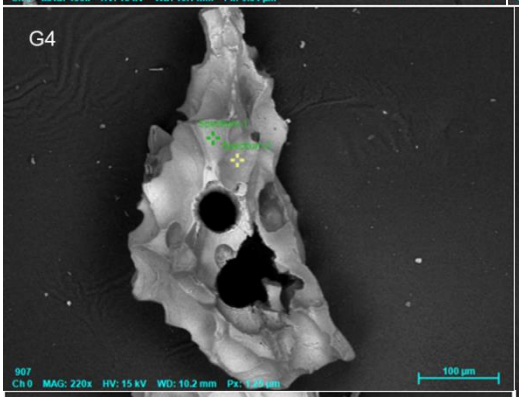

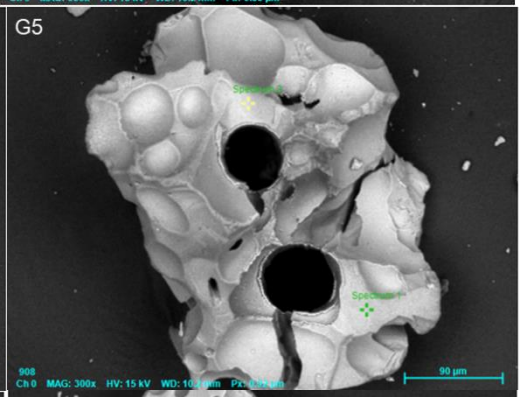

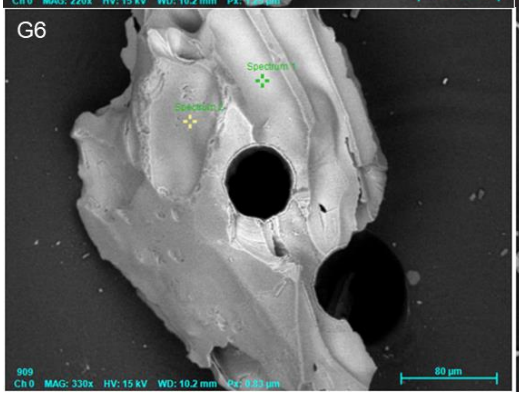

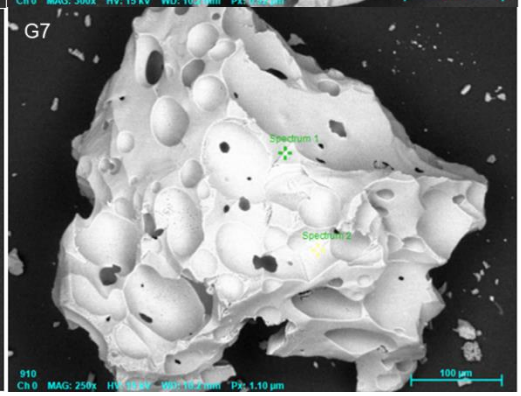

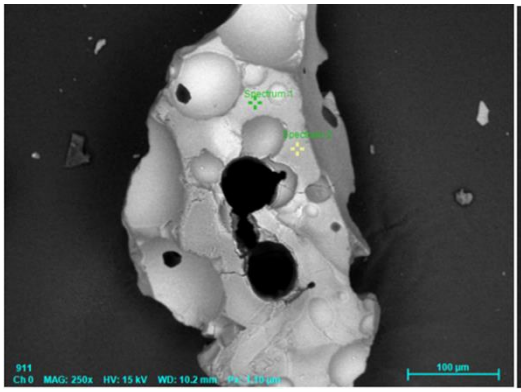

1232A-6H-6W-118 >149µ

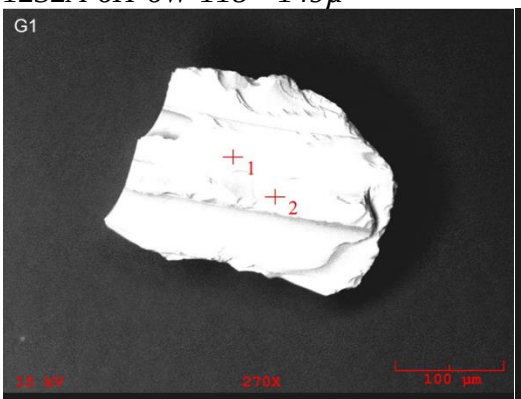

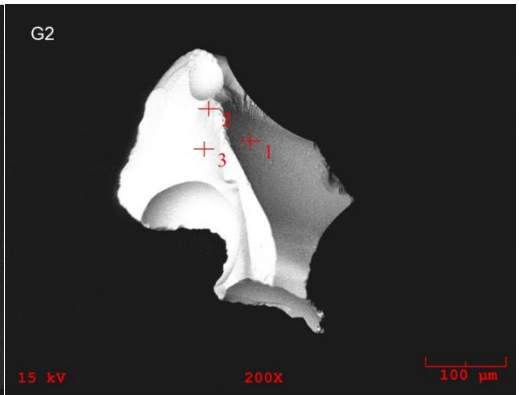

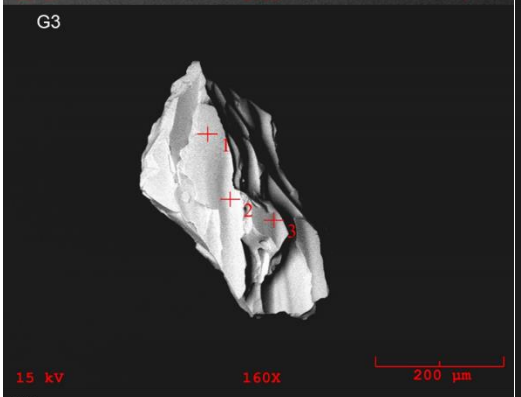

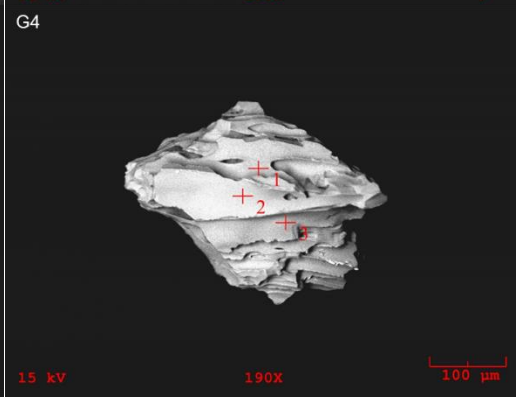

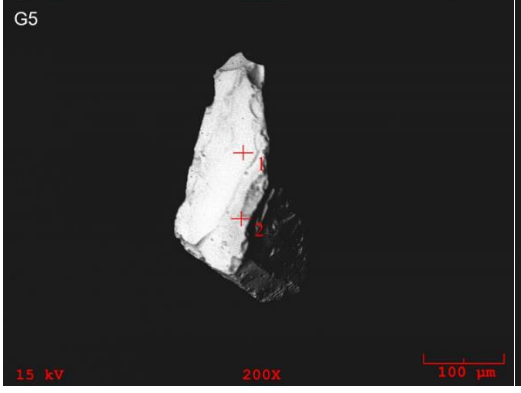

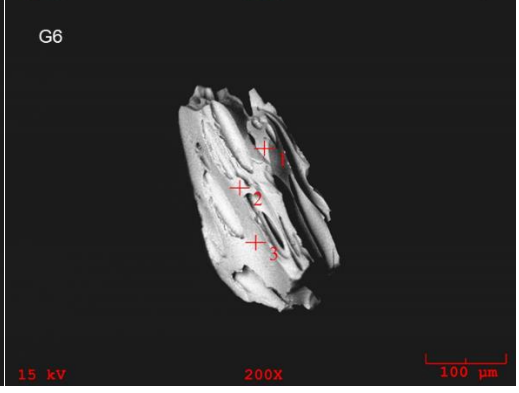

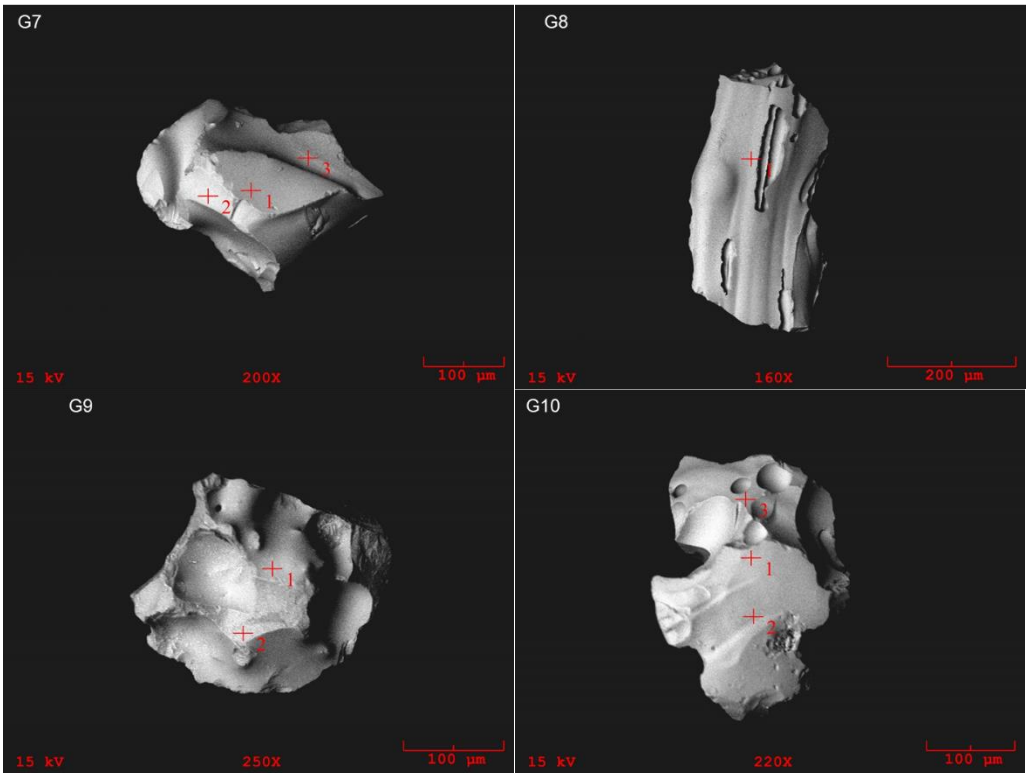

1232A-6H-6W-118 >210µ

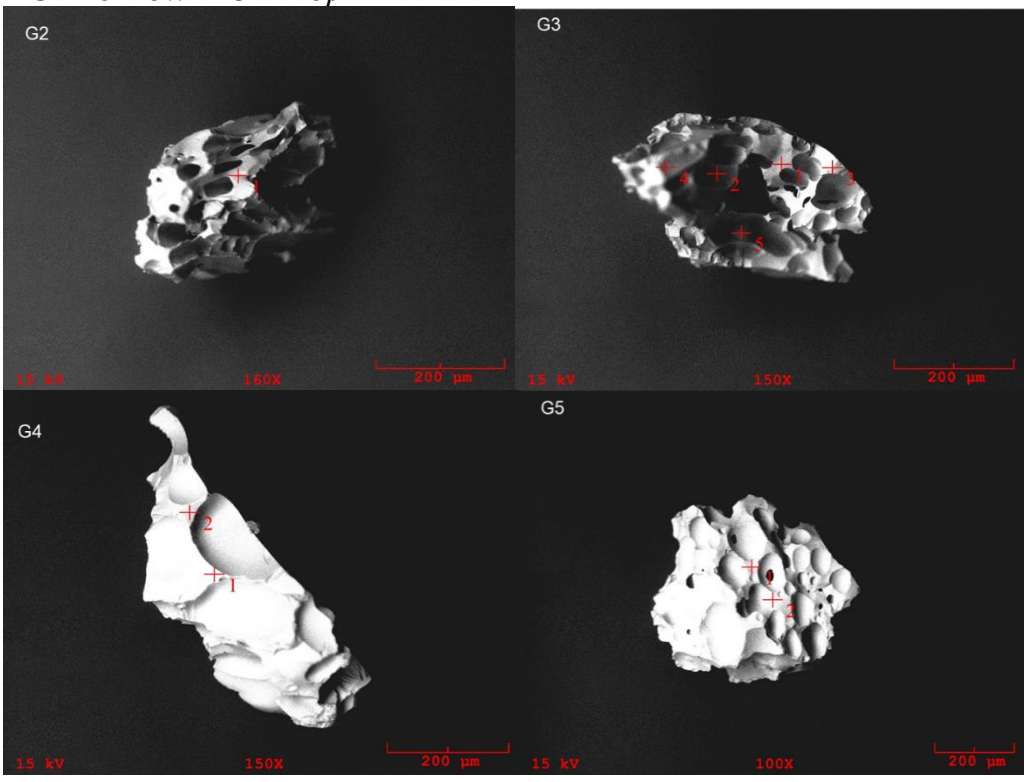

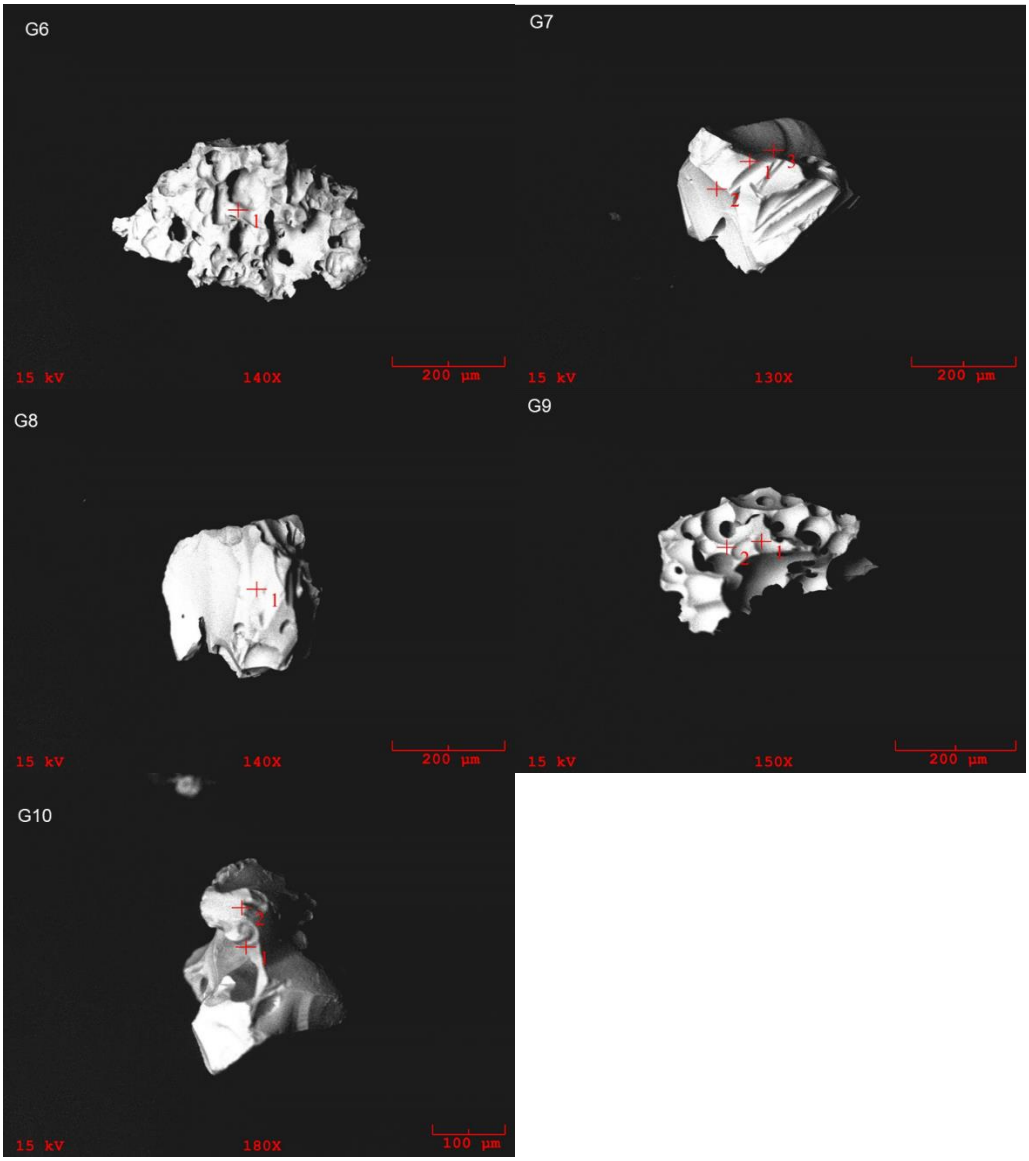

1232A-7H-2W-86 >149µ

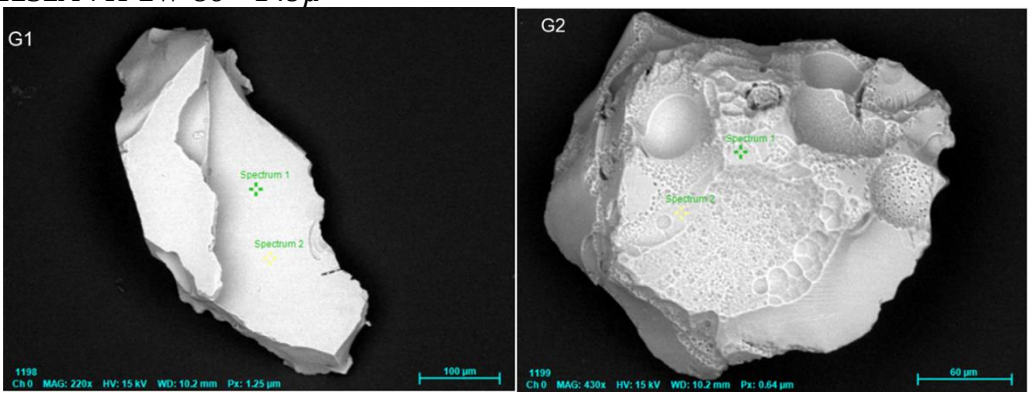

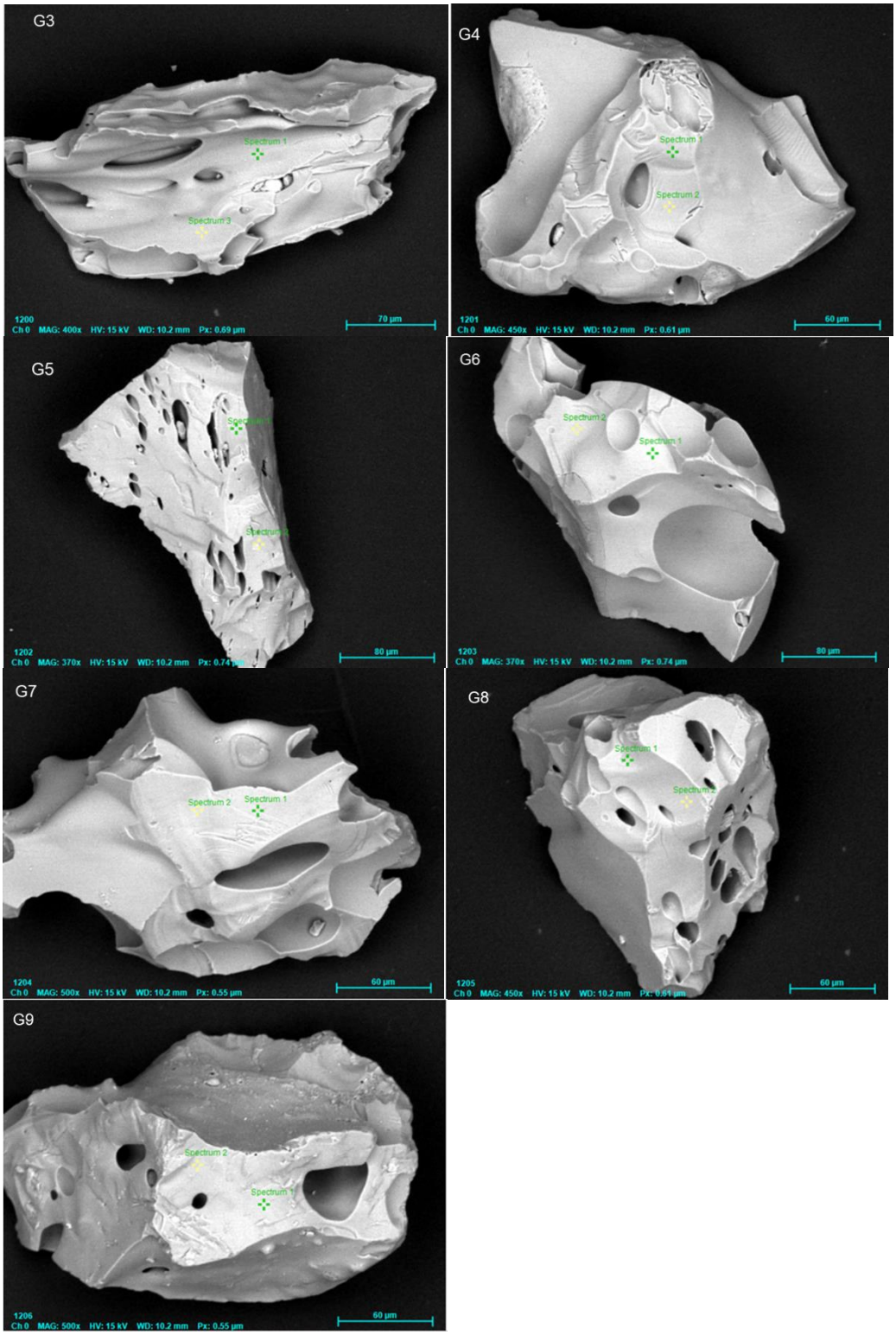

1232A-7H-2W-86 >210µ

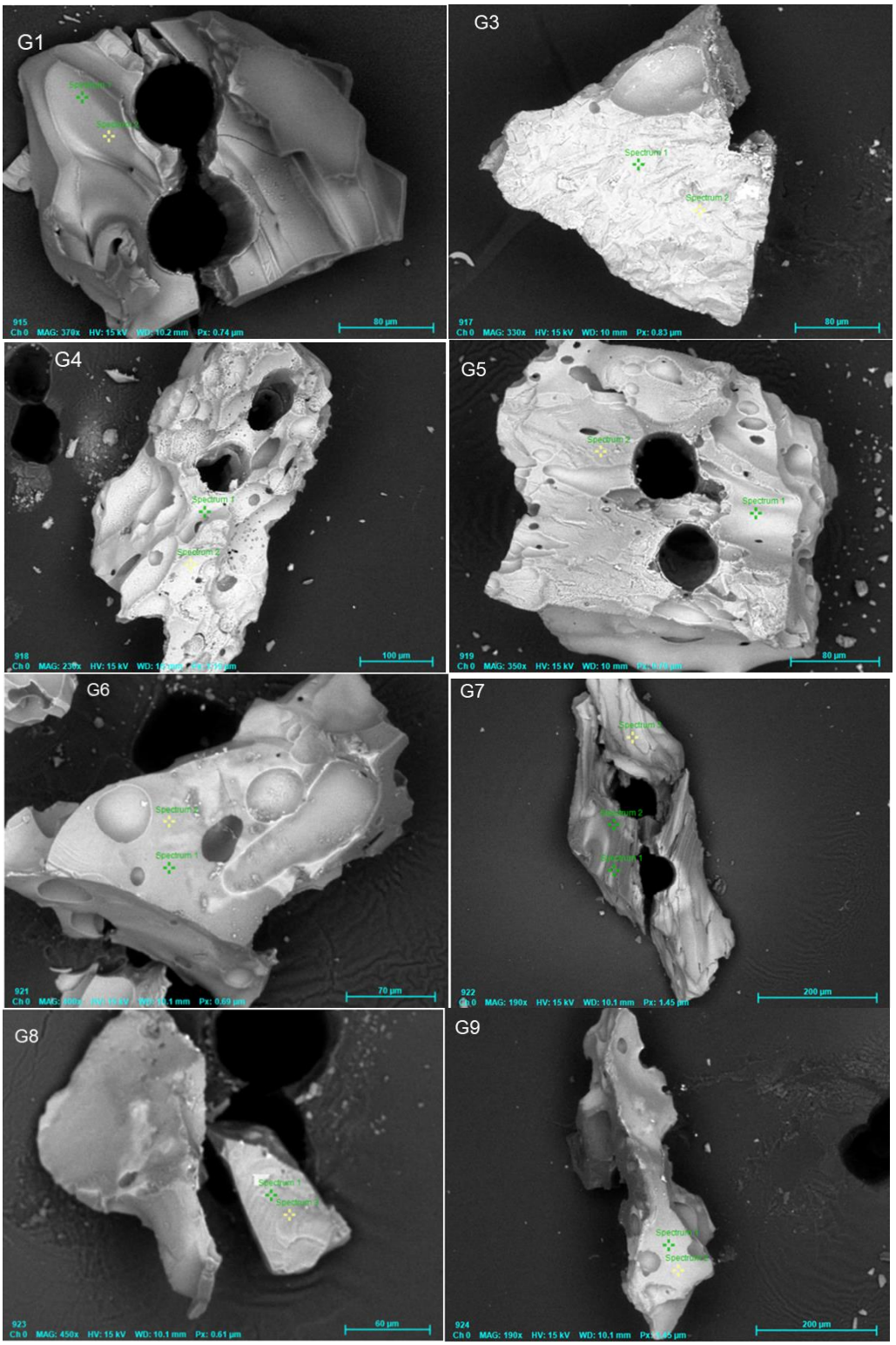

1232A-7H-5W-87 >149µ

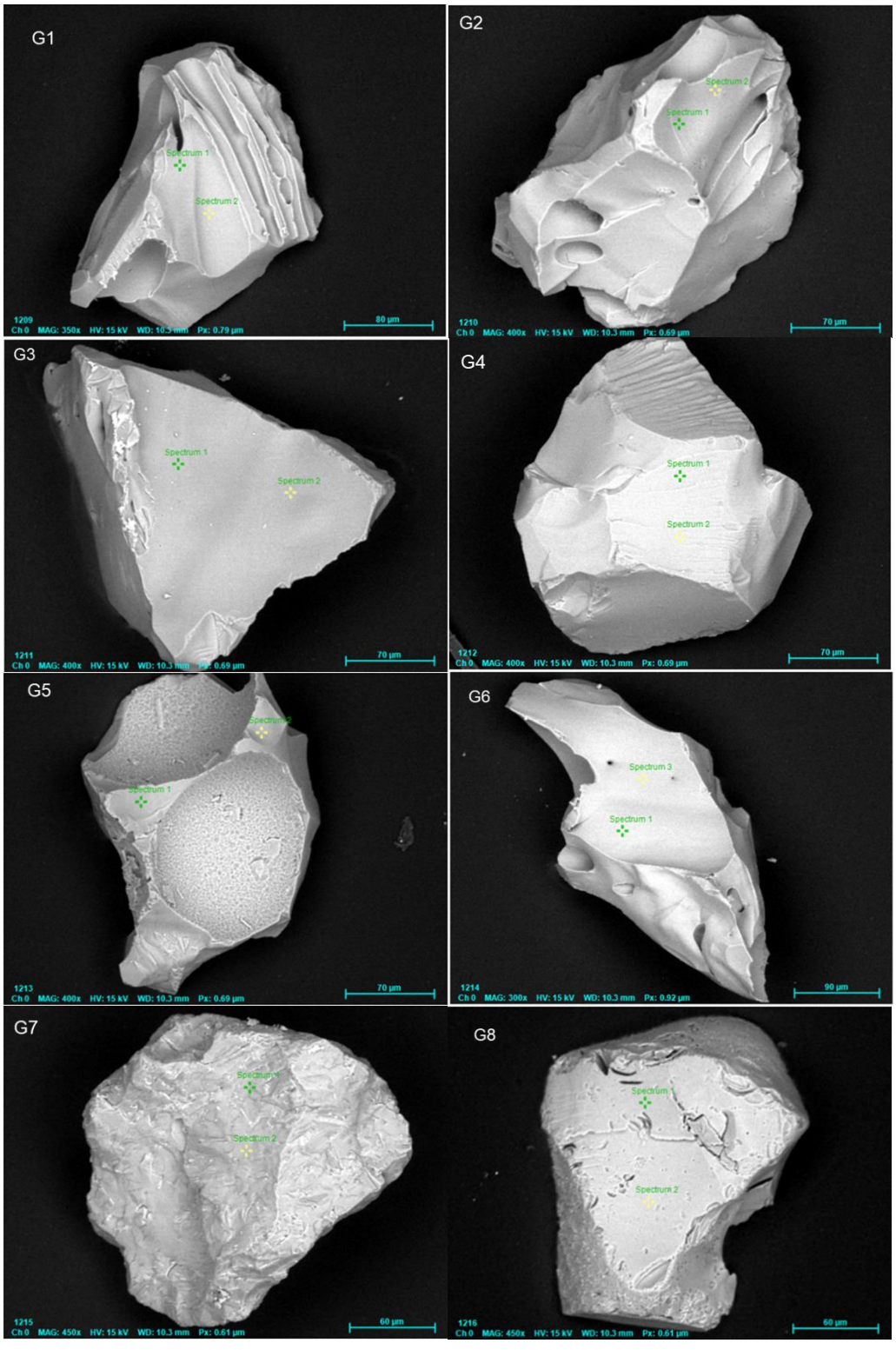
G1
Spectrum 1
Spectrum 2
1209
Ch 0 MAG: 350x HV: 15 kV WD: 10.3 mm Px: 0.79 µm
80 µm
G2
Spectrum 2
Spectrum 1
1210
Ch 0 MAG: 400x HV: 15 kV WD: 10.3 mm Px: 0.69 µm
70 µm
G3
Spectrum 1
Spectrum 2
1211
Ch 0 MAG: 400x HV: 15 kV WD: 10.3 mm Px: 0.69 µm
70 µm
G4
Spectrum 1
Spectrum 2
1212
Ch 0 MAG: 400x HV: 15 kV WD: 10.3 mm Px: 0.69 µm
70 µm
G5
Spectrum 2
Spectrum 1
1213
Ch 0 MAG: 400x HV: 15 kV WD: 10.3 mm Px: 0.69 µm
70 µm
G6
Spectrum 3
Spectrum 1
1214
Ch 0 MAG: 300x HV: 15 kV WD: 10.3 mm Px: 0.92 µm
90 µm
G7
Spectrum 1
Spectrum 2
1215
Ch 0 MAG: 450x HV: 15 kV WD: 10.3 mm Px: 0.61 µm
60 µm
G8
Spectrum 1
Spectrum 2
1216
Ch 0 MAG: 450x HV: 15 kV WD: 10.3 mm Px: 0.61 µm
60 µm

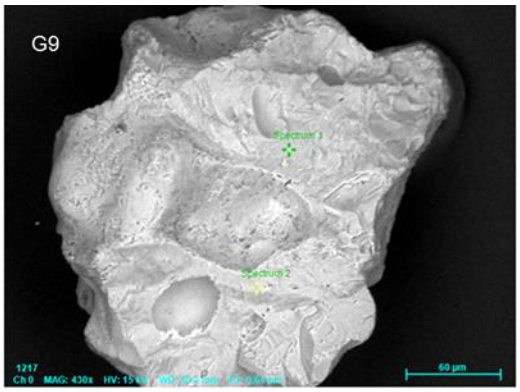

1232A-7H-5W-87 >210µ

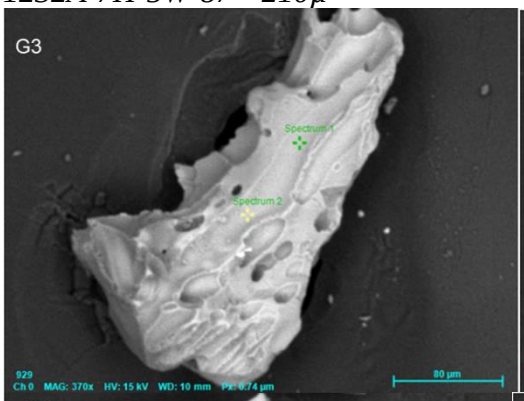

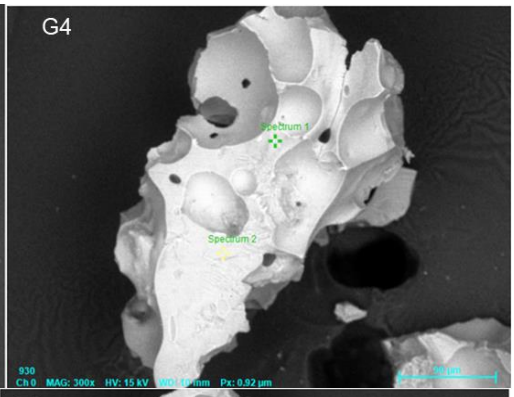

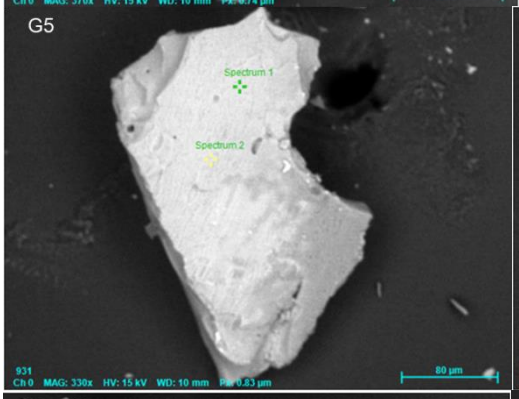

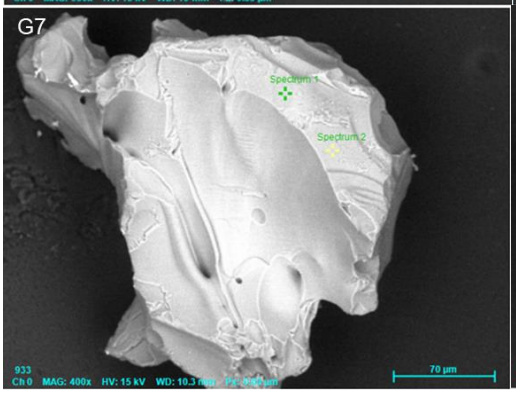

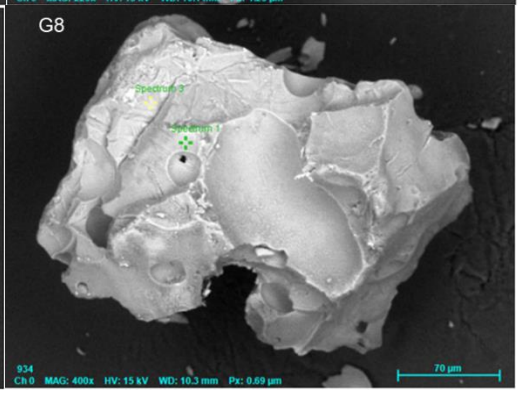

1232A-7H-6W-42 >149µ

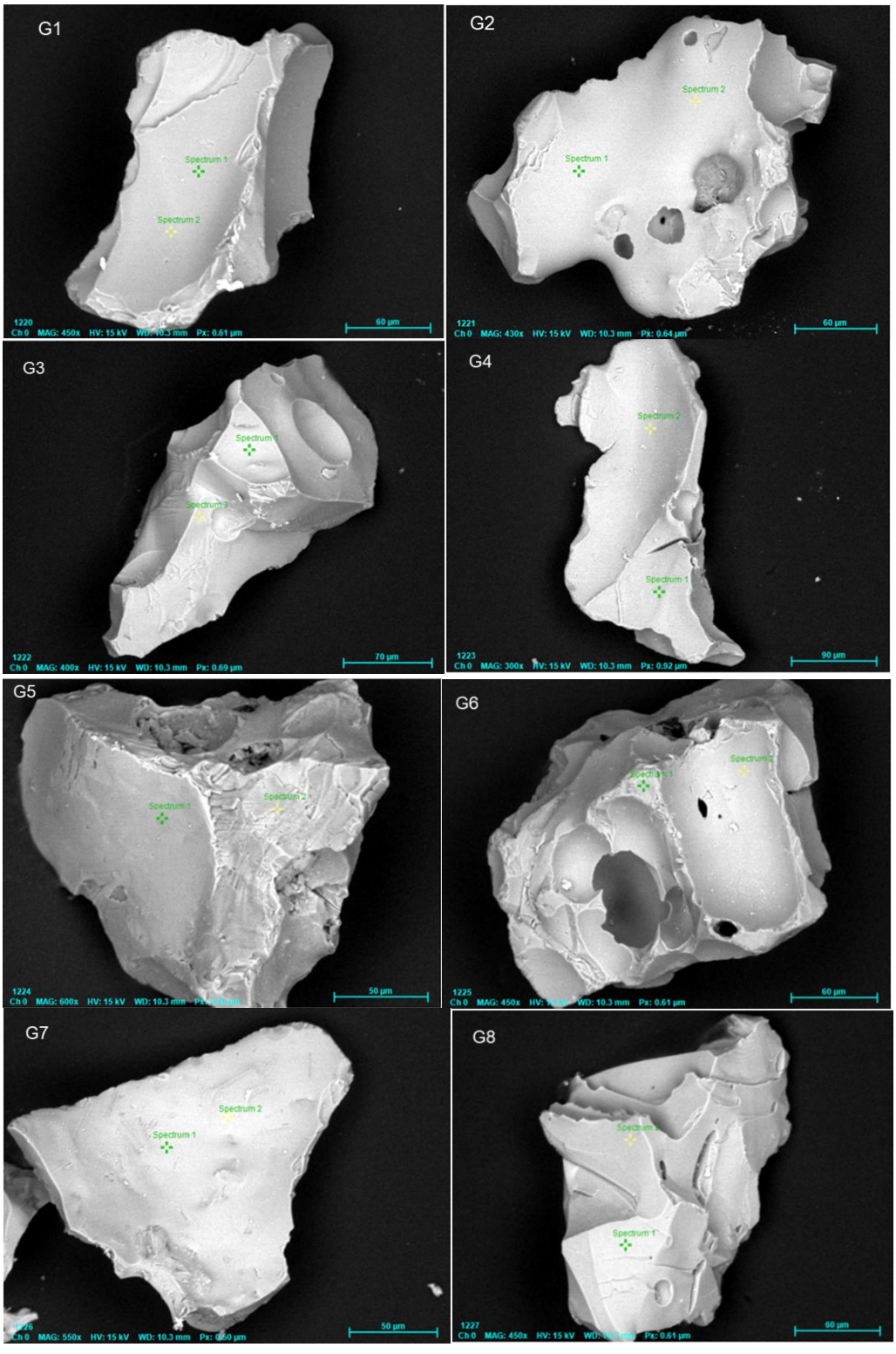
G1
Spectrum 1
Spectrum 2
1220
Ch 0 MAG: 450x HV: 15 kV WD: 10.3 mm Px: 0.61 µm
60 µm
G2
Spectrum 2
Spectrum 1
1221
Ch 0 MAG: 430x HV: 15 kV WD: 10.3 mm Px: 0.64 µm
60 µm
G3
Spectrum 1
Spectrum 2
1222
Ch 0 MAG: 400x HV: 15 kV WD: 10.3 mm Px: 0.69 µm
70 µm
G4
Spectrum 2
Spectrum 1
1223
Ch 0 MAG: 300x HV: 15 kV WD: 10.3 mm Px: 0.92 µm
90 µm
G5
Spectrum 1
Spectrum 2
1224
Ch 0 MAG: 600x HV: 15 kV WD: 10.3 mm
50 µm
G6
Spectrum 1
Spectrum 2
1225
Ch 0 MAG: 450x HV: 15 kV WD: 10.3 mm Px: 0.61 µm
60 µm
G7
Spectrum 2
Spectrum 1
Ch 0 MAG: 550x HV: 15 kV WD: 10.3 mm
50 µm
G8
Spectrum 1
1227
Ch 0 MAG: 450x HV: 15 kV
60 µm

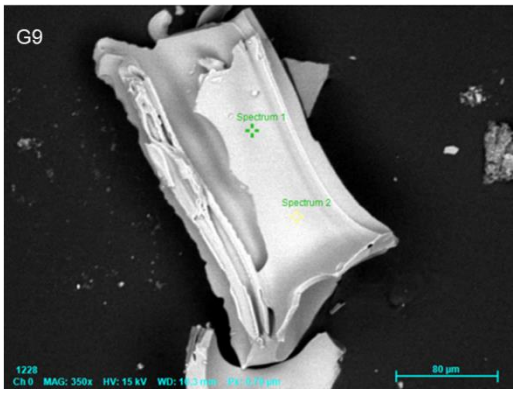

1232A-7H-6W-42 >210µ

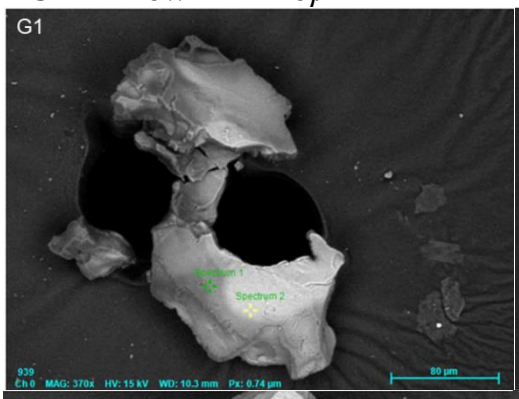

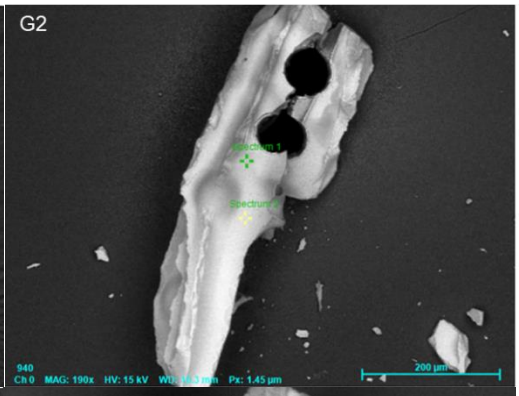

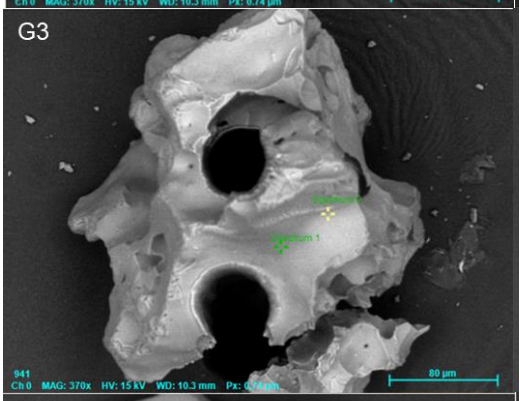

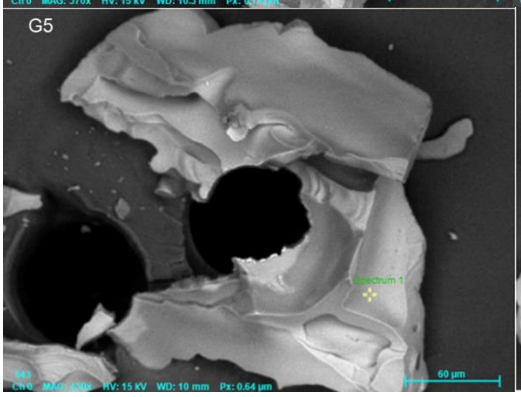

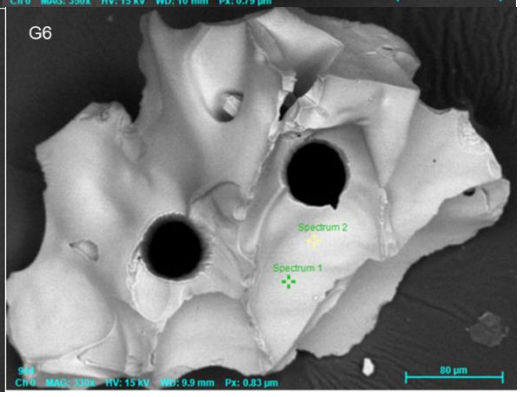

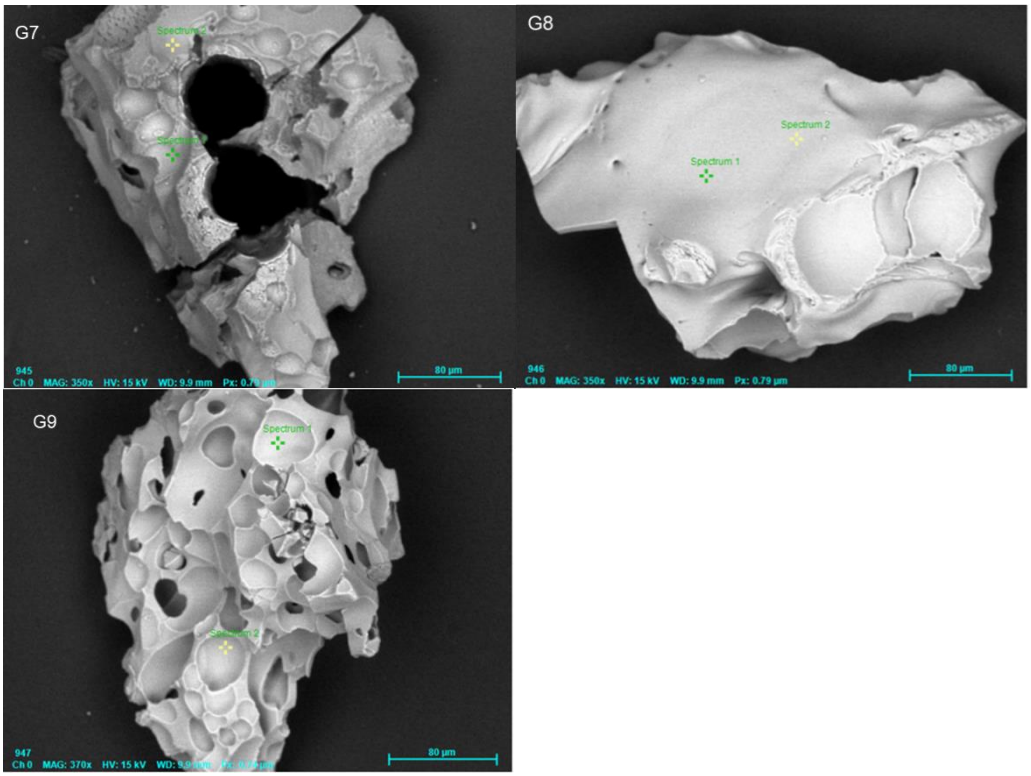

1232A-8H-1W-46 >149µ

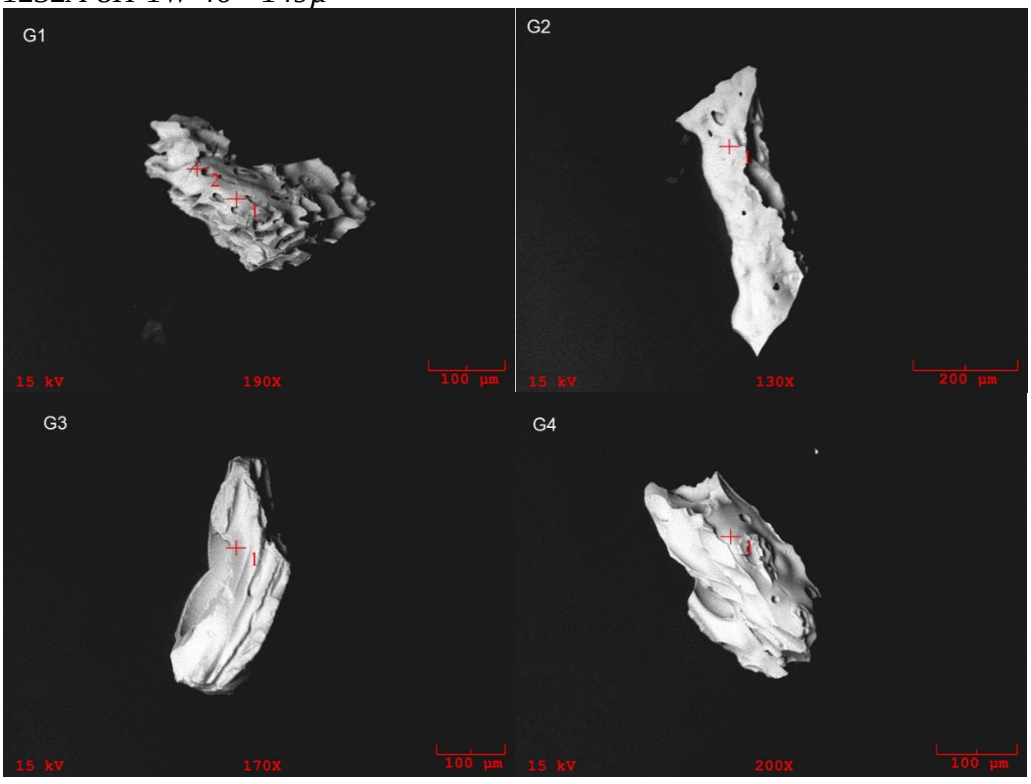

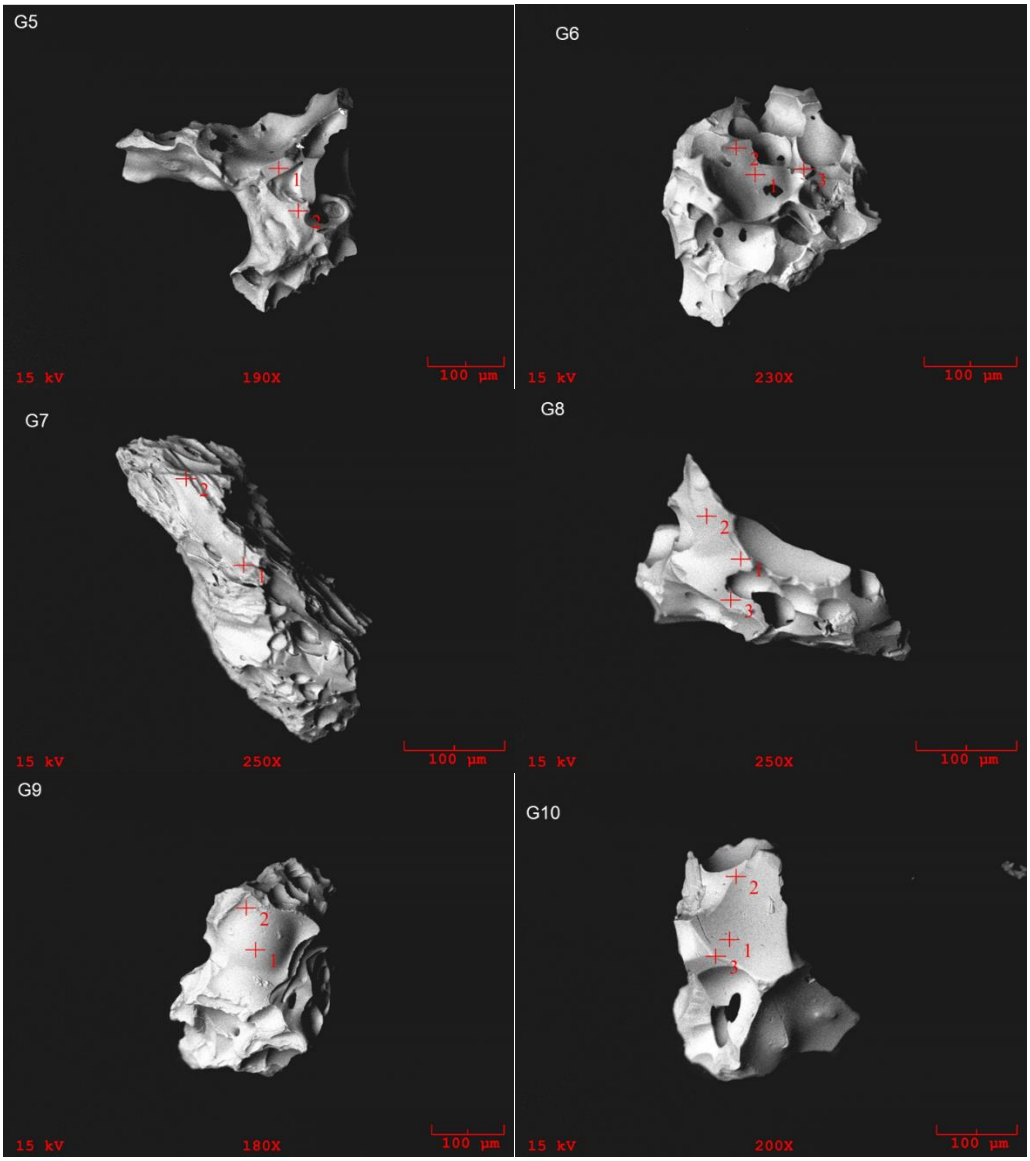

1232A-8H-1W-46 >210µ

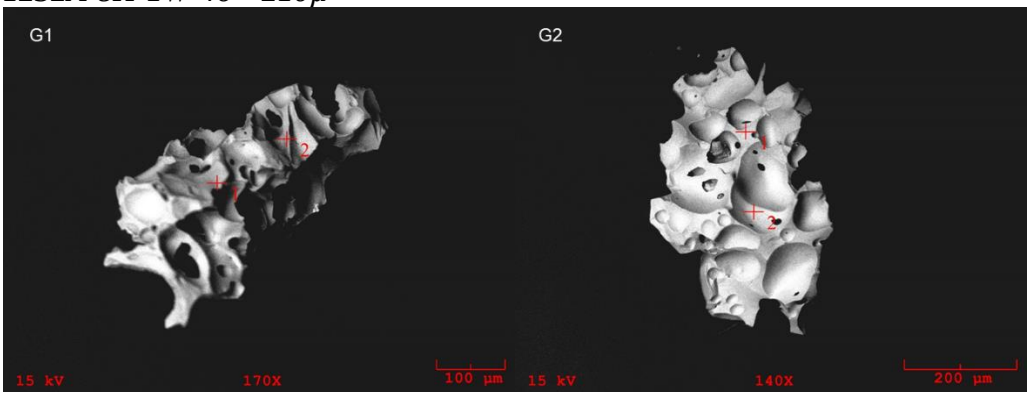

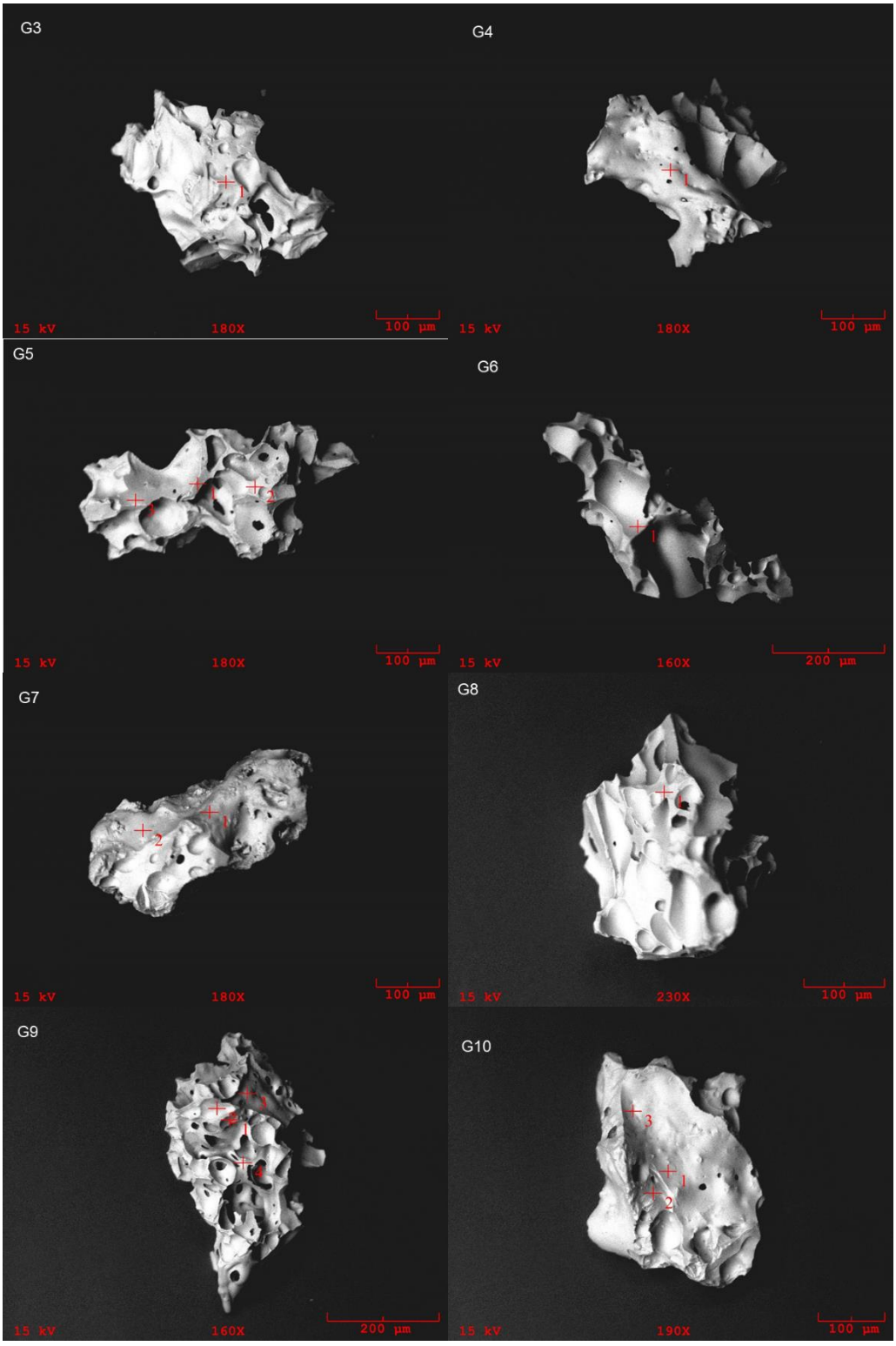

1232A-10H-3W-25 >149µ

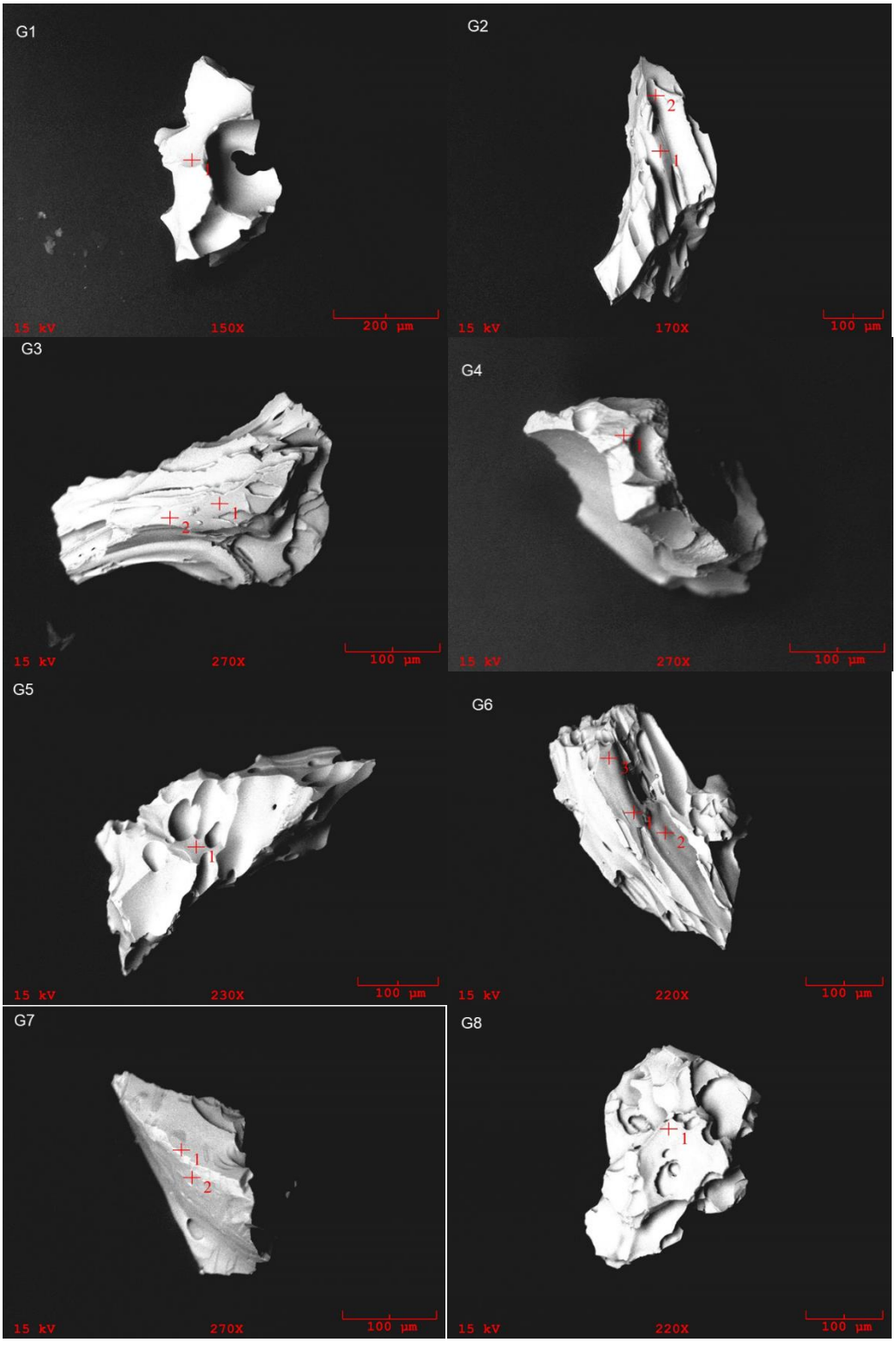
G1
15 kV
150X
200 µm
G2
15 kV
170X
100 µm
G3
15 kV
270X
100 µm
G4
15 kV
270X
100 µm
G5
15 kV
230X
100 µm
G6
15 kV
220X
100 µm
G7
15 kV
270X
100 µm
G8
15 kV
220X
100 µm

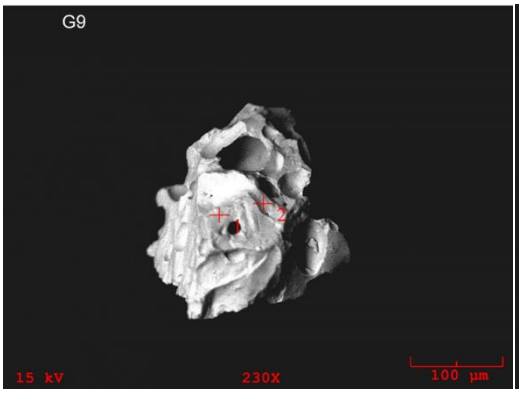

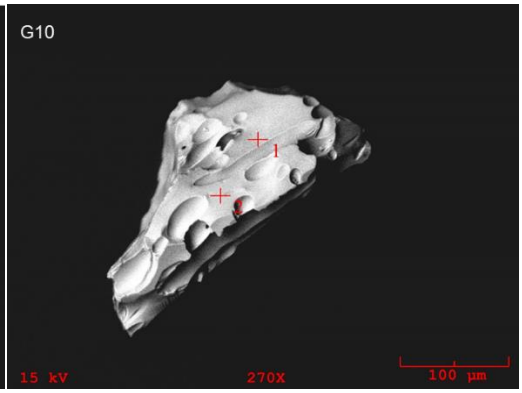

1232A-10H-3W-25 >210µ

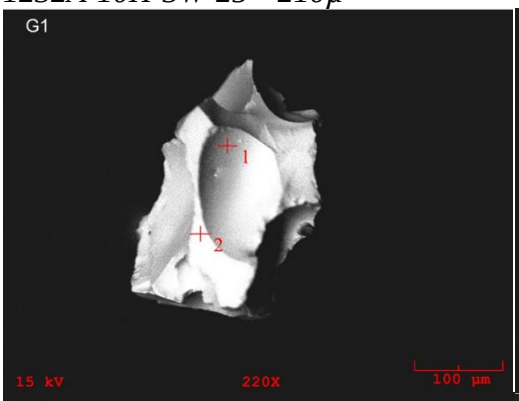

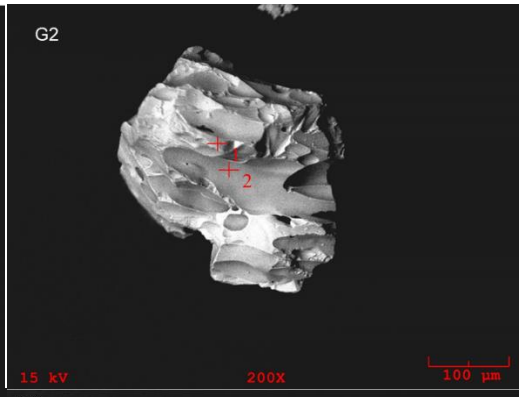

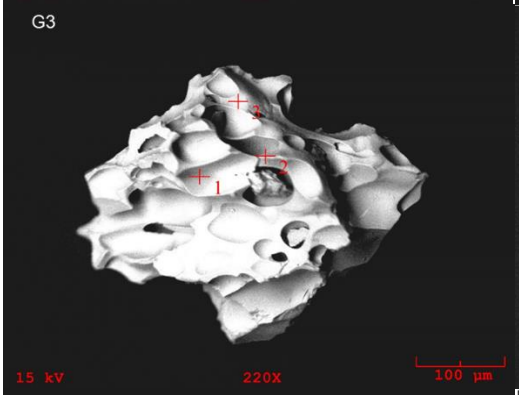

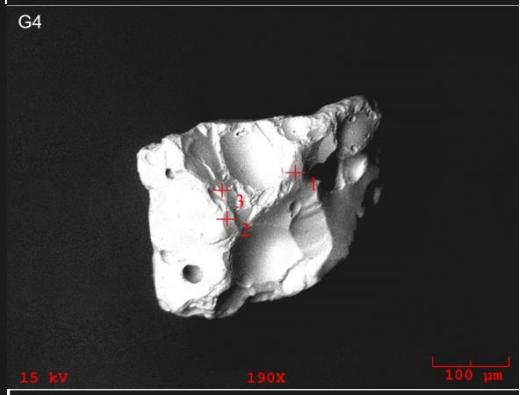

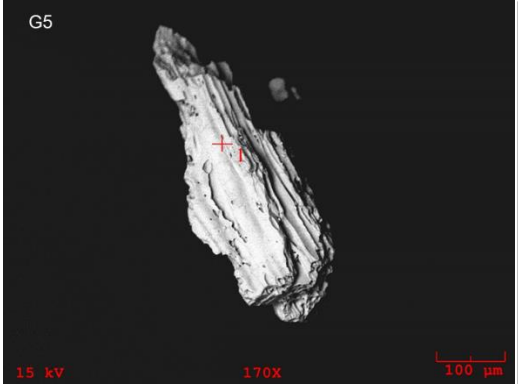

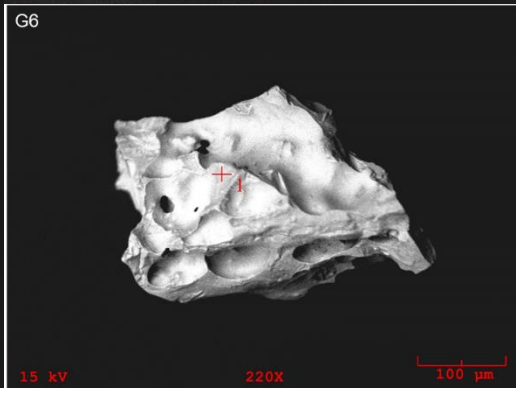

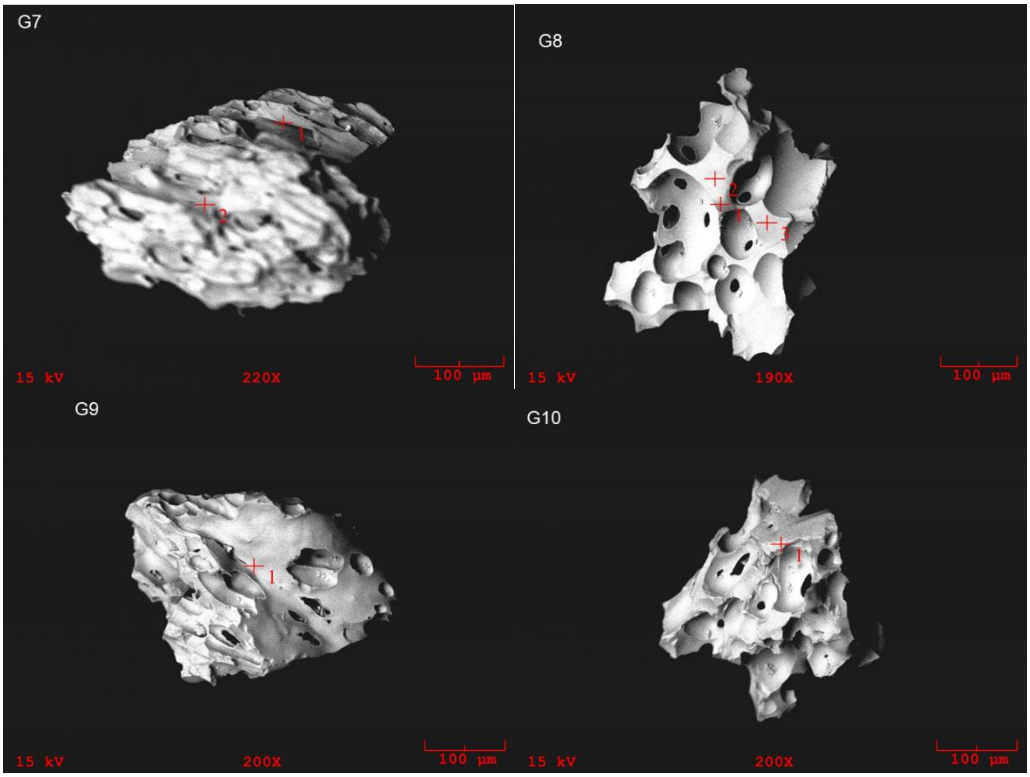

1232A-12H-1W-125 >149µ

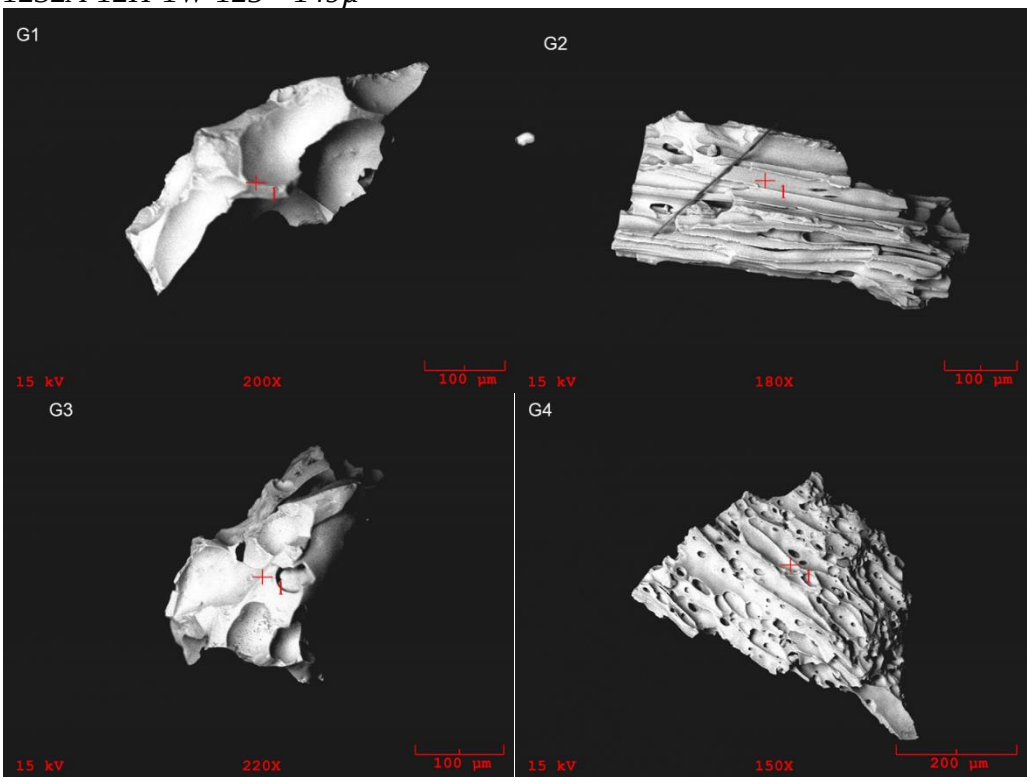

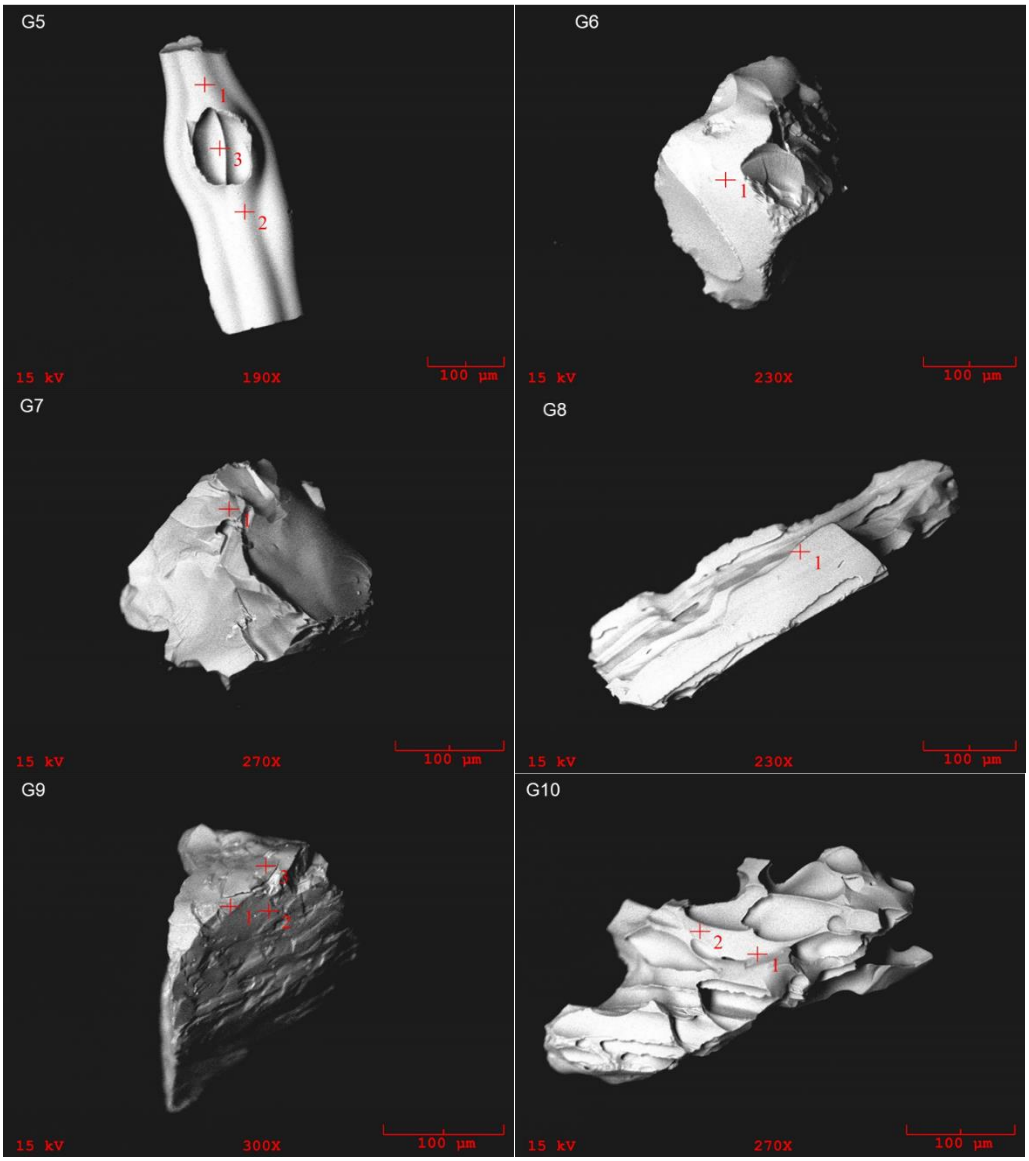

1232A-12H-1W-125 >210µ

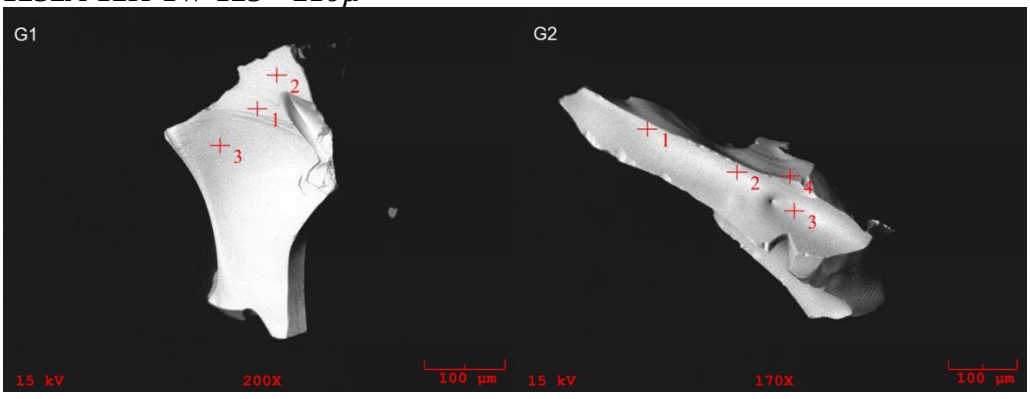

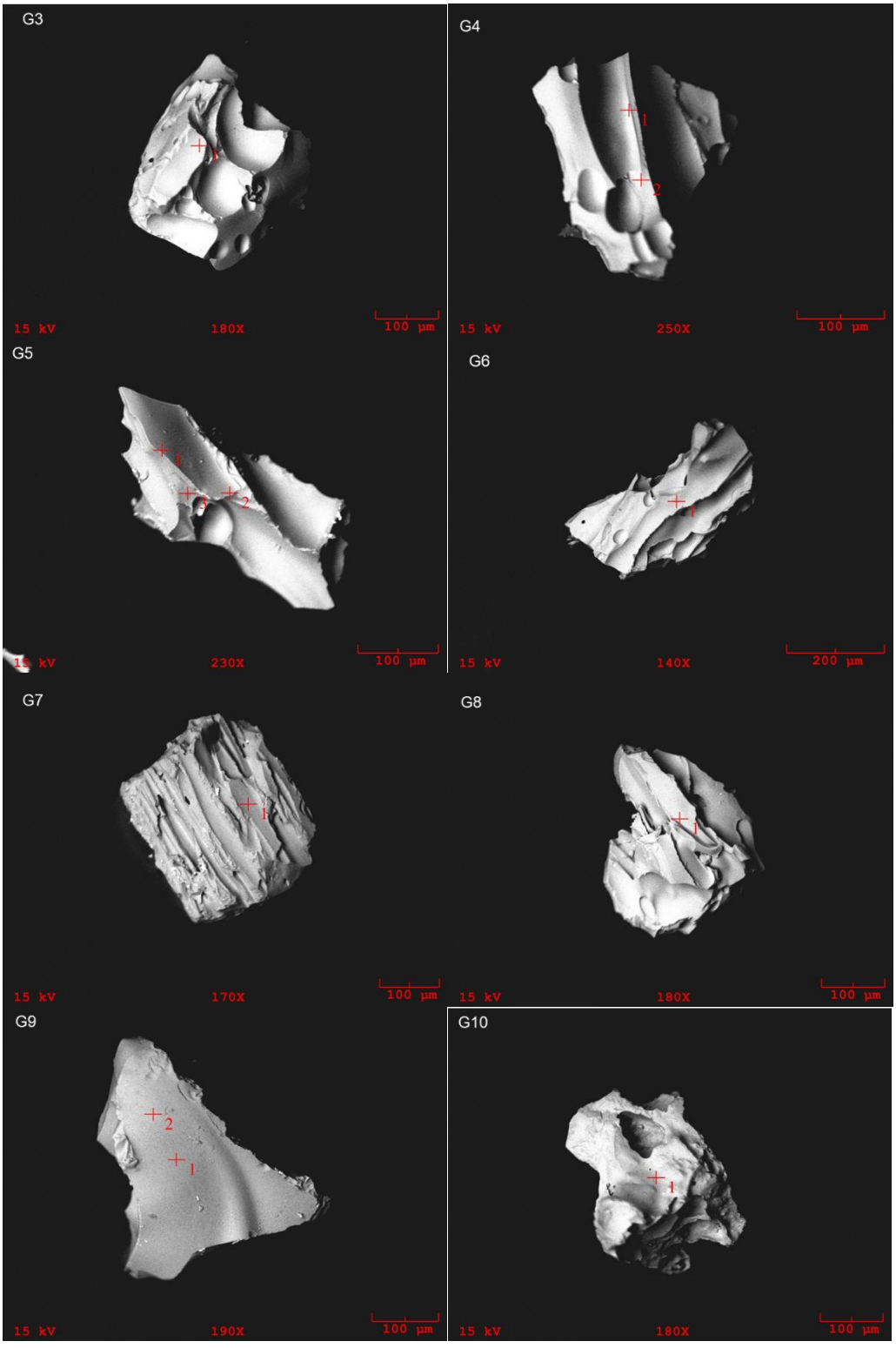

1232A-16X-1W-41 >149µ

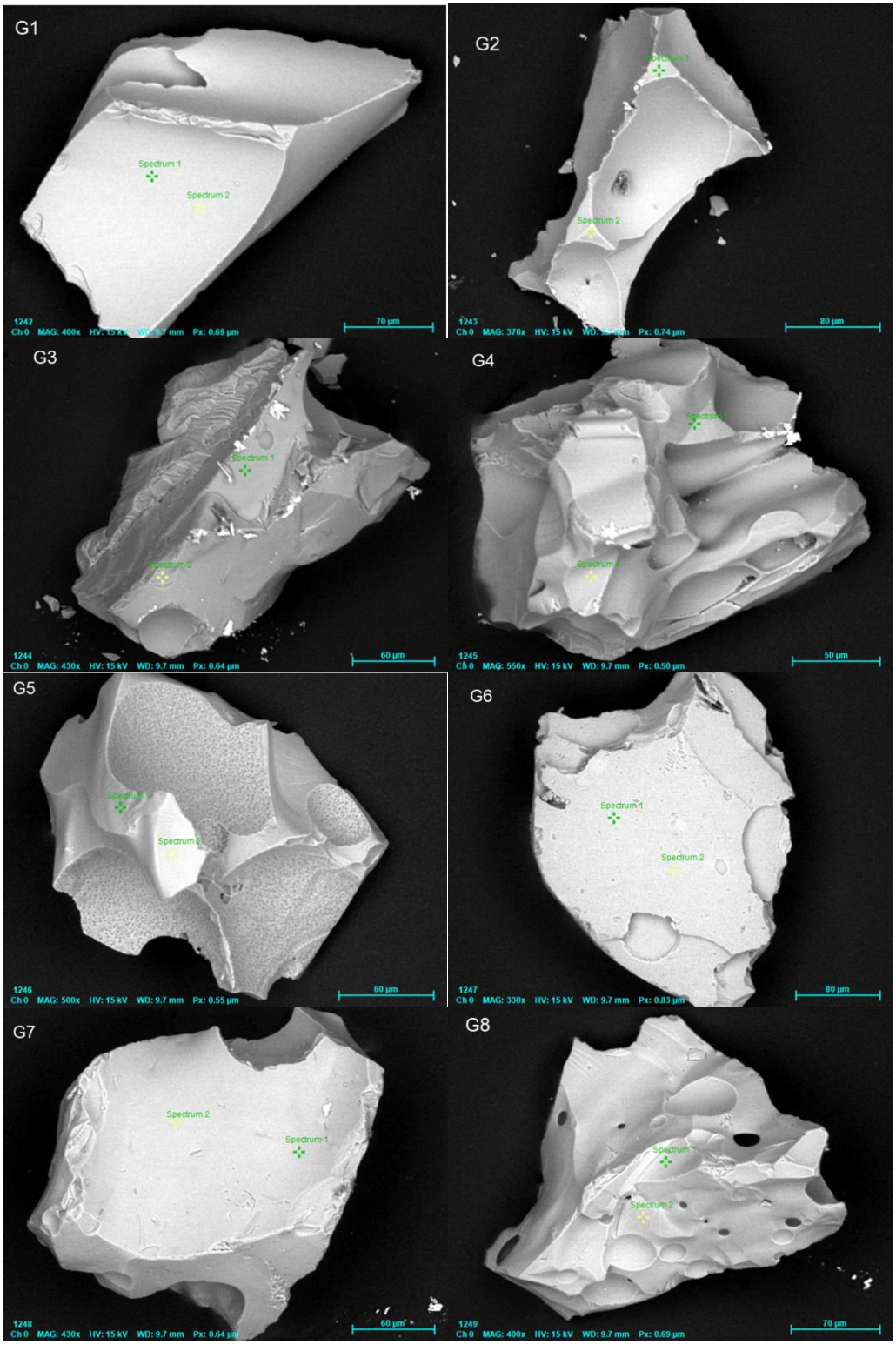
G1
Spectrum 1
Spectrum 2
1242
Ch 0 MAG: 400x HV: 15 kV WD: 9.7 mm Px: 0.69 µm
70 µm
G2
Spectrum 1
Spectrum 2
1243
Ch 0 MAG: 370x HV: 15 kV WD: 9.7 mm Px: 0.74 µm
80 µm
G3
Spectrum 1
Spectrum 2
1244
Ch 0 MAG: 430x HV: 15 kV WD: 9.7 mm Px: 0.64 µm
60 µm
G4
Spectrum 1
Spectrum 2
1245
Ch 0 MAG: 550x HV: 15 kV WD: 9.7 mm Px: 0.50 µm
50 µm
G5
Spectrum 1
Spectrum 2
1246
Ch 0 MAG: 500x HV: 15 kV WD: 9.7 mm Px: 0.55 µm
60 µm
G6
Spectrum 1
Spectrum 2
1247
Ch 0 MAG: 330x HV: 15 kV WD: 9.7 mm Px: 0.83 µm
80 µm
G7
Spectrum 2
Spectrum 1
1248
Ch 0 MAG: 430x HV: 15 kV WD: 9.7 mm Px: 0.64 µm
60 µm
G8
Spectrum 1
Spectrum 2
1249
Ch 0 MAG: 400x HV: 15 kV WD: 9.7 mm Px: 0.69 µm
70 µm

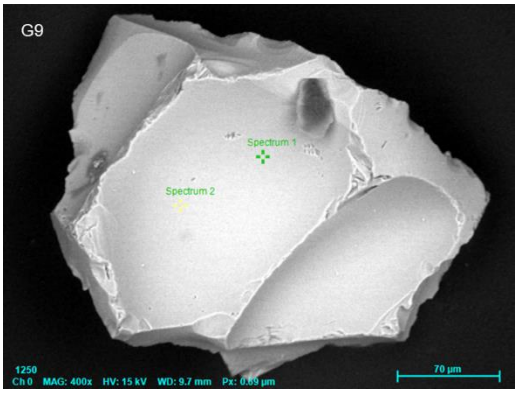

1232A-16X-1W-41 >210µ

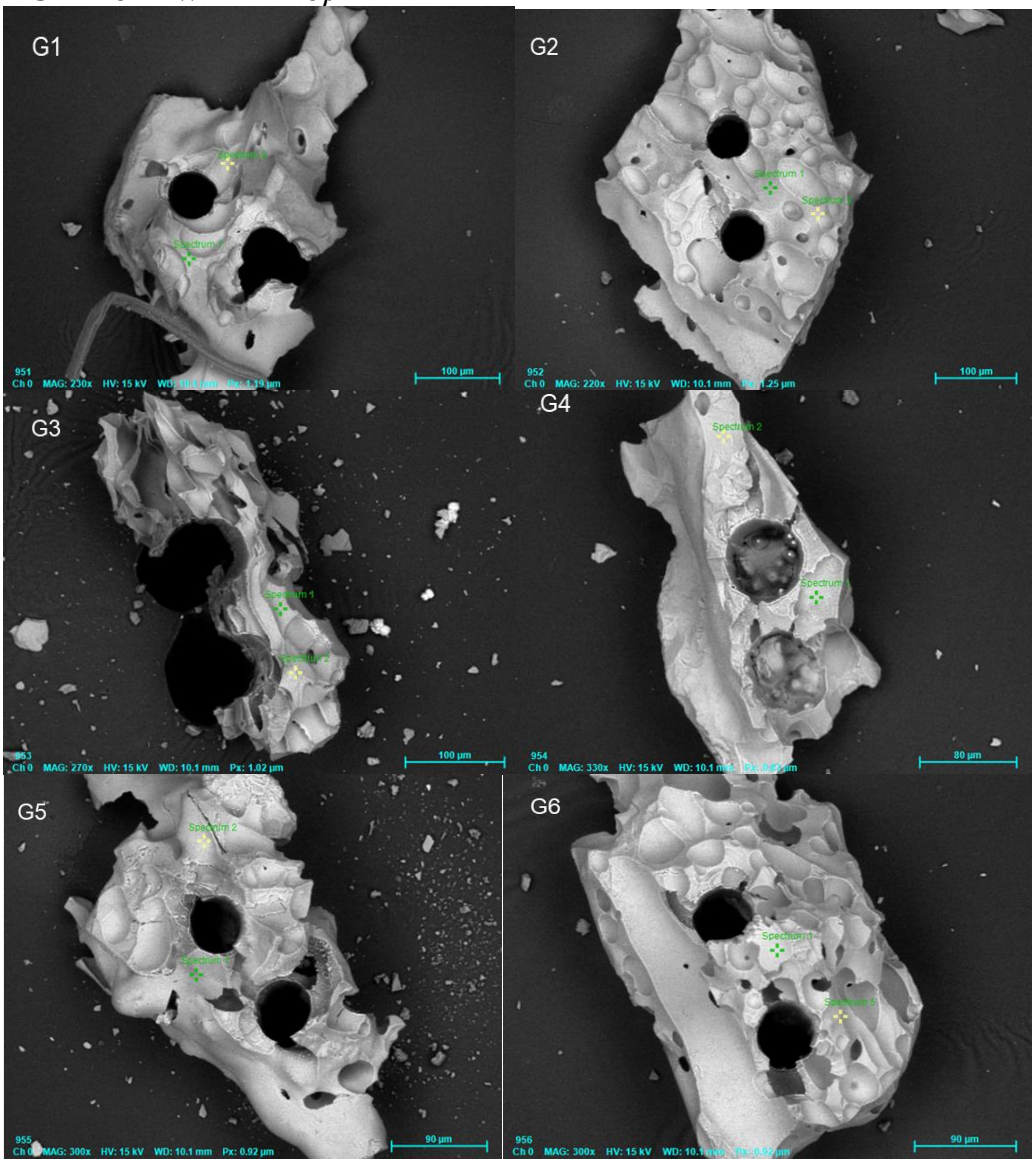

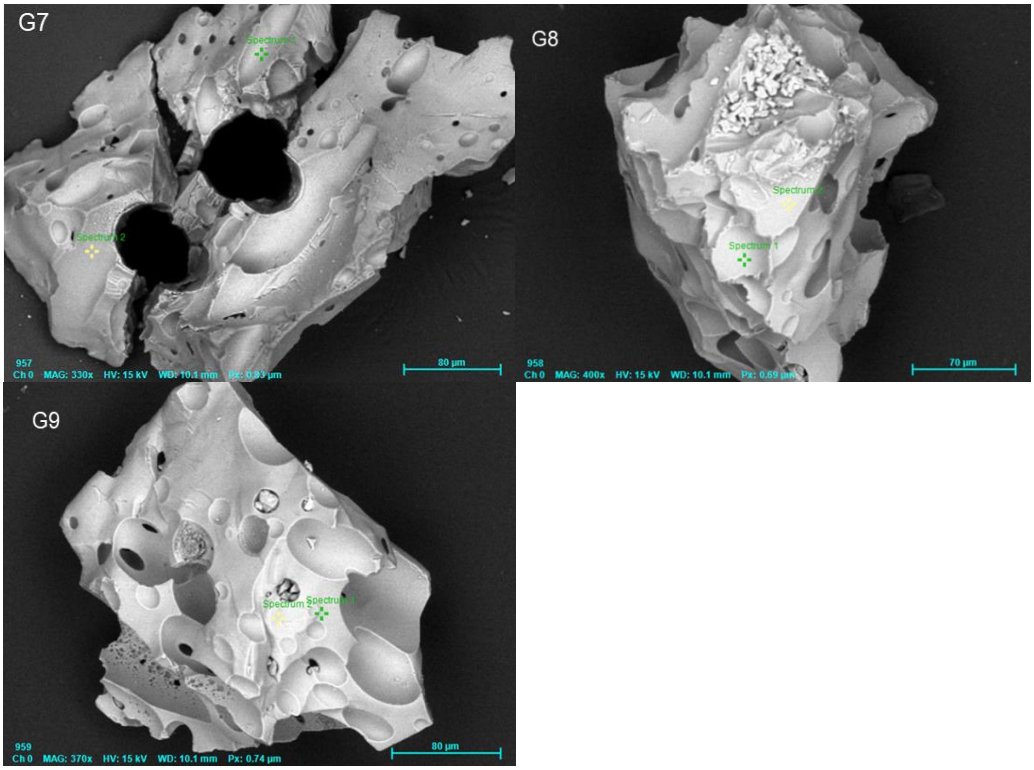

1232A-18X-1W-36 >149µ

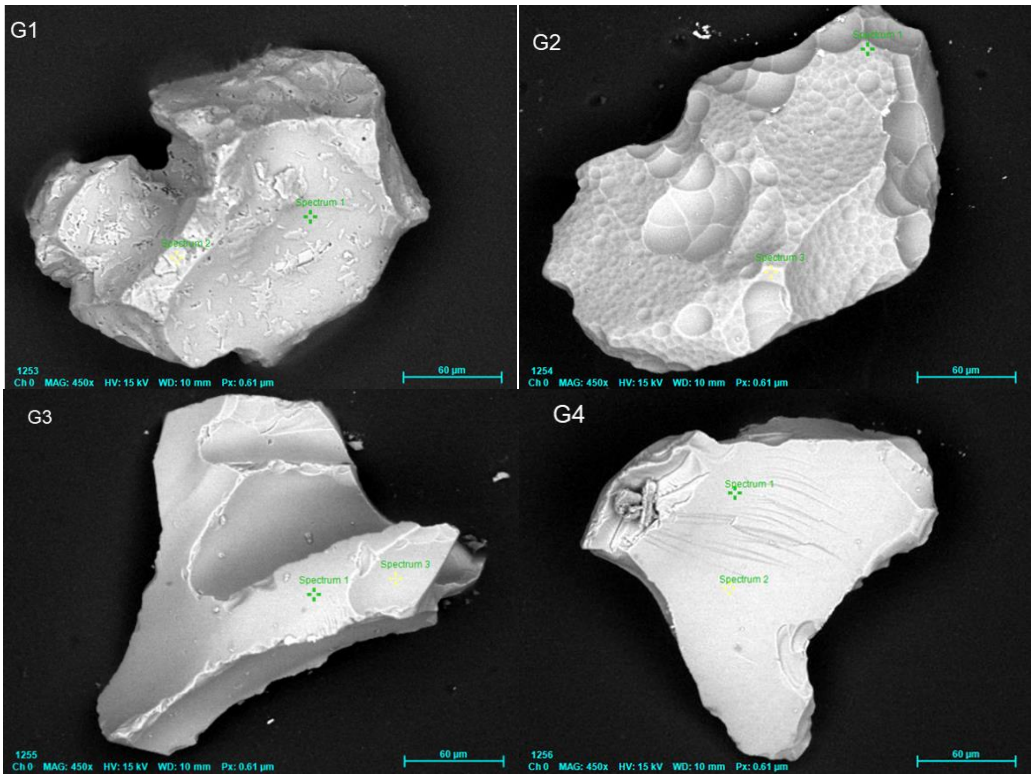

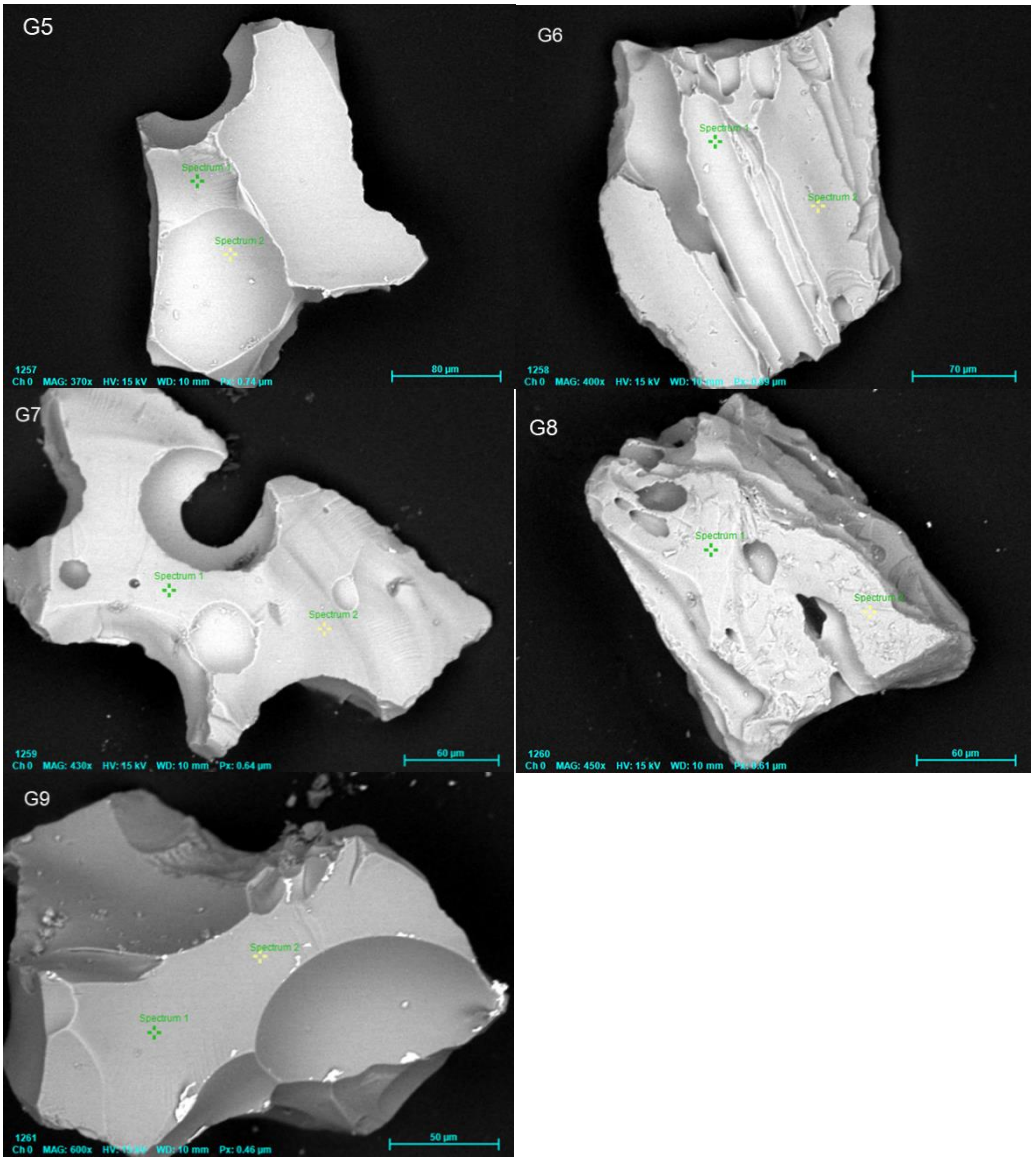

High resolution backscatter images of Site 1232B glass shards, taken using SEM

1232B-1H-2W-56 >149µ

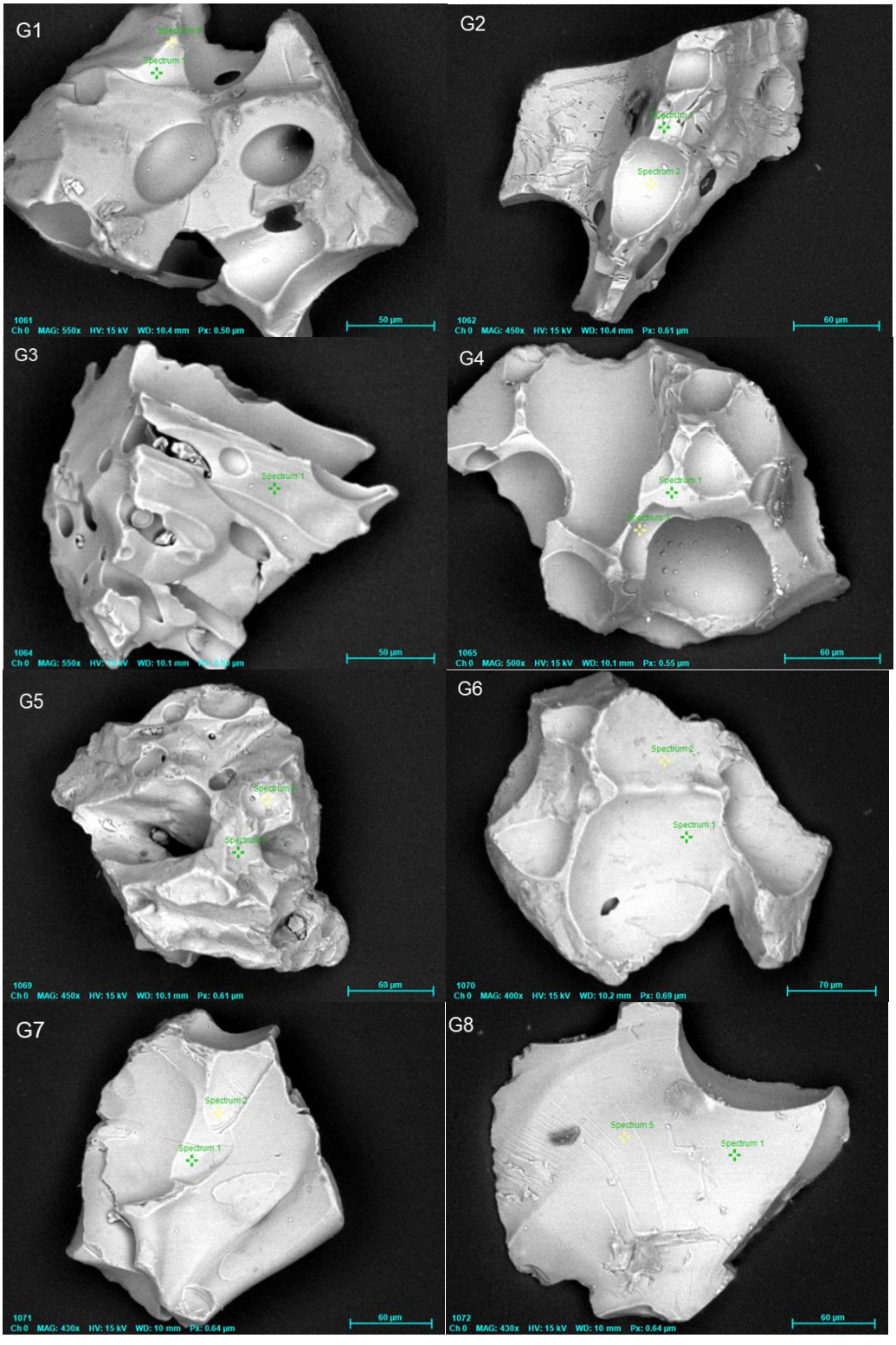
G1
Spectrum 1
1061
Ch 0 MAG: 550x HV: 15 kV WD: 10.4 mm Px: 0.50 µm
50 µm
G2
Spectrum 1
Spectrum 2
1062
Ch 0 MAG: 450x HV: 15 kV WD: 10.4 mm Px: 0.61 µm
60 µm
G3
Spectrum 1
1064
Ch 0 MAG: 550x
50 µm
G4
Spectrum 1
1065
Ch 0 MAG: 500x HV: 15 kV WD: 10.1 mm Px: 0.55 µm
60 µm
G5
Spectrum 1
1069
Ch 0 MAG: 450x HV: 15 kV WD: 10.1 mm Px: 0.61 µm
60 µm
G6
Spectrum 2
Spectrum 1
1070
Ch 0 MAG: 400x HV: 15 kV WD: 10.2 mm Px: 0.69 µm
70 µm
G7
Spectrum 2
Spectrum 1
1071
Ch 0 MAG: 430x HV: 15 kV WD: 10 mm Px: 0.64 µm
60 µm
G8
Spectrum 5
Spectrum 1
1072
Ch 0 MAG: 430x HV: 15 kV WD: 10 mm Px: 0.64 µm
60 µm

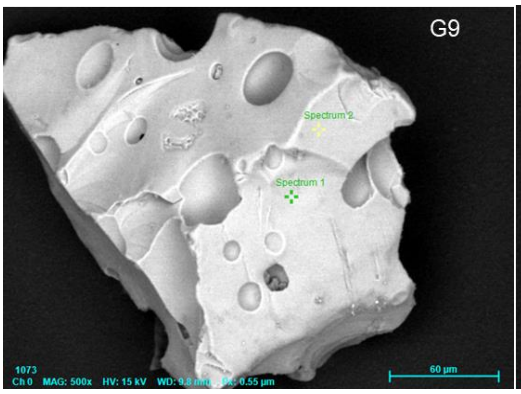

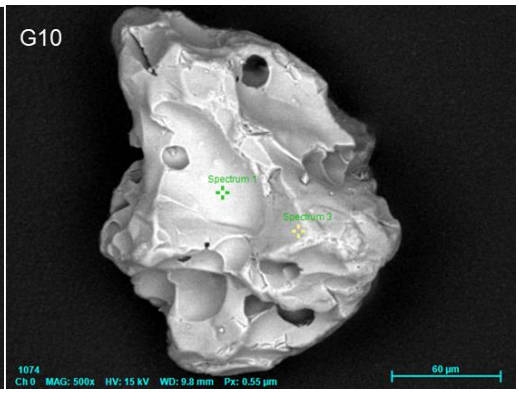

1232B-4H-1W-89 >149µ

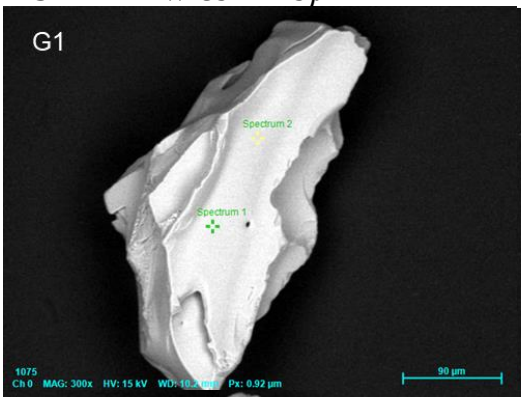

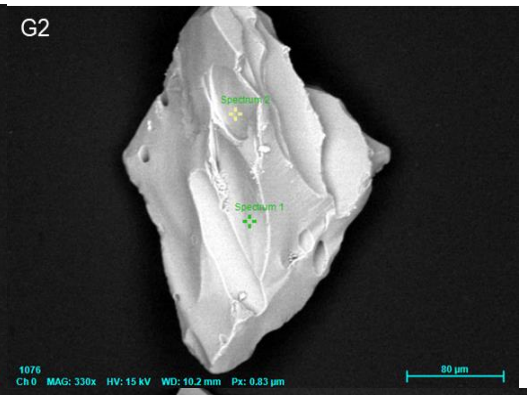

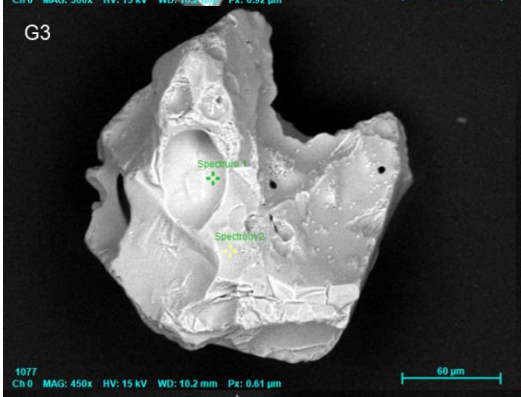

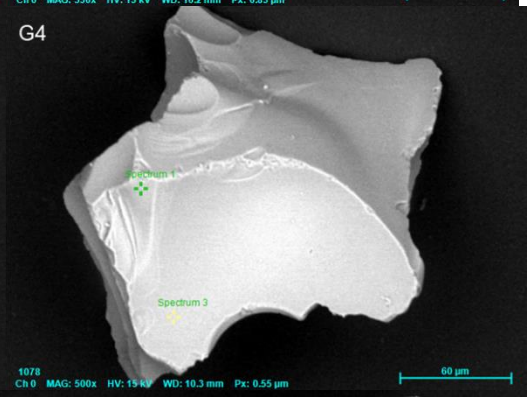

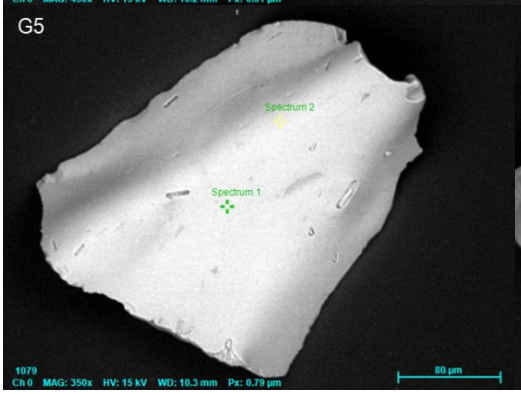

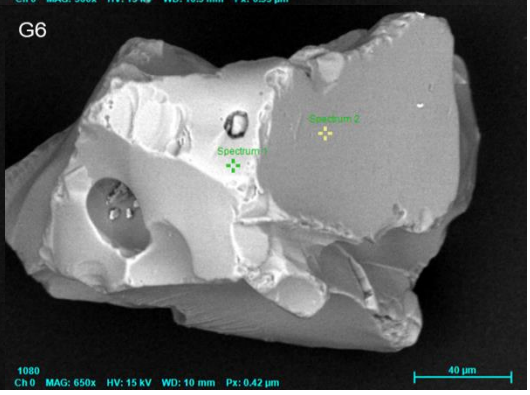

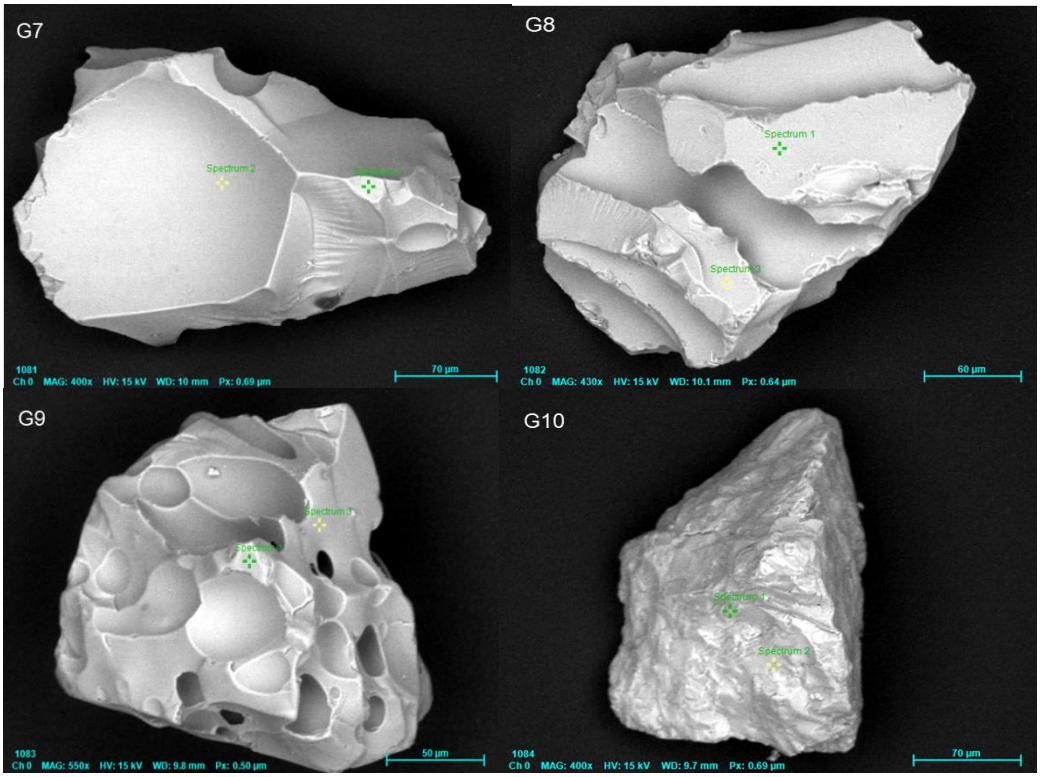

1232B-5H-5W-80 >149µ

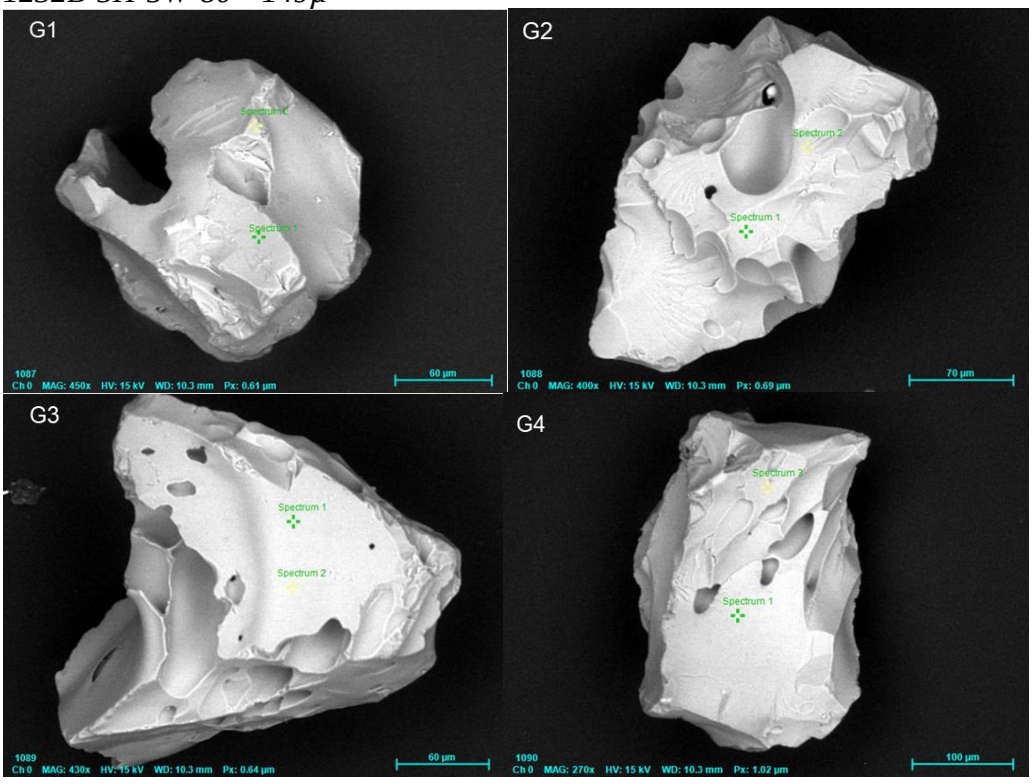

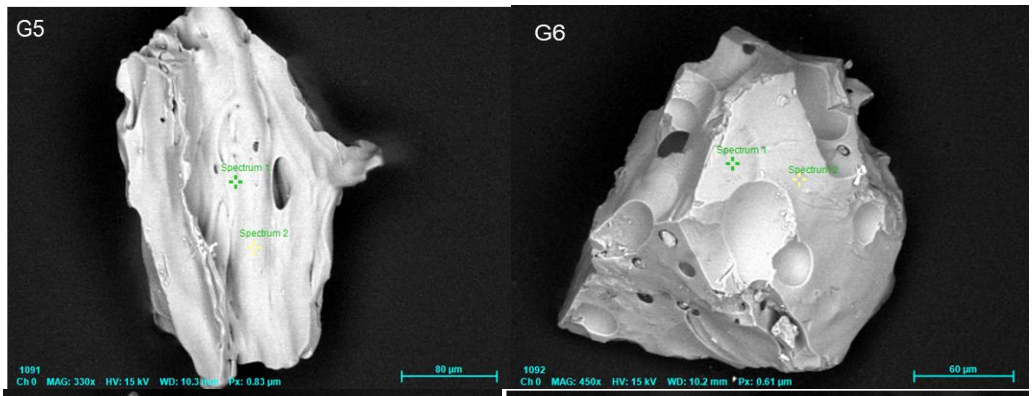

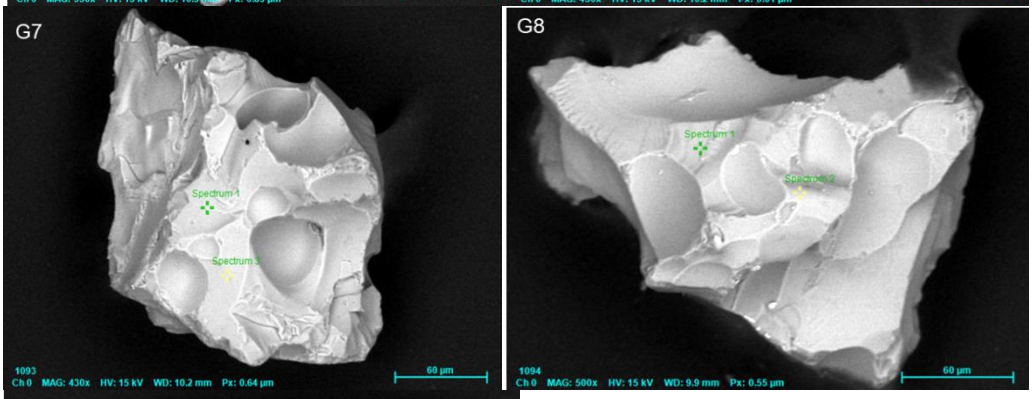

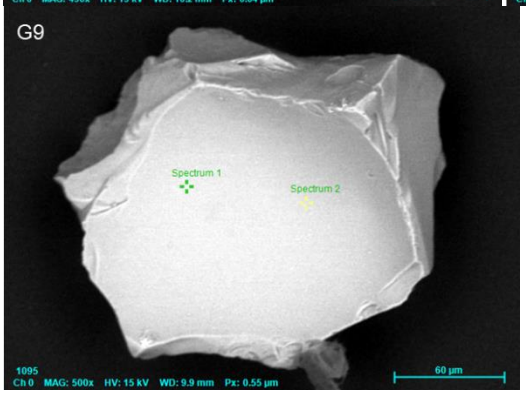

1232B-5H-5W-80 >210µ

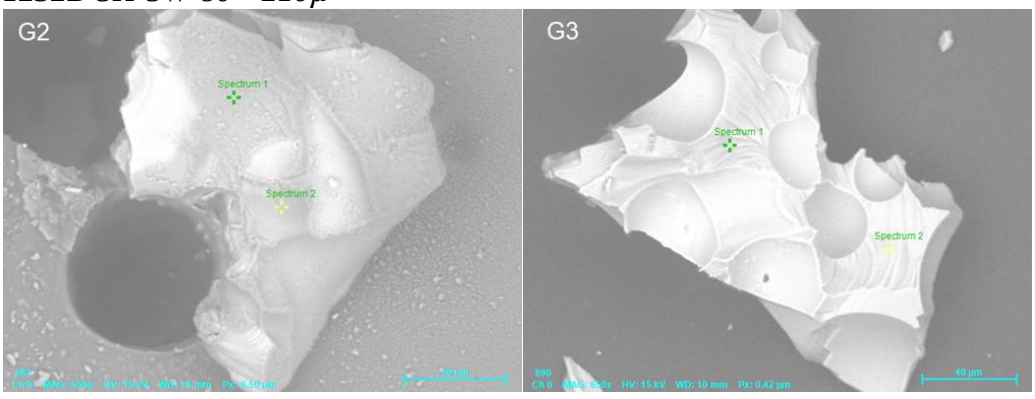

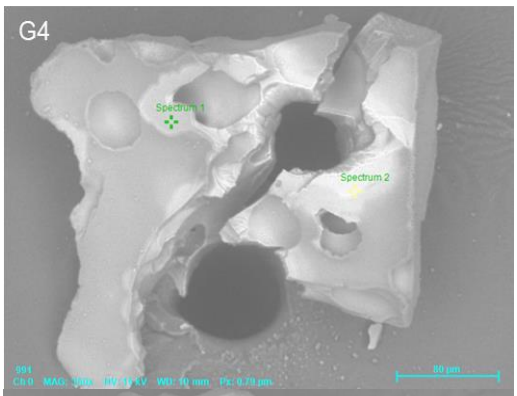

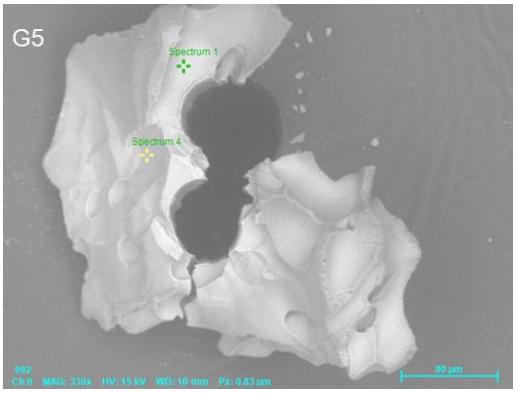

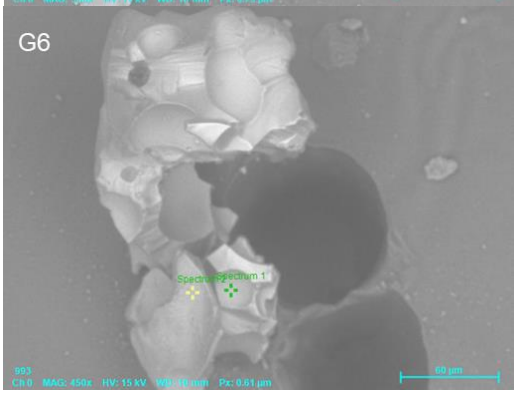

1232B-6H-7W-33 >149µ

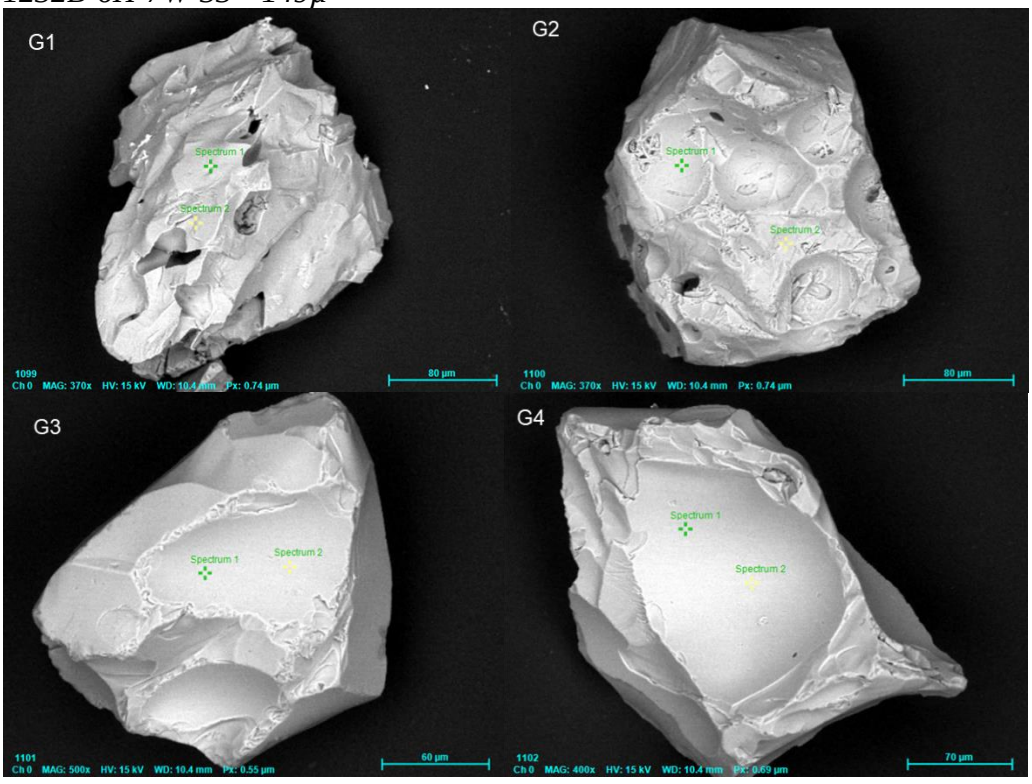

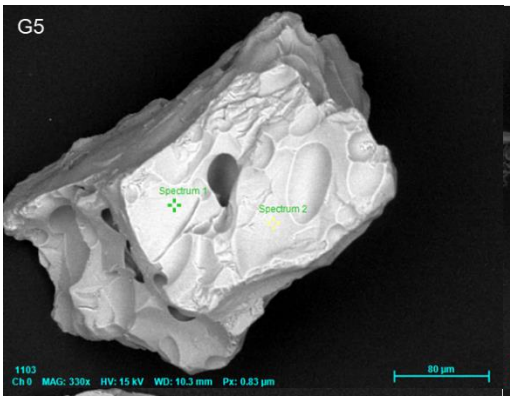

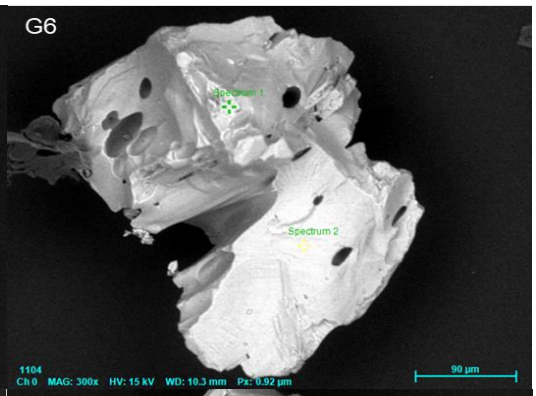

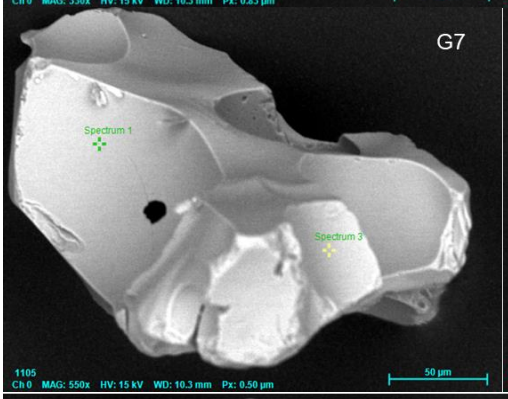

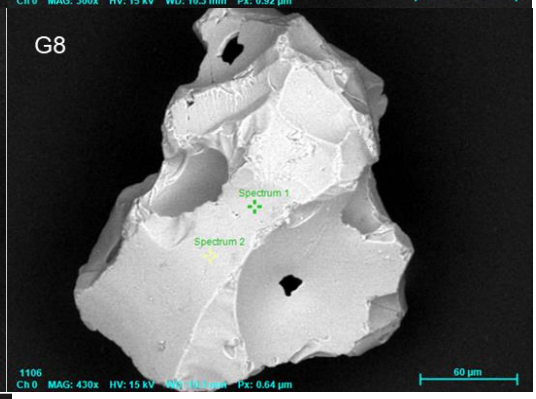

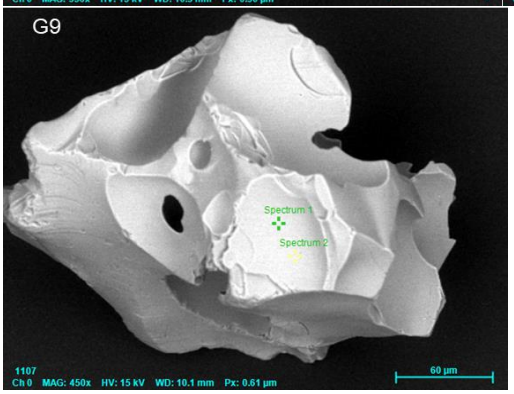

1232B-6H-7W-33 >210µ

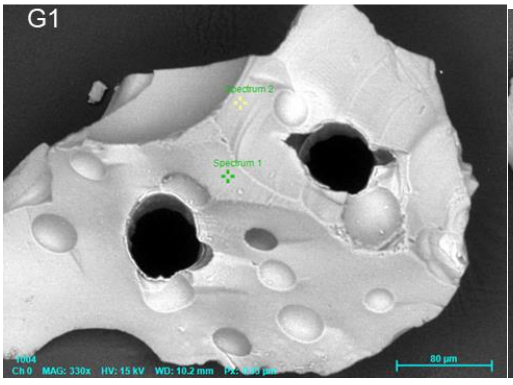

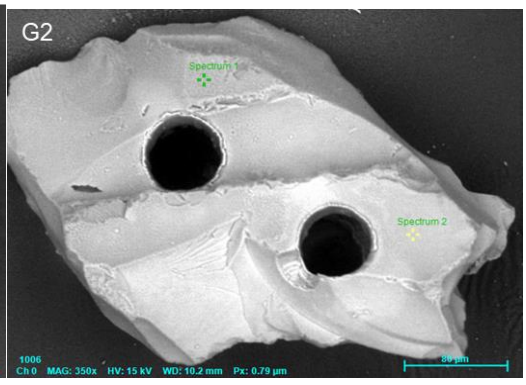

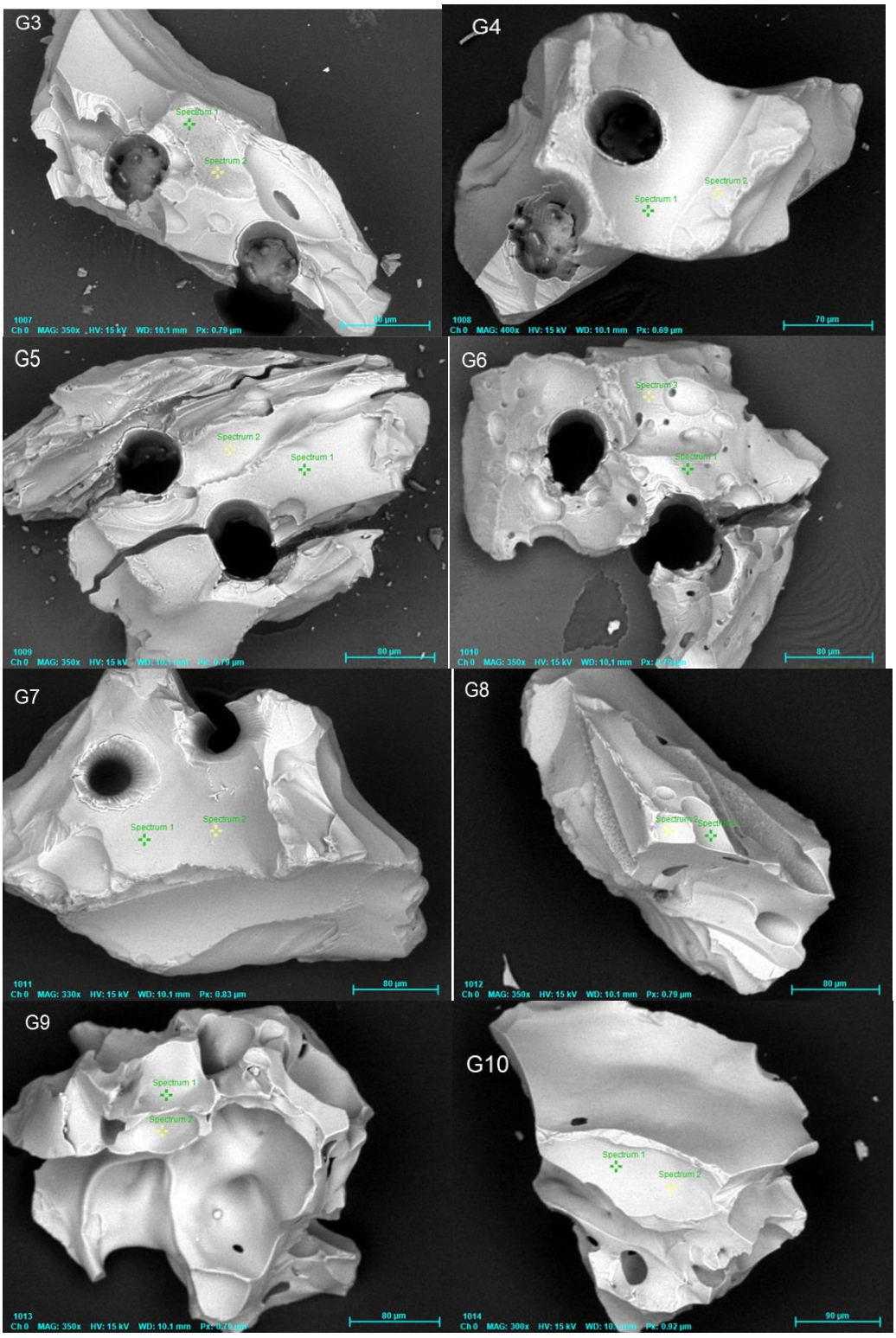

1232B-7H-2W-68 >149µ

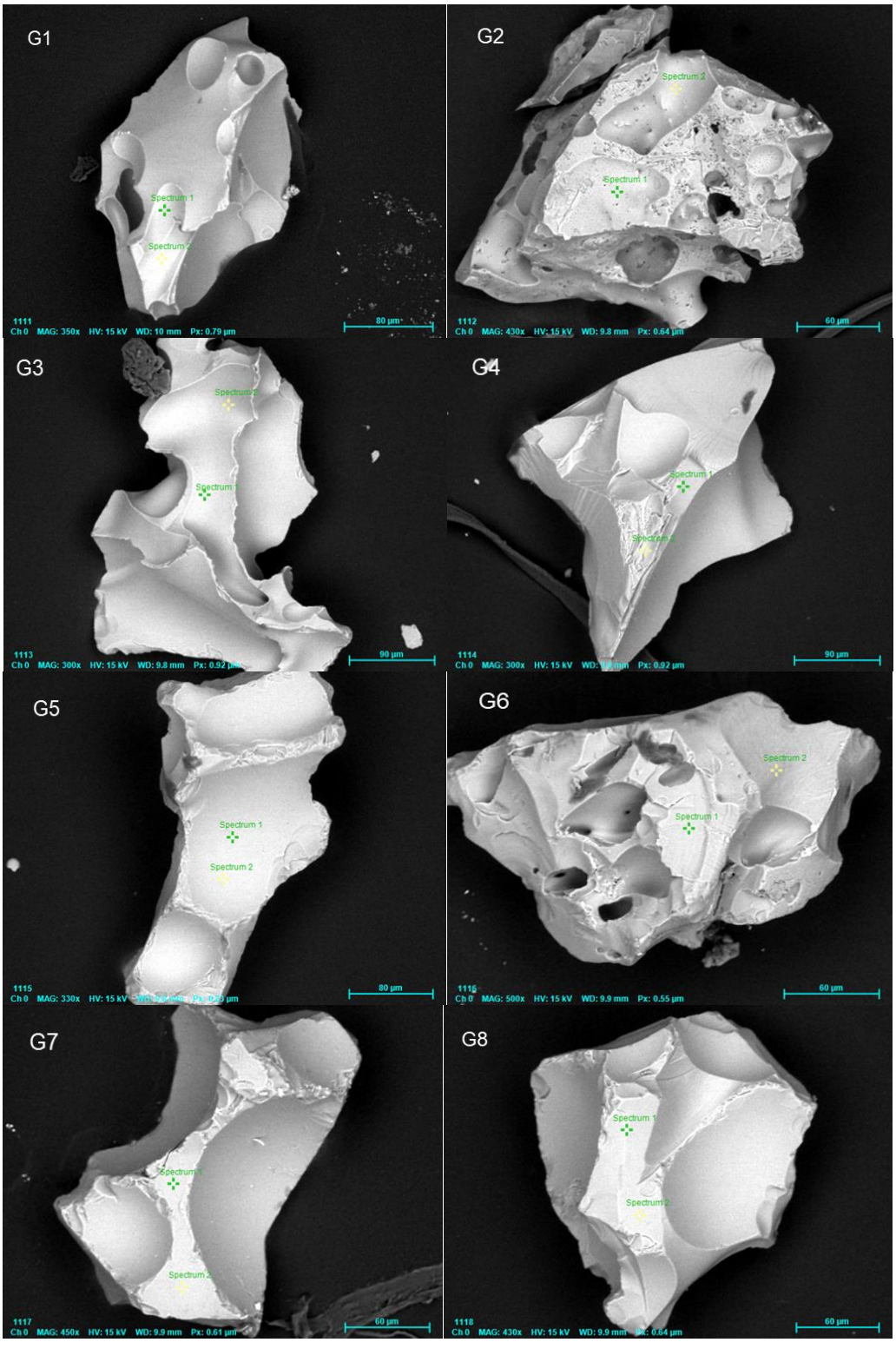
G1
Spectrum 1
Spectrum 2
1111
Ch 0 MAG: 350x HV: 15 kV WD: 10 mm Px: 0.79 µm
80 µm
G2
Spectrum 2
Spectrum 1
1112
Ch 0 MAG: 430x HV: 15 kV WD: 9.8 mm Px: 0.64 µm
60 µm
G3
Spectrum 2
Spectrum 1
1113
Ch 0 MAG: 300x HV: 15 kV WD: 9.8 mm Px: 0.92 µm
90 µm
G4
Spectrum 1
Spectrum 2
1114
Ch 0 MAG: 300x HV: 15 kV
Px: 0.92 µm
90 µm
G5
Spectrum 1
Spectrum 2
1115
Ch 0 MAG: 330x HV: 15 kV
80 µm
G6
Spectrum 2
Spectrum 1
1116
Ch 0 MAG: 500x HV: 15 kV WD: 9.9 mm Px: 0.55 µm
60 µm
G7
Spectrum 1
Spectrum 2
1117
Ch 0 MAG: 450x HV: 15 kV WD: 9.9 mm Px: 0.61 µm
60 µm
G8
Spectrum 1
Spectrum 2
1118
Ch 0 MAG: 430x HV: 15 kV WD: 9.9 mm Px: 0.64 µm
60 µm

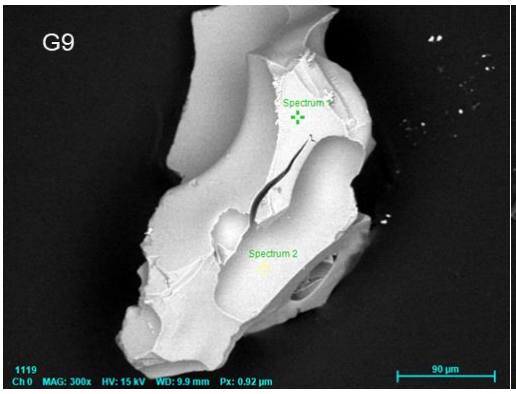

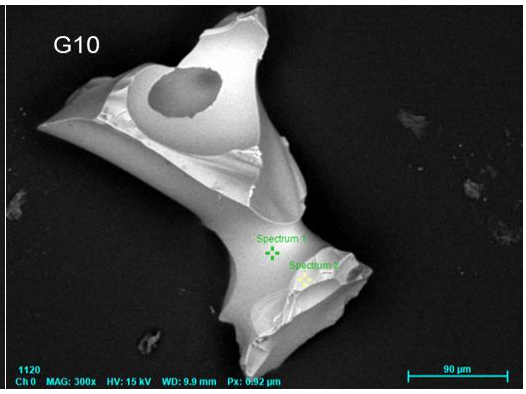

1232B-7H-2W-68 >210µ

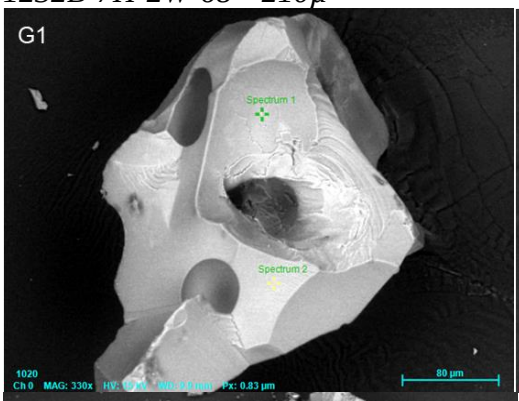

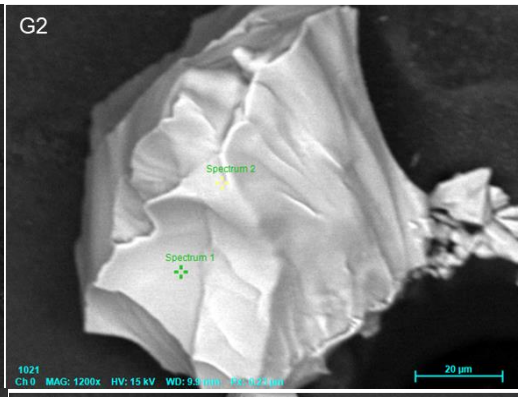

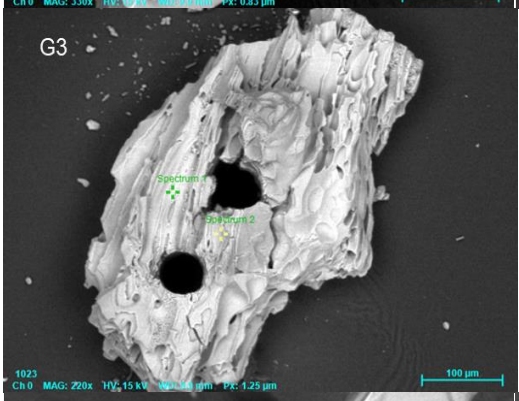

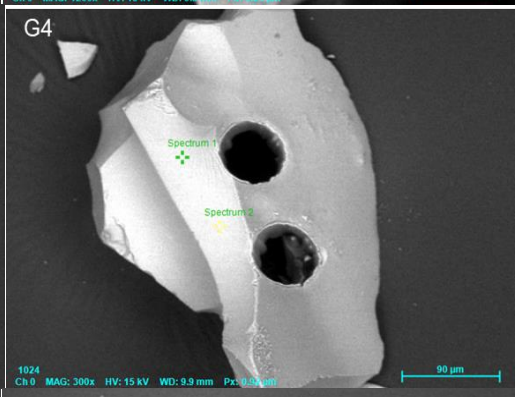

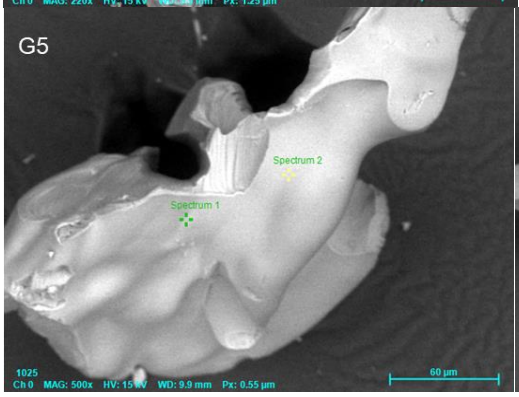

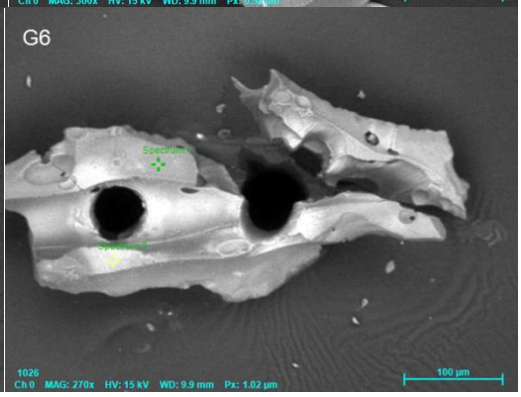

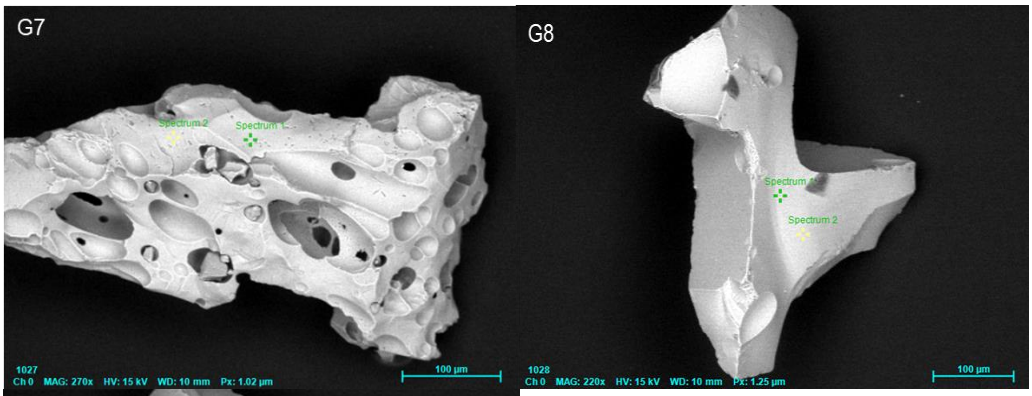

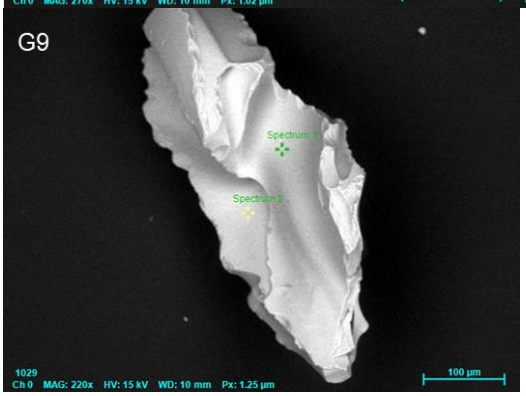

1232B-7H-3W-70 >149µ

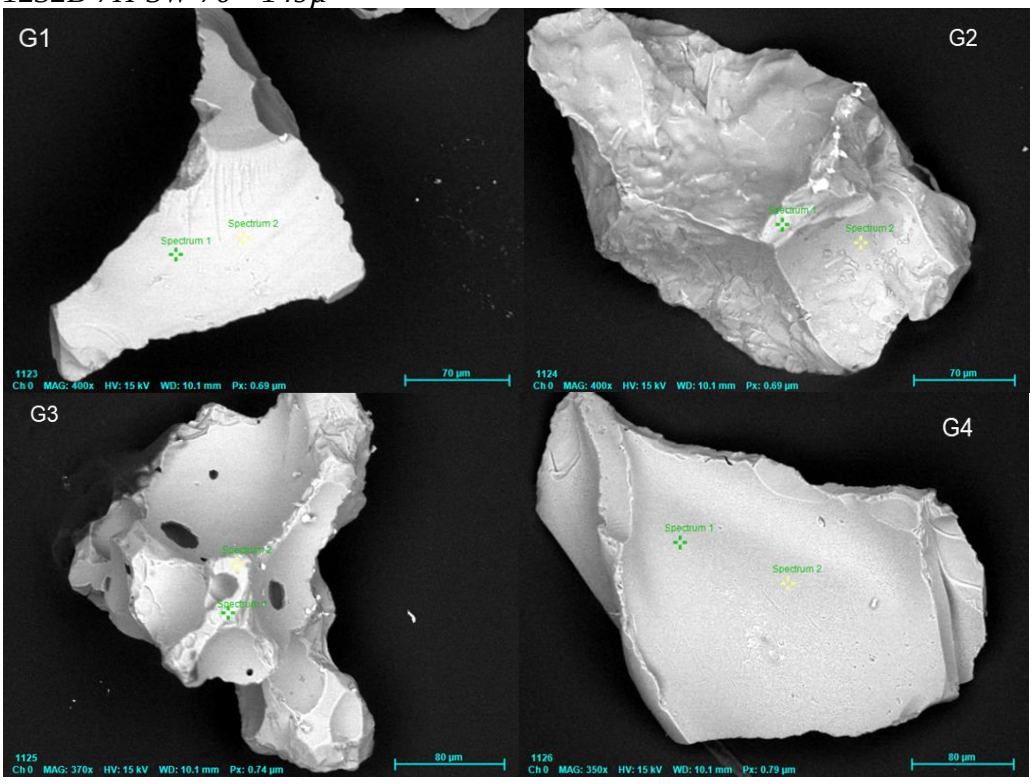

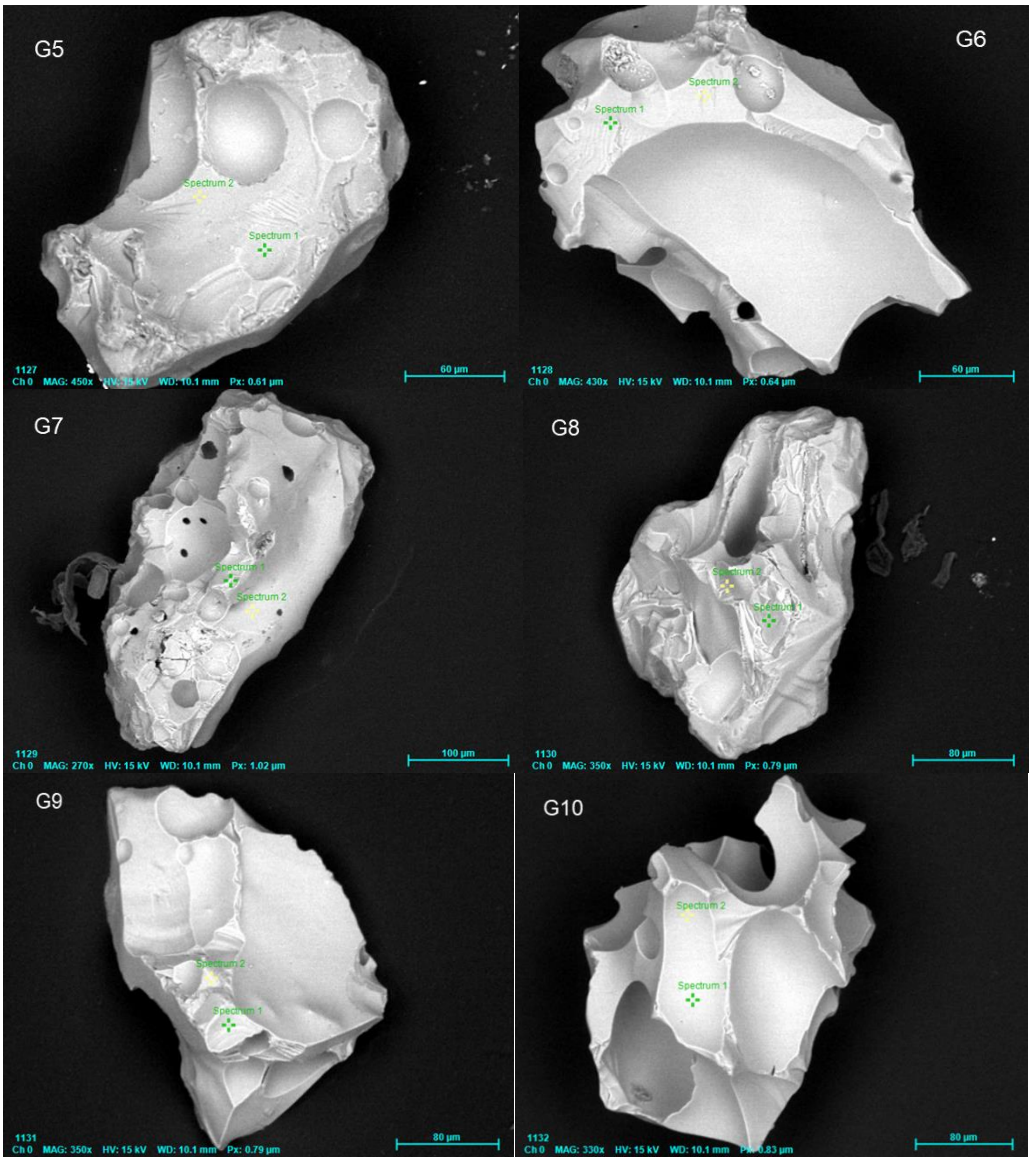

1232B-7H-3W-70 >210µ

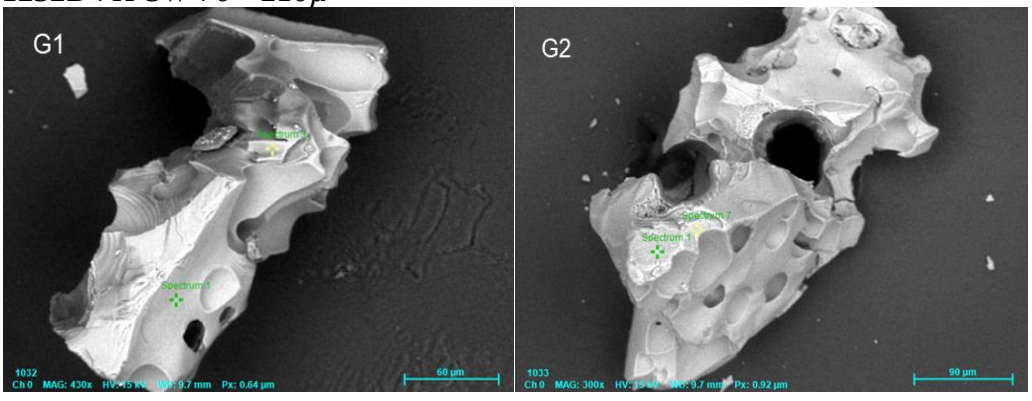

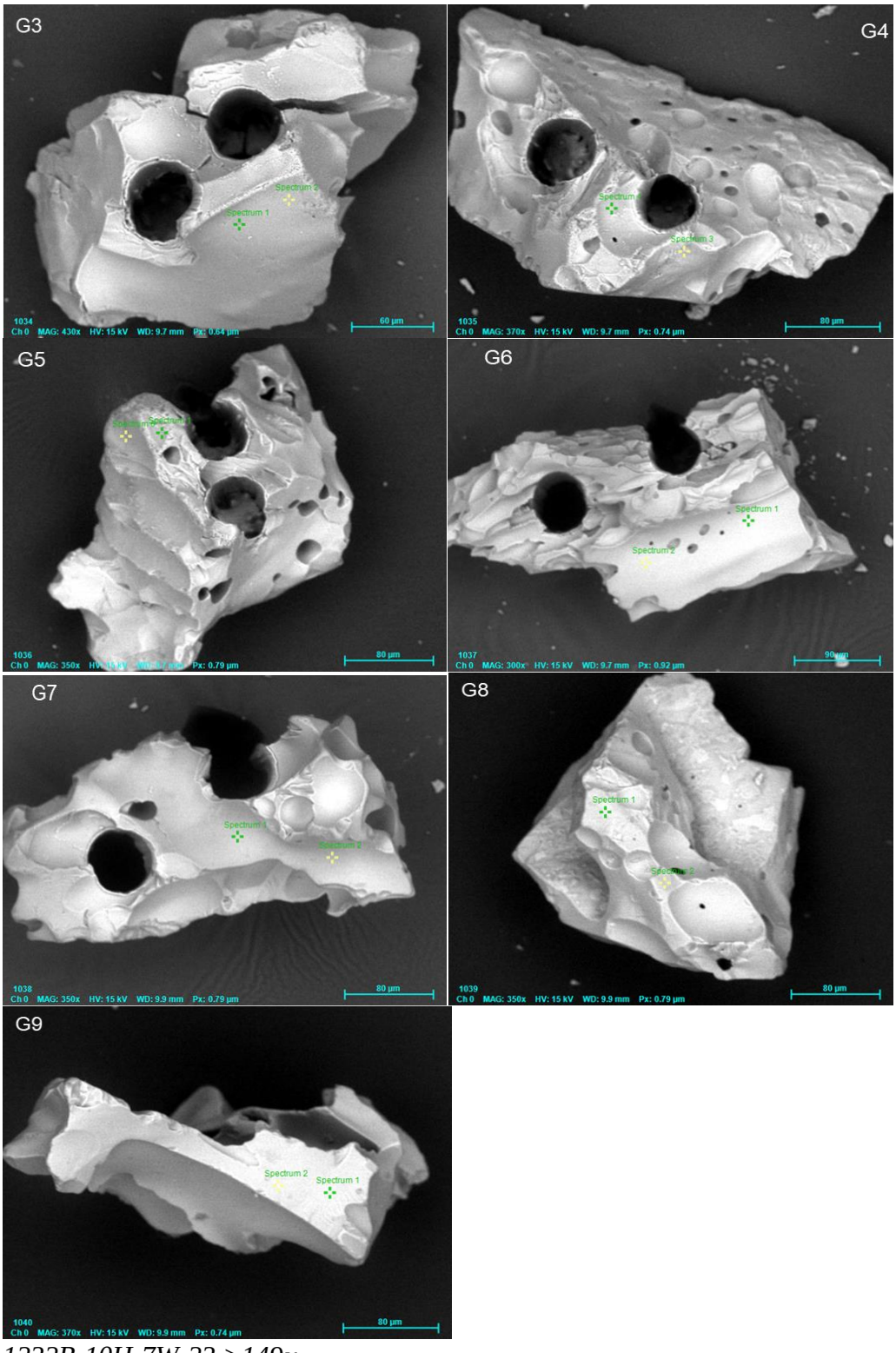

1232B-10H-7W-23 >149µ

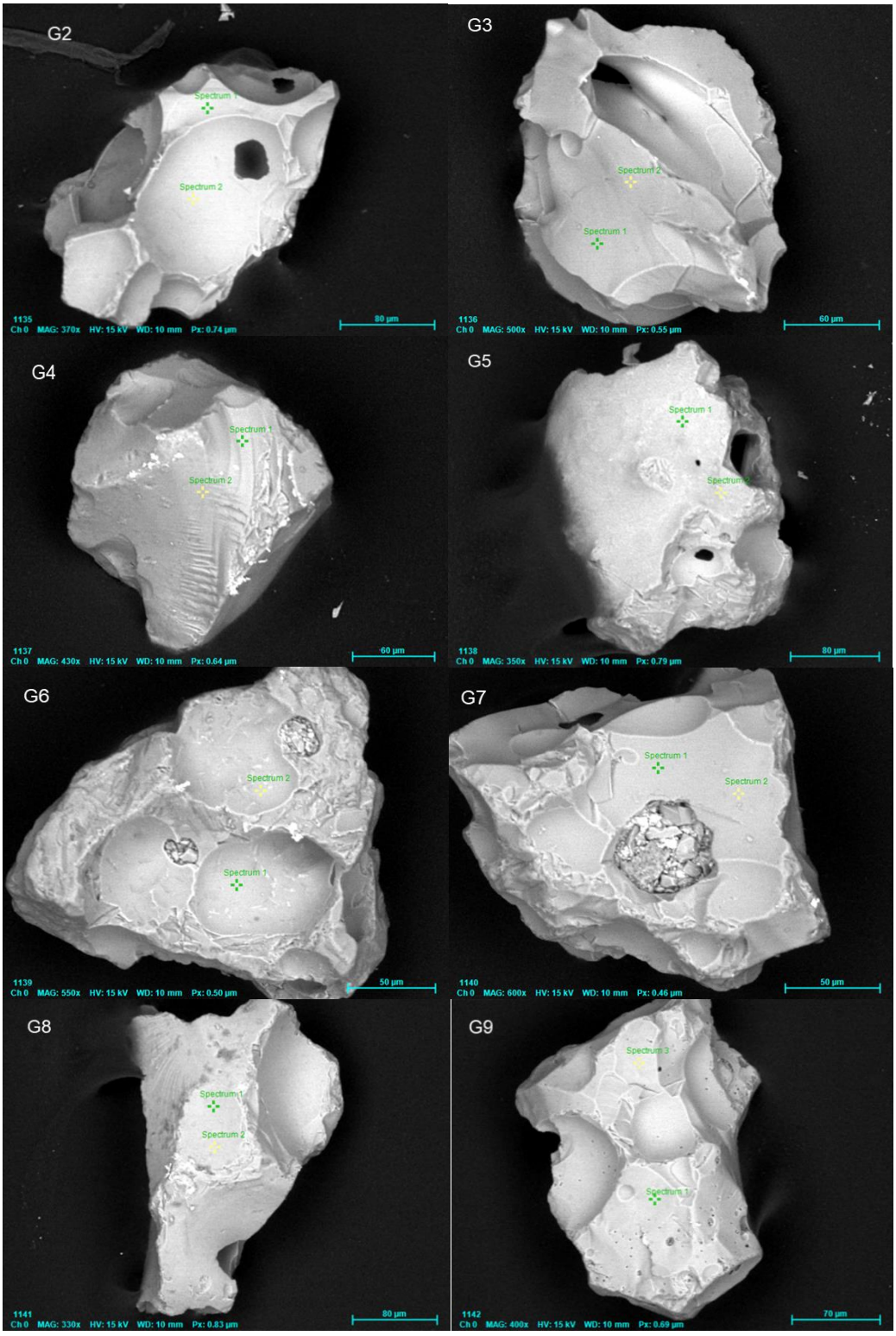

1232B-10H-7W-23 >210µ

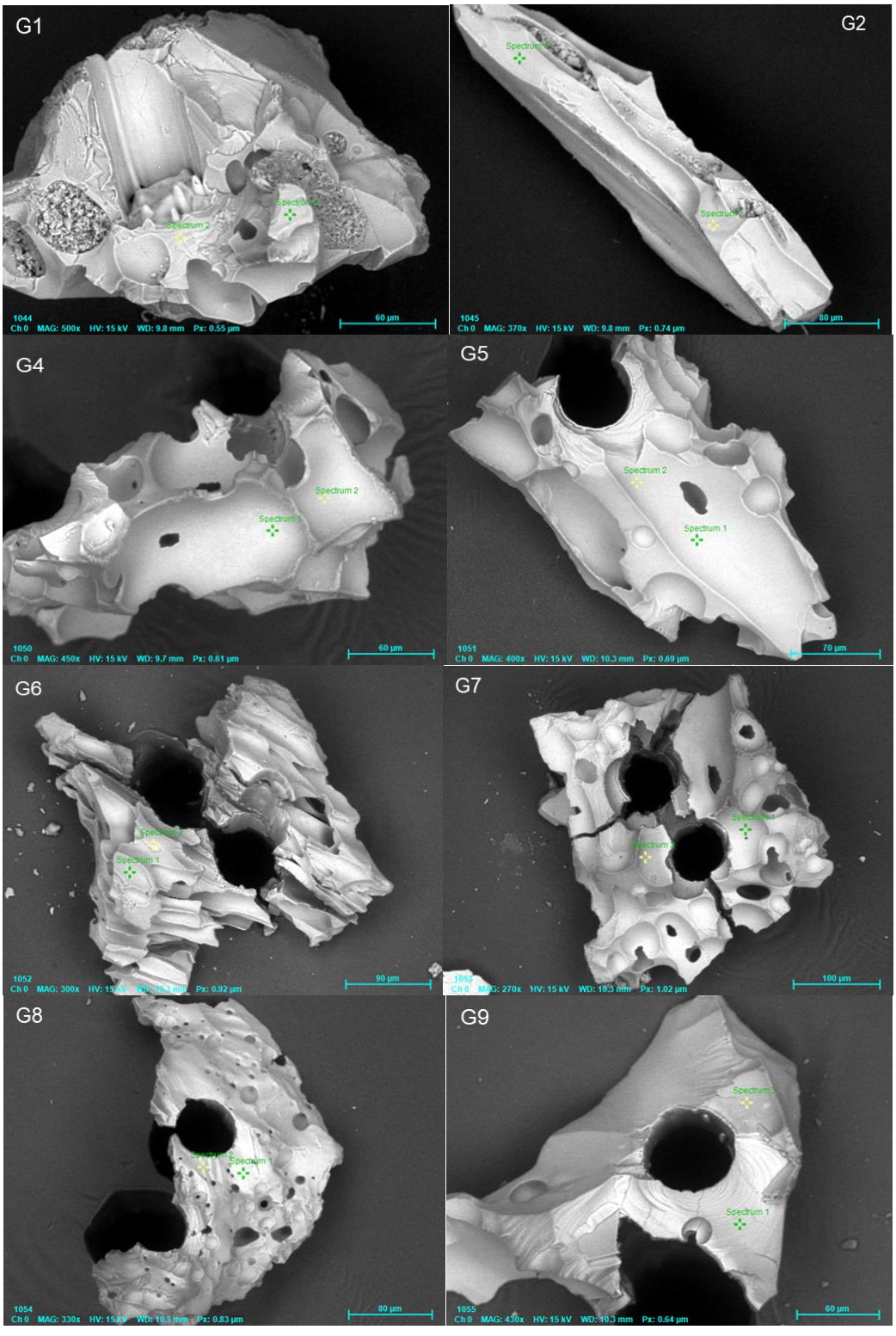
G1
Spectrum 2
1044
Ch 0 MAG: 500x HV: 15 kV WD: 9.8 mm Px: 0.55 µm
60 µm
G2
Spectrum 1
1045
Ch 0 MAG: 370x HV: 15 kV WD: 9.8 mm Px: 0.74 µm
80 µm
G4
Spectrum 2
Spectrum 1
1050
Ch 0 MAG: 450x HV: 15 kV WD: 9.7 mm Px: 0.61 µm
60 µm
G5
Spectrum 2
Spectrum 1
1051
Ch 0 MAG: 400x HV: 15 kV WD: 10.3 mm Px: 0.69 µm
70 µm
G6
Spectrum 1
90 µm
G7
100 µm
G8
80 µm
G9
Spectrum 1
60 µm

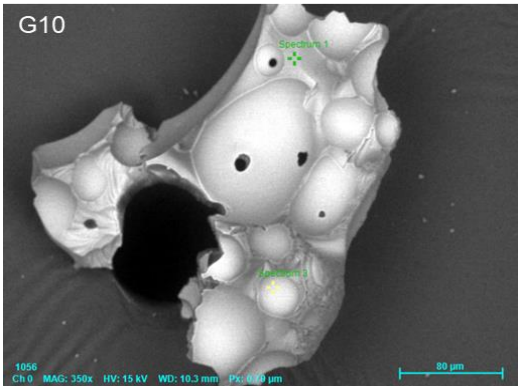
G10
Spectrum 1
Spectrum 2
1056
Ch 0 MAG: 350x HV: 15 kV WD: 10.3 mm
80 µm

VITA

KIMBERLY BECK

2004-2006	A.A., Elementary Education Broward College Ft. Lauderdale, Florida
2007-2012	B.S., Geosciences Florida International University Miami, Florida
2012	Award for Outstanding Service to the Department of Earth and Environment, College of Arts and Sciences
2012-2015	M.S., Geosciences Florida International University Miami, Florida
2015-2022	Ph.D., Earth Systems Sciences Florida International University Miami, Florida
2019	GSA Graduate Student Research Grant Recipient SEPM Student Research Grant Awardee
2020	Outstanding Poster Presentation Earth and Environment Graduate Research Symposium
2012-2021	Teaching Assistant Florida International University Miami, Florida
2022-2022	Adjunct Florida International University Miami, Florida

PUBLICATIONS AND PRESENTATIONS

- Manuscript in press, at Journal of South American Earth Sciences Beck, K., Hickey-Vargas, R., "Composition, Age and Origin of Pleistocene Turbidite Deposits at ODP Site 1232, Nazca Plate: Implications for Volcanism and Climate Change in Central South Chile" https://doi.org/10.1016/j.jsames.2022.103908.

- Department of Earth and Environment Graduate Research Symposium, Florida International University, March 6, 2020. Volcanic Glass in Nazca Plate Sediments at ODP Site 1232: Geochemical, Proportional and Temporal Variation

- Geological Society of America Annual Meeting, Phoenix, Arizona, September 22-26, 2019. Volcanic Glass in Nazca Plate Sediments at ODP Site 1232: Origin and Transport

- Department of Earth and Environment Graduate Research Symposium, Florida International University, February 22, 2019. A Detailed Investigation into the Provenance, Composition and Transport Processes of Pleistocene-Recent Turbidite Sediments of the SE Nazca Plate, ODP Site 1232

- Geological Society of America Annual Meeting, Baltimore, Maryland, November 1-4, 2015. Investigation of the Lead Isotope Signatures of Marine Sediments in Relation to the Lead Isotope Signatures of Northern Andean Ores